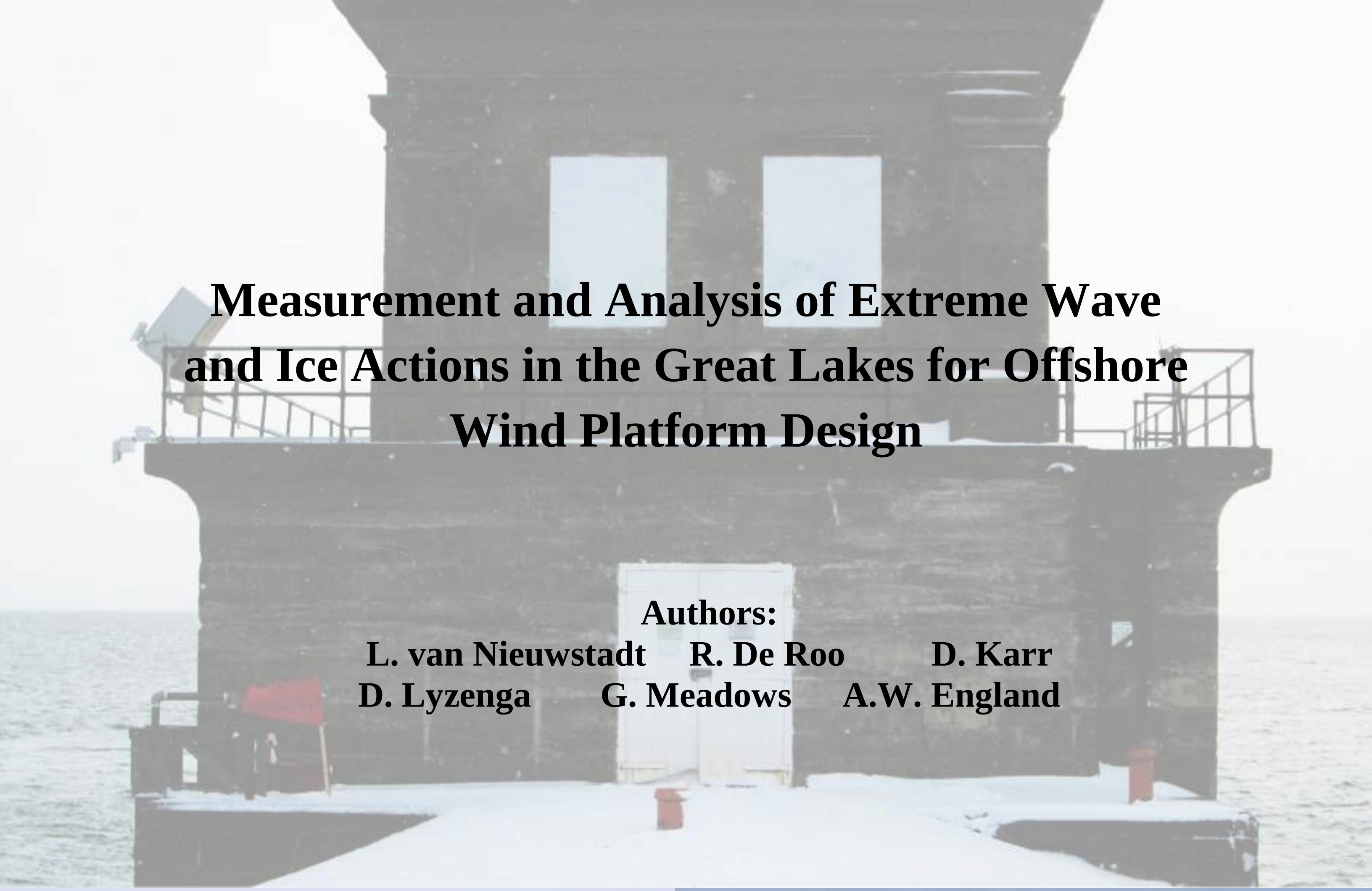

Measurement and Analysis of Extreme Wave and Ice Actions in the Great Lakes for Offshore Wind Platform Design

Authors:

L. van Nieuwstadt R. De Roo D. Karr

D. Lyzenga G. Meadows A.W. England

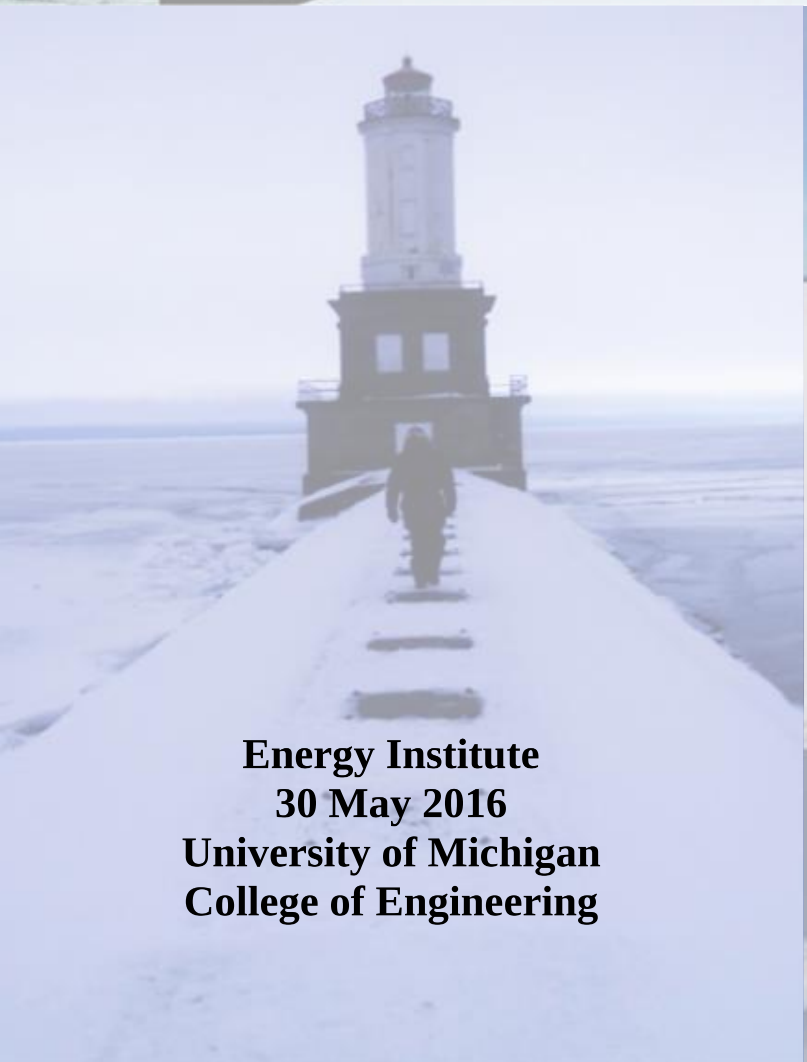

Energy Institute

30 May 2016

University of Michigan

College of Engineering

PARTICIPANTS & OTHER COLLABORATING ORGANIZATIONS

Individuals:

Prof. England, Principal Investigator, led the readjustments to the Project and the conceptual design of the Wideband AR ice thickness sensor, invested 15% effort and supported by the Project at 5%.

Prof. Meadows, Collaborator and Project Advisor, led the search for a more appropriate observation site, and secured the necessary permissions to use one of the entry lighthouses on the Keewenaw Waterway, unpaid support.

Prof. Karr, Co-Investigator, led development of the Ice Force Measuring System, supported by the Project based upon actual effort invested.

Dr. DeRoo, Co-Investigator, served as design engineer for the WiBAR ice thickness sensor and ISS, supported by the project based upon actual effort invested.

Dr. Lyzenga, Research Scientist, led development of the Scene Capture System instrument

Mr. D. Boprie, Senior Electronics Technician, fabrication support

Mr. R. Rizor, Electrical/Mechanical Designer, mechanical design and fabrication support.

Dr. J. Van Noord, Lead Engineer in Research (Mechanical), mechanical design support

Ms. E. Wong, graduate student, contributed to the design of the analog front end of the WiBAR sensor, unpaid support as a Masters level degree project.

Mr. N. Garg, graduate student, contributed to the design of IFSM, supported graduate student by Prof. Karr.

Ms. Y. Zhang, graduate student, contributed to the design of IFSM, data collection and data analysis, supported graduate student by Prof. Karr.

Mr. H. Nejadi, Ph.D. candidate, contributed to the WiBAR sensor development, focusing on the theoretical system analysis and system integration and test.

Mr. A. Venkitasubramony, graduate student, contributed to the development and implementation of the WiBAR, SCS, and ISS (DC power budget, solar panel selection)

Mr. K. Patel, undergraduate student, contributed to the mechanical engineering tasks of the WiBAR and WISN instruments mounting to the lighthouse platform.

Mr. B. Perkins, engineer, contributed to the ISS embedded system firmware.

Mr. T. Doyle, engineer, contributed to the ISS embedded system firmware and WISN operations phase.

Mr. C. Lachner, undergraduate student, contributed to the ISS embedded system firmware and WISN operations phase.

Mr. M. Irish, undergraduate student, contributed to the historical wave, wind, ice study.

Ms. S. Polisuk, undergraduate student, contributed to the historical wave, wind, ice study.

Ms. M. Chavez, undergraduate student, contributed to the historical wave, wind, ice study.

Dr. L. van Nieuwstadt, research scientist, served as systems engineer and project manager, 15% appointment support.

Ms. Shelly Sherman, administration officer for the Project, support covered by Indirect Cost

Mr. Bruno Vanzieleghem, Assistant Director of Operations, University of Michigan Energy Institute, contributes to the management requirements of the Project, supported by the project based upon actual effort invested

External Organizations:

- Collaboration with Michigan Technological University Great Lakes Research Center (Mr. M. Abbott, Mr. J. Anderson, Mr. C. Tyrell)
- Data analysis contribution by Mr. C. Kontoes, Nortek Inc. – Acoustic Wave and Current profiler
- Data analysis contribution by Dr. M. van Nieuwtadt – ice thickness historical study

Submitted to: DOE EERE – Wind & Water Power Program, DE-EE0005376

In fulfillment of contract awarded to the Regent of the University of Michigan, 073133571

TABLE OF CONTENTS

1 EXECUTIVE SUMMARY

This project, funded by the Department of Energy as DE-EE0005376, successfully measured wind-driven lake ice forces on an offshore structure in Lake Superior through one of the coldest winters in recent history. While offshore regions of the Great Lakes offer promising opportunities for harvesting wind energy, these massive bodies of freshwater also offer extreme and unique challenges. Among these challenges is the need to anticipate forces exerted on offshore structures by lake ice. The parameters of interest include the frequency, extent, and movement of lake ice, parameters that are routinely monitored via satellite, and ice thickness, a parameter that has been monitored at discrete locations over many years and is routinely modeled. Essential relationships for these data to be of use in the design of offshore structures and the primary objective of this project are measurements of maximum forces that lake ice of known thicknesses might exert on an offshore structure.

Our strategy for observing ice forces versus ice thickness was to instrument an existing offshore structure in a location on the Great Lakes that likely would be exposed to massive ice interactions during most winters. The Statement of Work for the project proposed two winter observing seasons with the option of a third winter observing season if the first two seasons had anomalously light ice cover. The schedule was based upon a start date in late fall of 2011. The actual start date was not until late spring of 2012, which did not leave enough time before the winter of 2012-13 to select a Great Lakes Observing Site (GLOS), and to design, build, and test even a rudimentary Wind and Ice Sensing Network (WISN). We chose the alternate path of using the first winter observing season, the winter of 2012-13, to examine several sites, one of which, Lake Superior's South Entry Light of the Keweenaw Waterway, became our GLOS for the winter of 2013-14, and to test a breadboard version of a new concept for remotely measuring snowpack and freshwater ice thickness, the Wideband Autocorrelation Radiometer (WiBAR). As the first field implementation of WiBAR, we felt it advisable to validate our design in an actual field setting before committing to its inclusion in our WISN for the primary observing season. The decision to make the winter of 2013-14 our primary observing season was fortuitous in that, as one of the coldest winters on recent record, ice on Lake Superior was near a historical maximum, allowing us to delete the possible option of a third observing season.

As previously noted, full scale, physical measurements of wave and ice force processes in sufficient detail to guide design decisions in the harsh winter environment of Lake Superior are challenging. Our successful acquisition of these measurements required development and deployment of WISN through our primary observing season, the winter and spring of 2013-2014. Using a cell phone command and data link and solar power, WISN operated autonomously for periods of days at a time. It sensed ice thicknesses using two techniques, (1) a combination of measured ice-surface height from digital photogrammetry and measured distance from lake-bottom to ice-base from an Acoustic Doppler Current Profiler (ADCP), and (2) a direct measure of ice thickness from the experimental WiBAR system. WISN sensed ice forces using a load cell, referred to as the Ice Force Measuring System (IFMS), which was designed, built, calibrated, and deployed at the GLOS for this task. Sophisticated data analytics allowed us to recover best estimates of ice thickness and pressure applied by the ice for the two-foot width of our load cell.

Processed ice thickness data from WiBAR (Chapter 6) and from combined digital photogrammetry (Chapter 7) and ADCP (Chapter 8) are placed in an historical context (Chapter

10) and summarized in Figure 1.1. Our observed ice thickness data are clearly consistent with historical temporal trends. The few outliers in the WiBAR data are discussed in Chapter 6.

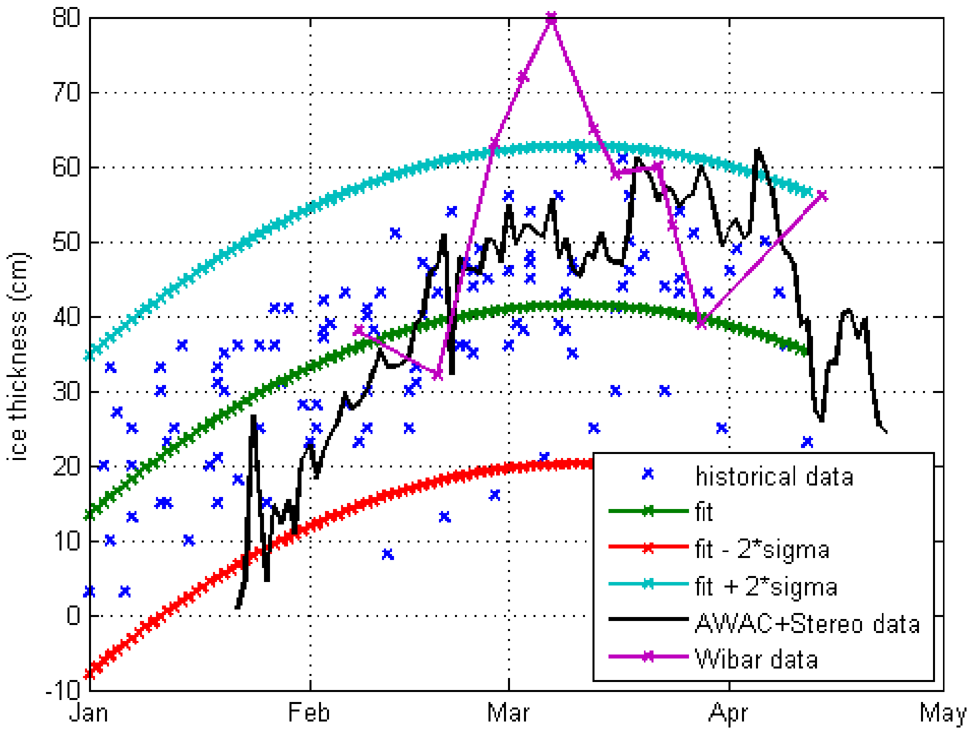

Figure 1.1. Observed ice thicknesses and their historical context at the South Entry Light of the Keweenaw Waterway during the winter of 2013-14.

Maximum inferred ice pressures as a function of time-of-year are summarized in Figure 1.2. IFMS instrumentation and data analysis for these measurements are described in Chapter 5 where maximum ice pressures are also compared with ice force measurements reported in the literature for other load cell structural widths.

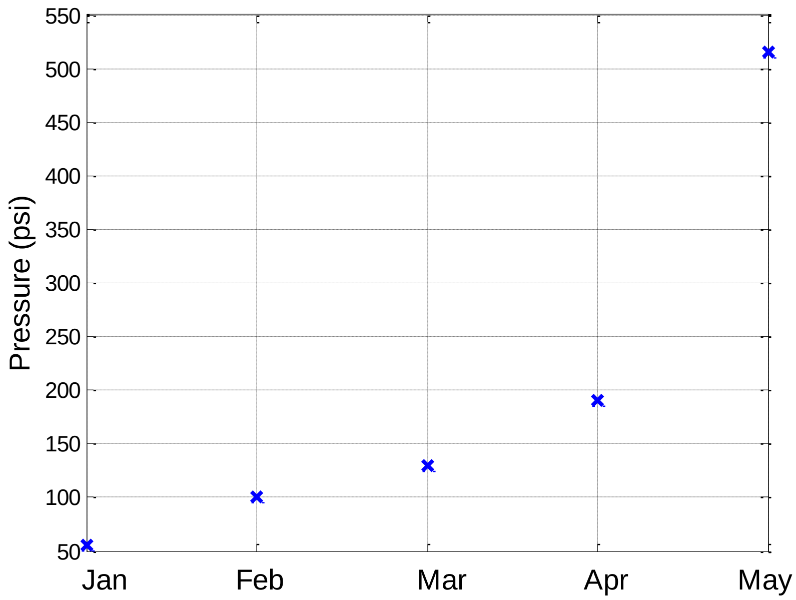

Figure 1.2. Ice pressure at GLOS for the primary observing season, winter 2013-14.

An historical wind/wave and ice climatology for the Great Lakes is reported in Chapter 10. Maximum Ice cover data for the Great Lakes, largely available from NOAA's Great Lakes Environmental Research Laboratory (GLERL), are shown in Figure 1.3. Prior to the Winter of 2013 -14, the upper Great Lakes had enjoyed a prolonged period (approximately 17 years) of mild and relatively warm winters with very low ice cover punctuated by winters of ice cover in excess of 90% occurring approximately every five to seven years (Figure 1.4).

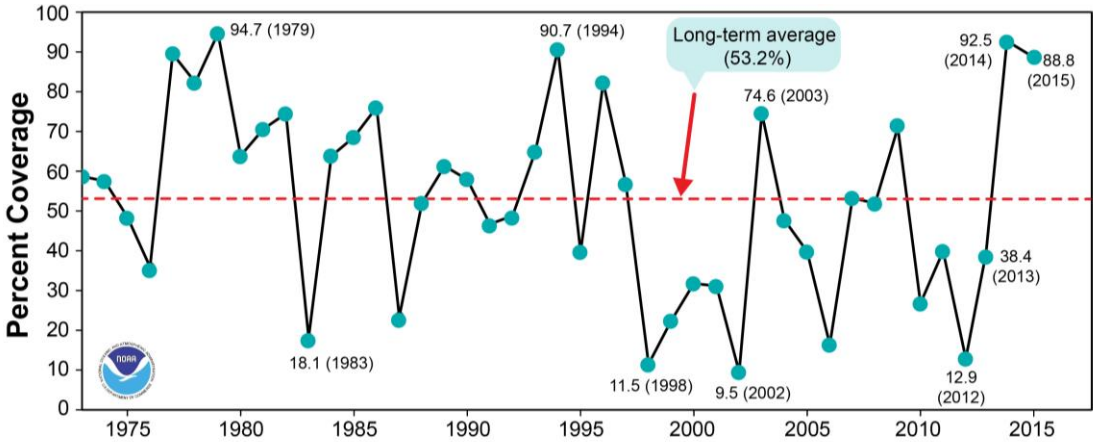

Figure 1.3. Annual maximum ice coverage averaged for the five Great Lakes, 1973-2016.

The primary observing season for this investigation occurred during the most significant ice year for Lake Superior since 1979 (35 years). The severity of this measurement year (Winter 2013-14) is captured in Figure 1.5, a MODIS Ice image of the Keweenaw Peninsula at a time near the peak of ice growth.

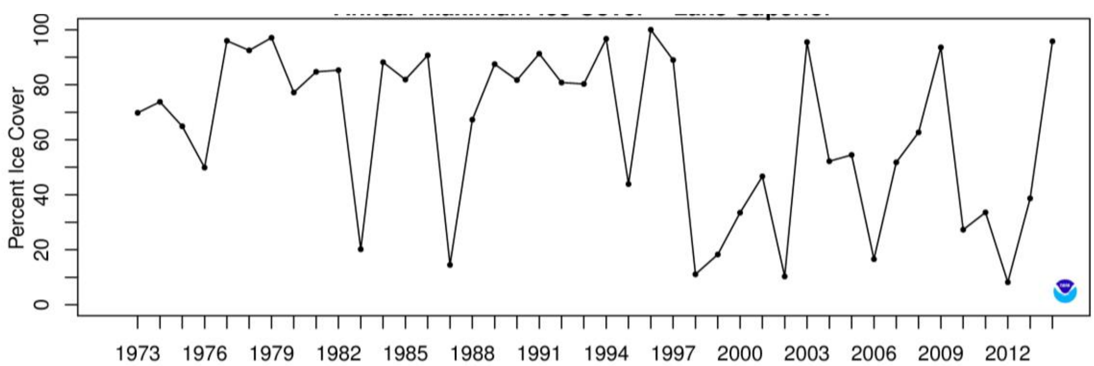

Figure 1.4. Annual maximum ice coverage for Lake Superior, 1973-2014.

Figure 1.5. MODIS image of Lake Superior ice coverage near the Keweenaw Peninsula, February 19, 2014.

We have executed the observing plan and obtained the measurements described in this report in the context of a severe Great Lakes winter. During Great Lakes winters most over-water monitoring systems (vessels, buoys, and non-automated observation stations) are not available so some processes are understood through inference. A reasonable assumption is that with severe ice years also come severe wind episodes. As can be seen in the MODIS ice image, very large blocks of ice are available to be set in motion by wind and currents, producing the potential for large ice impact loads on offshore structures. We believe that a large ice block, perhaps from a pressure ridge, was blown against the load cell in late winter during lake ice breakup causing the extreme pressure recorded in May and shown in Figure 1.2. During this period, the ADCP was knocked over. The ADCP was mounted on a tripod in 18 feet of water on the lakebed near our Ice Force Measuring System (IFMS). Figure 1.6 shows the ADCP lying on its side and Figure 1.7 shows a gouge in the lakebed that was not there at the beginning of the season. It appears that an ice mass large enough to have a keel extending 18 feet below the surface impacted the load cell. A primary goal of this effort has been to document such events and their ice force consequences.

Figure 1.6. Image showing the ADCP on its side after the high ice force event in May 2014. The image was taken by a remotely controlled submersible.

Figure 1.7. Image of gouged lakebed in 18 feet of water near the ADCP.

Our investigative team was comprised of members from the University of Michigan, the UM-Team, and members from the Michigan Technological University, the MTU-Team. The UM-Team was responsible for project design, instrument development or procurement, instrument integration into the WISN system, data analysis, and project management. The MTU-Team was responsible for system deployment, field support, management of the ADCP, and recovery of ADCP data.

ACKNOWLEDGEMENT. Both the UM-Team and the MTU-Team appreciate the opportunity provided by the Department of Energy (DOE) to work on this interesting problem. Our outcomes advance the community's understanding both of the Great Lakes ice environment and, particularly, of approaches to monitoring Great Lakes ice. We also appreciate the latitude given us by DOE project monitors as we adjusted to the exigencies of successfully completing such a challenging project on time and within budget.

2 REQUIREMENTS REVIEW

The project's objectives and requirements are included in this section to complete the project final report and to serve as references to the details of project accomplishments.

From the Statement of Proposed Objectives (SOPO), the primary objectives of this project "…will concentrate on the following three primary offshore turbine design considerations:

- Trends and periodicities in wind power availability through both a "typical" Great Lakes four-season cycle, as well as through a decadal wind power regime as a function of storm tracks, incident wave intensities and ice development (both ice floes and structural icing).
- Lake ice structural loading and accretion thicknesses on a proposed structure of opportunity as a function of the above environmental parameters.
- Extreme structural loading on structures from the combined effects of wind, waves, ice and air mass contributions with the goal of providing design guidance on return frequency and structural reliability."

The project was re-scoped into two budget periods, with specified tasks for each budget period.

<u>Budget Period I Tasks:</u>

Task I.I. Historical review and preliminary analysis of climatological data
<u>Deliverable:</u> For Lake Michigan and Western Lake Erie, a shoreline map of available annual and seasonal wind energy will be provided based upon both WIS and GLCFS outputs.

Task I.II. Site selection, and securing logistic support and approval
<u>Deliverable:</u> Based upon the above historical data and a preliminary evaluation of the climatology as provided in Task I.I, the initial site will be selected and permissions will be secured.

Task I.III. Field instrument testing and evaluation
<u>Deliverable:</u> Initial instrument package for winter deployment on and below "structure of opportunity."

Task I.IV. Initial winter field measurement program
<u>Deliverable:</u> Data report outlining measurements, successes and areas of improvement required for the next winter field season.

Task I.V. Initial reduction and analysis of field data
<u>Deliverable:</u> Data report outlining measurements, successes and areas of improvement required for the next winter field season.

Task I.VI. Dissemination of initial findings
<u>Deliverable:</u> Technical presentation and written publication submitted to peer reviewed journal.

Task I.VII. Time-scale analysis of climatological data

Deliverable: Technical presentation and written report, linking observed basin –wide meteorological and ice conditions with observed structural loads.

Task I.VIII. Final reduction and analysis of field data
Deliverable: Technical presentation and written report identifying important gaps in the data collection that need to be filled in the deployment and important factors for the development of a model of structural loading on turbine support structures.

Task I.IX. Final winter field measurement program
Deliverable: Technical presentation identifying the second structure of opportunity and measurements to be made to further the overall goals of the project. Instrument substitutions and enhancements may be required.

Task I.X. Initial reduction and analysis of second field data
Deliverable: Data report outlining measurements, successes and recommended future improvements.

Task I.XI. Dissemination of preliminary findings
Deliverable: Technical presentation and written publication submitted to peer reviewed journal.

Budget Period II tasks:

Task II.I. Final data reduction and analysis
Deliverable: Technical presentation and written report identifying any remaining gaps in the data collection that need to be addressed in future work and important factors for the development of a model of structural loading on turbine support structures.

Task II.II. Development of dynamic models for structural loading
Deliverable: Field, environmental and ancillary data collected in Budget Period I will be evaluated to establish the proper modeling for dynamical response of offshore turbines in the Great Lakes subjected to forces from the Lakes' wind/wave/ice environment.

Task II.III. Development of design criteria
Deliverable: Technical report identifying sound design criteria for offshore wind platforms in the Great lakes will be produced based on the field studies of the forces and response of ice features in the region, in combination with the climatological return frequencies of threshold events.

Task II.IV. Workshop/dissemination of final results
Deliverable: Technical presentation and written publication submitted to peer reviewed journal.

Task III. Project Management and Reporting
Deliverable: Reports and other deliverables will be provided in accordance with the Federal Assistance Reporting Checklist following the instructions included therein.

3 SYSTEM OVERVIEW

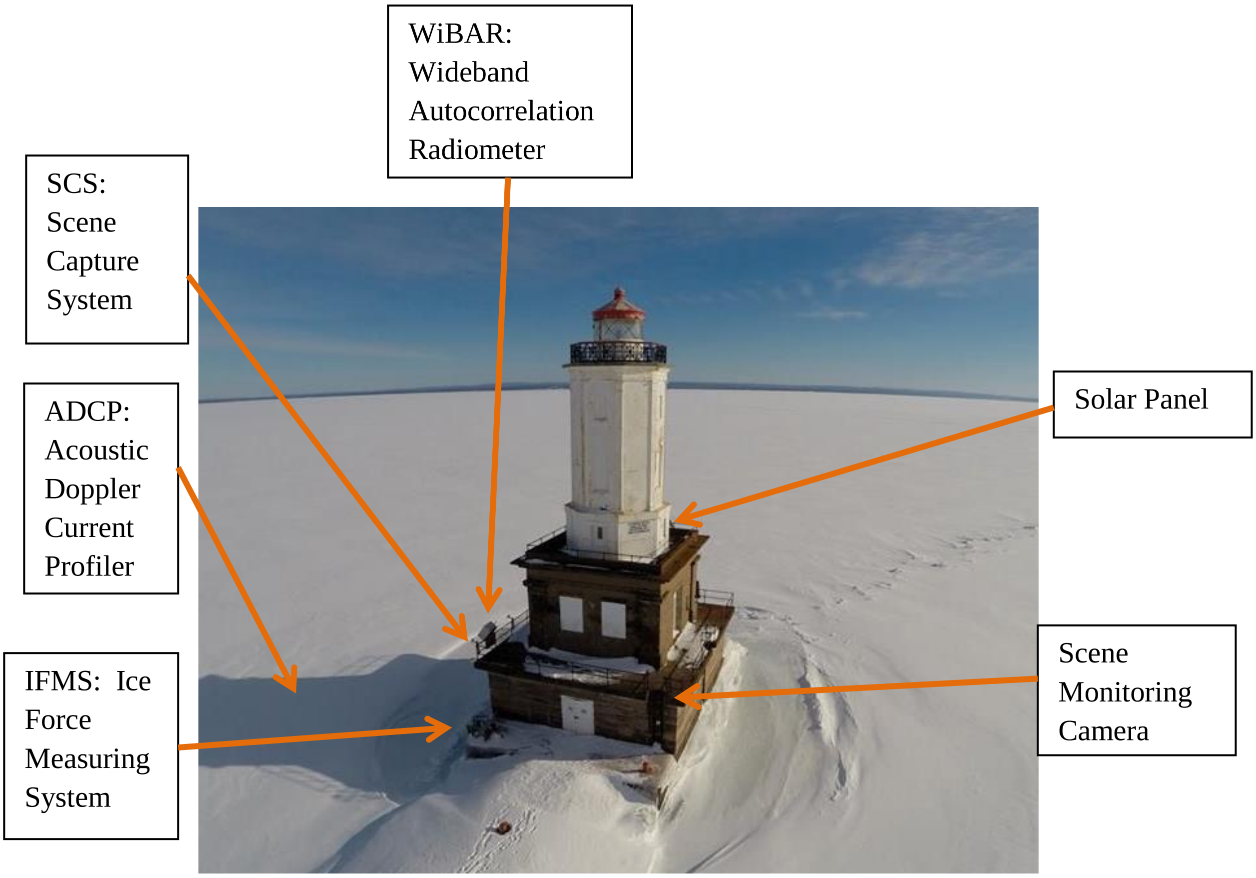

Figure 3.1 Photograph courtesy of Kite Aerial Photograph with Nathan Invincible (March 2014)

This aerial photograph captures a winter scene of the experiment site, the South Entry Light of the Keweenaw Waterway. The WISN components are identified by their systems names. Translating the project's objectives to engineering requirements, we went through a set of system design iterations to arrive at a set of remote sensors and in-situ sensors which met the experiment site constraints and budget limits, as well as data collection season constraints (winter months).

With a preliminary list of instruments we could deploy, we focused on the selection of the observation site. Conflicting parameters for the site selections were ease of access (for instrument deployment and maintenance) and optimum expected ice action occurrence. Physical locations where large ice actions are expected are generally difficult to access and hazardous to the experimental team. Following an exploratory trip in March 2013, we selected the South Entry Lighthouse of the Keweenaw Waterways as our experimental site. This particular lighthouse is a historical landmark requiring special permission for access, which we acquired from the historical society with the promise that none of the instrumentation would be in intimate contact with the structure.

Once the experiment site was selected, the instruments design was refined with these primary considerations: DC power generation and capacity (no access to power grid), operating temperature (-25ºC to + 40ºC), instruments physical parameters (size, shape, and weight), schedule constraint (must be operational by winter 2014 season), and available funding. The resulting WISN suite of instruments has two remote sensors (WiBAR, SCS), two *in-situ* instruments (IFMS, ADCP), and supporting equipment (solar powered battery, scene monitoring camera, cellular communication units). The schedule of the instruments design and fabrication is fundamentally driven by the winter season experiment timeline – the WISN was set to collect data over winter 2014. Winter 2014 turned out to be among the longest and coldest in the recorded history of the Great Lakes.

All instruments requiring DC power were supported by the solar powered storage batteries. Instruments mounting interfaces were designed to protect against the harsh Lake Superior winter and prevent damage to the historical lighthouse.

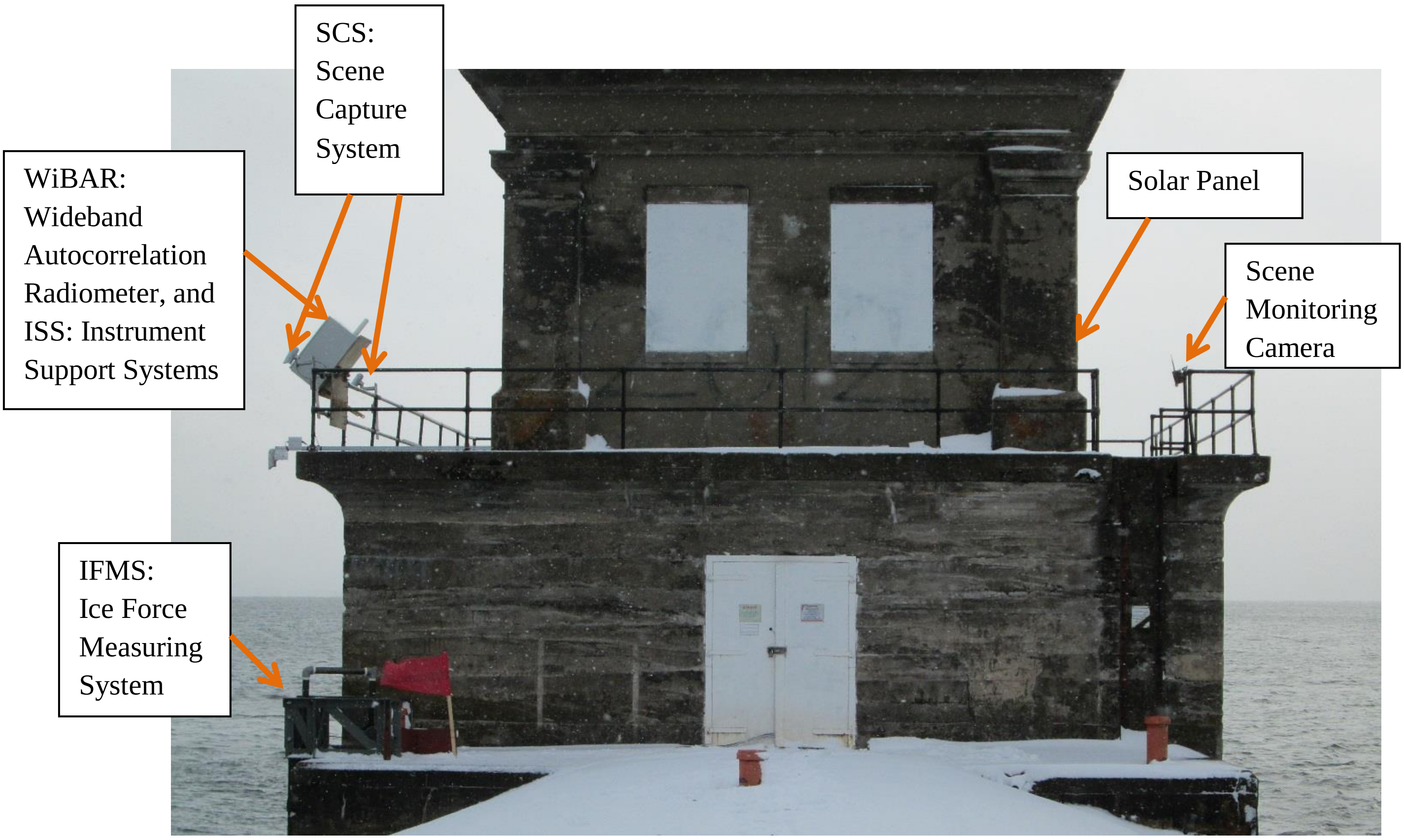

Figure 3.2 WISN instruments: Scene Capture System (SCS), Wideband Autocorrelation Radiometer (WiBAR), Ice Force Measuring System (IFMS), Instrument Support Systems (ISS), solar panel and batteries, scene monitoring camera.

4 SITE SELECTION

The South Entry Lighthouse of the Keweenaw Waterway was selected as the experimental site. We selected this site following an exploratory trip in winter 2013. We diverted from the original suggested locations (North Manitou Light in Lake Michigan and Port Gratiot in Lake Huron) for a variety of reasons. Perhaps the most practical consideration was the transition of the proposing Principal Investigator of this project from University of Michigan to the director post of the Great Lakes Research Center (GLRC) at Michigan Technological University in Houghton, MI. Prof. Meadows and his GLRC team were largely responsible for the selection of the experiment site. They proposed two sites on the Keweenaw Peninsula in Lake Superior: North Entry Light and South Entry Light to the Keweenaw Waterways.

Figure 4.1 North Light Entry to the Keweenaw Waterway, March 2013

Figures 4.1 through 4.3 capture the winter scenes at the North Light Entry point to the Keweenaw Waterway. At this site, there are two possible experiment sites, one at either end of the channel as can be observed in Figure 4.2. We soon concluded that the access to the southern site of the North Light Entry point is rather difficult; the terrain is a challenge to traverse, see Figure 4.1. As to the northern site of the North Light Entry, we observed that the structure geometry would prove difficult for the design and deployment of a pressure-sensing instrument. A valuable observation we made during the site visit is the magnitude of ice impact the in-situ sensing instrument could expect – as shown in Figure 4.3, large icebergs are common. This visit provided a good opportunity for assessment of the harsh ambient operating environment for the proposed instruments and for personnel safety considerations.

Figure 4.2 North Light Entry to the Keweenaw Waterway, March 2013

Deliberating over the challenges we would be faced with at the North Entry Light, challenges with the instruments deployment, maintenance, and possible repair, we visited the South Entry Light to assess its physical geometry and access (Figure 4.4). It became apparent to us that the South Light Entry was the better choice as the experimental site. The access to the South Entry Light is via a quarter-mile long jetty, which provides a relatively easy access to the lighthouse.

Figure 4.3 A large iceberg was observed; note the comparison to Dr. Deroo who stands at 6’5” tall.

Figure 4.4 South Entry Light to the Keweenaw Waterway, March 2013

5 ICE FORCE MEASURING SYSTEM (D. KARR)

The design, fabrication and installation of the Ice Force Measuring System (IFMS) were completed in the fall of 2013 for operations during the winter of 2013-2014. The instrumentation was deployed in Lake Superior on a Keweenaw Peninsula lighthouse, where a large-scale laboratory for cold regions engineering experimentation is naturally formed. A data acquisition system captured readings from strain gauges encased in the IFMS.

Photographs of the installation are shown in Figures 5.1, 5.2, and 5.3 below. A bollard collar was used as the support interface between a permanent bollard on the lighthouse deck and the support framework for the Ice Force Measuring System. The bollard collar (see Figure 5.2) was manufactured by Universal Metals of Calumet, MI. A team from the University of Michigan installed the collar at the lighthouse in June 2013.

Figure 5.1 Side view (looking southerly) of the bollard collar, framing and ice force measuring plate after installation. The ice force measuring plate can be seen, at the bottom left, protruding above the waterline.

The deck frame for the support structure was designed at the University of Michigan and manufactured by Universal Metals of Calumet, MI. A team from the University of Michigan received the frame in August and installed the frame on the deck at the lighthouse. More details of the connection of the deck frame to the bollard are shown in Figures 5.2 and 5.3. The lighthouse is a registered historical sight in the state of Michigan and special permission to use the site for these operations was granted from the Michigan Historical Society and the United States Coast Guard. The entire assembly was designed for attachment and removal without any remaining alterations to the lighthouse features.

Figure 5.2 Bollard collar and deck frame after installation

The data acquisition system included strain gauges, their adhesive systems, and three cables leading from the IFMS to transmit data from the strain gauges within the IFMS plate to a data logger. The cables were encased in piping from the top of the IFMS plate over the deck frame; they can be seen in Figure 5.3(b) leading from the end of the piping. The data logger is shown at the site in Figure 5.4, housed in the lower level of the lighthouse superstructure.

Figure 5.3.(a) Installation of Ice Force Measuring System's pressure plate

Figure 5.3(b) Top view of the bollard (orange), bollard collar (darker orange), deck and vertical frames (gray) shown supporting the ice force measuring plate. The vertical and horizontal piping encases the data cabling which can be seen on the deck leading from the IFMS to the data logger.

Figure 5.4 IFMS Data Logger housed within the lighthouse superstructure.

5.1 PLATE DESIGN AND INITIAL TESTING

The plate is composed of evenly distributed stiffeners and readily lends itself to application of strip beam theory for converting strains to ice pressure for uniform loading and to orthotropic plate theory for full plate analyses. These conversion approaches are discussed in further detail is Section 5.3. Details of the measuring plate are shown in Figure 5.5. The IFMS was constructed of steel with 1-inch sidebars, which were also extended vertically for attachment to the deck framing (see Figure 5.5a).

The faceplate was reinforced with horizontal rib stiffeners, spaced on 6-inch centers. The plate was fabricated by Hosford and Co. of Ann Arbor, MI. From there, the plate was transported to the University of Michigan, Civil and Environmental Engineering department's Structural Engineering Laboratory. This lab was used for installation of the strains gauges attached to the inside of the faceplate and to stiffener ribs of the plate. Figure 5.5b shows the plate during strain gauge installation. Candidate strain gauges and their adhesive systems were obtained from HBM Inc. and procedures practiced on sample steel plating.

The design of this plate was completed using a safety factor of 2.0 against the yield limit state. The critical state was yielding of the steel ribs due to bending at the extreme fibers of the reinforcing ribs. For this reason, linear strain gauges were placed at this location to determine the maximum strains. Strain gauges were applied also between ribs on the back of the faceplate. These gauges were aligned vertically to determine local plate bending stresses between ribs. A number of "shear" strain gauges were also placed near the ends of the ribs as a source of additional data to serve as back-up system if needed. The physical dimensions of the IFMS plate with the numbering of ribs and the allocation of linear strain gauges are sketched in Figure 5.6.

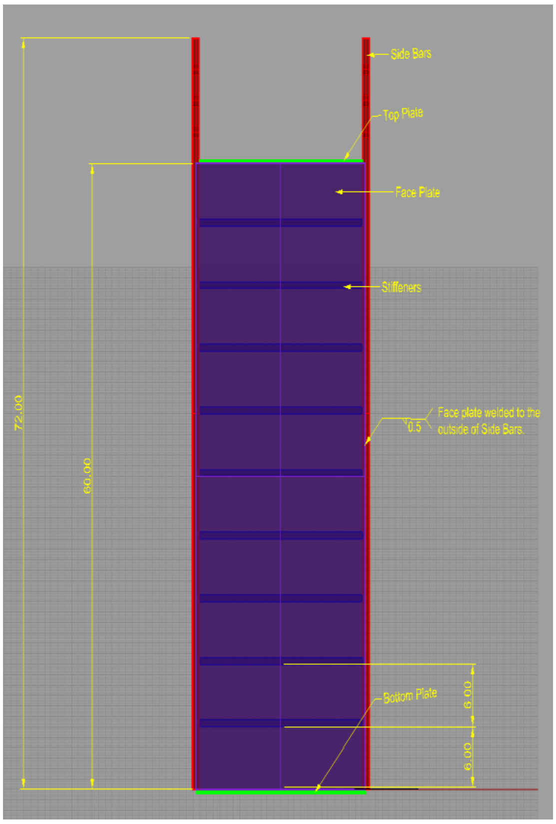

Figure 5.5 (a) Ice Force Measuring Plate Design, front view. (b) Photograph of the plate during strain gauge installation.

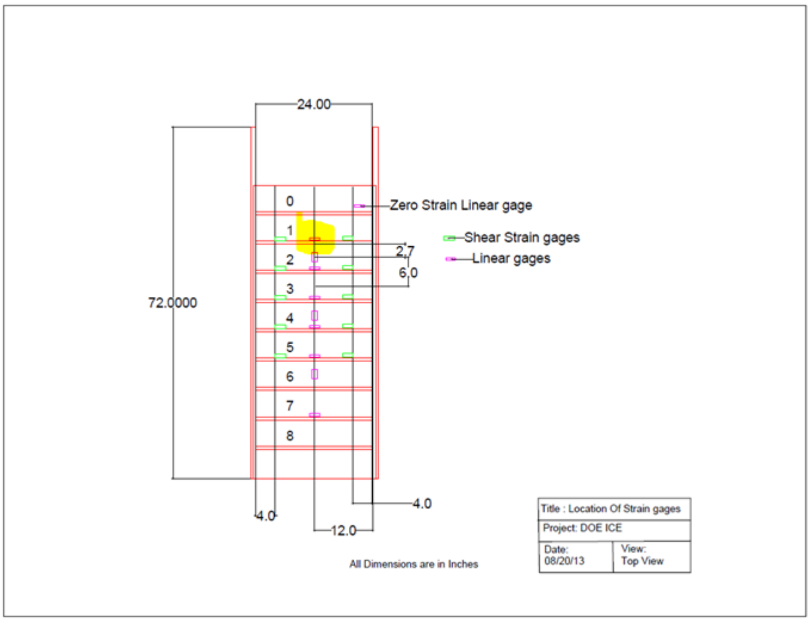

Figure 5.6 Elevation sketch of IFMS showing the strain gauge locations. The linear horizontal strain gauges are located on ribs 1 (highlighted in yellow) through 5 and rib 7.

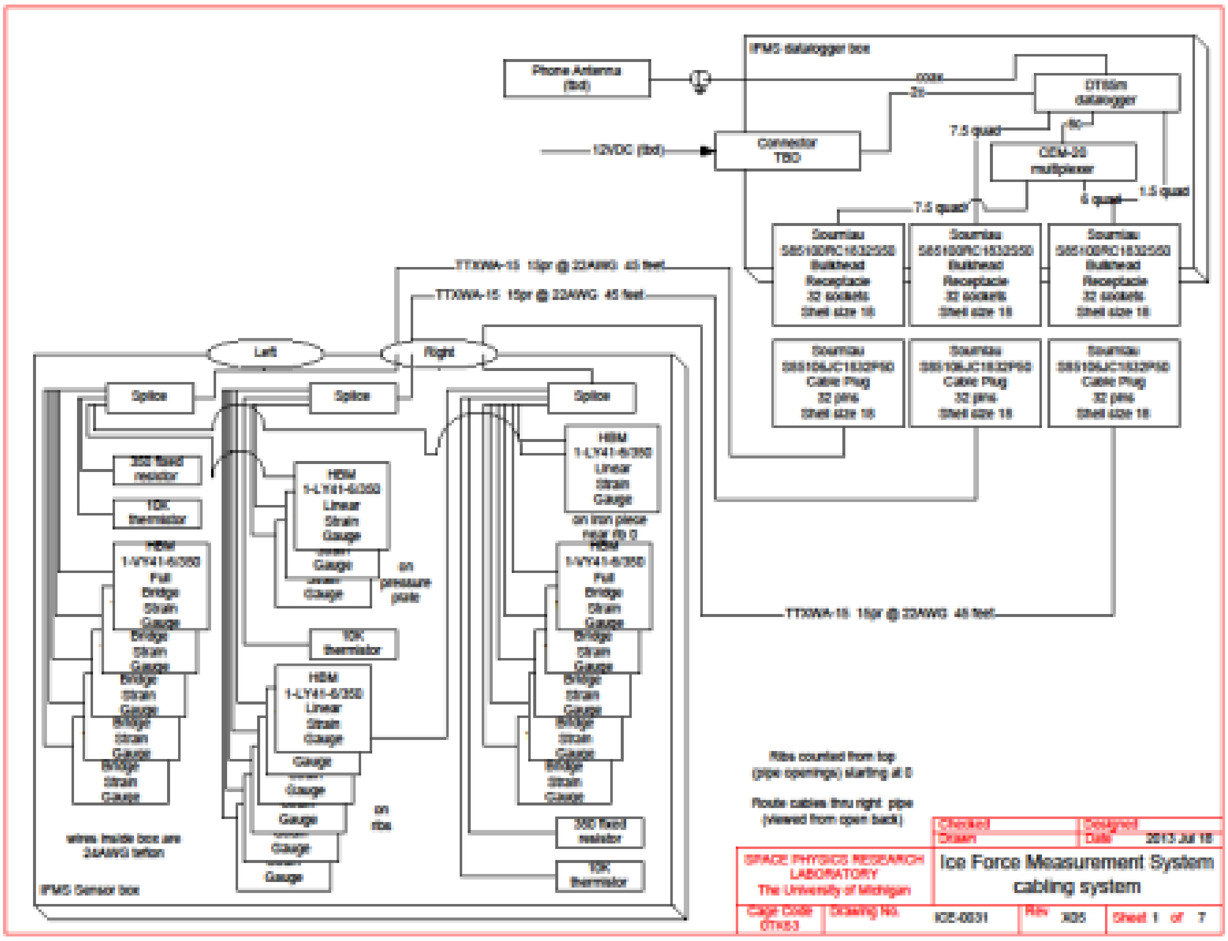

Figure 5.7 Cabling System for the data acquisition from the IFMS strain gauge readings.

Mechanical testing of the IFMS was undertaken for calibration and data acquisition verification. The IFMS plate load test (without the back plate) was performed at the Civil and Environmental Engineering (CEE) Structural Engineering Laboratory in August, 2013, and was carried out using a 14-inch diameter loading cylinder with a 14-inch square steel plate attached to the bottom of the cylinder. The test machine is shown in Figure 5.8. The IFMS faceplate was loaded gradually from zero to 20 Kips in the first round. In the second round, the plate was reloaded at 5 Kip or 10 Kip steps until a maximum of 50 Kips. The variation of the resistance measured in the gauges is sketched in Figure 5.9 - linear relationships between loading and gauge resistance were observed as expected.

To simulate the loading and the structural response in the lab test, we developed a finite element analysis (FEA) model of the IFMS plate in ABAQUS. Considering the stiffness of the loading cylinder and the attached square plate compared to the IFMS plate, it is reasonable to assume that the contact area between the loading panel and the back of the IFMS plate to be the circumferential line of the cylinder at the bottom of the contact perimeter. In the model, we prescribe the same value of displacement for the chosen shape of the contact area on the IFMS face, shown schematically in Figure 5.10.

Figure 5.8 Loading panel and the IFMS plate without the back plate.

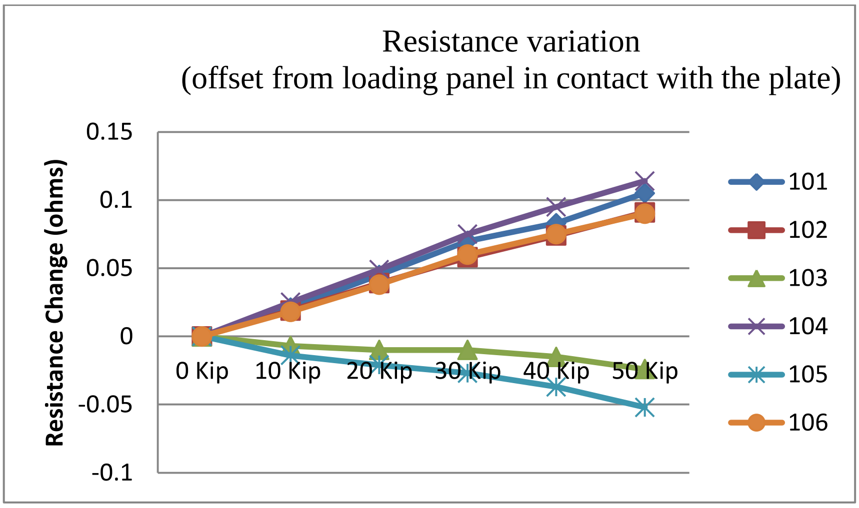

Figure 5.9 Resistance variation of six linear strain gauges of IFMS plate (without back plate) on 2 August 2013 in CEE Lab.

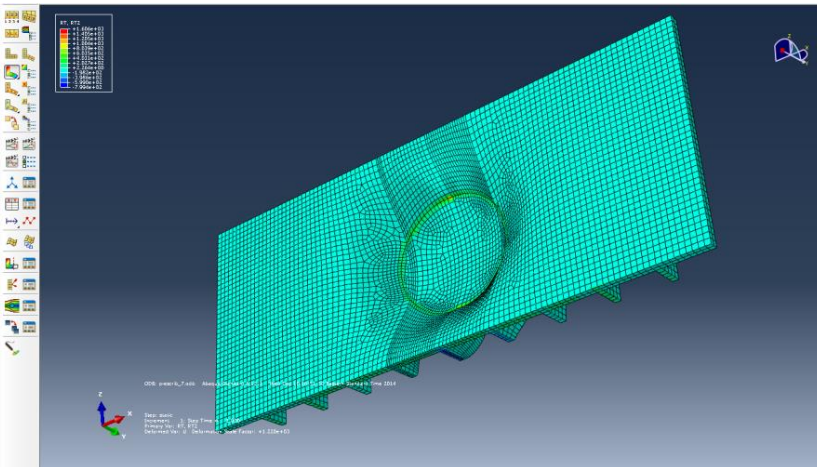

Figure 5.10 FEA model of the loaded IFMS plate subjected to prescribed ring loading.

From the relationship between linear strain ϵ_{linear} and the resistance variation δR, $\epsilon_{linear} = 0.0014\delta R\ ohms^{-1}$, we convert the resistance variation measured in CEE lab tests to compare with the strain response obtained from the finite element model for the same total loading force. Results from comparisons of two horizontal linear strain values (on rib 3 and rib 4) from the FEA model are shown in Figure 5.11. It is observed the prescribed circular displacement from the finite element analysis gives satisfactory correlation for the total force and converted strains found from the laboratory results.

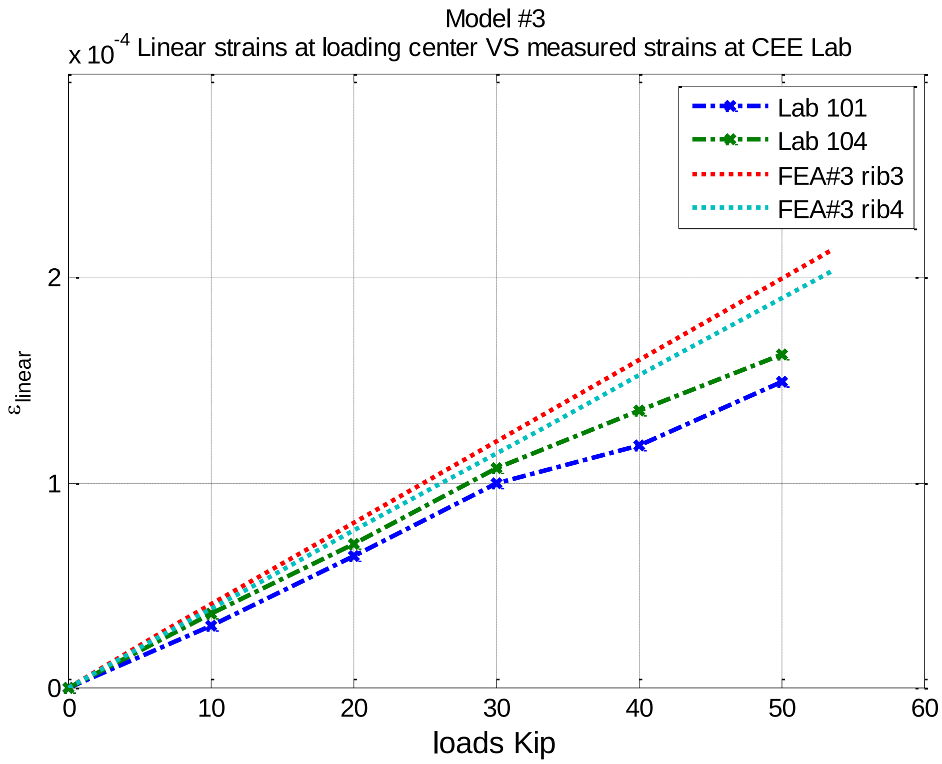

Figure 5.11 Linear strain ϵ_{linear} variation from the FEA of prescribed points-displacement of the stiffened plate (x axis is the total loading force on the modeled IFMS plate).

To further study the response of other linear strain gauges, comparisons of the strains converted from the lab result ($\epsilon_{linear} = 0.0014\delta R\ ohms^{-1}$) and the strains calculated from the FEA model of prescribed circular displacement are shown in Figure 5.12. It can be observed that both the linear horizontal strain gauges and the linear vertical strain gauges compare reasonably well to the calculated strains obtained from the loading tests conducted on 20 August 2013. The FEA model calculated strains were very sensitive to the location of the loading circle. These results provided support for the conclusion that the linear strain gauges were behaving healthily.

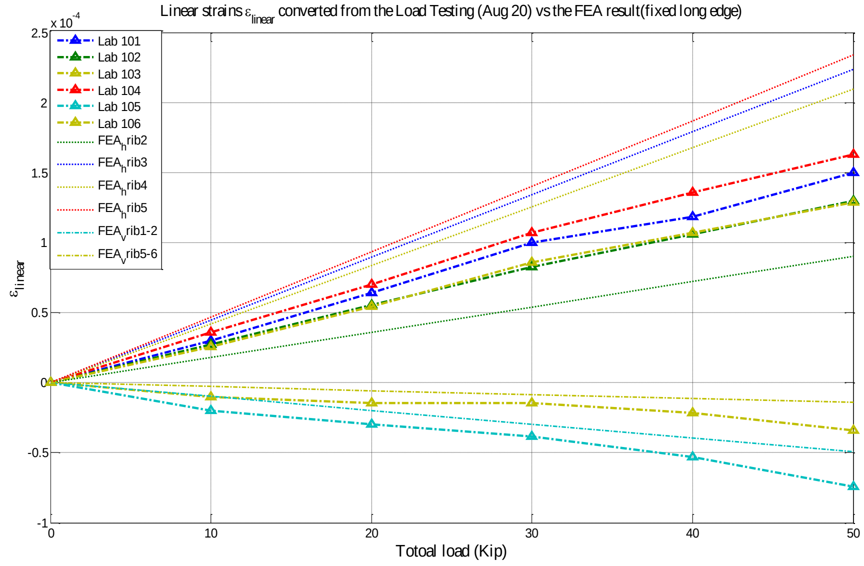

Figure 5.12 Strain converted from 20 August 2013 Test compared to strain obtained from FEA model with prescribed circular displacement

The IFMS was then transported to Universal Metals of Calumet, MI, for welding of the back plate of the IFMS. Also at Universal Metals, the vertical frame for the IFMS support structure was manufactured and attached to the ice force measuring plate in October 2013. A second test was performed at Michigan Technological University for calibration of the system with the back plate installed on the IFMS. A team from the University of Michigan and Michigan Technological University installed the IFMS to the deck support system on site at the South Entrance lighthouse with assistance from Universal Metals on 27 October 2013.

5.2 DATA COLLECTION AND PRELIMINARY ICE PRESSURE ESTIMATION

With the IFMS in place, resistance measurements from strain gauges on the Ice Force Measuring System (IFMS) at the South Entrance lighthouse in Lake Superior at the Keweenaw Peninsula were monitored from January through May. Weather was also monitored throughout the winter of 2013-2014. The month of March offered the best ice force readings during the early months of 2014. Figure 5.13 shows temperature barometric pressure, wind speed and wind directions in the Keweenaw area for the month of March. Some significant ice interaction events occurred March 17 through March 19 of 2014. With sufficiently low temperatures and favorable winds, the ice formation impinged against the structure, as can be seen in Figure 5.14. The figure shows the ice formation at the IFMS when significant winds from the east had forced the ice against the IFMS faceplate.

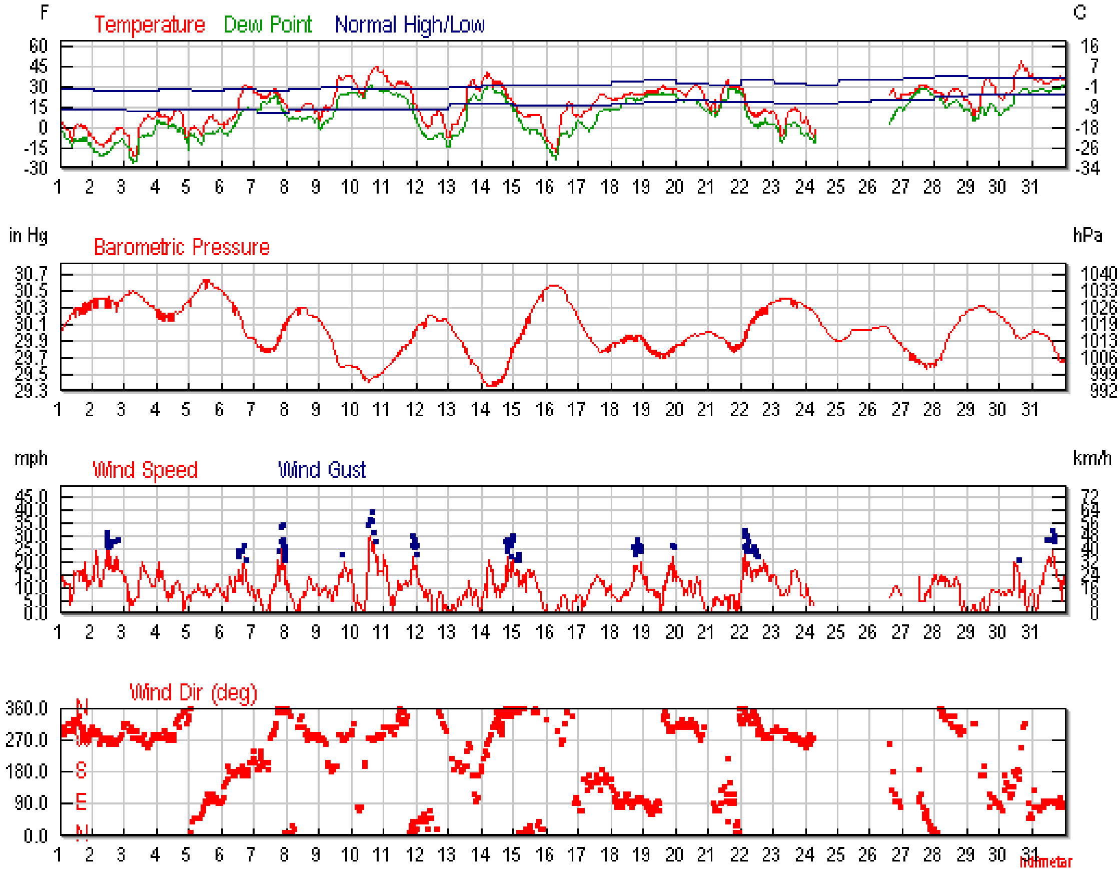

Figure 5.13 Temperature barometric pressure, wind speed and wind directions March 2014 (Source UndergroundWeatherhttp://www.wunderground.com/history/airport/KCMX /2014/3/28/MonthlyHistory.html).

The photograph of the IFMS shown in Figure 5.14 was taken from the upper deck of the lighthouse on 18 March 2014. The faceplate of the IFMS is obscured from view in the figure; it is located just below the ice and snow surface. Above the faceplate and protruding above the snow surface is the x-bracing (painted red) of the vertical frame.

The change in resistance of the strain gauges is used to calculate the strain on the steel plating and stiffeners or ribs. The changes in resistance of the gauges are also compared to the changes in resistance for an unloaded “control” gauge also located inside the IFMS. Figure 5.15 shows example changes in resistance measured on 18 March 2014. The differences in resistance are then used for conversion to strains. The calculated strains are then used to determine the stress field in the stiffeners and the ice pressures causing the deformation.

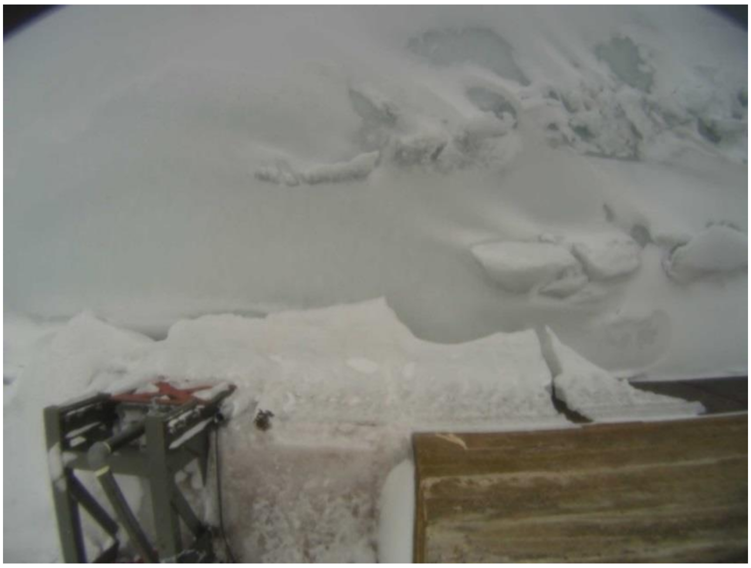

Figure 5.14 Top view of IFMS, the measuring plate in contact with ice, 18 March 2014.

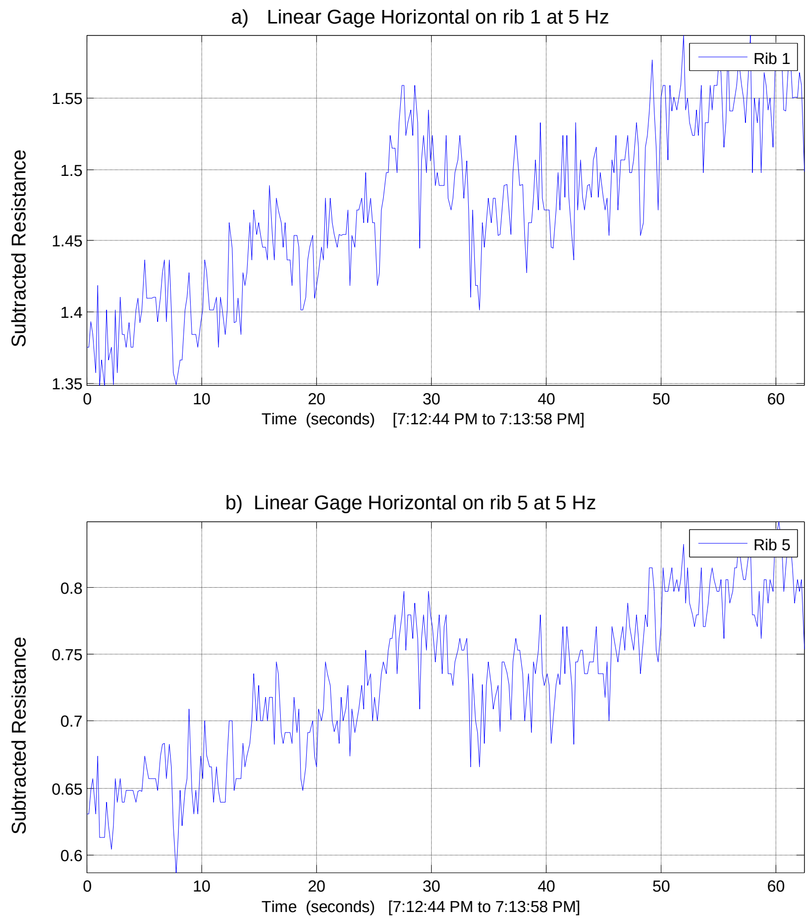

Figure 5.15 Change in resistance for Ribs 1 and 5, 18 March 2014. These gauges are located on horizontal stiffeners or ribs.

For our preliminary assessment of the ice pressures acting on the faceplate, we assumed that the pressure was uniformly distributed over the width of the faceplate and calculated the pressure from the stress field in the stiffener. This allows us to use beam theory for each of the rib stiffeners and calculate the pressure based on the strain readings from each individual rib. Here we modeled the stiffeners as a beam fixed at both ends from which the bending moment in the stiffener and thus stress at the middle of the span (center of the plate) can be calculated. This approach was used throughout the winter and spring months of 2014 to estimate ice pressures. The resulting pressures determined for 18 March 2014 are shown in Figure 5.16. Details of the analysis models using beam theory and orthotropic plate theory are provided in the Appendix 5.1.

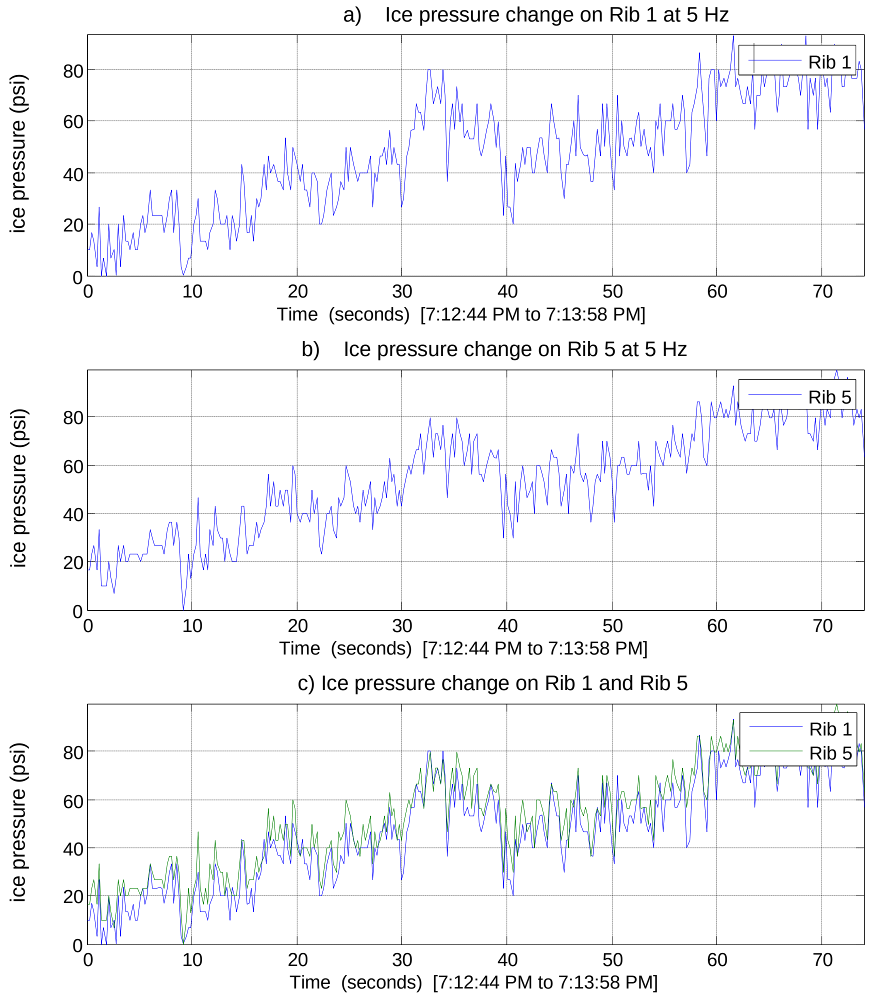

Figure 5.16 Estimated changes in ice pressures on the IFMS faceplate opposite ribs 1 and rib 5, 18 March 2014. The representative contact area for each of these ribs is approximately 1 square foot.

Another view of the IFMS is shown in Figure 5.17, a photograph taken on April 28, 2014, again from the upper deck of the lighthouse. Here we see that the ice field has broken up with some drifting of the ice away from the lighthouse. Figure 5.18 shows that the ice field has returned to the eastern face of the lighthouse; the photograph was taken on April 29. Evidently with favorable winds, the ice formation drifted back towards the east and impinged against the structure.

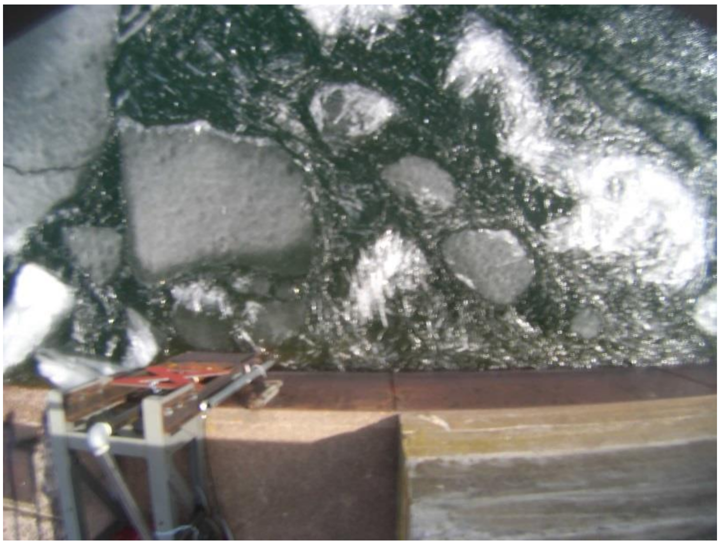

Figure 5.17 Top view of IFMS showing the measuring plate and a broken ice field, 28 April 2014.

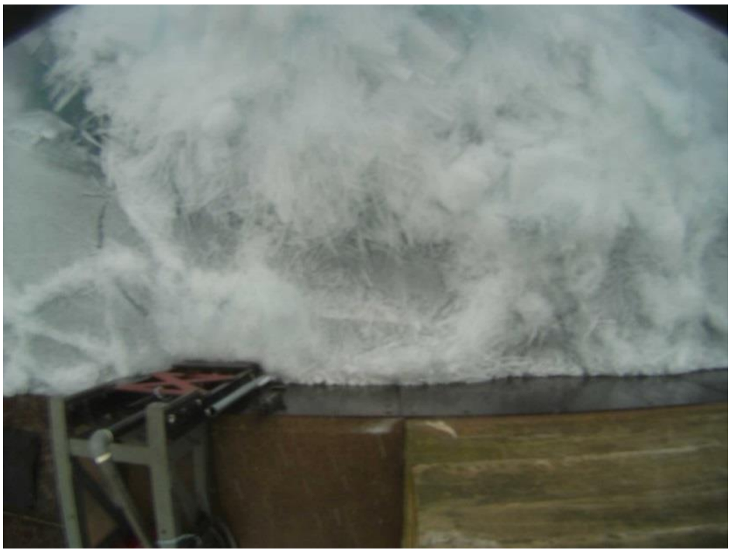

Figure 5.18 Top view of IFMS showing the measuring plate in contact with ice, 29 April 2014.

As further examples of our data analysis, we examined in some detail the strain gauge readings for April 29. Three example gauges are located on horizontal stiffeners 1, 3 and 5. These results are shown in Figures 5.19 with an expanded view of the results for rib 3 shown in Figure 5.20.

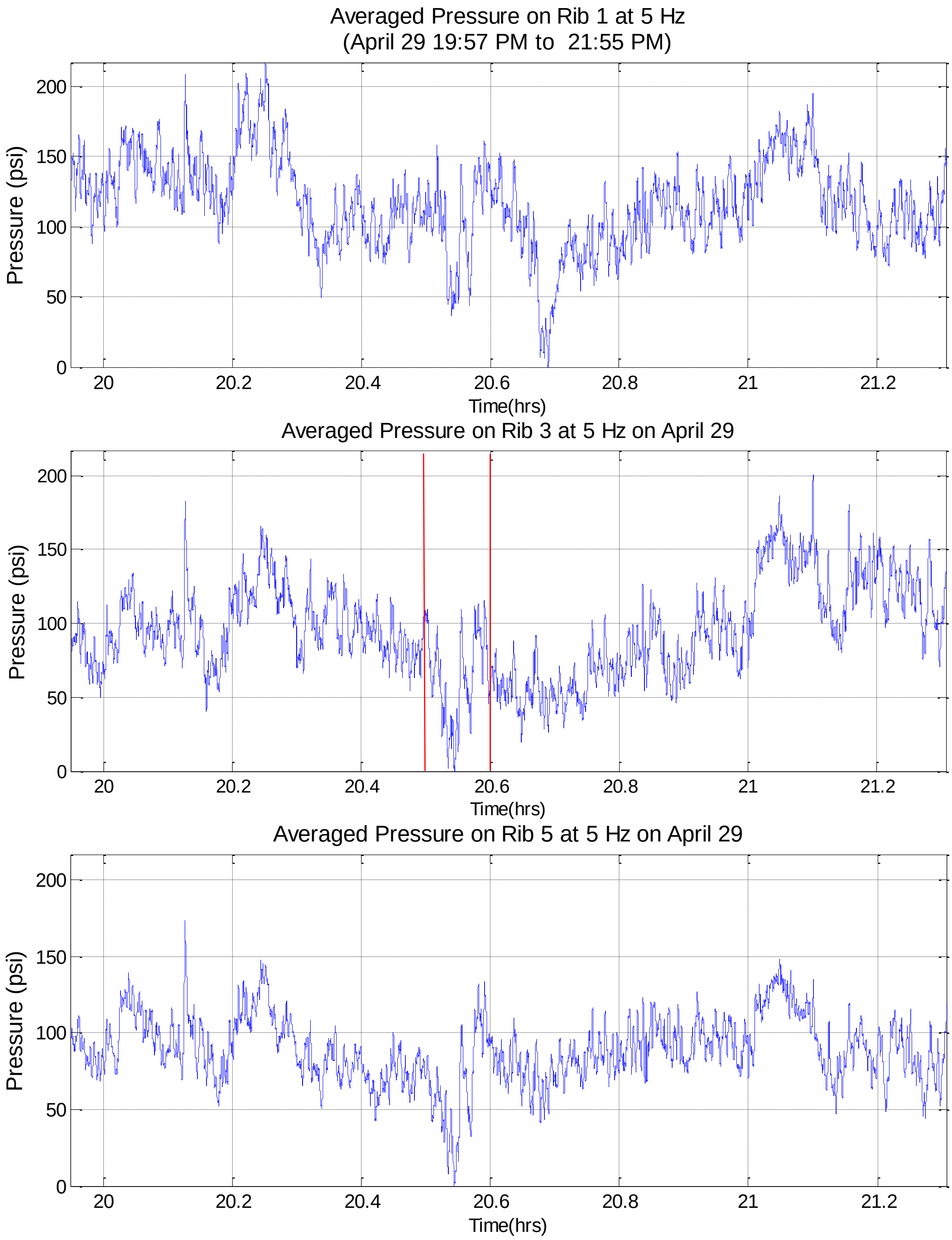

Figure 5.19 Estimated changes in ice pressures on the IFMS faceplate opposite ribs 1 and rib 5. These gauges are located on horizontal stiffeners or ribs. The representative contact area for each of the pressure calculations is approximately on square foot.

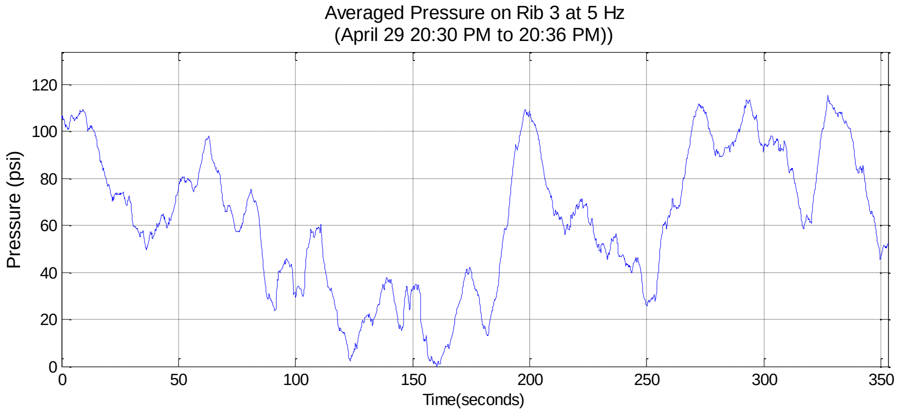

Figure 5.20 Estimated changes in ice pressures on the IFMS faceplate opposite rib 3, 29 April 2014.

Some of the most interesting ice dynamics and most significant ice interaction events occurred during the last days of April and first days of May. It is interesting to note that although local wind speeds decreased on May 1, high-pressure readings continued to be seen on 1 May 2014. By May 2 we see the ice field near the IFMS had again broken up (see Figure 5.21). Higher wind speeds then redeveloped from the east from May 5 to May 7. Figure 5.22 shows the ice features impinging against the IFMS on May 7. Some small lateral motion of the ice force measurement system and the vertical framework were observed which indicated some northerly directed force from the ice. This indicates that the ice force acting perpendicular to the plate (which is the force component measured by the strain gauges) may have been reduced because impact was not perpendicular to the faceplate.

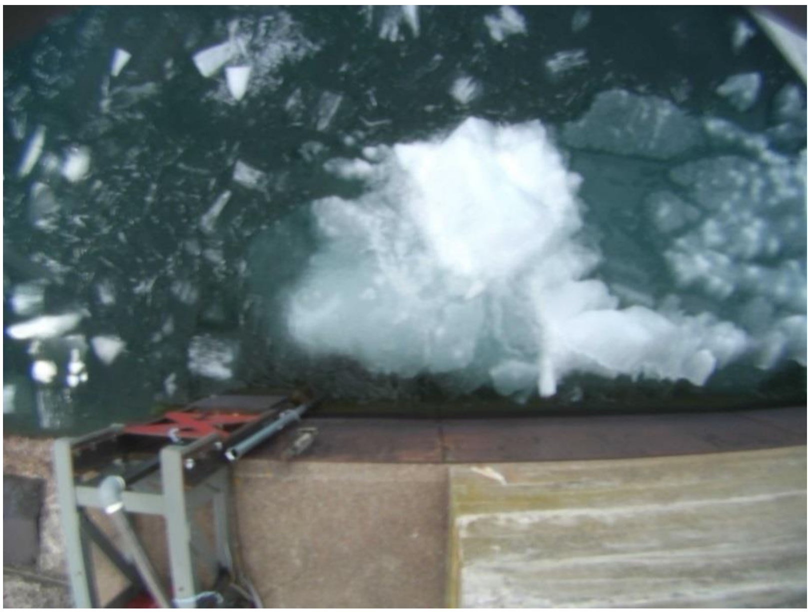

Figure 5.21 Top view of IFMS measuring plate in contact with ice, 2 May 2014.

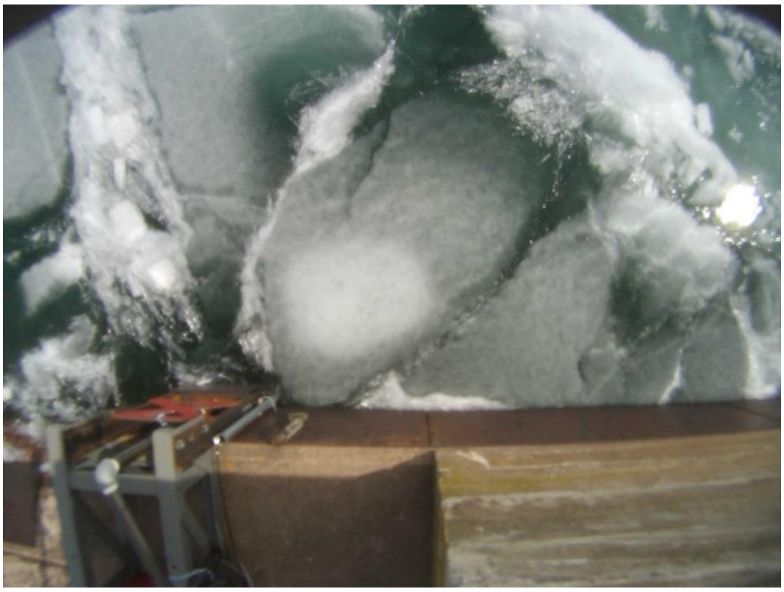

Figure 5.22 Top view of the IFMS showing the measuring plate with ice contact, 7 May 2014.

The maximum ice pressure estimates for the year occurred on May 1. Unfortunately we have no images of the ice field for May 1 although our highest readings of the season occurred on that date. Figure 5.23 shows the results for example strain readings for May 1. Figure 5.24 shows the results for the pressure estimations for May 1, again using strip beam theory for the structural analyses required for converting measured strains to applied pressure. These analyses indicate maximum pressures of about 500 psi or 3.44 MPa. These values compare very reasonably to other full-scale ice load measurements.

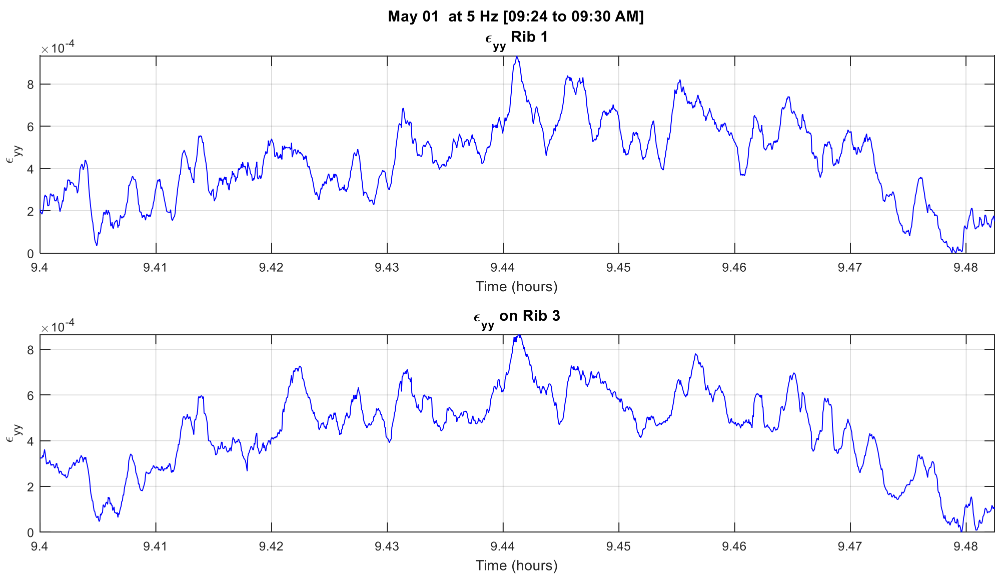

Figure 5.23. Experimental measured linear strain variation on May 01 at 5 Hz.

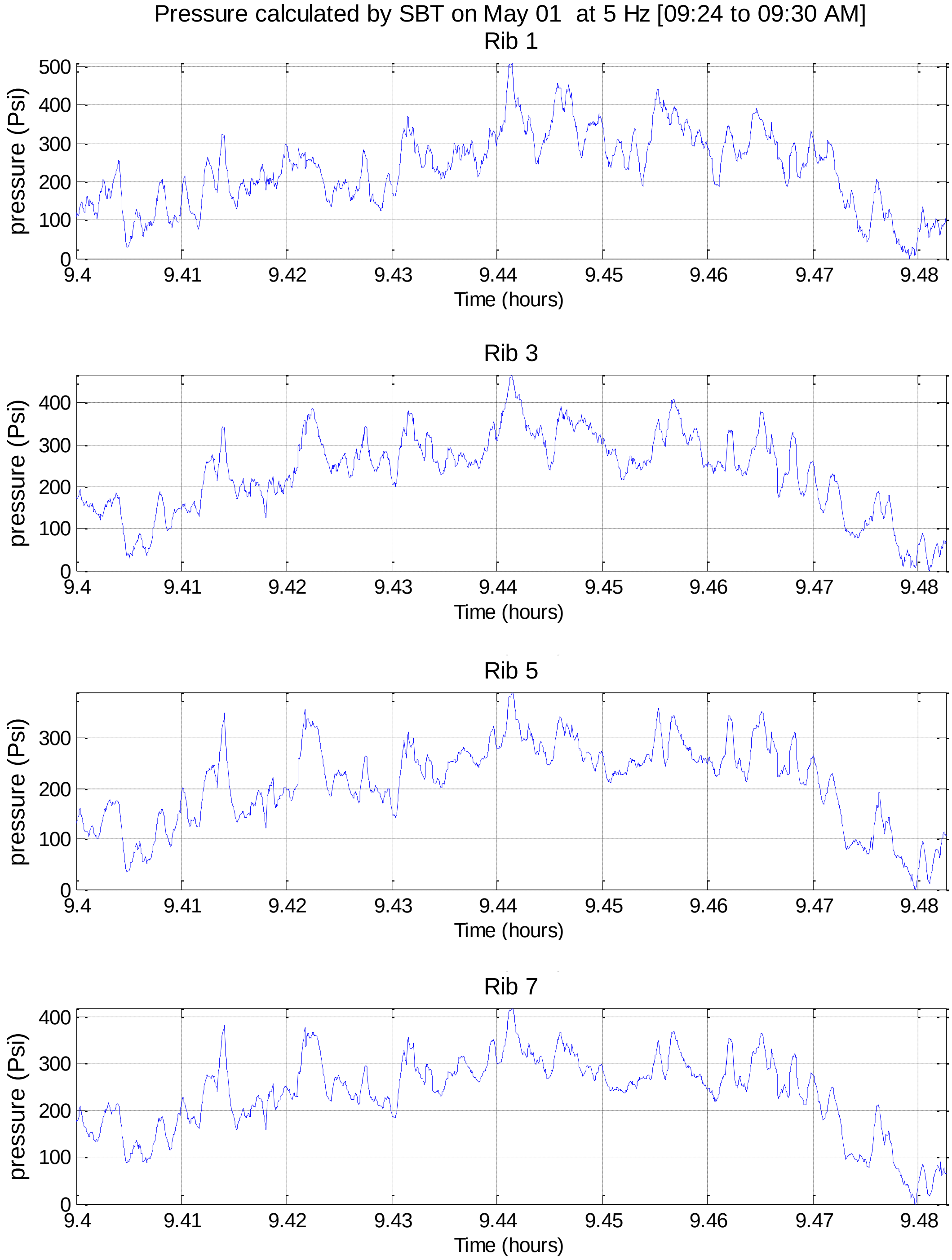

Figure 5.24 Estimated changes in ice pressures on the IFMS face plate opposite ribs 1 and rib 5. The representative contact area for each of these ribs is approximately 1 square foot.

5.3 REFINEMENTS OF ICE PRESSURE ESTIMATION

The full details of several models used for estimating the ice pressures based on the strain readings in the field are presented in the paper entitled "Determining Ice Pressure Distribution on a Stiffened Panel using Orthotropic Plate Inverse Theory," which has been submitted to the *Journal of Structural Engineering*. The submitted manuscript is provided in Appendix of this report. An abridged presentation of the methods used for ice pressure calculations and described in the manuscript is also presented in the following.

In the preliminary analyses for the ice pressure estimates, beam theory was used for individual strain gauge readings. Pressures calculated from each strain gauge were considered independently from the response of adjacent gauges. A portion of the plate evenly spaced at a distance, C, between two stiffeners was idealized as an Euler-Bernoulli strip beam. The dimensional parameters of the resulting T-shaped cross section were used to determine the section's moment of inertia. The vertical boundaries, of the beam of length b are considered as fixed in our scenario. Also, we assume a uniformly distributed load q on the horizontal beam. The effective elastic modulus of the beam E_e is calculated by assuming a state of plane strain in the upper flange. Hence we obtain the relationship of strain located in the mid span of the beam, and at the bottom of the stiffener, under given distributed load q:

$$\varepsilon = \frac{\mathrm{Cb}^2}{24\mathrm{E_e I}} q = 1.85 \times 10^{-9} q \cdot m/N \qquad (1)$$

Equation (1) allows determination of the pressure loading from the measured strains.

Similarly, we may select a vertical strip beam having rectangular cross section with a thickness equal to that of the plate and length equal to that of the stiffener spacing. The distributed beam load is calculated by $q_v = pt_v$. Based again on the Euler-Bernoulli strip beam theory, we obtain the general relationship of strain-loading relationship for the vertical strain gauges:

$$\epsilon_{xx} = \frac{h_s a_0^2}{48 E_{ev} I_x} q_v = 1.30 \times 10^{-9} q_v \cdot m/N \qquad (2)$$

An important consideration in the design of offshore structures for ice resistance is that both the strength of the ice and the area of contact are factors in determining ice forces. Further analyses were therefore conducted to include the use of multiple gauges for establishing the variable pressure distributions over the entire contact area. This more refined analysis, using orthotropic plate theory, requires an estimation of the ice pressure contact region, for example by the use of the estimated ice thickness.

Ice has a tendency to fail non-simultaneously and therefore as the area of ice contact increases, the average total force increases but the average pressure decreases. A useful design aid is therefore the "pressure-area diagram" relating the average ice pressure to the ice-structure contact area. This dependency of the ice pressure varying with contact region is also sometimes displayed by representing ice pressure versus the contact width.

5.3.1 Structural Orthotropic Plate Theory (OPT)

The panel with closely distributed stiffeners can be formulated as a structurally equivalent orthotropic plate. This idealization is to replace the stiffened plate by an orthotropic homogeneous plate with rigidities averaged in two orthogonal directions over the plate with respect to the type of orthotropy. The small-deflection theory of bending of thin plates is then applied additionally to the orthotropic plate theory (OPT) formulation to calculate the response of the plate. We set up two models for OPT analyses; both models apply Navier's method to formulate the deflection surface and express the distributed load in the form of a Fourier series. The first OPT model (OPT I) assumes the Fourier coefficients of the pressure to be expanded over the entire plate; while the second OPT model (OPT II) constrains the pressure coefficients to be expressed within an area covered by the depth of the ice thickness. This second model thus presumes there is no pressure from current acting on the plate beneath the ice.

OPT I—Pressure Acting Over Entire Plate

Based on the IFMS geometry, we assume clamped boundaries along the long edges of the plate, and pinned boundary along the top and bottom of the plate. To satisfy the boundary conditions at the edges of the plate, we compose a double Fourier series function for the displacement field and the pressure field. Let m=1..M, n=1..N_n, where M is the expected order of coefficients to be retained along x, and N_n is the order of convergence along y direction:

$$w(x,y) = \sum_{m=1}^{m=M}\sum_{n=1}^{n=N_n} W_{mn} \sin\left(\frac{m\pi x}{a}\right)\left(1-\cos\left(\frac{2n\pi y}{b}\right)\right) \tag{3}$$

$$p_{opt1}(x,y) = \sum_{m=1}^{m=M}\sum_{n=1}^{n=N_n} P_{1_{mn}} \sin\left(\frac{m\pi x}{a}\right)\sin\left(\frac{n\pi y}{b}\right) \tag{4}$$

In our current analysis, uniform pressure along the y direction is assumed. We then express the Fourier series of the pressure field p_{opt1} by employing the coefficients P_{1_m}:

$$p_{opt1}(x,y) = \sum_{m=1}^{m=M}\sum_{n=1,3,5..}^{n=N_n} \frac{4}{n\pi} \sin\left(\frac{m\pi x}{a}\right)\sin\left(\frac{n\pi y}{b}\right)\cdot P_{1_m} \tag{5}$$

Based on the assumptions of Kirchhoff's small-deflection plate bending theory and orthotropic plate theory, the strain energy of bending for orthotropic plate is expressed in integral form over plate area:

$$U = \frac{1}{2}\iint_A \; D_x\left(\frac{\partial^2 w}{\partial x^2}\right)^2 + D_y\left(\frac{\partial^2 w}{\partial y^2}\right)^2 + 2D_{xy}\frac{\partial^2 w}{\partial x^2}\frac{\partial^2 w}{\partial y^2} + 4D_s\left(\frac{\partial^2 w}{\partial x\partial y}\right)^2]dA \tag{6}$$

The flexural and torsional rigidities of the equivalent orthotropic plate have been given for several commonly encountered stiffener formations by:

$$D_y = \frac{EI}{t}, D_x = \frac{Eh^3}{12\left(1-\frac{b_s}{t}+\frac{hb_s^3}{H_1^3}\right)}, D_{xy} = 0, D_s \approx \frac{C_t h^3}{12} + \frac{C_t}{2t} \tag{7}$$

After applying equation (3), substituting (7) into (6) and integrating, we obtain the strain energy for bending of the orthotropic plate expressed by Fourier displacement terms:

$$U = \frac{1}{2}\sum_{m=1}^{m=\infty}\sum_{n=1}^{n=\infty}\left(\frac{3bm^4\pi^4}{4a^3}D_x W_{mn}^2 - \frac{2m^2n^2\pi^4}{ab}D_{xy}W_{mn}^2 + \frac{4an^4\pi^4}{b^3}D_y W_{mn}^2 + \frac{4m^2n^2\pi^4}{ab}D_s W_{mn}^2\right) \tag{8}$$

Also, the external potential energy is written as a function of the displacement and pressure terms defined in equations (3) and (5):

$$V = \iiint_v \; w(x,y)p(x,y)dv = \sum_{m=1}^{m=N_m}\sum_{n=1}^{n=\infty}\sum_{j=1,3,5..}^{j=N_n} \frac{4abP_{1m}W_{mn}}{\pi^2 j}\left\{\frac{1}{j} - \frac{1}{2(j+2n)} - \frac{1}{2(j-2n)}\right\} \tag{9}$$

Applying the principle of stationary total potential energy $\frac{\partial U}{\partial w_{mn}} - \frac{\partial V}{\partial w_{mn}} = 0$, we retain the same number of terms of deformation coefficients to that of pressure terms, in which case the m and n ranges are m=1..M, n=1..N_n:

$$W_{mn} = \frac{\sum_{j=1,3,5..}^{j=N_n} \frac{4ab}{\pi^2 j}[\frac{1}{j} - \frac{1}{2(j+2n)} - \frac{1}{2(j-2n)}]}{\frac{3bm^4\pi^4}{4a^3}D_x - \frac{2m^2n^2\pi^4}{ab}D_{xy} + \frac{4an^4\pi^4}{b^3}D_y + \frac{4m^2n^2\pi^4}{ab}D_s} P_{1_m} \tag{10}$$

The horizontal strains are found from the displacement Fourier series and the strain-displacement relations:

$$\epsilon_{yy} = -z_0 \sum_{m=1}^{m=M} \sum_{n=1}^{n=N_n} W_{mn} \left(\frac{2n\pi}{b}\right)^2 \sin\left(\frac{m\pi x}{a}\right) \cos\left(\frac{2n\pi y}{b}\right) \tag{11}$$

Finally the linear relationship of the strain value to the pressure Fourier coefficient terms P_{1_m} is:

$$\epsilon_{yy} = -z_0 \sum_{m=1}^{m=M} \sum_{n=1}^{n=N_n} \left(\frac{2n\pi}{b}\right)^2 \sin\left(\frac{m\pi x}{a}\right) \cos\left(\frac{2n\pi y}{b}\right) \cdot \frac{\sum_{j=1,3,5..}^{j=N_n} \frac{4ab}{\pi^2 j}[\frac{1}{j} - \frac{1}{2(j+2n)} - \frac{1}{2(j-2n)}]}{\frac{3bm^4\pi^4}{4a^3}D_x - \frac{2m^2n^2\pi^4}{ab}D_{xy} + \frac{4an^4\pi^4}{b^3}D_y + \frac{4m^2n^2\pi^4}{ab}D_s} P_{1_m} \tag{12}$$

OPT II—Pressure Acting Ice-covered Area

Satisfying the same displacement boundary conditions stated in the previous model, we keep the same displacement equation (5), and assume ice-covered area to be $t_{ice}b$. The pressure field p_{opt2} on the constrained area, upon assuming uniform pressure along y, is then expanded by the coefficients P_{2_l}. M and N_n coefficient terms along x and y directions respectively are expected:

$$p_{opt2}(x, y) = \sum_{l=1}^{l=M} \sum_{j=1,3,5..}^{j=N_n} \frac{4}{\pi j} \sin\left(\frac{l\pi\tilde{x}}{t_{ice}}\right) \sin\left(\frac{j\pi y}{b}\right) \cdot P_{2_l} \tag{13}$$

Here $\tilde{x} = x - x_1$, $\tilde{x} \subseteq [0, t_{ice}]$, $x_1$is the starting coordinate along x for the ice contact area.

From substituting (6) into equation (13) as well as the external energy integral equation in (9), and by applying stationary total potential energy, we obtain the relationship of Fourier coefficients for W_{mn} as a function of pressure coefficients P_{2_l} over the confined ice-covered area. Let $k = \frac{m}{a}$, the W_{mn} terms are then expressed as follows:

$$W_{mn} = \sum_{l=1}^{l=M} \sum_{j=1,3,5..}^{j=N_n} \frac{4b}{k\pi^3 j}\left[\frac{1}{j} - \frac{1}{2(j+2n)} - \frac{1}{2(j-2n)}\right] \cdot \frac{a^2 l t_{ice}\left[(-1)^{l+1}\sin\left(\frac{m\pi(x_1+t_{ice})}{a}\right) + \sin\left(\frac{m\pi x_1}{a}\right)\right]}{\pi(a^2l^2 - m^2t_{ice}^2)\left(\frac{3bm^4\pi^4}{4a^3}D_x - \frac{2m^2n^2\pi^4}{ab}D_{xy} + \frac{4an^4\pi^4}{b^3}D_y + \frac{4m^2n^2\pi^4}{ab}D_s\right)} \cdot P_{2_l}, \text{ if } al \neq m;$$

$$W_{mn} = \sum_{m=1}^{m=M} \sum_{j=1,3,5..}^{j=N_n} \frac{4b}{k\pi^3 j}\left[\frac{1}{j} - \frac{1}{2(j+2n)} - \frac{1}{2(j-2n)}\right] \cdot \frac{\left[\cos(k\pi x_1)k\pi t - \frac{1}{2}\cos(k\pi x_1)\sin(2k\pi t_{ice}) + \sin(k\pi x_1)\sin^2(k\pi t_{ice})\right]}{\frac{3bm^4\pi^4}{4a^3}D_x - \frac{2m^2n^2\pi^4}{ab}D_{xy} + \frac{4an^4\pi^4}{b^3}D_y + \frac{4m^2n^2\pi^4}{ab}D_s} \cdot P_{2_l}, \text{ if } al = mt_{ice} \tag{14}$$

where m=1..M; n=1..N_n.

The linear relationship of the strain value ϵ_{yy} at (x, y) to the pressure Fourier coefficient terms for the application of OPT II is calculated by substituting equation (14) into equation (11):

$$\epsilon_{yy} = -z_0 \sum_{m=1}^{m=M} \sum_{n=1}^{n=N_n} \left(\frac{2n\pi}{b}\right)^2 \sin\left(\frac{m\pi x}{a}\right) \cos\left(\frac{2n\pi y}{b}\right) \sum_{j=1,3,5..}^{j=N_n} \sum_{l=1}^{l=M} \frac{4b}{k\pi^3 j}\left[\frac{1}{j} - \frac{1}{2(j+2n)} - \frac{1}{2(j-2n)}\right] \cdot \frac{a^2 l t_{ice}\left[(-1)^{l+1}\sin\left(\frac{m\pi(x_1+t_{ice})}{a}\right)+\sin\left(\frac{m\pi x_1}{a}\right)\right]}{\pi\left(a^2 l^2 - m^2 t_{ice}^2\right)\left(\frac{3\mathrm{bm}^4\pi^4}{4\mathrm{a}^3}\mathrm{D_x} - \frac{2\mathrm{m}^2\mathrm{n}^2\pi^4}{\mathrm{ab}}\mathrm{D_{xy}} + \frac{4\mathrm{an}^4\pi^4}{\mathrm{b}^3}\mathrm{D_y} + \frac{4\mathrm{m}^2\mathrm{n}^2\pi^4}{\mathrm{ab}}\mathrm{D_s}\right)} \cdot P_{2_l}, \text{ if } al \neq mt_{ice};$$

$$\epsilon_{yy} = -z_0 \sum_{m=1}^{m=M} \sum_{n=1}^{n=N_n} \left(\frac{2n\pi}{b}\right)^2 \sin\left(\frac{m\pi x}{a}\right) \cos\left(\frac{2n\pi y}{b}\right) \sum_{j=1,3,5..}^{j=N_n} \sum_{l=1}^{l=M} \frac{4b}{k\pi^3 j}\left[\frac{1}{j} - \frac{1}{2(j+2n)} - \frac{1}{2(j-2n)}\right] \cdot \frac{\left[\cos(k\pi x_1)k\pi t - \frac{1}{2}\cos(k\pi x_1)\sin(2k\pi t_{ice}) + \sin(k\pi x_1)\sin^2(k\pi t_{ice})\right]}{\frac{3\mathrm{bm}^4\pi^4}{4\mathrm{a}^3}\mathrm{D_x} - \frac{2\mathrm{m}^2\mathrm{n}^2\pi^4}{\mathrm{ab}}\mathrm{D_{xy}} + \frac{4\mathrm{an}^4\pi^4}{\mathrm{b}^3}\mathrm{D_y} + \frac{4\mathrm{m}^2\mathrm{n}^2\pi^4}{\mathrm{ab}}\mathrm{D_s}} \cdot P_{2_l}, \text{ if } al = mt_{ice} \quad (15)$$

5.3.2 Orthotropic Plate Inverse Theory (OPIT)

Rather than conventionally determining displacement and strain fields from applied loading, we are faced with the inverse problem: that of estimating applied pressures from limited strain measurements. From the use of Fourier coefficients of the variable displacement W_{mn} just described, equations (10) and (14) can be expressed in linear matrix form:

$$\{W_l\}_n = [A_l]_n\{P_l\} \quad (16)$$

Similarly, we configure the strain-displacement relationship in equation (11) using the matrix $[S]_n$ with the same subscript n representing the order along the y direction, the strain vector is expressed for the l_{th} OPT algorithm:

$$\left\{\epsilon_{yy_i}\right\} = \sum_{n=1}^{n=N_n}[S]_n\,\{W_l\}_n \quad (17)$$

The inverse relation of the strain vector to the deformation coefficient is then expressed as:

$$\{W_l\} = \sum_{n=1}^{n=N_n}[S]_n^{-1}\left\{\epsilon_{yy_i}\right\} \quad (18)$$

We assume the index of the input element i=1..I_{inp}, where I_{inp} is the total number of input. The maximum number of coefficient terms M is restricted to the strain input number I_{inp} . We then substitute (18) into (16), sum the coefficient matrix to order of N_n, and obtain the general orthotropic inverse coefficient matrix operation in the form:

$$\{P_l\} = \sum_{n=1}^{n=N_n}[A_l]_n^{-1}[S]_n^{-1} \cdot \{\epsilon_{yy_i}\} \quad (19)$$

OPIT I

In the scenario of I_{inp} equals 6, the maximum number of coefficients is $M_1 = I_{inp}$ to be retrieved through the linear matrix operation described in (19). The coefficient vector is described as:

$$\{\mathrm{P_1}\} = [\mathrm{P_{1_1}}\ \mathrm{P_{1_2}}\mathrm{P_{1_3}}\ \mathrm{P_{1_4}}\ \mathrm{P_{1_5}}\ \mathrm{P_{1_6}}]' \quad (20)$$

The strain measurements are, for example, from ribs #1 to rib #5 plus rib #7; we then define the six linear strain input elements as $\epsilon_{yy_i},\ i = 1..I_{inp}$.

$$\{\epsilon_{\mathrm{yy}}\} = [\varepsilon_{yy_1}\varepsilon_{yy_2}\varepsilon_{yy_3}\varepsilon_{yy_4}\varepsilon_{yy_5}\varepsilon_{yy_6}]' \quad (21)$$

The strain values can be calculated from equation (11). In the case of the horizontal linear strain gauges, $y_0 = \frac{b}{2}$, and x_i are the coordinates of the horizontal linear strain gauges, we find:

$$\epsilon_{yy}(x_i, y_0) = \epsilon_{yy_i} = z_0 \left(\frac{2\pi}{b}\right)^2 \sum_{m=1}^{m=6} \sum_{n=1}^{N_n} \sin\left(\frac{m\pi x_i}{a}\right) \cos(\frac{2n\pi y_0}{b}) W_{mn} \tag{22}$$

The element for the nth strain-displacement matrix $[S]_n$is:

$$S(i, m)_n = z_0 \left(\frac{2\pi}{b}\right)^2 \cdot \sin(\frac{m\pi x(i)}{a}) \cdot \cos(\frac{2n\pi y_0}{b}) \tag{23}$$

In the following we let N_n equal 33, which sufficiently allows for converge of uniform pressure assumption along the y direction. Then the elements in the diagonal displacement-pressure coefficient matrix $[A_1]_n$ can be found from equation (10) as follows:

$$A_1(m, m)_n = \frac{\sum_{\mathrm{j=1,3,5..}}^{\mathrm{j=33}} \frac{4ab}{j\pi^2}[\frac{1}{j} - \frac{1}{2(j+2n)} - \frac{1}{2(j-2n)}]}{\frac{3\mathrm{bm}^4\pi^4}{4\mathrm{a}^3}\mathrm{D_x} - \frac{2\mathrm{m}^2\mathrm{n}^2\pi^4}{\mathrm{ab}}\mathrm{D_{xy}} + \frac{4\mathrm{an}^4\pi^4}{\mathrm{b}^3}\mathrm{D_y} + \frac{4\mathrm{m}^2\mathrm{n}^2\pi^4}{\mathrm{ab}}\mathrm{D_s}} \tag{24}$$

Let the strain-pressure coefficients relation matrix $[C_1]$ for OPIT I be defined by,

$$[C_1] = \sum_{n=1}^{n=Nn} [S]_n \, [A_1]_n \tag{25}$$

The strain-pressure relationship is then established as,

$$\left\{\varepsilon_{yy_i}\right\} = [\mathrm{C_1}]\{\mathrm{P_1}\} \tag{26}$$

Inversely,

$$\{P_1\} = [C_1]^{-1}\{\epsilon_{yy_i}\} \tag{27}$$

The coefficient matrix $[C_1]^{-1}$ solution is then found as:

$$[C_1]^{-1} = (\sum_{n=1}^{n=Nn} [S]_n \, [A_1]_n)^{-1} \tag{28}$$

The matrix $[C_1]^{-1}$ is a well posed full-matrix with condition number roughly equals 8.0 for any case.

OPIT II

Following a similar procedure for OPIT I with the same amount of strain inputs I_{inp}, we extract the Fourier coefficients of pressure on the constrained ice covered area by letting $l = 1 \dots M_2$, where M_2 is the maximum number of the pressure coefficients we intend to extract through the linear matrix operation. The pressure-displacement matrix $[A_2]_n$ is expressed from the equation (14) in linear matrix form. Let:

$$e_2(m, l)_n = \frac{a^2 l t_{ice}}{\pi(a^2 l^2 - m^2 t_{ice}^2)} \left[(-1)^{l+1} \sin\left(\frac{m\pi(x_1 + t_{ice})}{a}\right) + \sin\left(\frac{m\pi x_1}{a}\right)\right], \text{if } al \neq mt_{ice}$$

$$e_2(m, l)_n = \frac{1}{2k\pi}\left[\cos(k\pi x_1)\, k\pi t - \frac{1}{2}\cos(k\pi x_1)\sin(2k\pi t_{ice}) + \sin(k\pi x_1)\sin^2(k\pi ti)\right], \text{if } al = mt_{ice} \tag{29}$$

The elements of $[A_2]_n$ are:

$$A_2(m,l)_n = \frac{\sum_{j=1,3,5..}^{j=33} \frac{b}{2j}\left[\frac{1}{j} - \frac{1}{2(j+2n)} - \frac{1}{2(j-2n)}\right] \cdot e_2(m,l)_n}{\frac{3bm^4\pi^4}{4a^3}D_x - \frac{2m^2n^2\pi^4}{ab}D_{xy} + \frac{4an^4\pi^4}{b^3}D_y + \frac{4m^2n^2\pi^4}{ab}D_s} \tag{30}$$

where the maximum order is M_2 for both m and l.

The strain-displacement coefficient matrix $[S]_n$ is independent of the form of pressure applied, and it is the same as in equation (23) for OPIT I. We then obtain the coefficient matrix $[C_2]^{-1}$ relating the strain vector to the pressure terms as the summation of the products of $[S]_n$ and $[A_2]_n$:

$$[C_2]^{-1} = (\sum_{n=1}^{n=Nn}[S]_n\,[A_2]_n)^{-1} \tag{31}$$

We note the coefficient matrix of $[C_2]$ is ill posed when we set M_2 equal to the number of input strains $I_{inp} = 6$.

Examining the performance evaluations of the $[C_2]$ matrix in OPIT II, it is found that the practical limit on the number of trigonometric pressure coefficients is reduced when the confined area for pressure is reduced. The truncated singular value decomposition method (TSVD) is applied as the optimization procedure to determine the maximum coefficients number M_{trun} as the limit to be extracted under specific conditions. The philosophy of the optimization procedure is to truncate the terms of zero or close-to-zero singular values to control the condition number of the coefficient matrix within the range of non-triviality. The optimal number of pressure coefficients M_{trun} is determined through the TSVD procedure by controlling the condition number to be within the range of robustness. The optimization algorithm is sketched in Figure 5.25. As a rule of thumb, the order k of the condition number $\kappa = 10^k$ indicates the digits of accuracy due to loss of precision from the arithmetic method. We observed the error level of 5% to 15% between the OPT II solutions at low frequencies of 3 to that obtained in more accurate FE solutions.

Finally, applying the least square fit to extract M_{trun} of coefficients values, we have obtained a coefficient matrix $[C_2]$ of I_{inp} by M_{trun}:

$$[C_2] = \sum_{n=1}^{n=Nn}[S]_n\,[A_2]_n \tag{32}$$

$$[C_2]^+ = [C_2]^T([C_2][C_2]^T)^{-1} \tag{33}$$

$$\{P_2\} = [C_2]^+\{\epsilon_{yy_i}\} \tag{34}$$

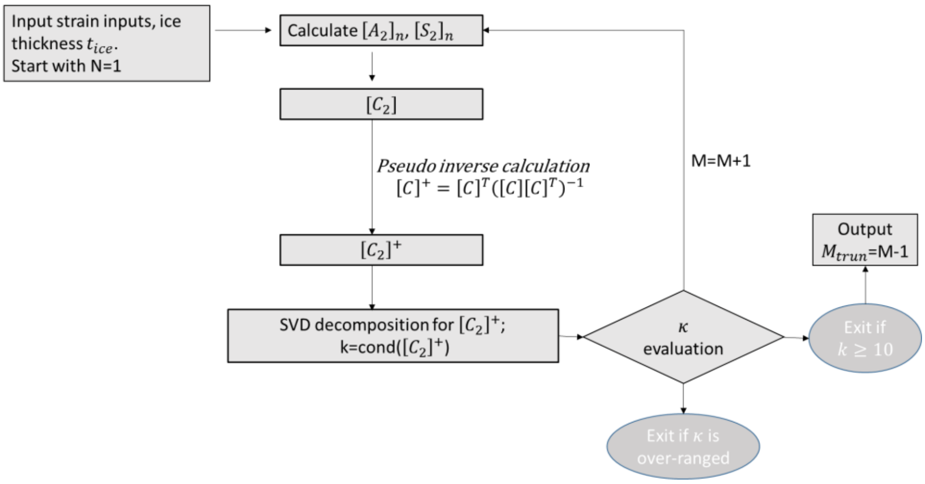

Figure 5.25 Optimization procedure in seek of N_{trun} throughT SVD method.

5.3.3 Data Analysis and Field Experimental Results

The algorithms just described were applied using the field-measured strains recorded by the IFMS system on March 18, April 17, and May 01, 2014. The recorded ice thicknesses measured from February to May are plotted in Figure 5.26. As mentioned in Section 5.2, the maximum strain variations recorded through the winter were observed on May 1. The pressures are calculated by both OPIT I and OPIT II. The recorded strain values and the calculated forcing pressures are shown in Figures 5.27, 5.28 and 5.29.

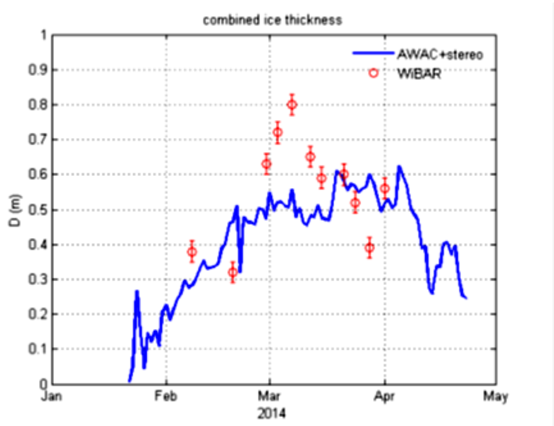

Figure 5.26 Estimate of the ice thickness from field measurements by the WiBAR and the Acoustic Doppler Current Profiler + Scene Capture System.

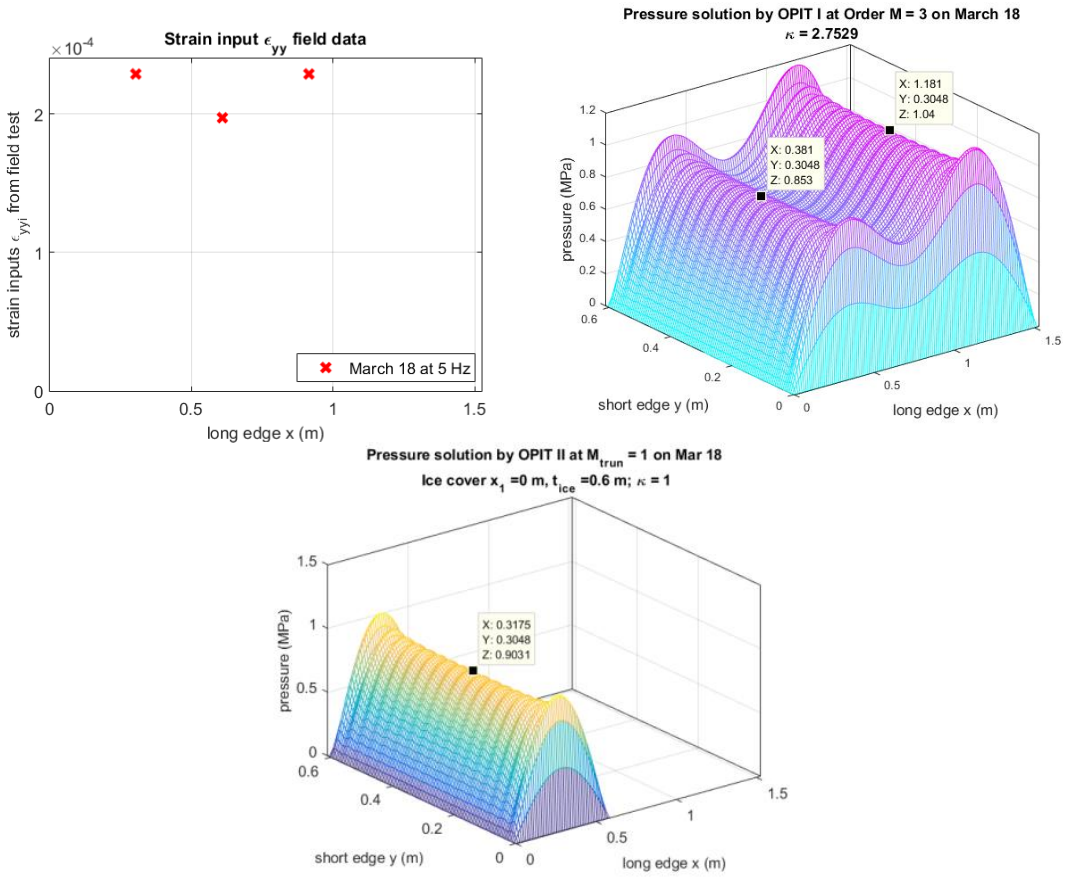

Figure 5.27. Strain measurement and pressure solutions for 18 March 2014.

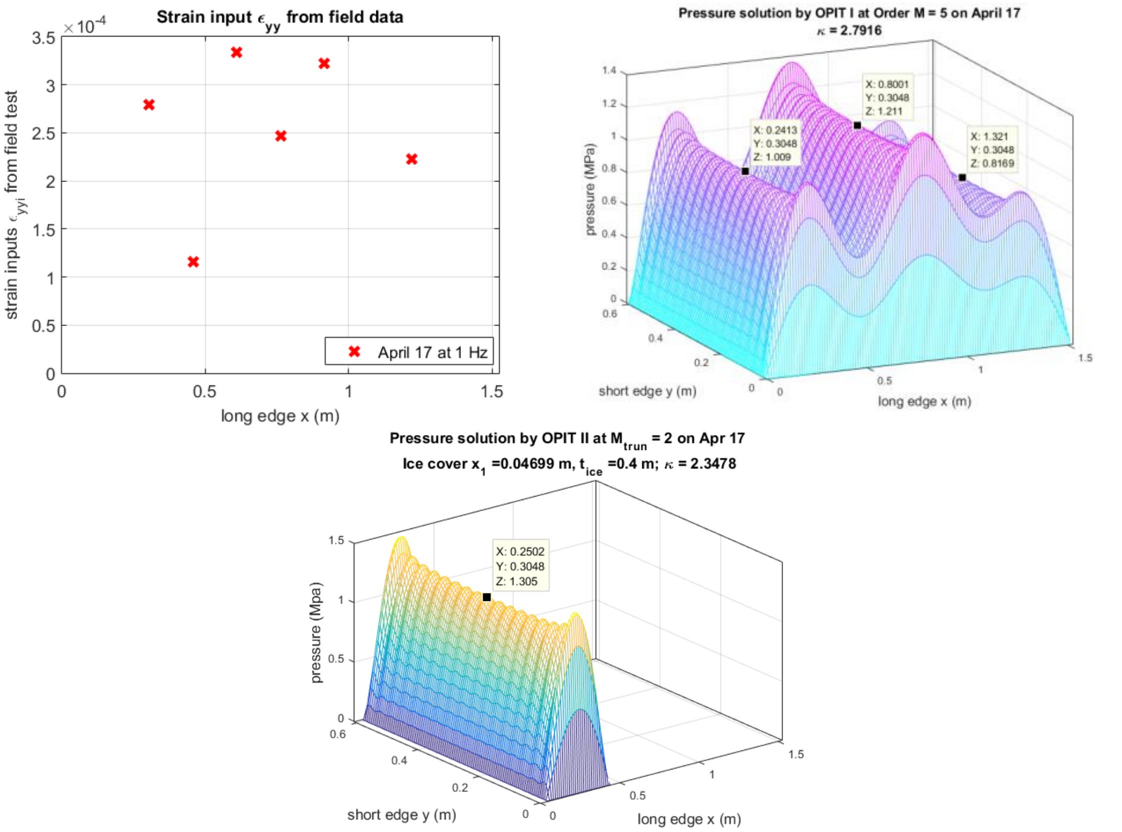

Figure 5.28. Pressure solution by OPIT I and OPIT II using strain inputs from 17 April 2014.

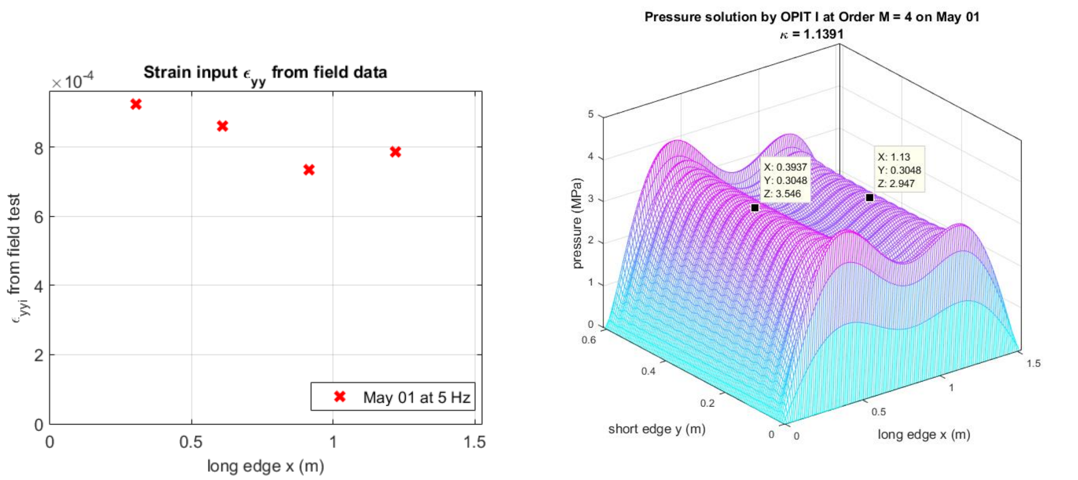

Figure 5.29 Maximum strain inputs on 1 May 2014 and calculated pressure by OPIT I using strain input values.

The pressure calculated by SBT correlates well with the results obtained by OPIT I and II, as is shown in Table 5.1, justifying the averaging effect of the Strip Beam Theory (SBT) approach as a reasonable approximation for the initial evaluations.

Table 5.1. Calculated peak pressure for field measurements by the SBT and the OPIT methods

Analysis Result		**Peak Pressure Value (MPa)**		
Measurement date	Ice thickness (m)	solution by SBT	solution by OPIT I	Solution by OPIT II
Mar 18 2014	0.6	0.81	0.85 and 1.04	0.90
Apr 17 2014	0.4	1.18	1.01, 1.21 and 0.82	1.31
May 01 2014	--	3.44	3.55 and 2.95	--

Due to the lack of sufficient data for the ice-thickness on May 1, the pressures are calculated by only OPIT I for May 1 (Figure 5.29).

5.3.4 Ice Design Criteria

We indicate the peak measured ice pressures vs. the structural width in Figure 5.30. This figure is adapted from Bjerkas (2007). The peak pressure of May 01 (red four-point star) by OPIT I agrees well with the result calculated by the classic method of SBT (Strip Beam Theory) (blue four-point star) and is slightly higher, a reflection of a possible non-uniform interfacial peak value. Both of the calculations reside well within the region for previously measured ice pressures for this specific structural width. The peak pressures on April 17 (red square) and on March 18 (blue star) are located within the lower range for ice-pressure diagram in Figure 5.30. The maximum ice pressure measured during the winter of 2013-2014, which was a relatively severe winter, was approximately 3.6 MPa, this lies in the upper range.

Two important aspects of design of offshore wind turbines in ice are horizontal forces from fast ice cover and from moving ice. Most our measurements recorded during the winter were from fast ice and forces are a result of thermal expansion and contraction and wind shear. <u>*Our best estimates for fast ice at the site are in the 1.0-1.3 MPa range.*</u> These values however do not represent the ice crushing strength; failure or crushing of the ice at these values was not generally observed. Readings from March 18, 2014 are near 1.0 MPa and ice was definitely fast ice at that time. April 17 readings are somewhat higher but at that time the ice may have been beginning to break up and therefore had some additional dynamics contributing to ice forces. <u>*The maximum ice pressures recorded were approximately 3.6 MPa, these readings were from moving ice*</u>. These pressures were however acting over limited area on a structure (the IFMS) of less than 1 m in width as the ice crushed against the IFMS plating.

Figure 5.31 shows suggested design pressures for Arctic ice loading. Of particular interest is the lower curve for first year ice. Our peak measurements compare closely with this curve developed for prediction of extreme pressures for sea ice impacts.

Of course with a properly estimated ice pressured used in design, an ice thickness must also be established for calculating the estimated forces acting on the structure. The proposed IEC 61400-31 Design Requirements for Offshore Wind Turbines suggests a choice of ice thickness, h, based on freezing degree days K_{max} :

$$h = 0.032\sqrt{0.9\,K_{max} - K_0} \tag{35}$$

where K_0 is a constant and has been established as 50 degree-days for northern Europe. These values seem to give reasonable growth rate for the site of our study but overestimate the ice thickness beyond roughly 0.5 m. Examining the temperatures in the area from January 20, 2014 to March 1, 2014 we have 40 days of below freezing temperatures with average temperature of -14.5 degrees centigrade. This yields $K_{max} =$ 580 degree days. The estimated ice thickness is 0.70 m whereas the measured thickness is roughly 0.55 m. As shown in section 6.2, the growth rate of the ice thickness, averaged over several days decreases in later February and early March even though the freezing degree days continue to increase through mid-March. This may be due to the water depth at the site but it also may indicate some limitations to the application of formulae of the type in equation (35). Further data should be established for specific sites in this regard.

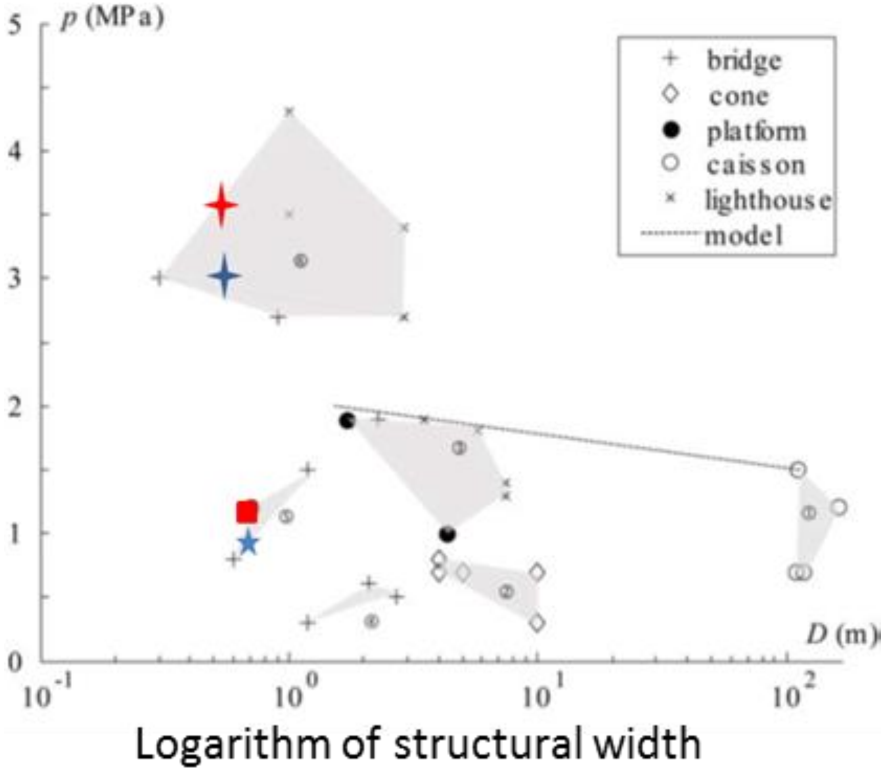

Figure 5.30. Effective ice pressure vs. the structural width (adapted from Bjerkas 2007[1]). Four point star: peak of May 1 by OPIT I (red) and SBT (blue); Square (red): peak of April 17 by OPIT II; Five point star (blue): peak of March 18 by OPIT I.

[1] Bjerkås, Morten. "Review of measured full scale ice loads to fixed structures." *ASME 2007 26th International Conference on Offshore Mechanics and Arctic Engineering*. American Society of Mechanical Engineers.

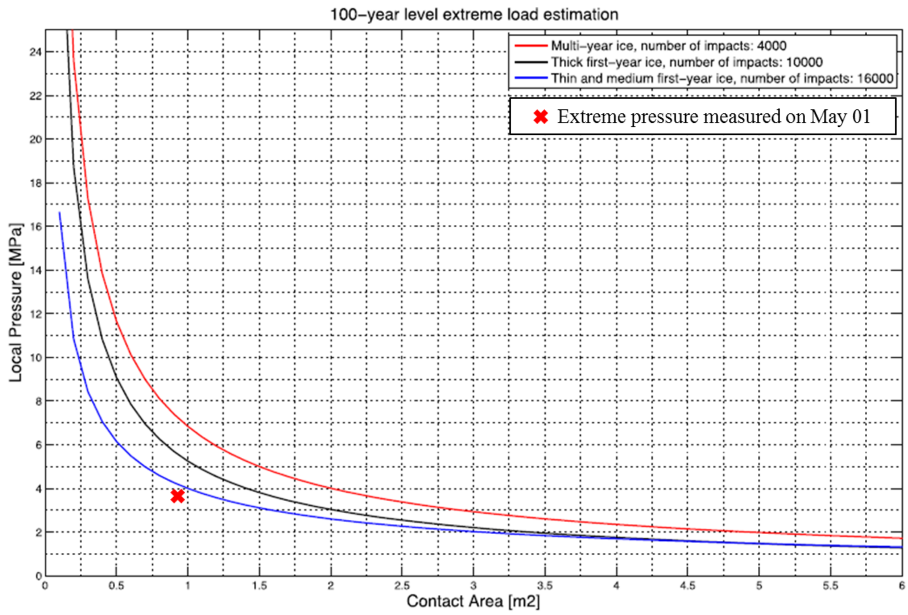

Figure 5.31. Predicted extreme load pressure for the specific route and comparison to the extreme load pressure measured by IFMS on May 01. (adapted from Tõns et al., 2015b[2])

5.4 A DYNAMICS MODEL FOR STRUCTURAL LOADING

The coupled response of the ice structural interaction dynamics is affected by the size, stiffness and resulting dynamic response of the wind turbine foundations as well as the ice feature characteristics. Frequency lock-in is an important issue for offshore structures in ice; here the response of the structure influences the ice breaking pattern and vice versa. The net result can be dynamical response in which forces and deflections of the structure are increased well beyond the effects of static application of the ice forces. These coupled responses of ice and structure thus may strongly affect the peak displacements of the structure and the time cycles involved in the response. Understanding this phenomenon and predicting this behavior are important for assessing the strength of the structure and the fatigue cycles that the system may undergo. According to IEC 61400-31, turbines must be checked for dynamic effects from ice loading and lock-in is almost always possible.

We have therefore developed a new modelling technique for rapid assessment of lock-in behavior. Continuous brittle crushing occurs in the movement of an ice sheet against an offshore structure. Matlock's ice-structure interaction model is used to simulate the behavior of the ice crushing by modeling ice teeth indentation contacting an idealized structural system for the offshore turbine support structure. The dynamic behavior of this ice-structure interaction system is studied using Fourier analysis to predict the response of specific periodicity. The system's equations of motion are established based on the assumption of continuous ice indentation with intermittent ice failure. The time histories are expressed through the non-linear dynamic equations. The kinematic initial conditions of the system can be predicted at targeted periodicity via the Fourier analysis.

[2] Tõns, T., Ralph, F., Ehlers, S. & Jordaan, I. Probabilistic Design Load Method for the Northern Sea Route. submitted to OMAE2015, 2015b St. Johns, Canada.

Using the new modelling technique allows rapid estimation for the range of motion and the evaluation of structural contact forces. The amplitudes predicted by our Fourier analysis solution correspond well to the simulation results obtained from closed-form solutions with random initial condition selections. Also, with the calculated structural periodic responses, the mean value and the magnitude of the oscillating contact forces can be obtained. These output parameters are key factors for strength and fatigue life assessment. The model is presented in detail in Appendix 5.2

6 WIDEBAND AUTOCORRELATION RADIOMETER (R. DEROO)

The Wideband Autocorrelation Radiometer is a novel instrument developed for this project for the purpose of monitoring ice thickness. It supplements the Scene Capture System (SCS), which monitors the vertical location of the upper surface of the frozen material on the lake, and Acoustic Doppler Current Profiler (ADCP), which monitors the vertical locations of the lower surface of the frozen materials and the water level. Unlike these instruments, which put an upper bound on the ice thickness, the WiBAR provides a lower bound of ice thickness.

The WiBAR uses the microwave portion of the electromagnetic spectrum to see in all weather conditions and through snow pack and ice pack with minimal attenuation. Dielectric mismatches between the constituent materials, namely air, snow pack, ice, and water, cause reflections that can be observed. The concept is similar to a 'profiling' radar, which could have been used for the same purpose, except for a major operational difference: a radar would have to be positioned directly over the patch of ice to be monitored, while the WiBAR can observe the same patch of ice at a wide range of incidence angles. As such, a costly and precarious mechanical assembly extending over the lake from the lighthouse is eliminated by the decision to use a WiBAR rather than a radar. The WiBAR looks obliquely to the patch of ice by being robustly attached to the lighthouse in a similar manner and location as the SCS cameras.

The WiBAR concept utilizes the Planck radiation of the water under the ice as the signal source. The manuscript included in Appendix 6.1, which has been submitted for publication, describes the technique and some results that demonstrate the technique. Despite the fact that this source of radiation is incoherent, the plane-parallel structure of lake ice on water produces constructive and destructive interference in the emission. This occurs because a ray traveling upward from the water through the ice and into the air experiences not just refraction at the ice-air interface, but also reflection. This downwardly reflected ray can then reflect off the ice-water interface and resume its upward travel. The fact that this delayed ray is an exact copy of the direct ray, albeit at a smaller amplitude, manifests itself as coherent interference of the Planck radiation observed above the ice, with the constructive interference occurring when the difference in travel times of the delayed and direct rays corresponds to an integer number of wavelengths and destructive interference at half-integer number of wavelengths. Thus, wideband monitoring of the Planck spectrum can unambiguously determine the ice thickness by locating the periodic maxima and minima of the microwave emissivity.

Horizontal polarization was selected to maximize the signal to noise ratio. For planar dielectric interfaces at a given incidence angle, the horizontally polarized reflectivity is always larger than the vertically polarized reflectivity. We have made observations at both polarizations of various targets at several frequencies, and while we occasionally have had difficulty observing the H-polarized delay signal, we have never been able to observe the V-polarized delay. Thus, the instrument was developed with a single H-polarized channel.

The region of the microwave spectrum chosen for the operation of the WiBAR was 7 to 10 GHz (X-band). This region of the spectrum was selected for several reasons. There is a distinct advantage in going towards higher frequencies, as a wider bandwidth is easier to achieve at higher operating frequencies. The bandwidth determines the minimum measurable ice thickness, which for our 3GHz system is around 10cm. Above this thickness, the instrument has high resolution in the ice thickness measurement (at least as good as 1cm). At higher frequencies (shorter wavelengths) we may see small-scale imperfections in the ice that would violate the plane-parallel assumption needed for making the measurement. Moreover, a survey of spectrum usage indicated that this portion of the spectrum would harbor a relative minimum of anthropogenic sources of radio frequency interference. Observations of the spectrum at the South Entry light revealed a consistent lack of observable interference.

Numerous experiments determined the reliability of the X-band WiBAR measurement of the ice pack. These and other measurements also confirmed the theoretical expectation that snow-air interface does not produce a reflection strong enough to be confused with the ice-snow interface. Thus, the X-band WiBAR is not observing the snow pack on top of the ice. The WiBAR measurement is therefore an important supplement to the SCS cameras, which only see the location of the top snow surface. However, liquid water is opaque to microwaves, and any time moisture appears in the icepack column, it determines the lower level of the icepack, as far as the WiBAR is concerned. Thus, days with temperatures above freezing produce moisture at the top of the snowpack and or icepack, and the WiBAR delay drops to zero. Similarly, events in which lake water is splashed or seeps up to the top of the ice pack can similarly drive the WiBAR delay to zero. While this appears to be a disadvantage of the technique, it enables us to more fully understand the evolution of the ice pack than simply monitoring the vertical distance between the upper and lower surfaces.

6.1 INSTRUMENTATION

Figure 6.1 shows photographs of the field-deployed WiBAR instrument, mounted on the railing of the Southlight. The WiBAR mounting structure was designed to allow for tilt angle (view angle) variation, as well as ease of installation onto the lighthouse railing.

(a)

(b)

(c)

Figure 6.1 (a) WiBAR as it is pointed to 'view' the water surface (b) WiBAR antenna opening, protected by water-proof radome (c) WiBAR with one of the Scene Capture System cameras in the foreground.

As the prototype WiBAR is described in detail in Appendix 6.1, we focus our discussion on the design and fabrication of the field deployed WiBAR. First, the block diagram of the WiBAR is shown in Figure 6.2. The components that make up the radiometer includes: high gain horn antenna, isolators, amplifiers, switches, ambient load, bandpass filers and a spectrum analyzer.

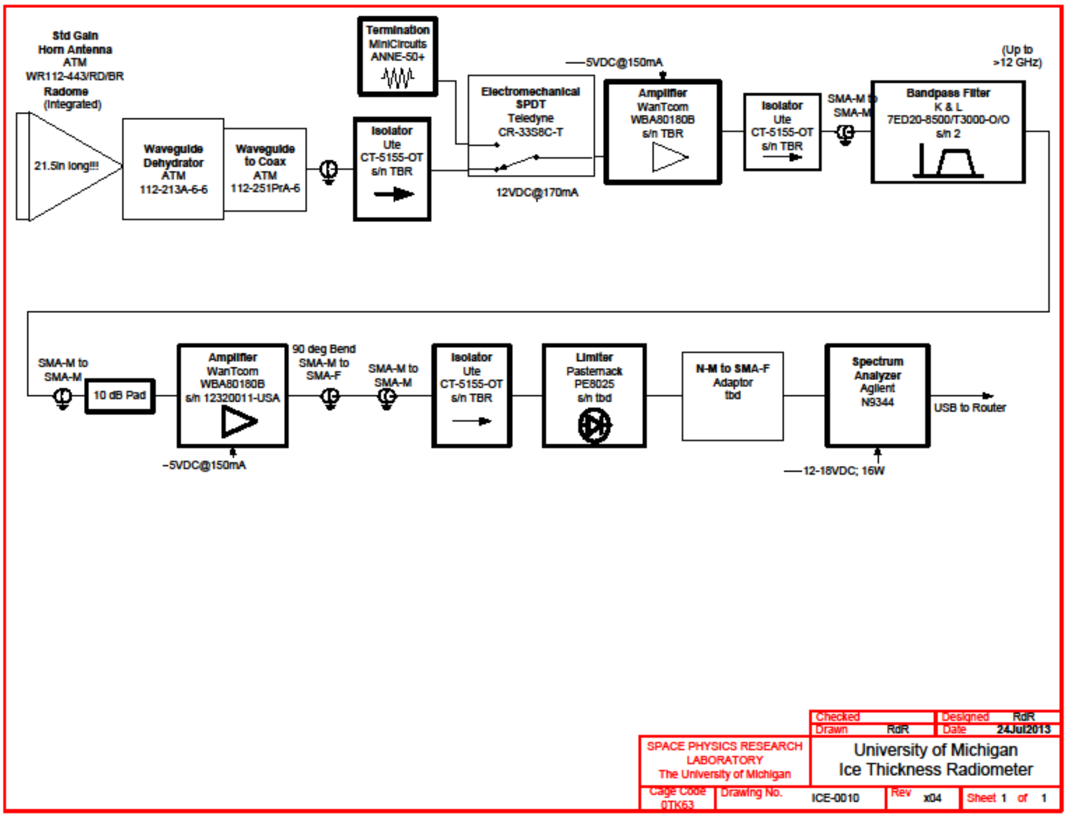

Figure 6.2 WiBAR block diagram

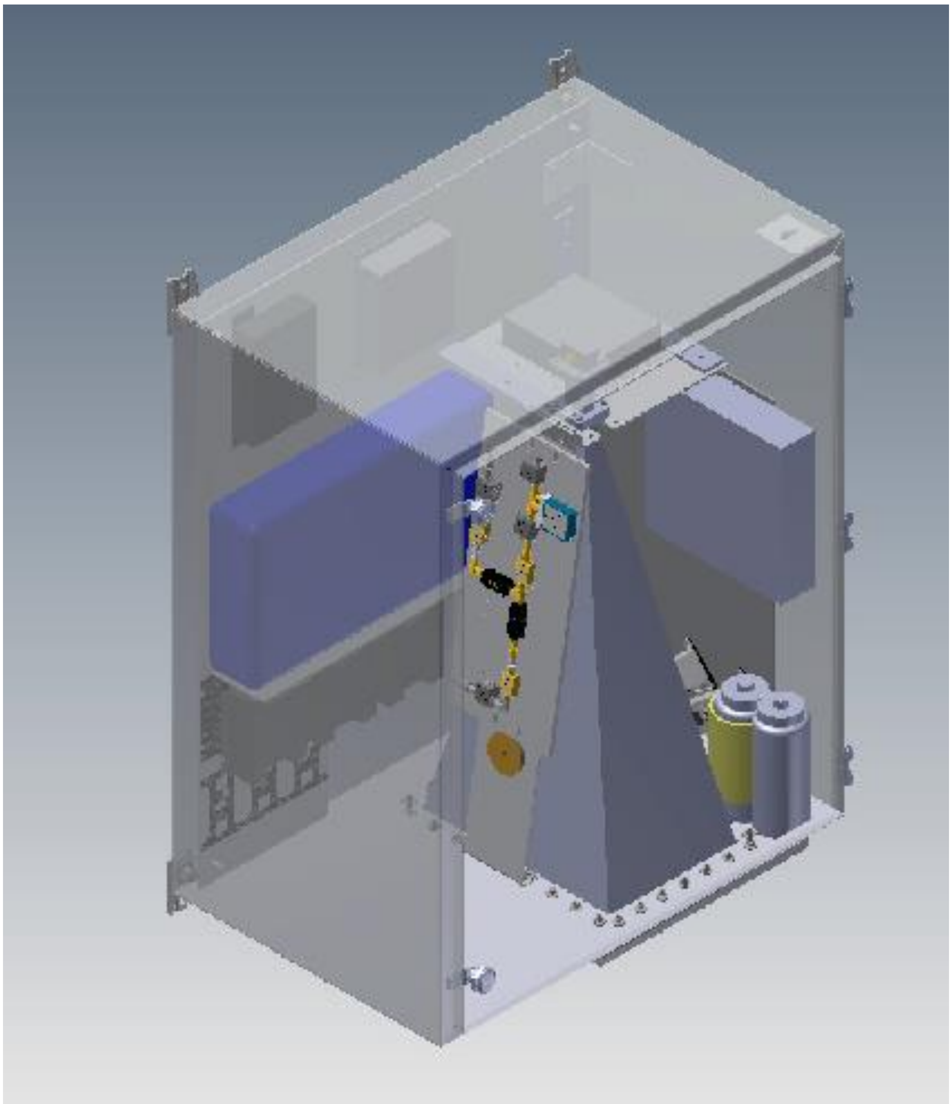

Figure 6.3 Assembly drawing of the WiBAR water-proof enclosure showing internal components placement

Considering the expected harsh experimental environment, the WiBAR is housed in a waterproof enclosure. Pieces of the Instrument Support System (ISS) are also placed in this waterproof enclosure, specifically the data acquisition and monitor board, the cellular link hardware (data router and transceiver), and the DC power conditioning units for the SCS cameras. All components of the WiBAR were selected for their capability to operate in harsh temperature conditions, from -25ºC to +40ºC. The assembly drawing of the WiBAR inside the waterproof enclosure is shown in Figure 6.3. It illustrates the placements of some of the components of the ISS (instrument support system); specifically: (1) data acquisition and system control; (2) cellular data link hardware including a router and external antenna; and (3) DC power conditioning circuitry. Details of the ISS components will follow in chapter 9. The mounting structure for the WiBAR enclosure, shown in Figure 6.4, was designed to allow the radiometer to be positioned at several 'view angles' as specified in Figure 6.4(b). Figure 6.5 shows photographs of the completed WiBAR system.

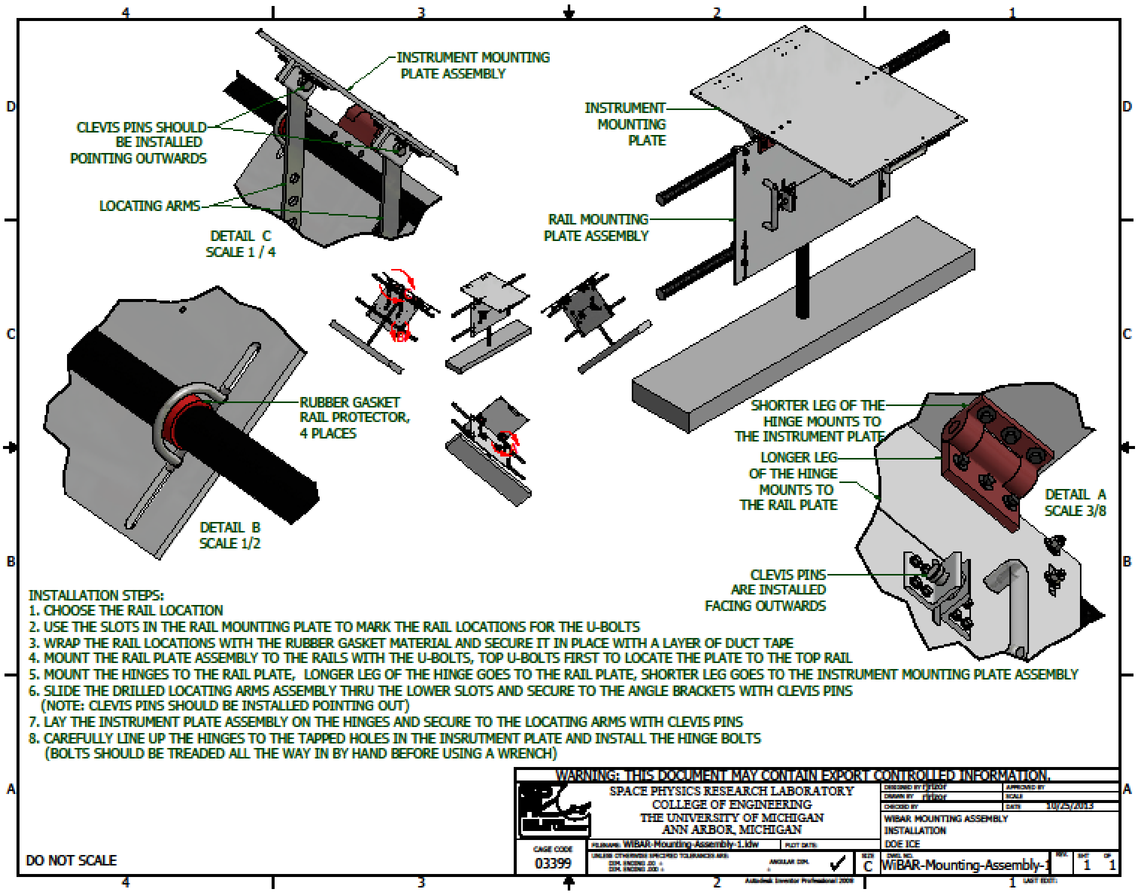

(a)

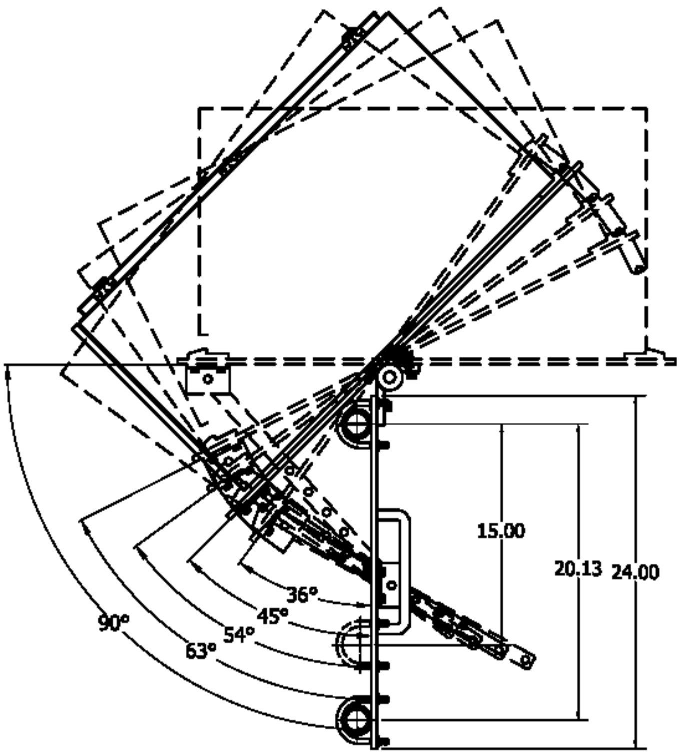

(b)

Figure 6.4 Mounting structure for the WiBAR water-proof enclosure

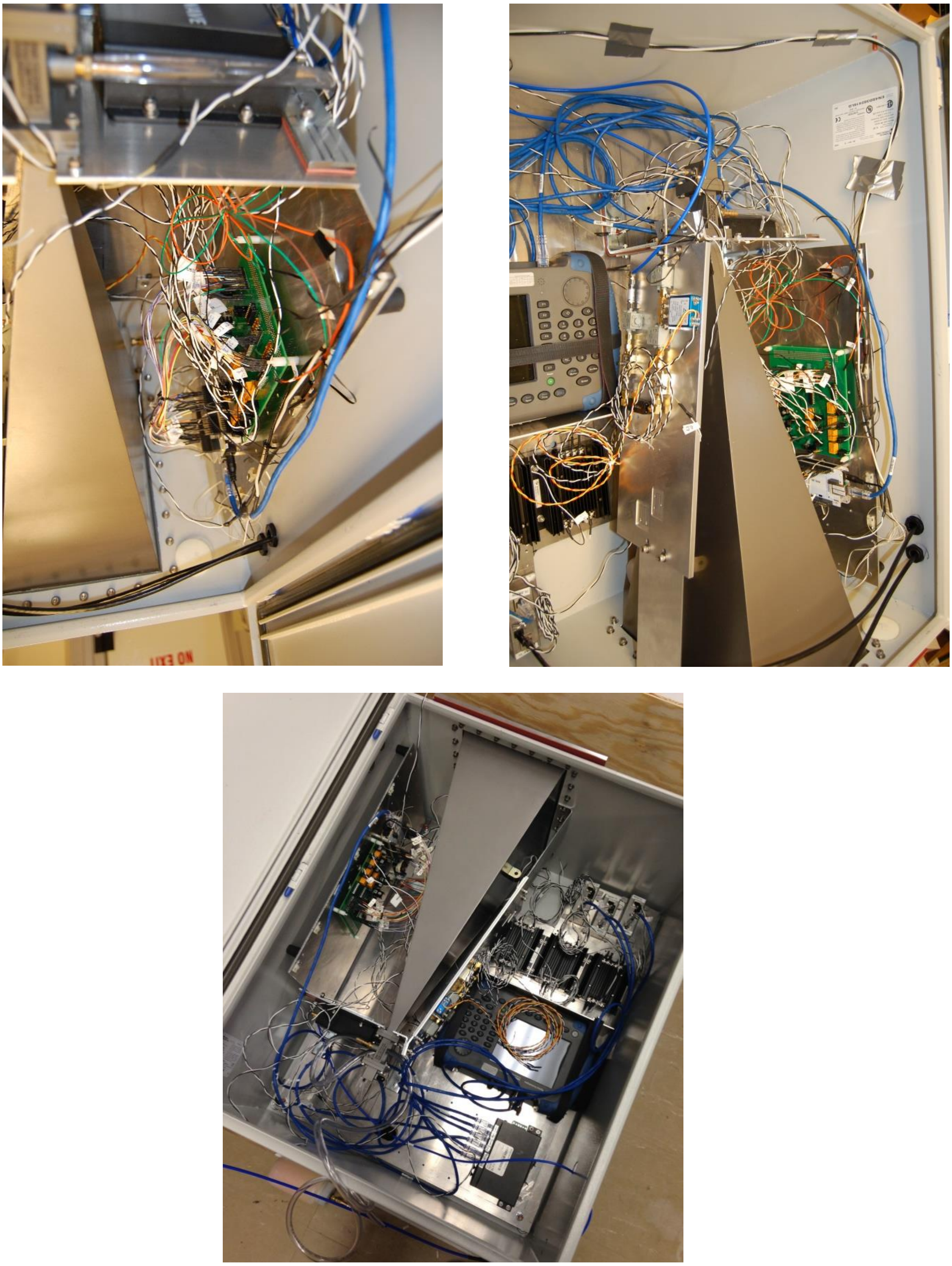

Figure 6.5 WiBAR completed assembly

6.2 MEASUREMENTS RESULTS

The WiBAR was installed on the South Entry Light along with the rest of the instrumentation in late 2013; data collected is summarized in Figure 6.6. At the heart of this WiBAR instrument is an Agilent NX9934C spectrum analyzer. While this spectrum analyzer was designed to be field portable, and thus sufficiently rugged for the Keweenaw winter, it was intended to be operated by a human technician, not remotely as we deployed it. As a result, it was unfortunately easy to put the instrument into a non-communicative state. Recovery from this state required a manual power-up (even remote power-up was insufficient to restore communication).

In December and January, the conditions at the lighthouse were too harsh for human visitors: the ice had not yet formed sufficient cover over Keweenaw Bay to suppress wave action. On 08 Feb 2014, the ice cover was still discontinuous, but the calm conditions permitted a site visit from personnel from GLRC, who, among other tasks, did the manual reset of the spectrum analyzer. The field personnel reported significant ice cover on Keweenaw Bay (albeit without a thickness measurement, which would have been dangerous to try to collect), and rapid movement of the ice, including one instance of a very loud collision of ice floes. The WiBAR was operated for several hours after this site visit. The first two measurements produced the clearest signals of the ice thickness. Later comparisons to the combined stereo cameras and AWAC data showed satisfactory agreement. The next four measurements had a complete lack of a delayed signal, indicating that either the ice had gotten wet, or, more likely given the field team's report, that the ice flow moved away from the lighthouse and the WiBAR was again looking at open water.

While we collected data again the next morning, the spectrum analyzer had again become uncommunicative after that data set was acquired. Conditions permitted a site visit by Hamid Nejati on 19 Feb 2014 for the manual reset. By this time, we had discovered the rather non-intuitive recipe for successful operation of the spectrum analyzer: do not command it to shut down, but rather cut the power to it to shut it down. We had no further issues with the WiBAR that required a site visit, and a rather complete set of data was acquired from this date into May. Subsequent data gaps were related to other operational challenges, such as low battery power, but none required field personnel to rectify.

Despite the rather large volume of data collected from late February on to May, the signal to noise ratio was significantly reduced from the clear observations made on 08 Feb. To obtain the autocorrelation function, we employed more sophisticated inversions of the spectrum measured by the spectrum analyzer than the simple inverse Fourier transform (IFFT) that we had been using up to this point. Algorithms attempted include ESPRIT and SPICE; details of algorithms are included in Appendix 6.2. Results using these algorithms agreed with the IFFT for the high SNR measurements on 08 Feb, and were roughly consistent with each other for about half of the remaining measurements for which a delay could be extracted. We decided on SPICE as our algorithm of choice, primarily because it required no a priori inputs to the algorithm. The choice of parameters in the ESPRIT technique affected the results it reported.

The largest values of the ice thickness estimated by the WiBAR occur on 19 Feb and on 15 Mar, with thicknesses slightly greater than 50cm. These values correlate well with the measurements of the AWAC profiler and stereo cameras. After this, while the AWAC profiler and stereo cameras show increased ice thickness in late March and early April, the WiBAR is seeing a decline, with a majority of values being near 20cm. The reason for this is not clear, but we do know that the WiBAR will measure the thickness down to the first encounter with water, not the last, while the AWAC profiler measures up from the lake bottom to the bottommost ice. Thus, liquid water in the interior of the ice would be consistent with these observations. By the middle of April, the WiBAR was no longer showing any evidence of a delayed signal, consistent with the photographic evidence that by then the ice had broken up.

WiBAR ice thickness data, along with the AWAC and stereo imaging data, is shown in Figure 6.6; MatLab script to generate Figure 6.6 is in Appendix 6.3.

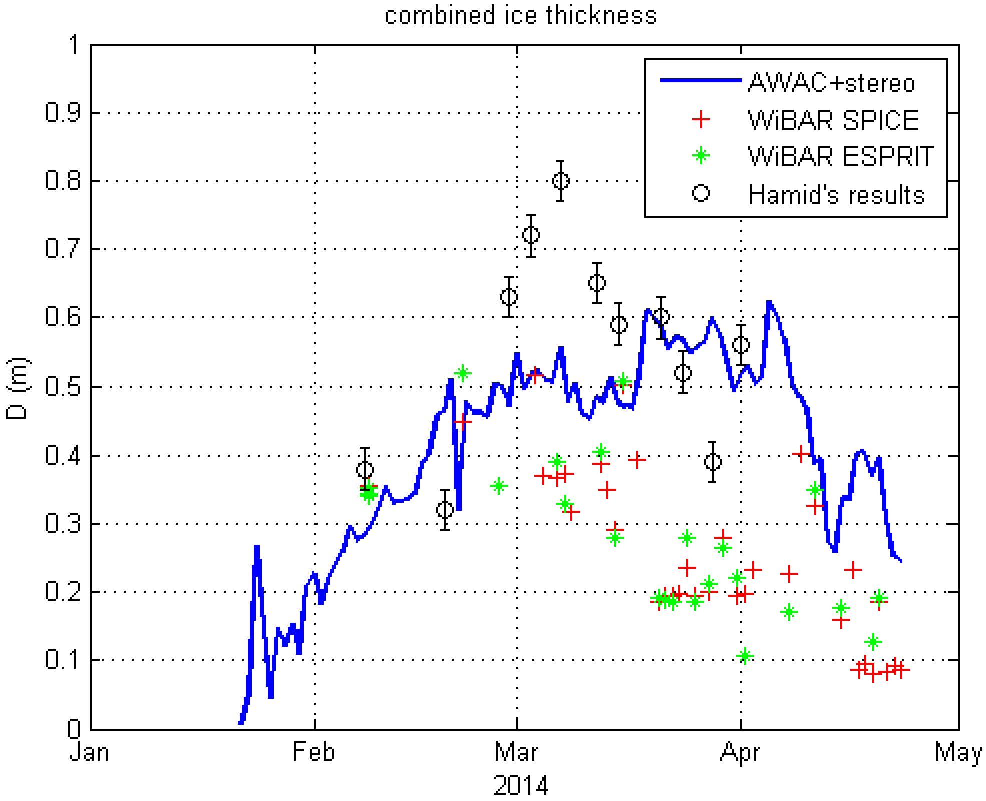

7 SCENE CAPTURE SYSTEM (D. LYZENGA)

The Scene Capture System (SCS) was initially intended to be a means of visually documenting the qualitative environmental conditions (primarily ice and snow cover) as an aid in interpreting the ice force and WiBAR ice thickness measurements. However, it soon evolved into a system for quantitative measurement of the ice surface elevation and ice motions as well. This section describes the instrumentation, analysis techniques, and results of these measurements. The surface elevation measurements are then used, along with independent measurements of the mean water level and estimates of the ice density, to estimate the ice thickness. Finally, the surface elevation measurements provided by this system are combined with AWAC data to provide more reliable and direct measurements of the ice thickness without the need for water level or ice density information.

7.1 INSTRUMENTATION

The SCS consisted of three Vivotek IP8372 Network cameras, two mounted on the east railing of the lighthouse and the third mounted on the northeast corner above the IFMS. The purpose of the two rail-mounted cameras was to image a region of the surface including the field of view of the WiBAR, and to make estimates of the ice surface elevation and motion. The purpose of the third camera was to image the IFMS itself and the immediately surrounding ice surface. Figure 7.1 shows a view of the lighthouse from the north, with the three cameras and other instrumentation on the left.

Figure 7.1. Photo showing general location of SCS instrumentation on the left (east) side of lighthouse.

The cameras are shown in more detail in Figures 7.2 and 7.3. Figure 7.2 is a view toward the north, showing the right stereo camera in the foreground, the WiBAR system in the center, and the downward-looking IFMS camera just visible below the WiBAR enclosure. The left stereo camera is behind the WiBAR in this view, and is shown in Figure 7.3.

Figure 7.2. Photo showing right stereo camera in foreground, WiBAR system (center), and IFMS camera below WiBAR.

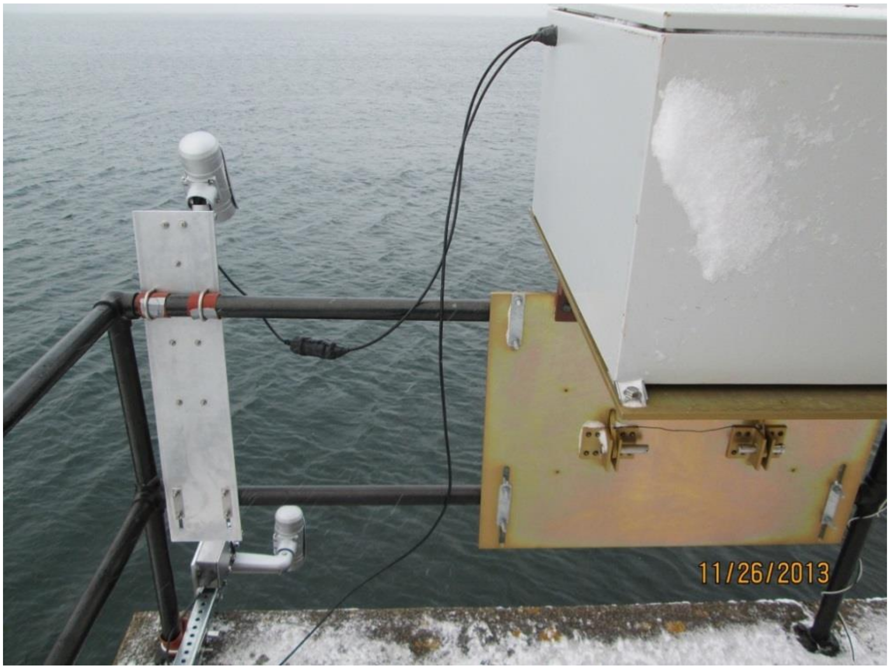

Figure 7.3. Photo showing left stereo camera (upper left) and IFMS camera (lower left).

The left and right stereo cameras were located approximately 18.5 feet above the water surface. They were separated horizontally by 127 inches and were oriented normally to the railing with a lookdown angle of approximately 60 degrees from the horizontal. The IFMS camera was mounted with its axis in the vertical direction. The cameras have zooming capability, but all were set so as to maximize the field of view, which is about ±26° in the vertical and ±34° in the horizontal direction.

The cameras were installed on 26 November 2013, and sent images via a cell phone modem on a regular twice-daily schedule through the end of the experiment. Some example images collected on 3 January 2014 are shown in Figures 7.4 and 7.5.

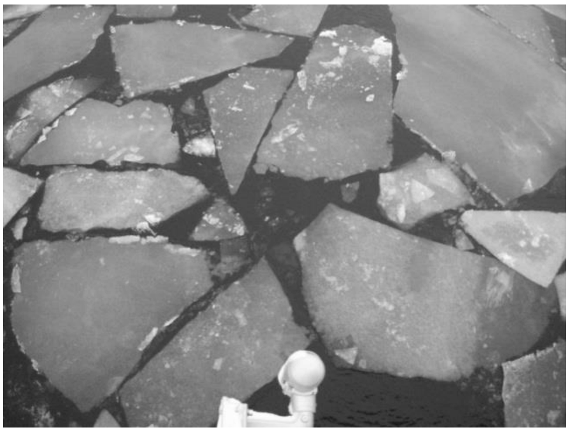

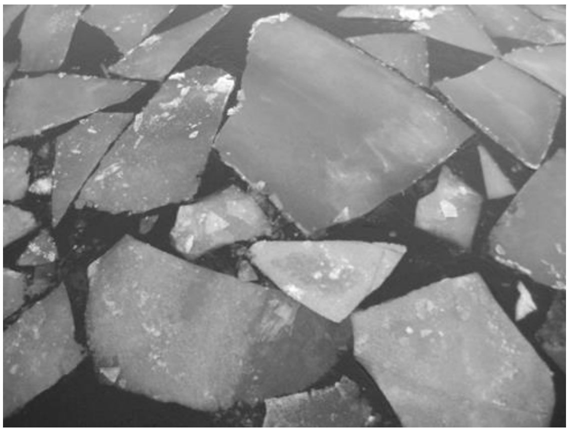

Figure 7.4. Images collected from left and right stereo cameras at 8:32 am on 3 January 2014.
Note IFMS camera is within the field of view of the left camera.

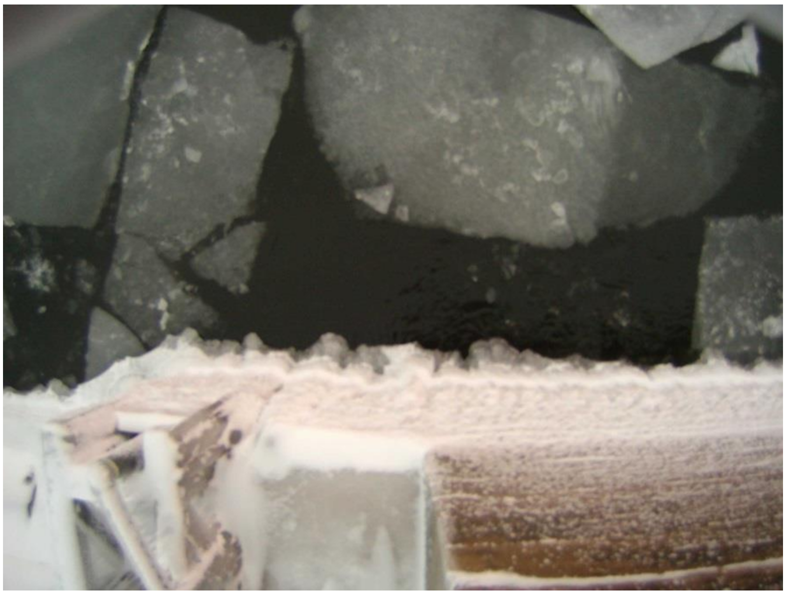

Figure 7.5. Image collected from IFMS camera at 8:34 am on 3 January 2014.

In order to facilitate stereo image processing and ice motion tracking, the cameras were geometrically calibrated using images collected prior to deployment. Actual locations of features in these images were compared with their image locations, as shown in Figure 7.6. A second-order fit to these data points was used to derive the relationship between the pixel location and viewing angle shown in Figure 7.7.

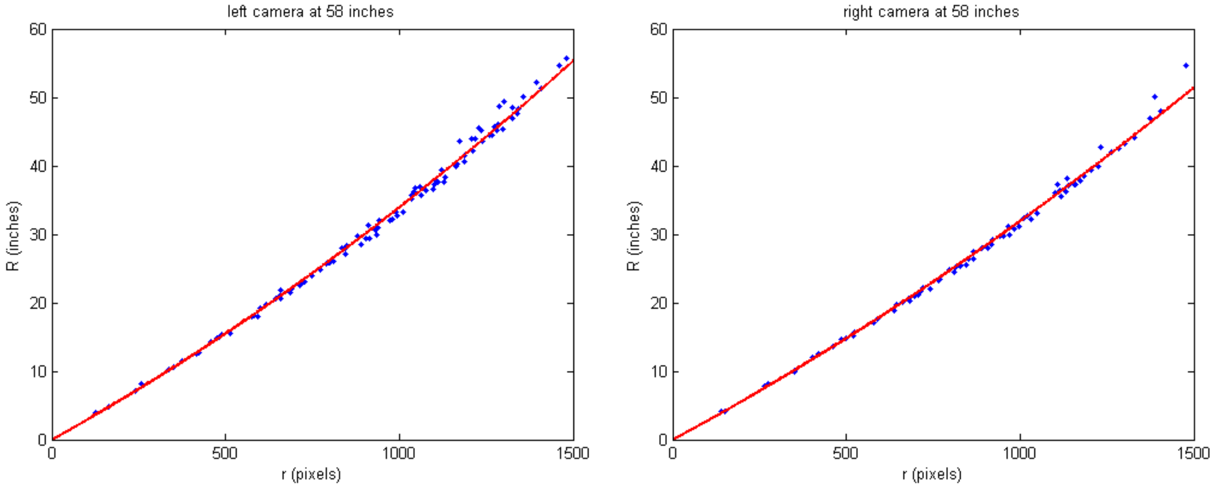

Figure 7.6. Geometric calibration data showing actual radial distances of image features compared with distances in images from left and right cameras.

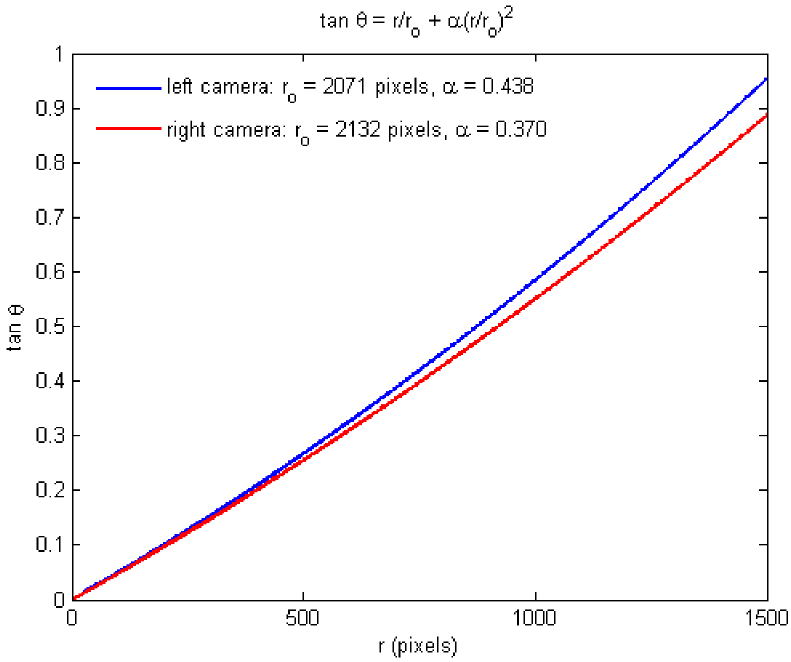

Figure 7.7. Geometric calibration curves showing relationship between pixel location and viewing angle for left and right cameras.

7.2 STEREO MEASUREMENTS

In concept, the stereo processing procedure involves identifying common features in both camera images, and computing the three-dimensional location of these features based on the angles at which the features appear in the images. These angles are defined by the direction vectors $\boldsymbol{n}_1$ and $\boldsymbol{n}_2$ pointing toward a given feature or location on the surface from camera 1 and camera 2, respectively. The line of sight or ray from the camera to the object is described by the equations $\boldsymbol{r} = \boldsymbol{r}_1 + \boldsymbol{n}_1 s_1$ for camera 1 and $\boldsymbol{r}' = \boldsymbol{r}_2 + \boldsymbol{n}_2 s_2$ for camera 2, where $\boldsymbol{r}_1$ and $\boldsymbol{r}_2$ are vectors describing the camera locations, and s_1 and s_2 are the distances along each line from the corresponding camera. Ideally, these lines would intersect at the object location, but due to various errors they may not actually intersect, so we define the object location as the point of closest approach of the two lines. The distance of closest approach can then be used as a measure of the error in the measurement. Details are provided in Appendix 7.1.

To implement this method, the camera positions and mounting angles were measured and the cameras were geometrically calibrated as described in the previous section. Although we attempted to mount both cameras with a 60 degree look-down angle from the horizontal, an analysis of the images indicated that the actual look-down angles were 62.5 degrees for the left camera (camera 1) and 58 degrees for the right camera (camera 2). In order to identify common features, both images were projected onto a horizontal plane, which removes the distortions in the images. A pair of such images is shown in Figure 7.8 below.

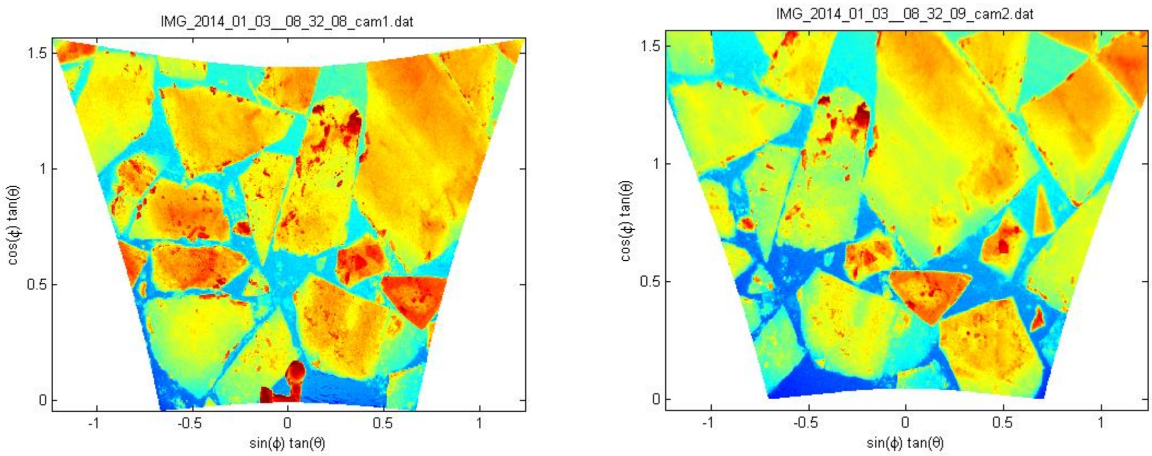

Figure 7.8. Images from left and right cameras projected onto a horizontal surface.

Next, the overlap region between the two images was determined. This region was subdivided into sub-regions with dimensions of 61x61-pixels each. The same set of sub-regions was used for processing each of the recorded image pairs. Each sub-region in the camera 1 image is correlated with the camera 2 image, and the location corresponding to the maximum correlation is recorded. The locations in both images are used to define the rays discussed above, and the (x,y,z) coordinates of the surface location corresponding to each sub-region are calculated as described above. These coordinates are recorded along with the minimum distance between the rays and the maximum correlation coefficient for each sub-region. The estimated point locations for one data set are shown in Figure 7.9.

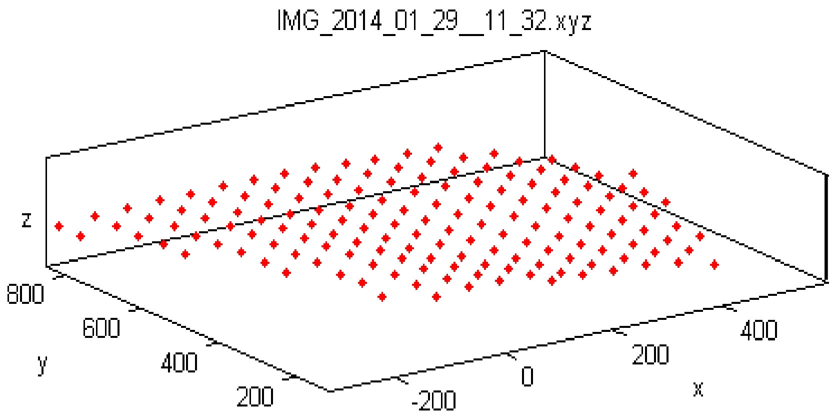

Figure 7.9. Display of extracted surface elevations for one example data set (29 January 2014).

Finally, the mean and standard deviation of the estimated surface elevations were calculated for each image pair using only those samples with error indices less than 10 cm and correlation coefficients greater than 0.8. These mean and standard deviation values are plotted versus time in Figure 7.10.

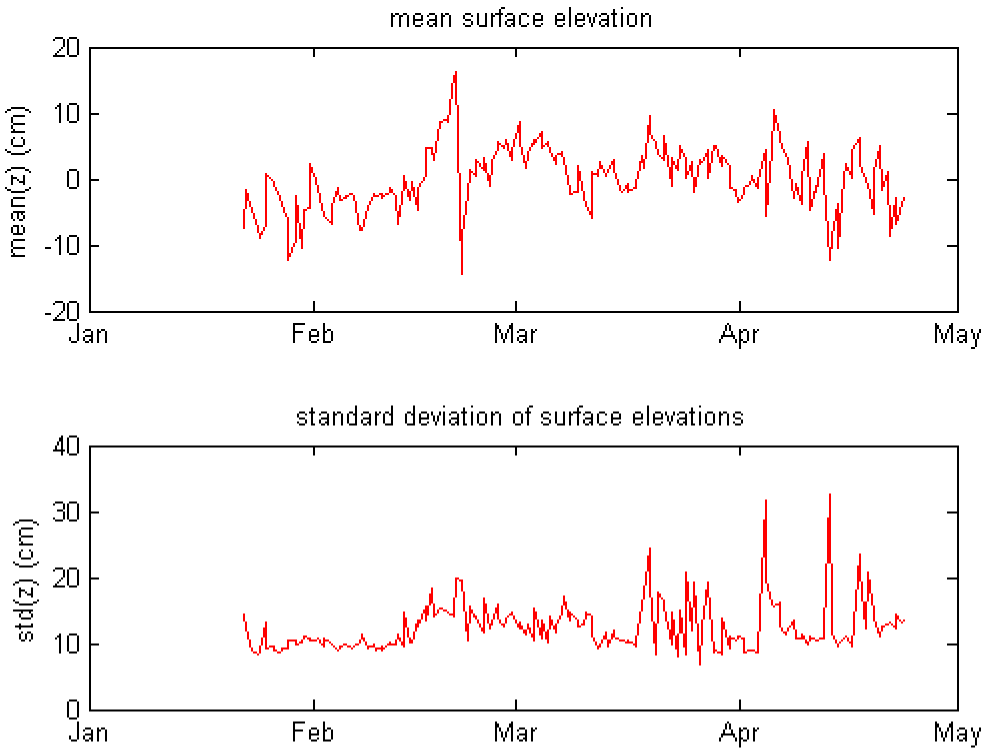

Figure 7.10. Mean and standard deviation of observed surface elevations.

7.3 ESTIMATION OF ICE THICKNESS FROM STEREO MEASUREMENTS

To interpret these results, we obtained mean water level measurements from the NOAA station in nearby Marquette, Michigan. These water level measurements were projected to the test site by harmonizing them with our surface elevation measurements during the first week, when the ice thickness was assumed to be small, and the results are shown in the upper panel of Figure 7.11. The difference between our mean surface elevation measurements and the mean water level for each day is shown in the lower panel.

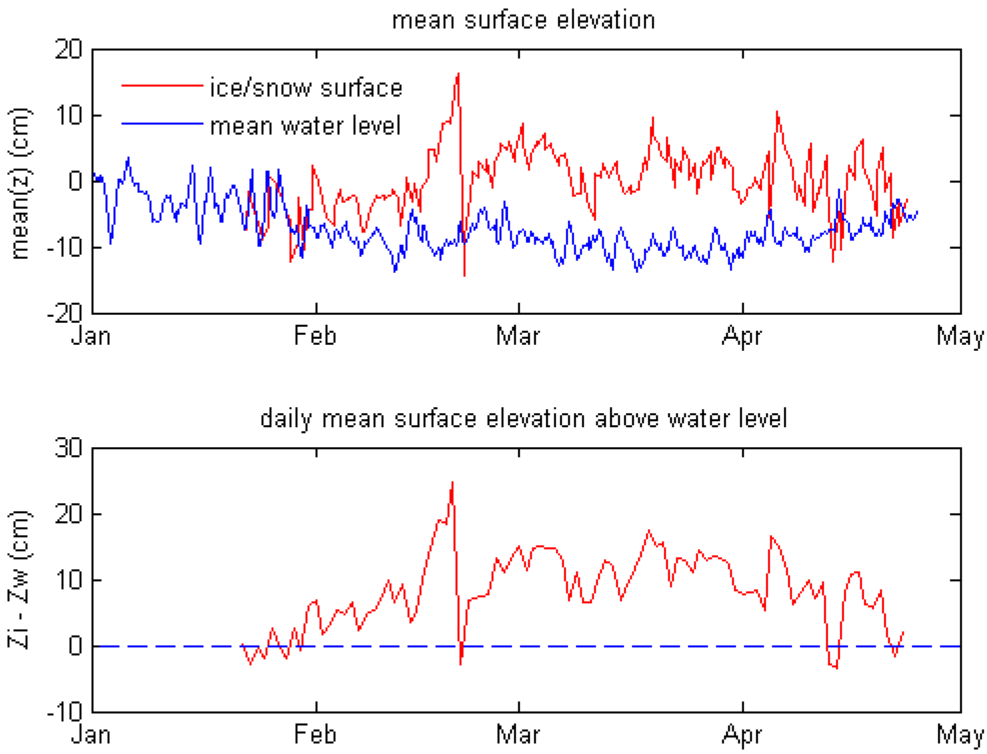

Figure 7.11: Comparison of mean ice surface elevations with mean water level data.

The surface elevation above the waterline is related to the thickness of the ice/snow cover. However, this relationship is determined by the average density of the ice/snow cover, which depends on the amount of snow cover and possibly on recent rainfall, and is thus highly uncertain. Specifically, the ice thickness is given by

$$D = \frac{h}{1 - \rho_i / \rho_w}$$

where

h is the surface height above the waterline

ρ_i is the density of the ice/snow layer

ρ_w is the density of water.

The average density of freshwater ice is generally assumed to be about 0.917 times the density of water. If we reduce this by 10 percent to partially account for the snow cover on the ice, the estimated thickness is 5.7 times the exposed elevation. The ice thickness calculated under this assumption is shown in Figure 7.12. This thickness estimate is highly uncertain because of uncertainties in the density of the ice/snow cover. Also, the inherent errors in the elevation measurements are multiplied by the same factor, and so become much larger when translated into thickness errors.

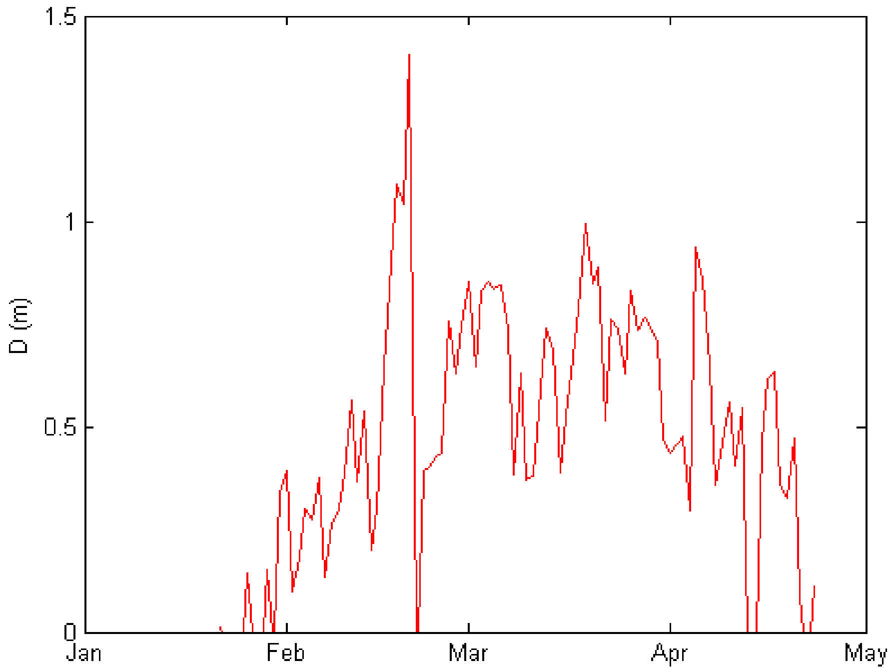

Figure 7.12: Estimated ice thickness assuming ρ_i / ρ_w = 0.825.

7.4 ICE THICKNESS FROM COMBINED STEREO AND AWAC DATA

A second and more reliable method of estimating the ice thickness is to combine the previously described stereo camera measurements of the upper ice surface elevation with measurements of the ice keel depth from the AWAC (Acoustic Wave and Current profiler) system (see chapter 8). The advantage of this method is that it is independent of the water level and the ice density, both of which are still somewhat uncertain. Figure 7.13 shows these absolute measurements, with the upper ice surface (z_u) between 5.5 and 6 m below the cameras, and the lower ice surface (z_l) between 5 and 5.5 m above the bottom-mounted AWAC sensor. The ice thickness can be calculated directly from these measurements, as $T = \Delta z + z_u - z_l$ where Δz =11.2 m is the vertical distance between the stereo cameras and the AWAC sensor. The ice thickness calculated in this way is shown in Figure 7.14.

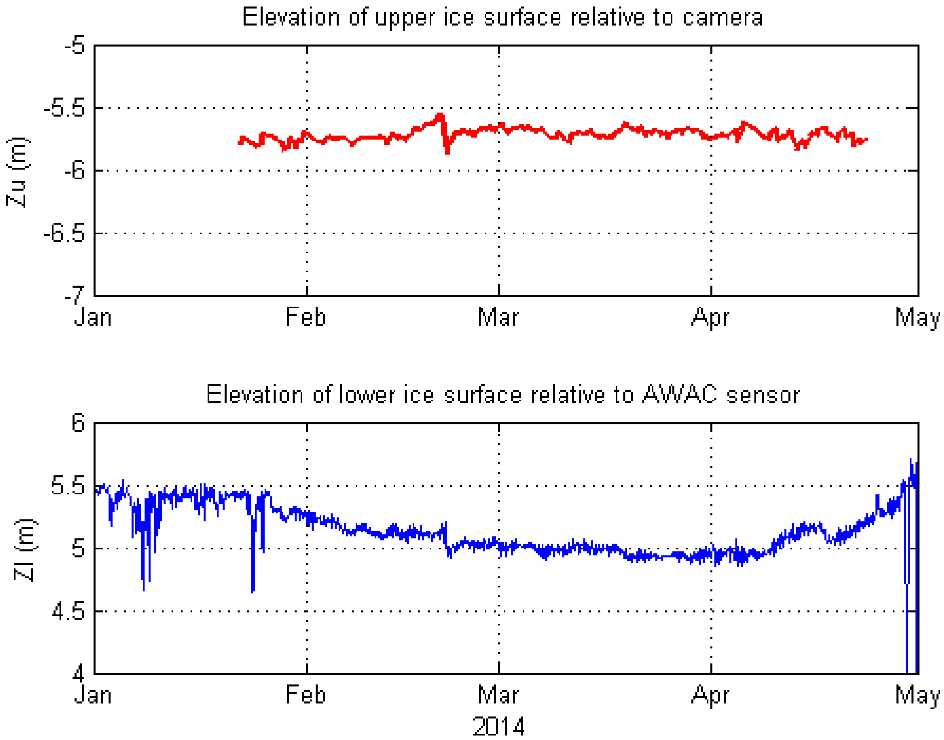

Figure 7.13. Measurements of the elevation of the upper surface (top panel) from the stereo camera system and the lower ice surface (bottom panel) from the AWAC system.

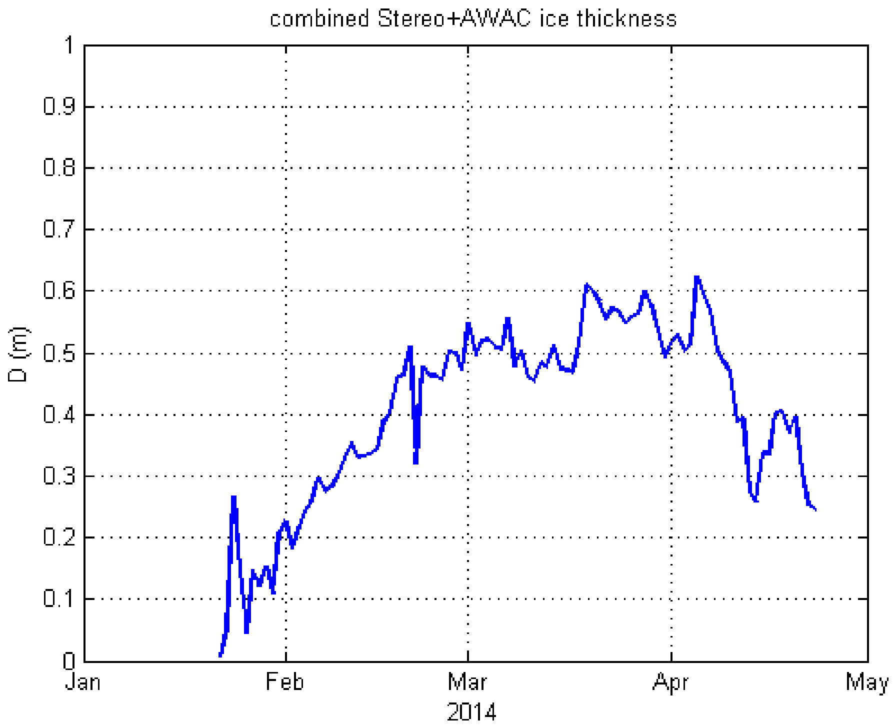

Figure 7.14. Estimates of ice thickness from the measurements shown in Figure 7.13.

An interesting feature in these plots is a small but sudden decrease in the elevation of the upper and lower ice surfaces on February 21, as observed in both the stereo and AWAC data. Because this change occurred on both the upper and lower surfaces, the ice thickness did not change very much during this event, but the entire surface dropped suddenly by approximately 20 cm. A possible explanation for this event is indicated in Figure 7.15, which shows the wind speed and direction for 20-27 February 2014 at NOAA station GTRM4 (about 20 miles from our test site). The wind speed was quite high and the wind direction reversed abruptly, coming from the east on February 20 and from the west after about noon on February 21. Thus, the winds may have piled up the ice at the test site and then dispersed it, leading to the changes in surface elevation shown in Figure 7.13.

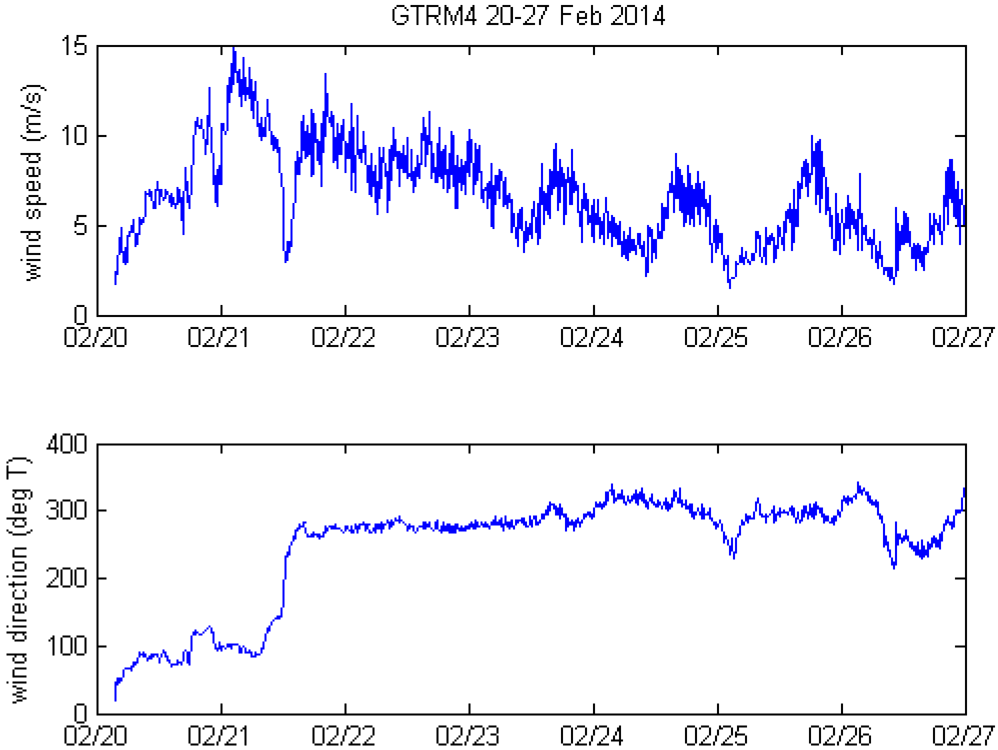

Figure 7.15. Wind speed and direction at NOAA weather station GTRM4, about 20 miles from test site. Note reversal in wind direction on February 21.

8 ACOUSTIC WAVE, ICE KEEL DEPTH, AND CURRENT PROFILER

The second of the two *in-situ* instruments is the Acoustic Wave and Current profiler (AWAC), shown in Figure 8.1. The AWAC system was purchased from Nortek, Inc. in partnership with the Michigan Technological University's Great Lakes Research Center (GLRC), with each institution providing 50% of the purchase cost. The system consisted of a 1 MHz four-beam acoustic sensor with a 4GB SD card data logger, RS-232 analog access, and a two Alkaline (540 Watt-hour) battery pack, and also included a pressure sensor to measure the depth of the sensor below the surface. The acoustic sensor is capable of Doppler current measurements but was operated in this case in a surface-tracking mode so as to measure the ice keel depth, using built-in acoustic surface tracking firmware. It was deployed by the GLRC technical team on 25 November 2013, with the transducer mounted in a vertical orientation at a depth of approximately 5.5 meters. The ADCP contained both an independent power source and an independent data storage system capable of operating over an entire winter season. This independence proved fortunate in that the data link between the ADCP and WISN was lost mid-season. The instrument was retrieved on 30 May 2014, after which the data was extracted from internal memory and processed.

Figure 8.1. (a) AWAC in custom tripod stand (b) MTU GLRC team deploying the AWAC to the east of the experimental site.

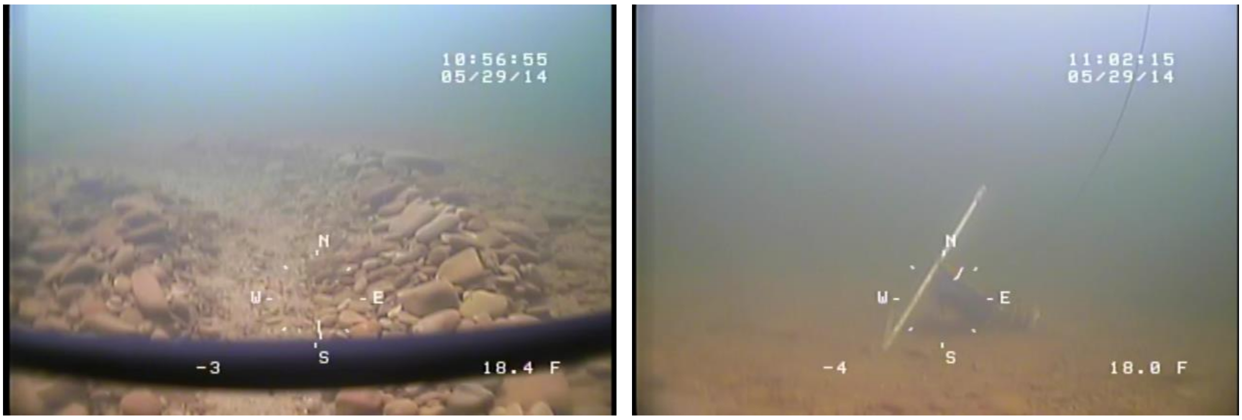

Figure 8.2. Images of AWAC taken during instrument recovery mission

8.1 DATA ANALYSIS

The AWAC data was initially processed by Chris Kontoes at Nortek, Inc. to provide time series data consisting of the distance from the transducer to the lower ice surface (from the acoustic measurement) and the barometric depth of the transducer (from the pressure sensor). The difference between these measurements is interpreted as the ice draft, or keel depth. These three quantities are plotted versus time in Figure 8.2. Note that the ice draft is not equivalent to the ice thickness, because some portion of the ice extends above the mean water level. The elevation of the upper surface was measured with the stereo camera system as described in section 7, and the ice thickness obtained by combining these measurements is shown in Figure 7.14. MatLab code is included in Appendix 8.

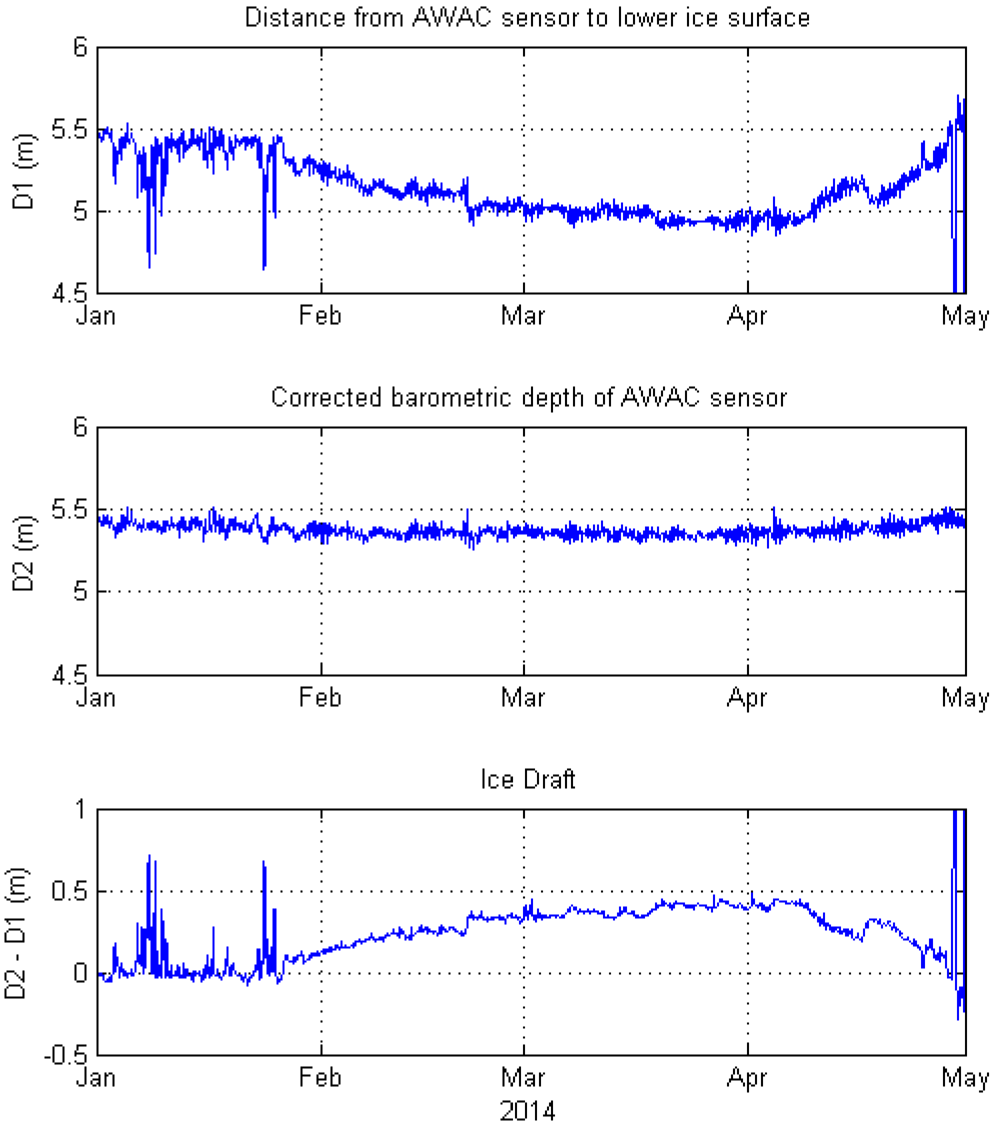

Figure 8.2. AWAC measurements during first four months of 2014.

9 INSTRUMENT SUPPORT SYSTEM (L. VAN NIEUWSTADT)

Providing the data acquisition control and handling, remote access to the on-board computer, and the needed power management and supply to the sensor network were the functions of the Instrument Support System (ISS). The ISS is comprised of:

(1) solar power generating and storage unit;
(2) data acquisition and system control;
(3) cellular data link hardware including a router and external antenna;
(4) DC power conditioning circuitry;
(5) scene monitoring camera (ScoutGuard);
(6) temperature sensors;
(7) IFMS health monitoring camera.

The top-level systems requirements for the ISS as determined by the selected sensors and the data collections operations are: (1) automatic data collection, (2) remote system access, (3) independent power generation and storage, and (4) system operating temperature of -25°C to +40°C. The block diagram of the system is shown in Figure 9.1. To note on this block diagram, the ISS serves solely as a DC power interface to the IFMS (ice force measuring system) data logger unit. For the WiBAR (wideband autocorrelation radiometer) and SCS (scene capture system), the ISS provides power management as well as command and data control. The command and data control functions were done by a microcomputer, a BBW (Beagle Bone White). A Python script was written and uploaded to the BBW. Remote upload of updated Python scripts was built into the operation of the ISS. The ISS had two cellular links: one internal to the scene monitoring ScoutGuard camera, and one in direct connection to the BBW. In total, the WISN instrument suites had three independent cellular connections – all three cellular links are denoted by the 'antenna' symbols in Figure 9.1.

For data collection, the ISS is programmed to automatically initiate and capture data from: solar powered battery voltage, SCS, temperature sensors, IFMS health monitoring camera, and WiBAR. Data collection happened twice daily, with the exact time-of-day adjusted as necessary. The scene-monitoring camera (ScoutGuard camera) operated independently, using its own disposable AA batteries and internal programmed settings. Among the factors dictating the actual time-of-day for the data collection were ambient temperature, percentage of cloud cover, and lake-ice/wave/wind conditions. For example, on predicted sunny and warm days, the WiBAR data collection time would be shifted to pre-dawn hours to avoid data collection when liquid water may form on top of the lake ice layer. Similarly for the IFMS, when a winter storm was predicted and high impact lake ice actions on the IFMS were expected, the IFMS data collection frequency would be increased during the predicted time period.

Figure 9.2 shows the system temperature log during the data collection period. As we can observe, there was an occasion when the ambient temperature did approach -25°C, the minimum temperature at which we had designed the WISN instrument to operate.

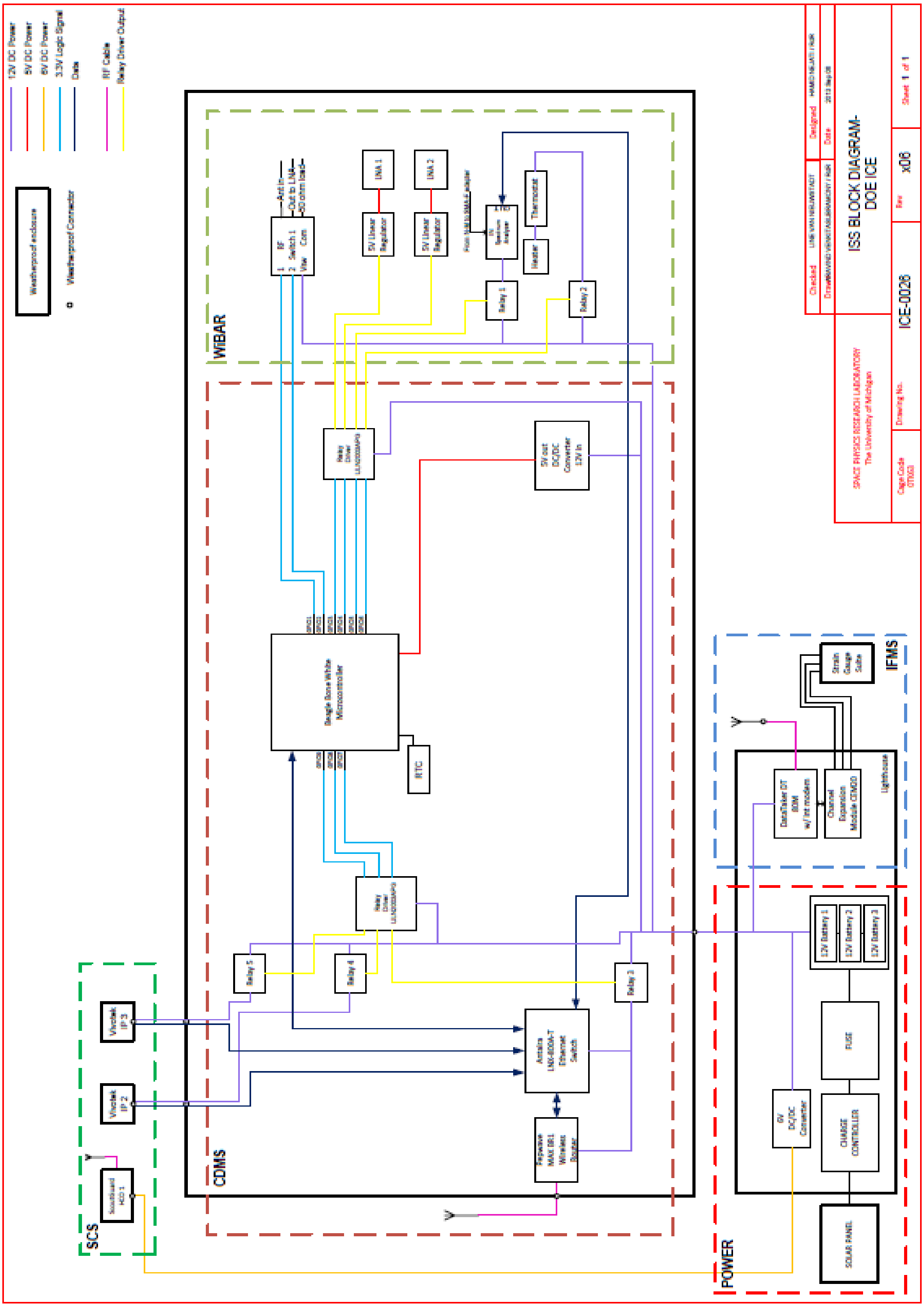

Figure 9.1 Instrument Support System block diagram

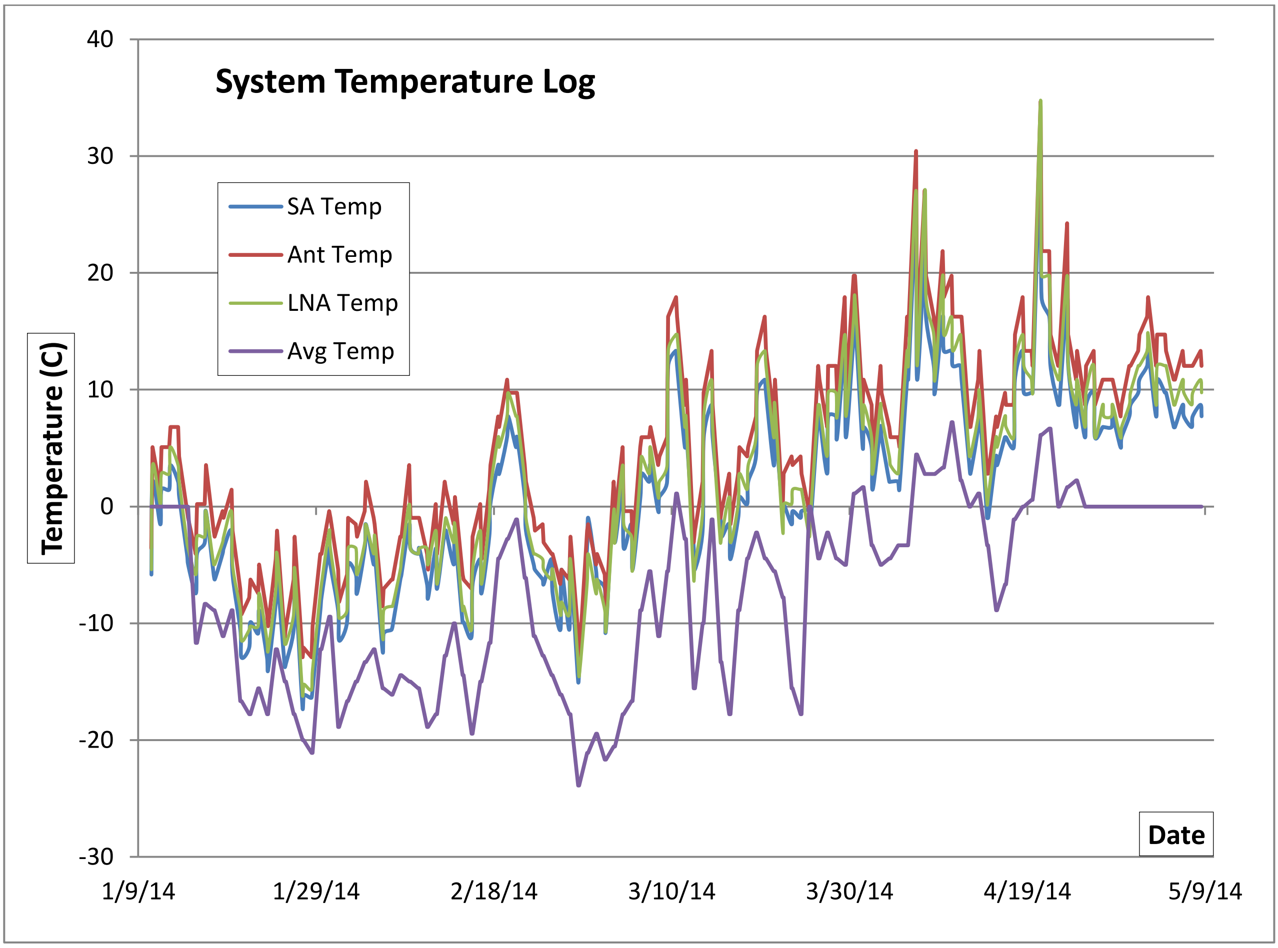

Figure 9.2 Instrument Support System temperature log during winter 2014

Each of the ISS components is detailed in the following sections.

9.1 SOLAR POWER GENERATING AND STORAGE SYSTEM

The solar power was designed to provide DC power to the sensor suite (except the ScoutGuard scene monitoring camera which had its own DC batteries) with a margin of seven cloudy days. We built in a 100% margin for the total instantaneous power draw and developed a DC power-operating budget. The seven-cloudy-days margin decision was driven by physical system size of the solar panels and storage batteries as well as budget and delivery constraints. Photographs of the solar power system are shown in Figure 9.3. The system was purchased from Patriot Solar.

Figure 9.3 [Left] Solar panel and battery box [Middle] Batteries and solar power condition circuitry in battery box [Right] Solar panel mounted on the south side of the lighthouse.

During data collection phase in winter 2014, storage battery voltage was monitored daily. Two example charts are included here (a complete set of battery voltage charts are available upon request). To note, the designed output voltage of the solar powered battery is 12 Volts, the minimum voltage required to power the WISN instruments. The first chart illustrates a cloud-covered week, while the second chart shows a sunny week. The vertical axes show the battery voltage, the horizontal axes show the day-of-the-week. On these charts, we can observe the daily 'charging' of the batteries when battery voltage measured greater than 14.5 Volts. During the cloudy week, as the battery voltage rarely went above the 13 Volts reading, the steady state battery voltage would decrease to below the required 12 Volts, see Figure 9.4. In contrast, on sunny days, we would observe the solar panel voltage reaching near 15 Volts, Figure 9.5.

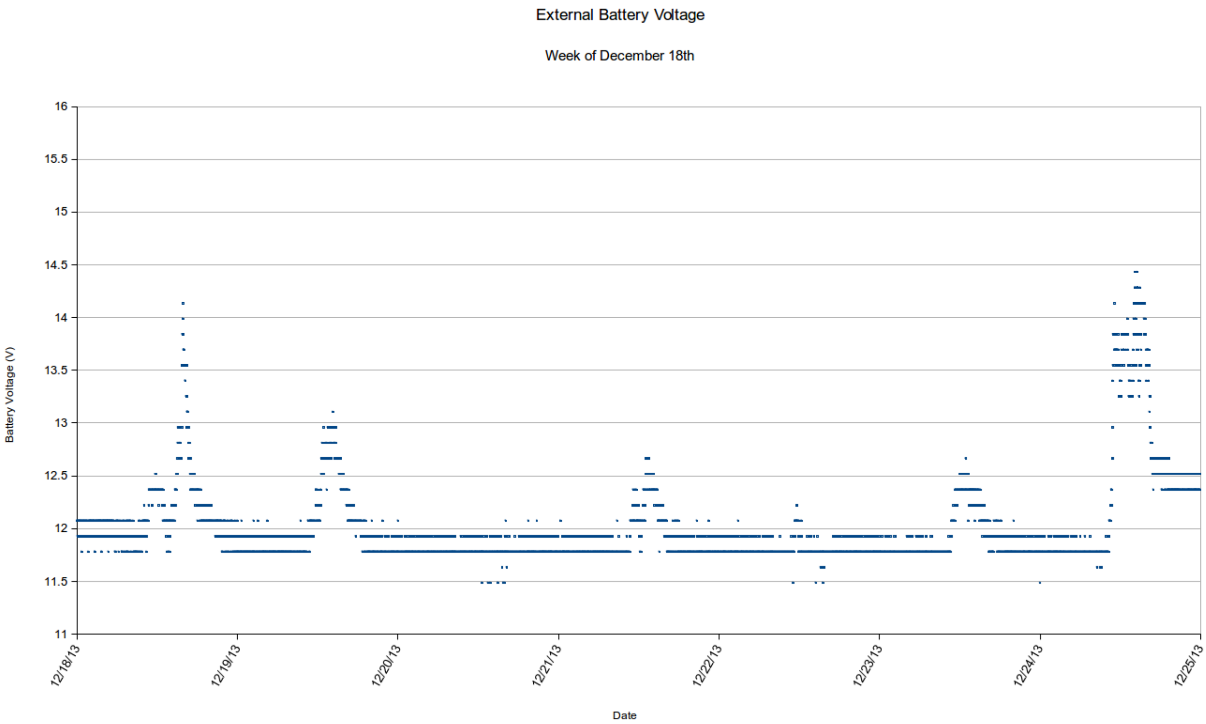

Figure 9.4 Solar powered battery voltage during a cloud-covered week.

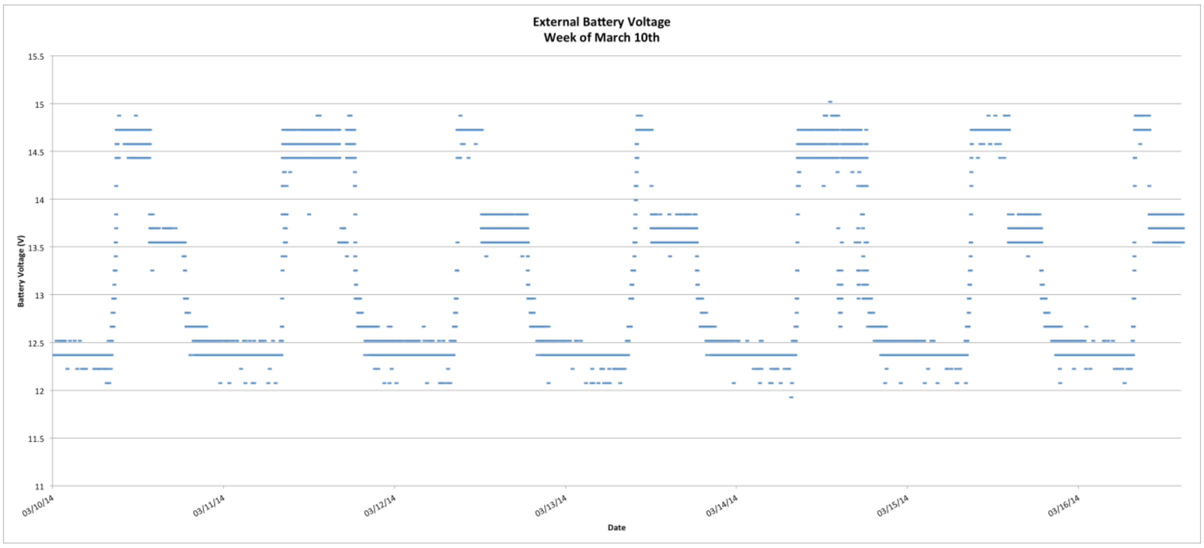

Figure 9.5 Solar powered battery voltage during a sunny week.

The power consumption management was developed in the form of a timing diagram, an operating current load chart, to prevent current draw overload.

9.2 COMMAND AND DATA HANDLING SYSTEM

Central to the data acquisition system is the Beagle Bone White (BBW) microcomputer which controlled, managed, and communicated the sensors' data via wireless router and cellular links. In our decision matrix to select the optimum configuration for the command and data handling, the main design drivers were: DC power consumption versus computing capability. In our assessment, microcontrollers would not provide the adequate data control and handling capability.

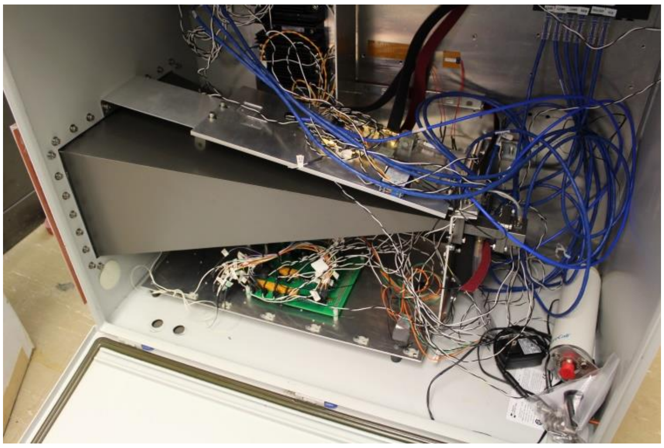

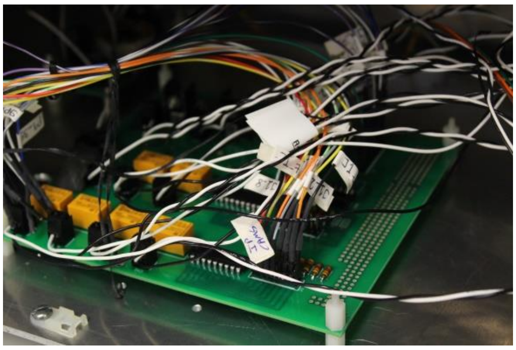

9.3 IFMS DATA LOGGER

To capture the pressure data from the Ice Force Measuring System, we procured the DT85 data logger with built-in cellular modem (http://datataker.com/DT85M.php) and its expansion module CEM20 (http://datataker.com/CEM20.php). A photograph of the two units inside the US Coast Guard storage container is shown in Figure 9.6: connections to the IFMS strain gauges are done via military-grade connectors and cabling. The combine cost of these two modules (totaling about $5,600) was well worth the investment, considering their successful field performance. These modules were built to operate in the -40ºC to +70ºC, 85% humidity ambient conditions, and they survived partial submersion during winter storm flooding onto the lighthouse floor.

Figure 9.6 IFMS DT85M data logger with built-in cellular modem and CEM20 extension module; shown during installation and test, resting on the South Light's floor.

9.4 SCENE MONITORING CAMERA

As a redundant system health monitoring unit, we acquired and installed a ScoutGuard camera. For the approximate purchase cost of $300, the ScoutGuard camera provided a visual health monitoring capacity. Expecting harsh winter conditions, we wanted to be able to see possible physical damage to the instruments. Possible damage due to vandalism was another practical consideration. Equipped with its own cellular data subscription, the camera sent us images via text messages to an email account which we monitored at www.mail.umich.edu, aoss-doeice, DoeIce123.

Figure 9.7 ScoutGuard camera mounted on the north east corner of the lighthouse, with the WiBAR and IFMS instruments in its field-of-view.

The ScoutGuard also stored these images in an internal storage disc in their original higher resolution versions compared to the compressed text images. The camera is motion-activated and has infrared image capture capability, as well as a temperature sensor. Figure 9.7 shows the mounting location of the ScoutGuard camera.

Some sample images are included (note the ambient temperature reading and time stamps):

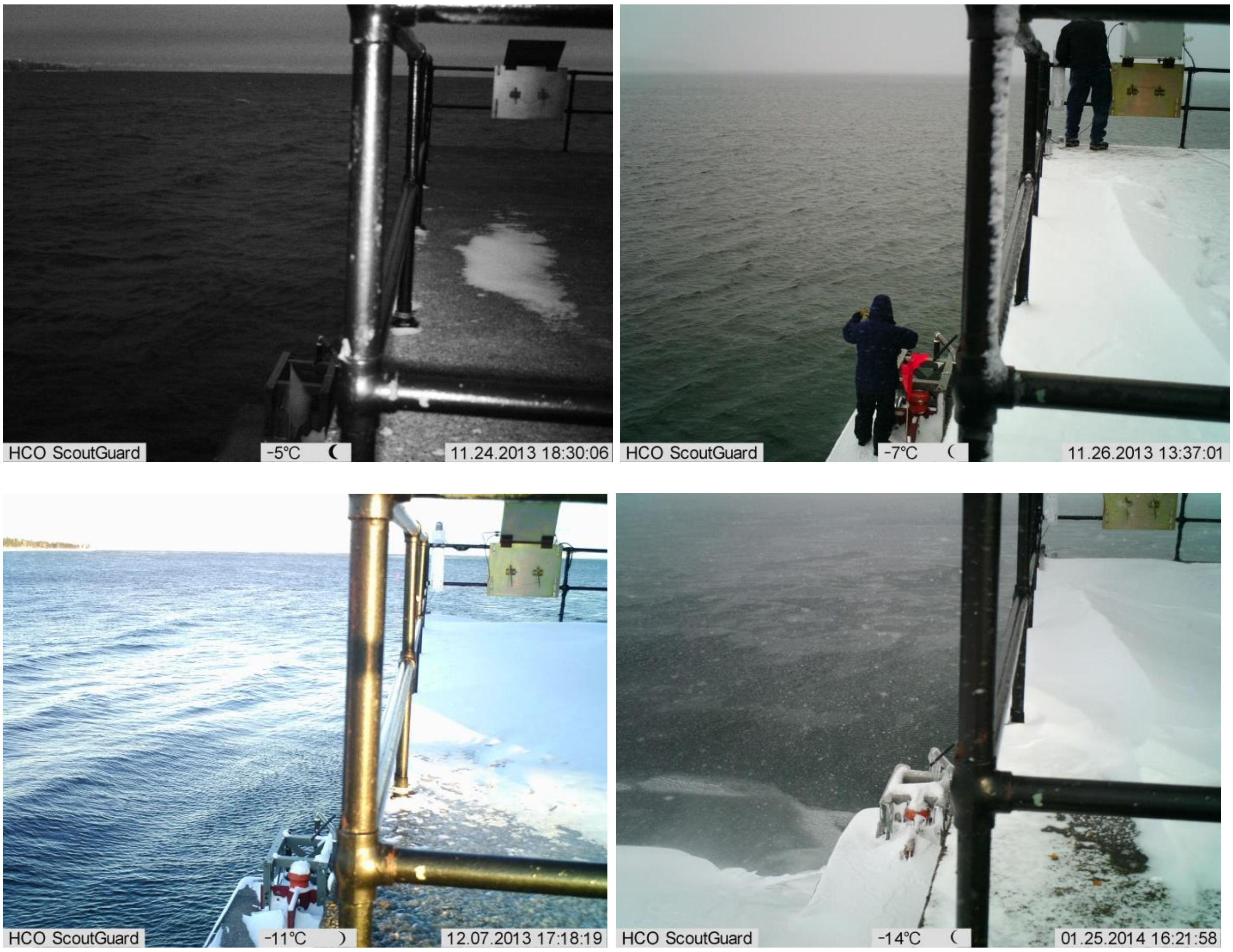


HCO ScoutGuard
-16°C
01.27.2014 02:14:49
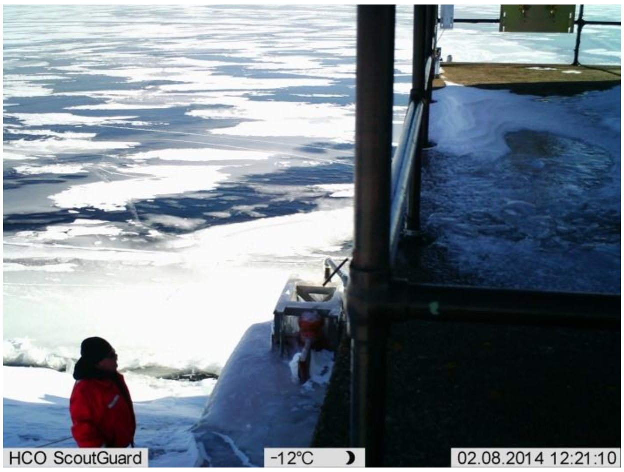
HCO ScoutGuard
-12°C
02.08.2014 12:21:10

HCO ScoutGuard
-16°C
03.05.2014 10:03:07
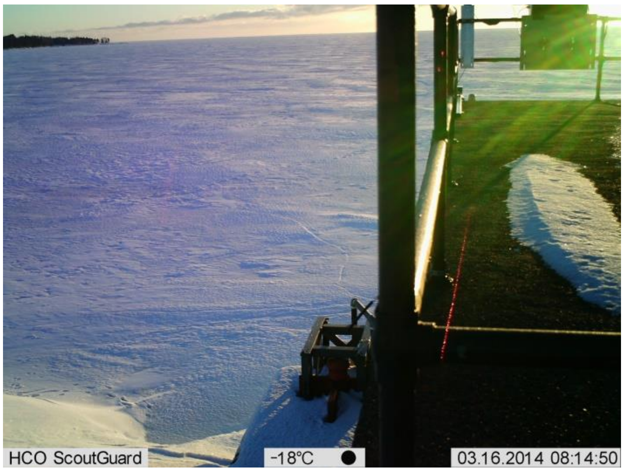
HCO ScoutGuard
-18°C
03.16.2014 08:14:50

HCO ScoutGuard
-4°C
04.14.2014 10:54:18

HCO ScoutGuard
7°C
04.20.2014 16:05:03

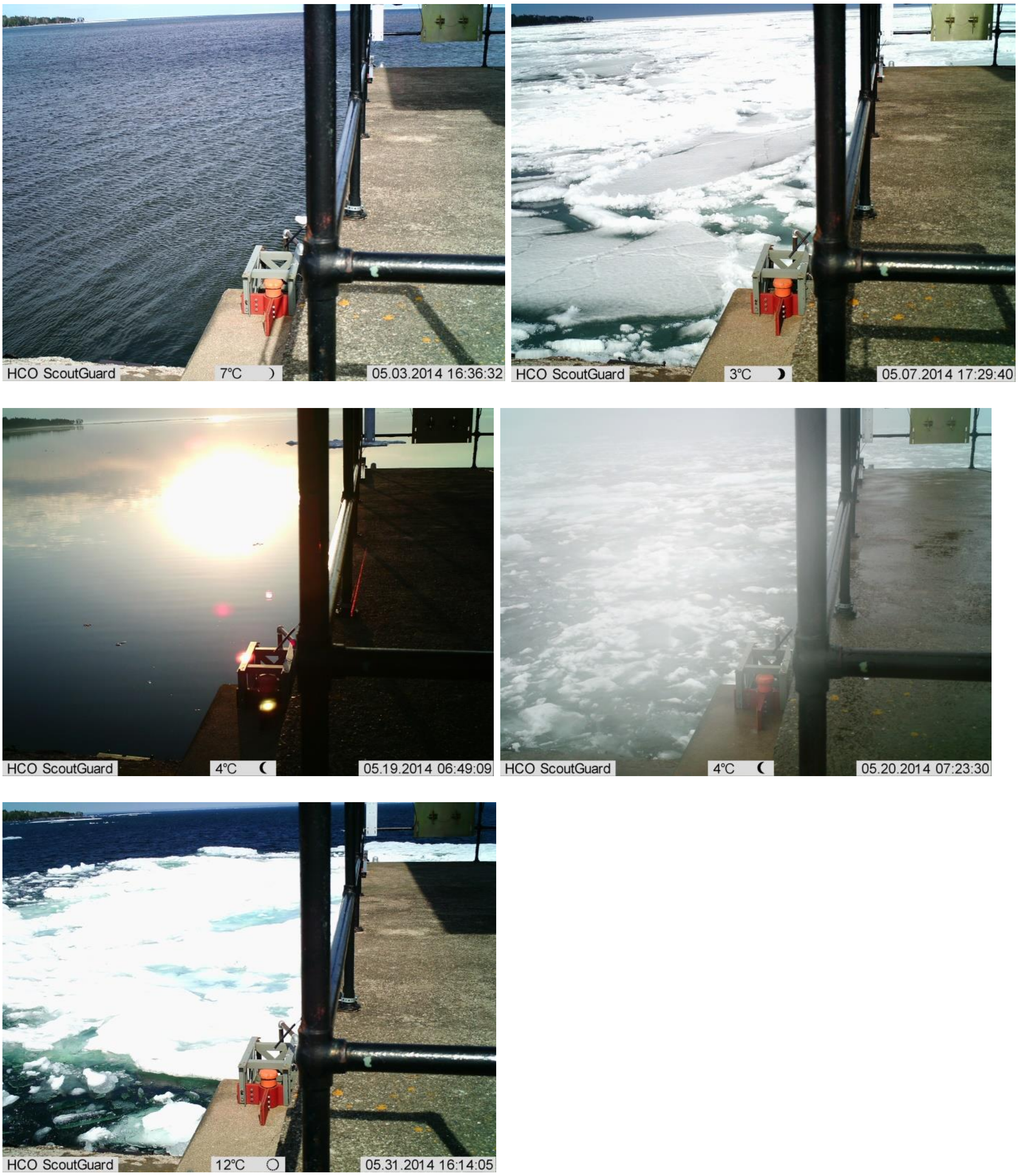

Figure 9.7 Sample images from the ScoutGuard scene-monitoring camera

These images and temperature readings were particularly useful in providing ambient conditions.

10 HISTORICAL WIND/WAVE AND CLIMATOLOGICAL STUDY

As this project collected data over a single winter season at one specific observation site, it was among the project's tasks to compare the experiment winter 2014 season with historical data. Of interest was historical wind, wave, and ice thickness in the Great Lakes regions. We were able to gather measured ice thickness data from the National Snow & Ice Data Center: http://nsidc.org/data/G00803. However, the wind and wave information are hindcast models, based on the Wave Information Studies initiative: http://wis.usace.army.mil/. We have gathered data from the National Data Buoy Center: http://www.ndbc.noaa.gov/, with limited availability of winter data.

In this section we include:

- Hindcast wind speed averages from 1979 to 2010 – with a single location measured data versus hindcast model comparison
- Hindcast wave height averages from 1979 to 2010
- Measured ice thickness data

10.1 HISTORICAL WIND STUDY

With data from the Wave Information Studies (http://wis.usace.army.mil/), average wind speeds are presented in this chapter. Figure 10.1 shows the average seasonal wind speeds, averages over the period of 1979 to 2010. We observed that wind speeds are higher in the winter months; with relatively small variation among the lakes. Lake Superior, the site of our experiment, shows the lowest wind speeds compared to the other Great Lakes.

Our next step was to look at one validation point for the WIS hindcast data. We compared the measured wind speeds at one buoy location, which has availability winter data. In Figure 10.2 (a), we marked the comparison locations with two 'green' circles: WIS data point 95500 and the closest available buoy data at Stannard Rock (about twenty miles away). The charts in Figure 10.2 (b) show that the WIS hindcast does track well to the measured data, however the measured data show consistently higher wind speeds.

In Figures 10.3 (a) – (e), the average wind speeds are graphically displayed using ArcGIS. With the aid of the color bars, regions of high/low wind speeds are highlighted. It should be noted that the color bar scale for Lake Ontario is smaller compared to scales used for the other lakes; surface wind speed ranges from 5.5 to 7 m/s rather than from 4 – 7 m/s. MATLAB scripts for data processing are included in Appendices 10.1 and 10.2.

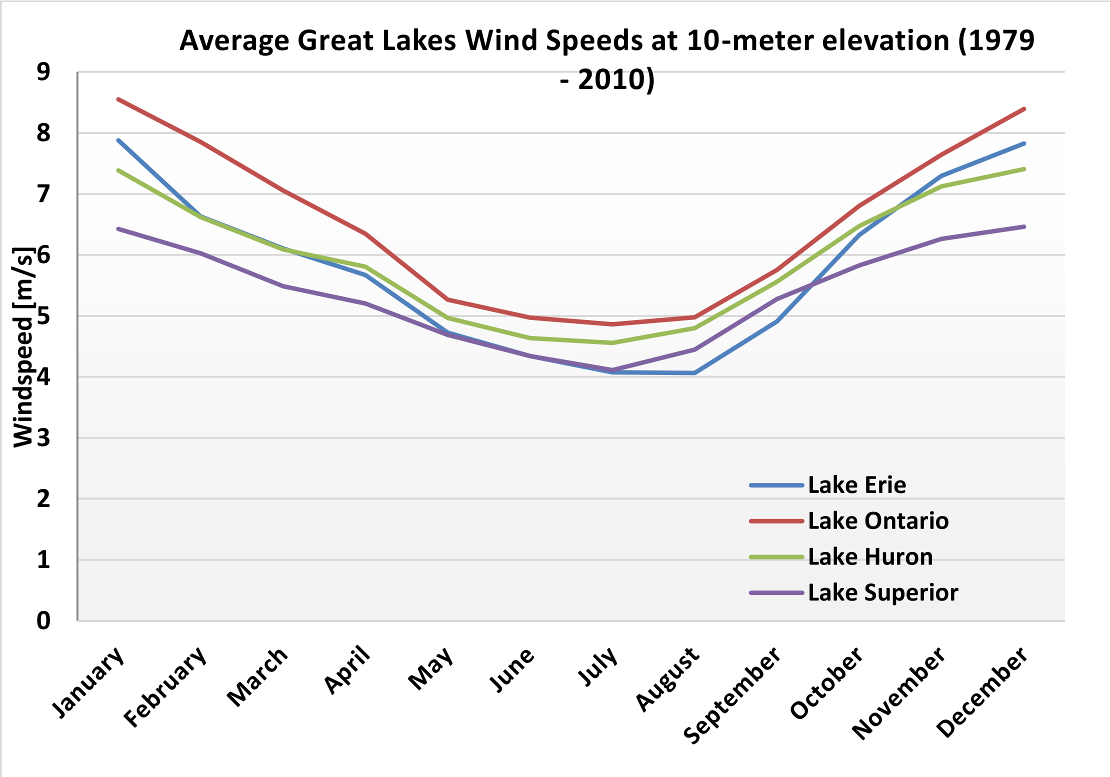

Figure 10.1 WIS hindcast average wind speed from 1979 - 2010

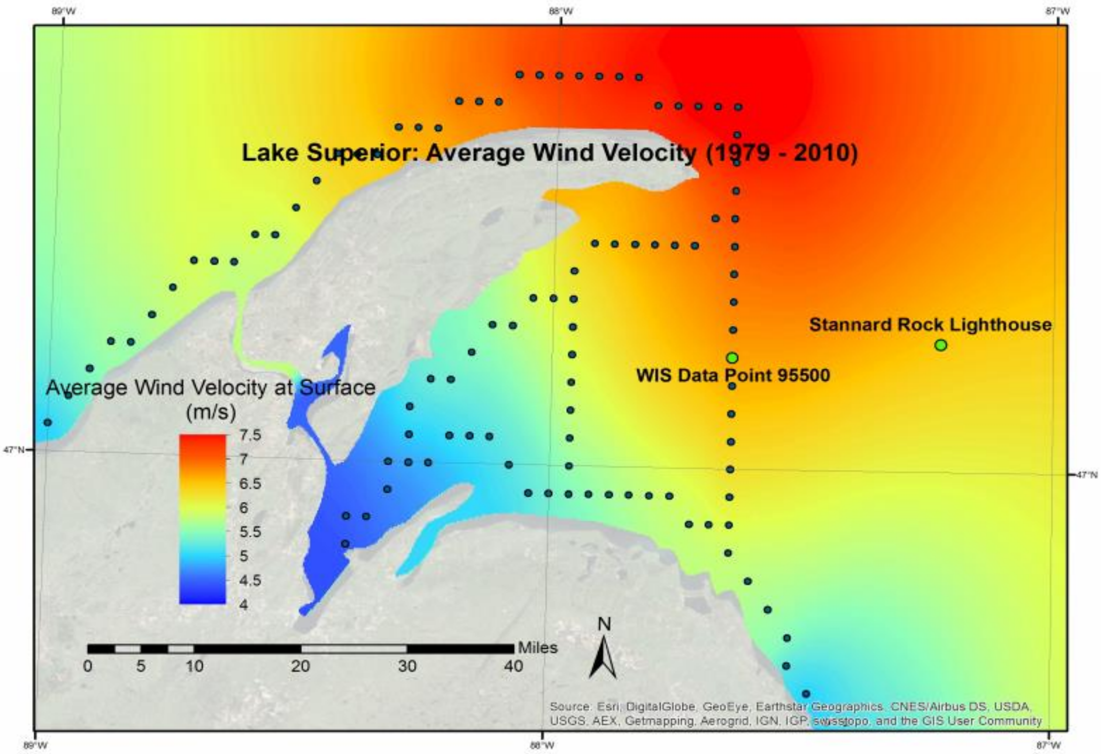

(a)

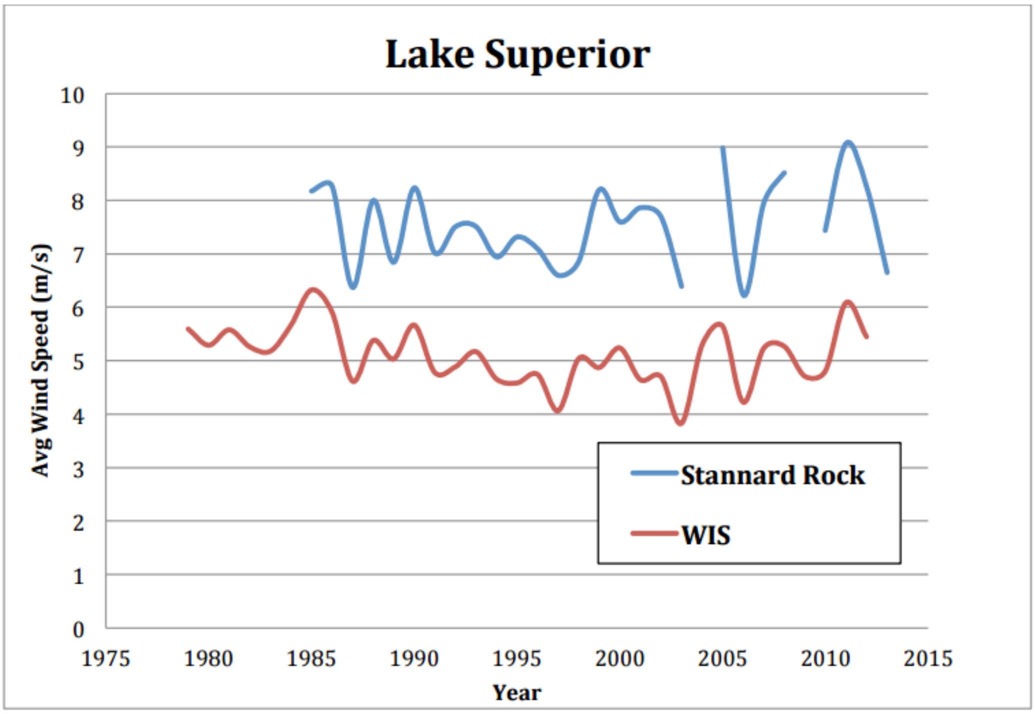

(b)

Figure 10.2 Comparing WIS data with NDBC (National Data Buoy Center) near the experiment site: (a) locations of WIS data point 95500 and Stannard Rock (b) average wind speed comparison between hindcast [red] and measured [blue].

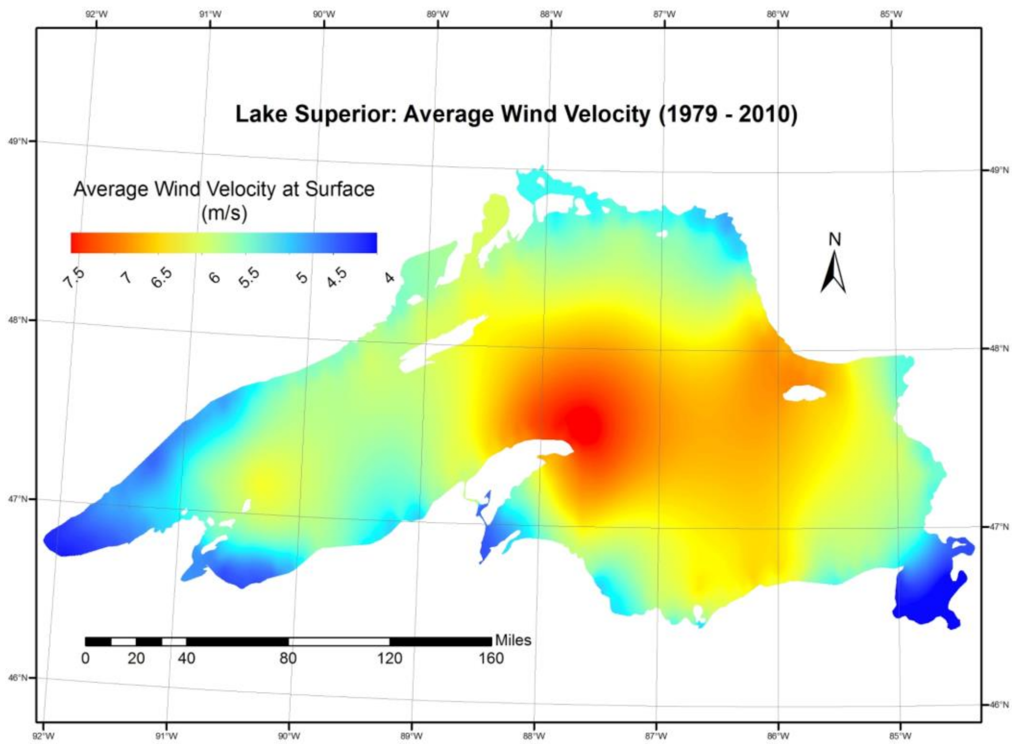

(a)

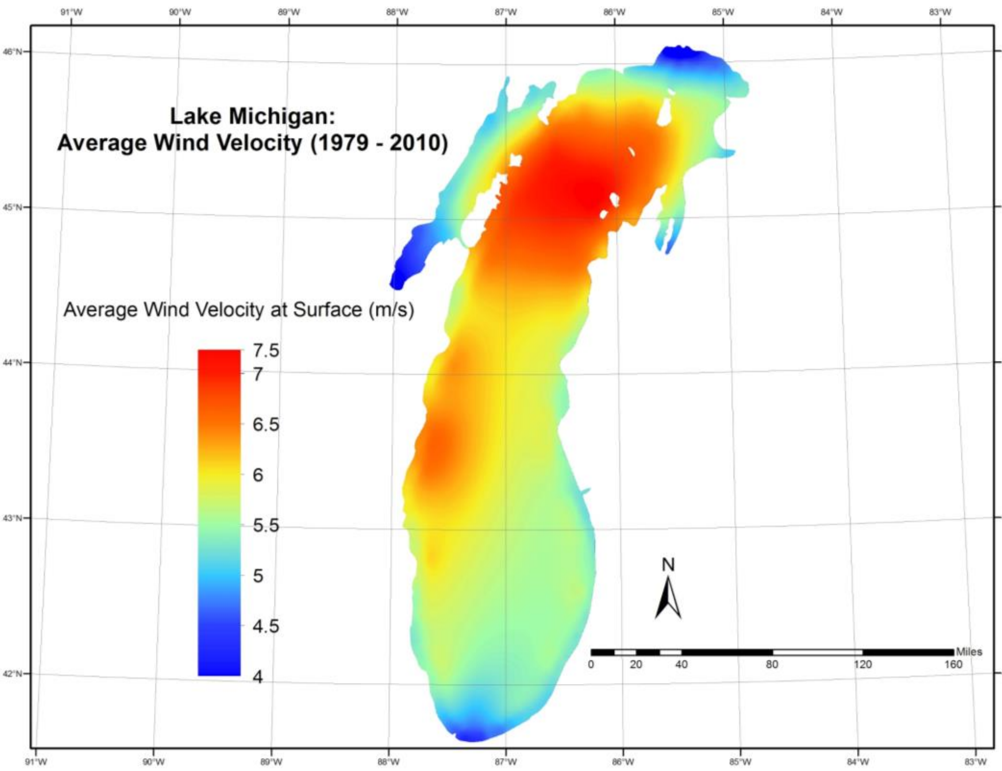
Lake Michigan:
Average Wind Velocity (1979 - 2010)
Average Wind Velocity at Surface (m/s)
7.5
7
6.5
6
5.5
5
4.5
4
N
0
20
40
80
120
160
Miles

(b)

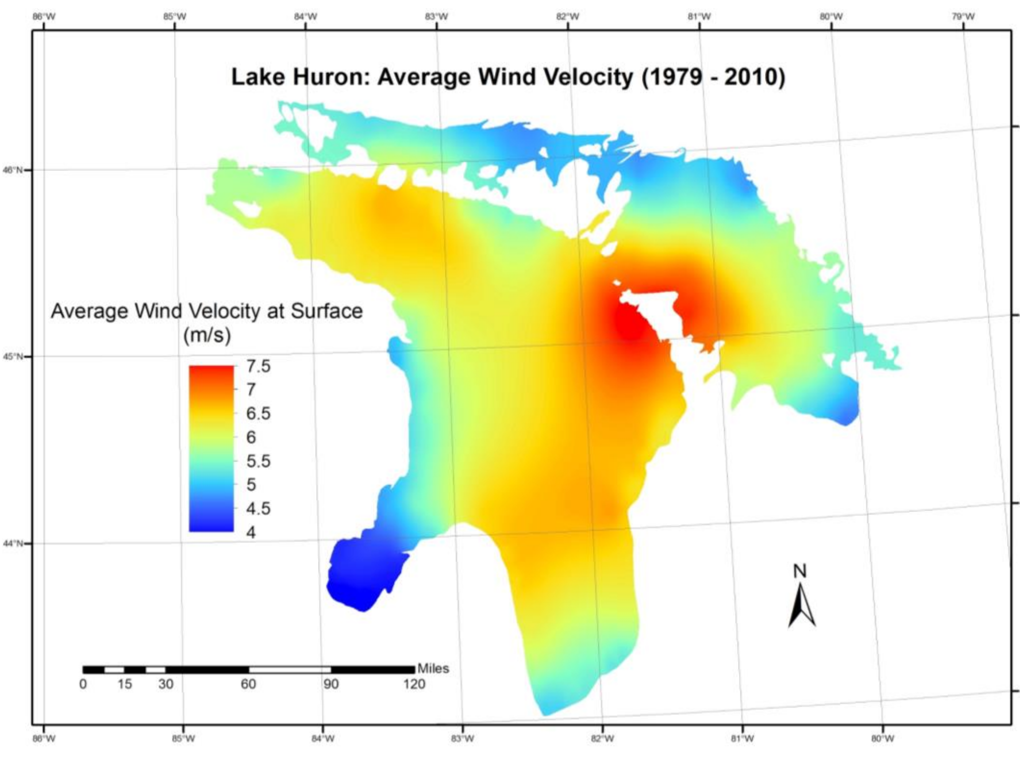
Lake Huron: Average Wind Velocity (1979 - 2010)
Average Wind Velocity at Surface
(m/s)
7.5
7
6.5
6
5.5
5
4.5
4
N
0
15
30
60
90
120
Miles

(c)

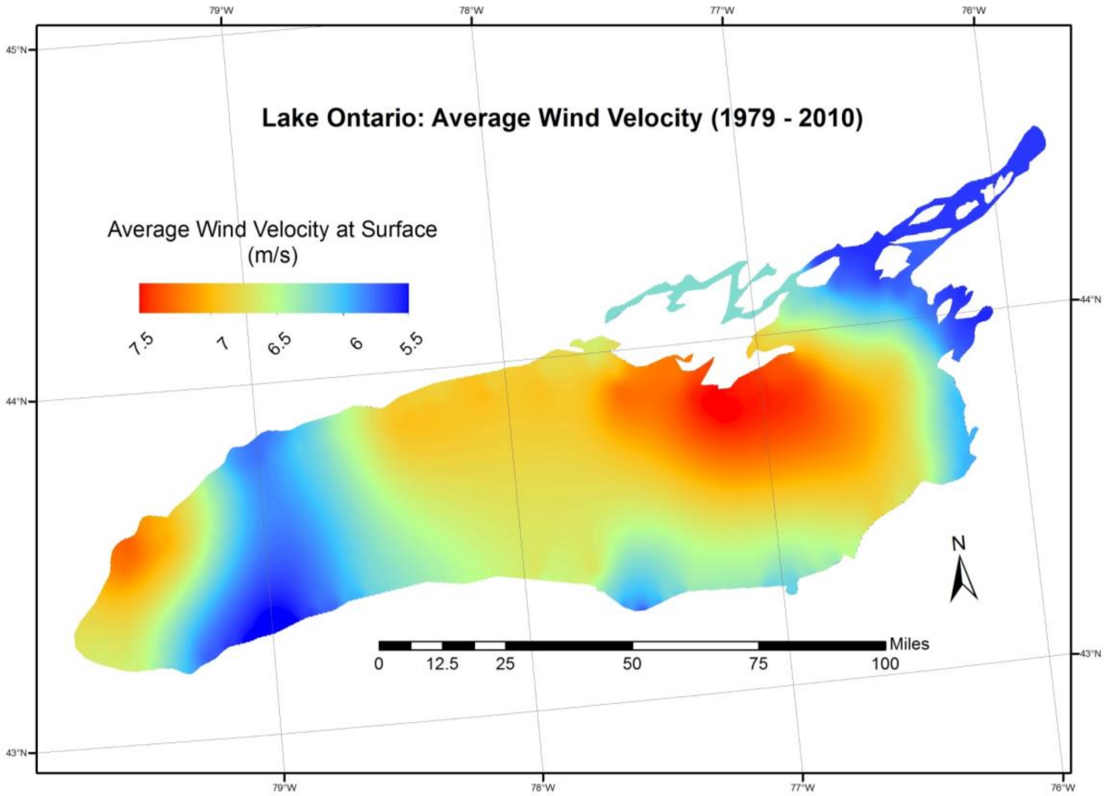

(d)

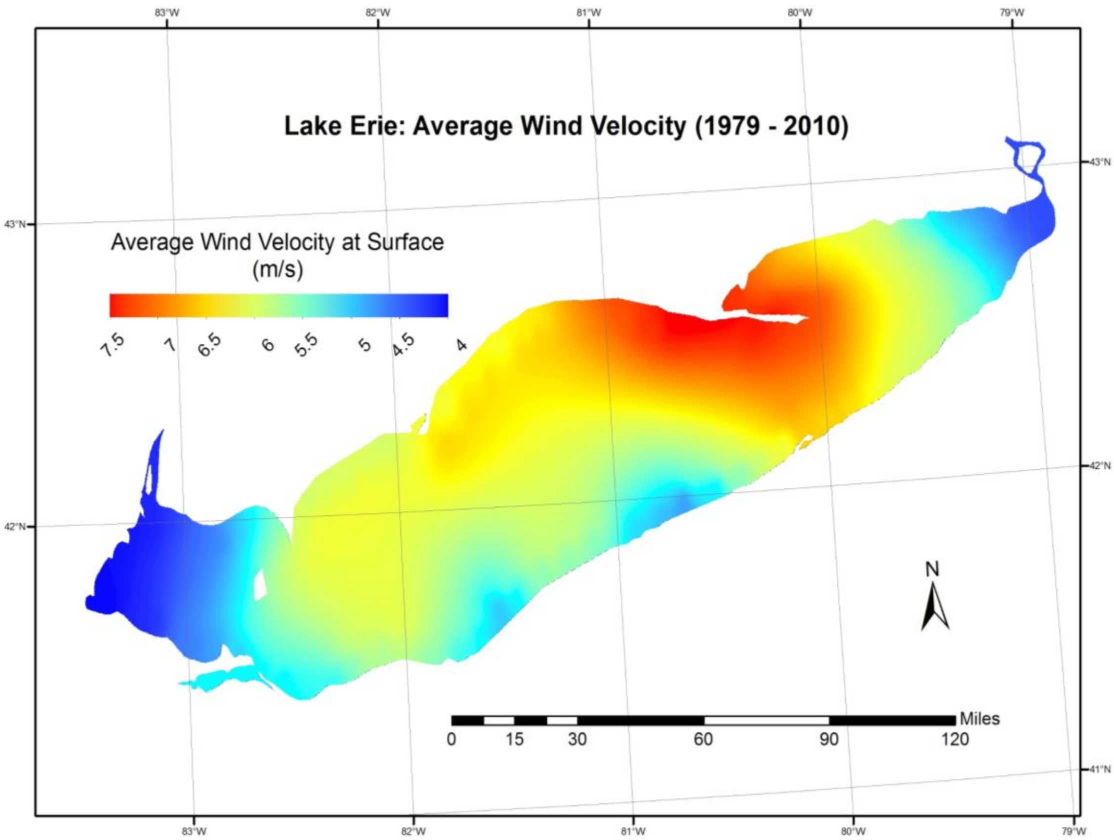

(e)

Figure 10.3 WIS hindcast wind speed from 1979 – 2010 of the Great Lakes

10.2 HISTORICAL WAVE STUDY

In a similar fashion, we present the hindcast wave height data from the Wave Information Studies (WIS). In the charts below, we summarize the hindcast wave height for each of the Great Lakes. Wave heights are plotted for March, June, September, and December – to show seasonal variations. In general, wave heights are highest during the winter months and most quiet during the summer months. Lakes Erie and Ontario have the highest wave action, with Lake Superior showing the lowest wave heights.

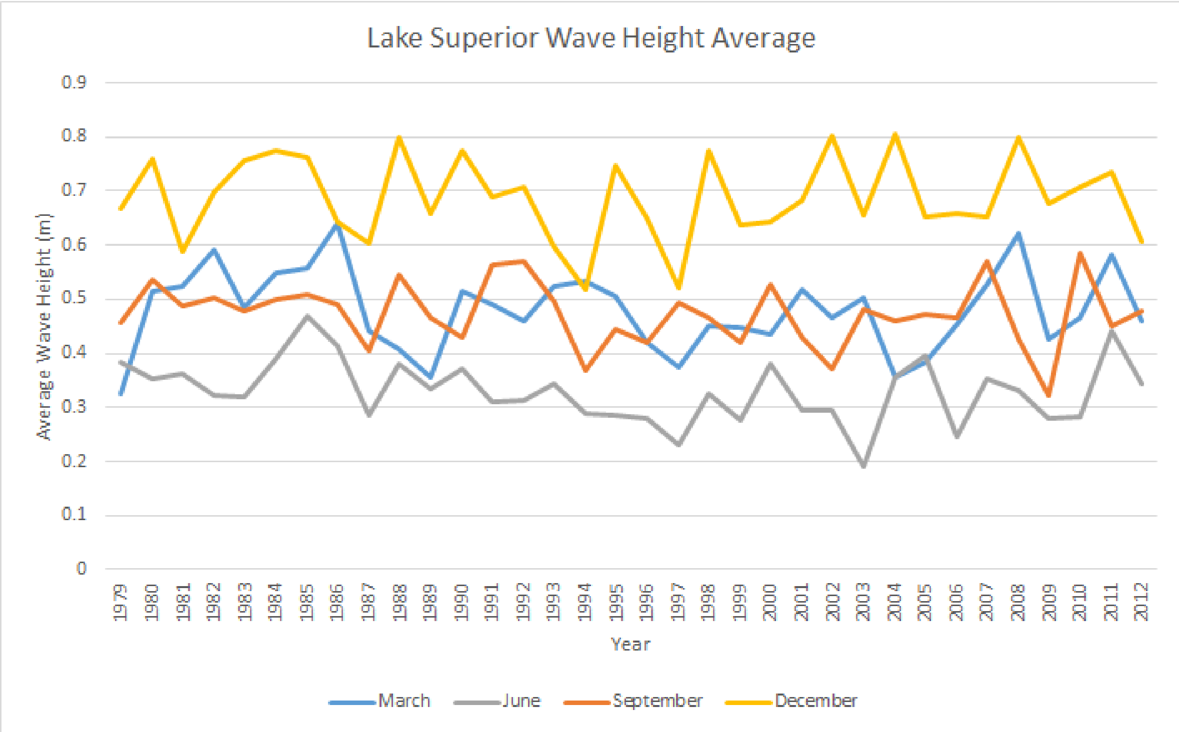

(a)

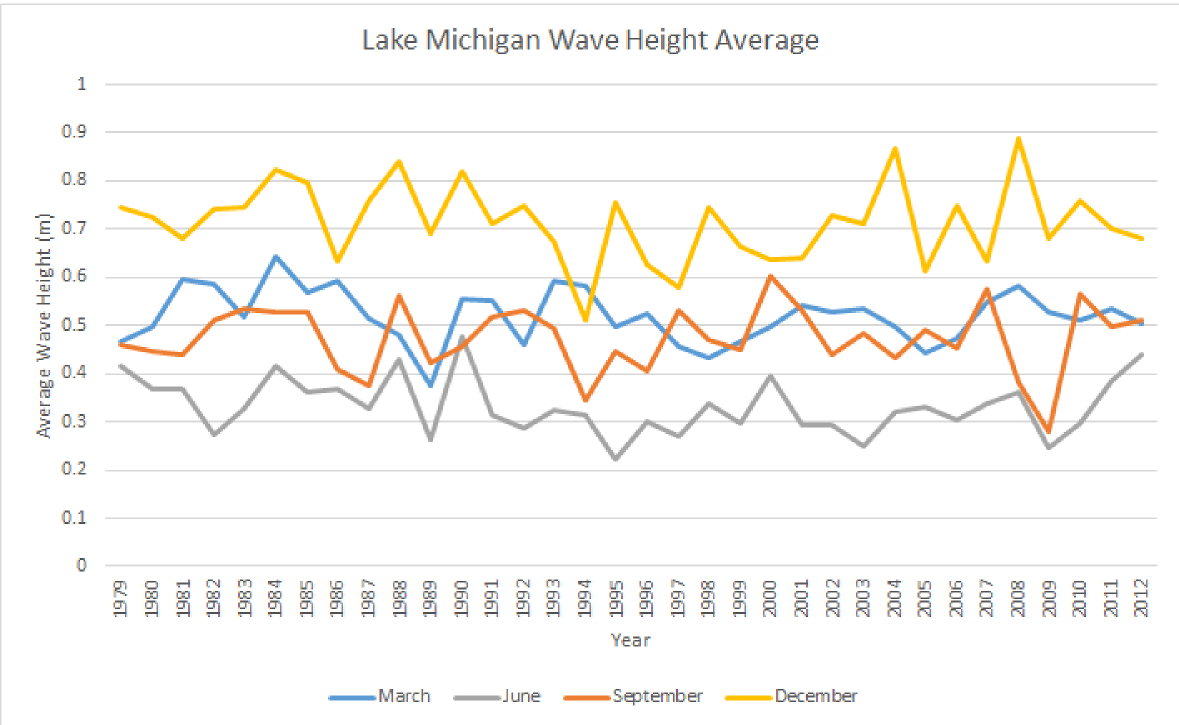

(b)

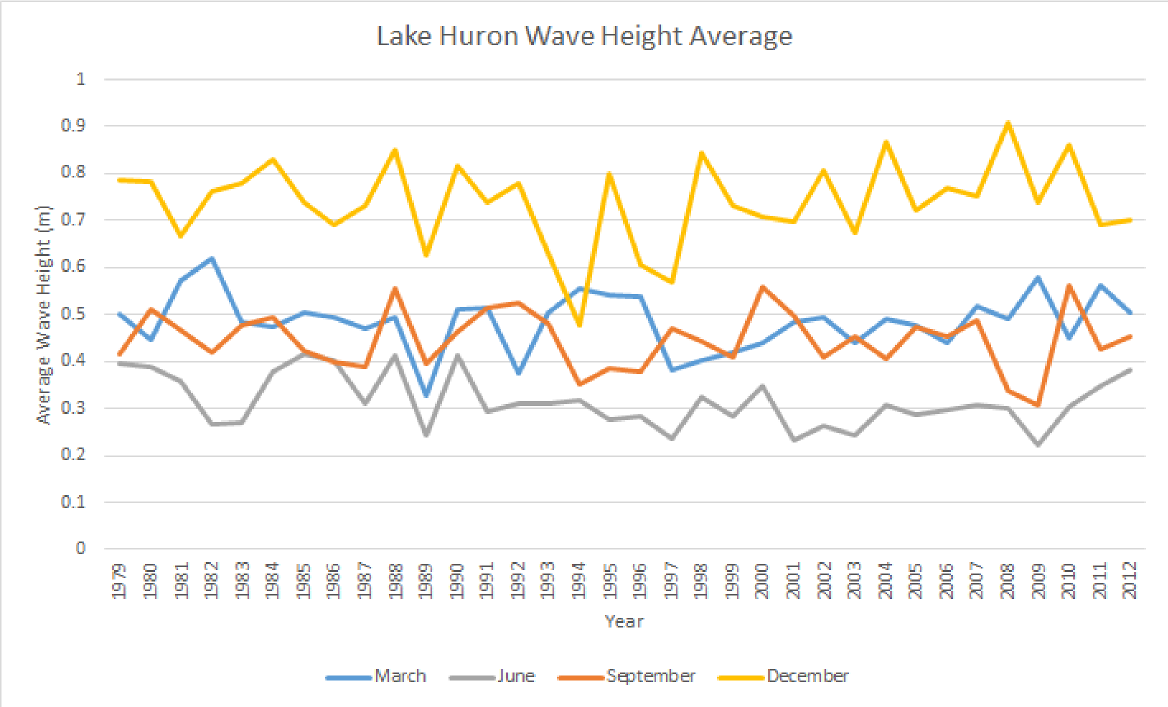

Lake Huron Wave Height Average
Average Wave Height (m)
Year
March
June
September
December

(c)

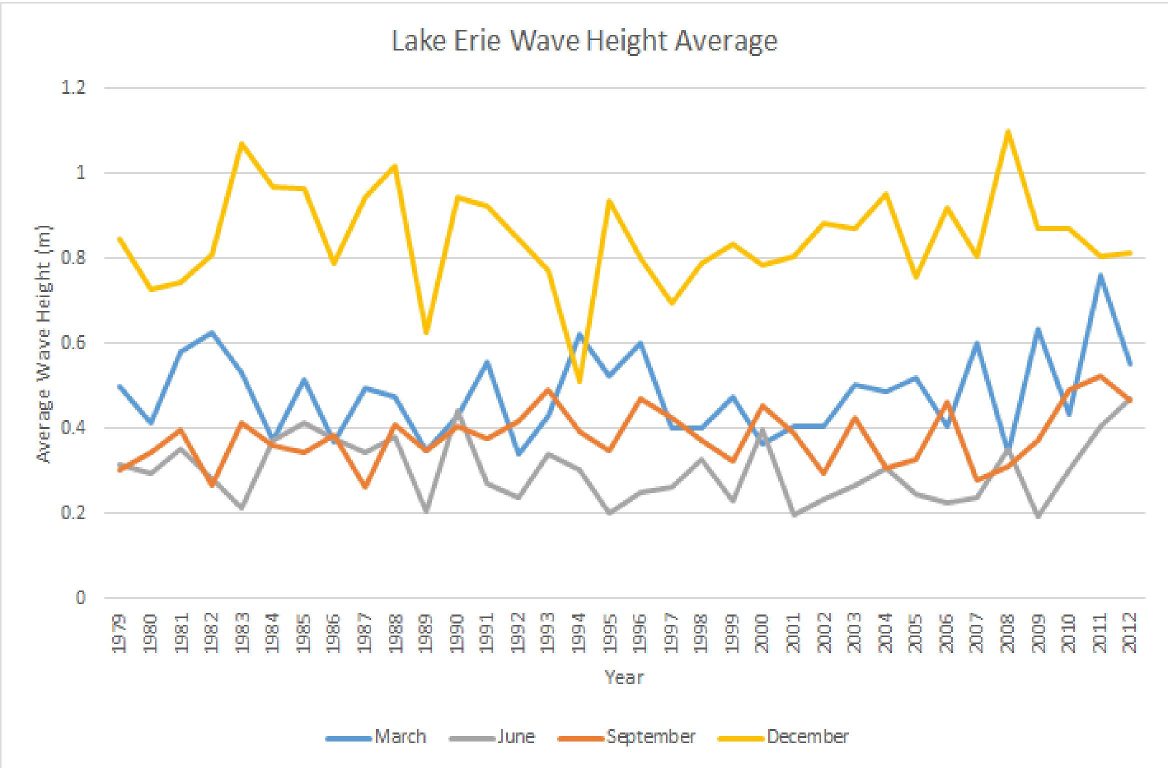

Lake Erie Wave Height Average
Average Wave Height (m)
Year
March
June
September
December

(d)

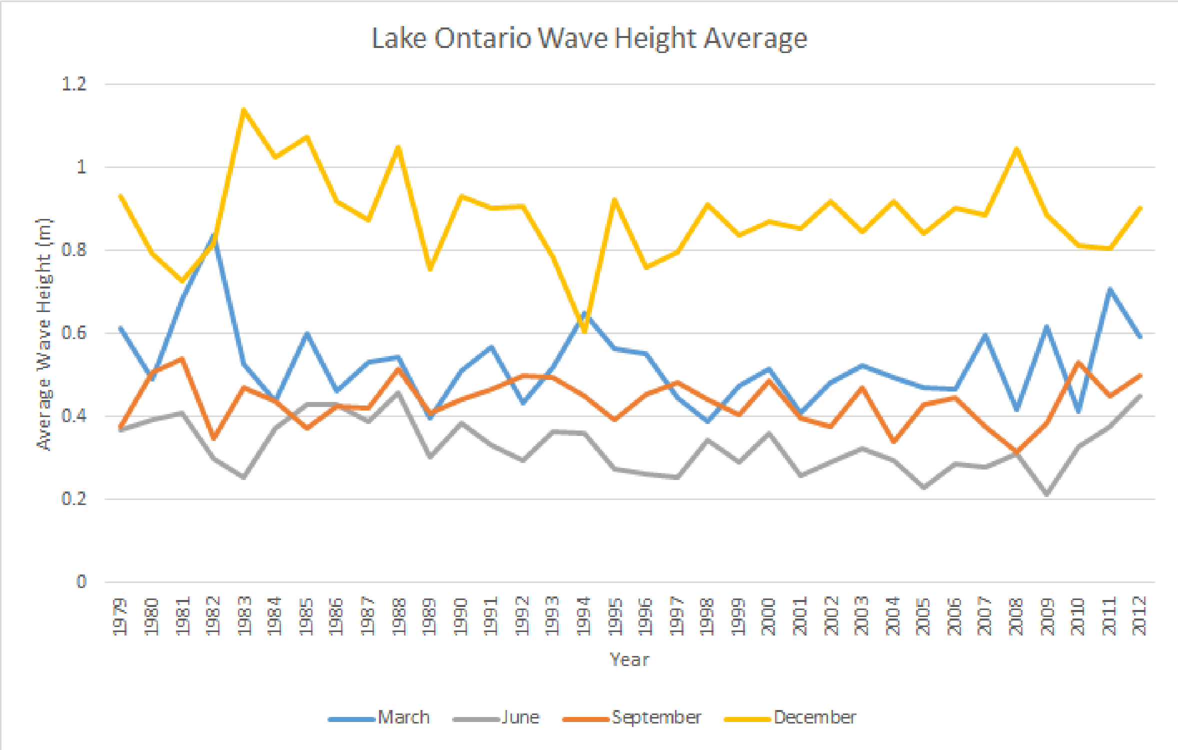

(e)

Figure 10.4. Hindcast wave heights for Lakes Superior, Michigan, Huron, Erie, and Ontario. Wave heights are highest with the last two lakes.

10.3 HISTORICAL ICE THICKNESS STUDY

In studying ice thickness trends in the Great Lakes, we were fortunate to come across data recorded by the National Snow & Ice Data Center: http://nsidc.org/data/G00803. However, the data was provided in a format unfamiliar to our team and was extremely dense in nature. This resulted in the use of a Python script to parse the data into a CSV file that could be more easily understood; Python script is included in Appendix 10.3. This data set has over one hundred locations where a variety of ice thickness readings were taken over a 10-year span. Analyzing the exact coordinates of each location led us to believe that the readings at L'anse Bay – Keweenaw Bay, MI, were the most useful due to the proximity to our readings in Jacobsville, MI. Additionally, the readings taken at this location followed a consistent weekly pattern over the 10-year span reassuring our confidence in the accuracy of the readings. Ice thickness charts from two locations are shown in Figures 10.5 and 10.6

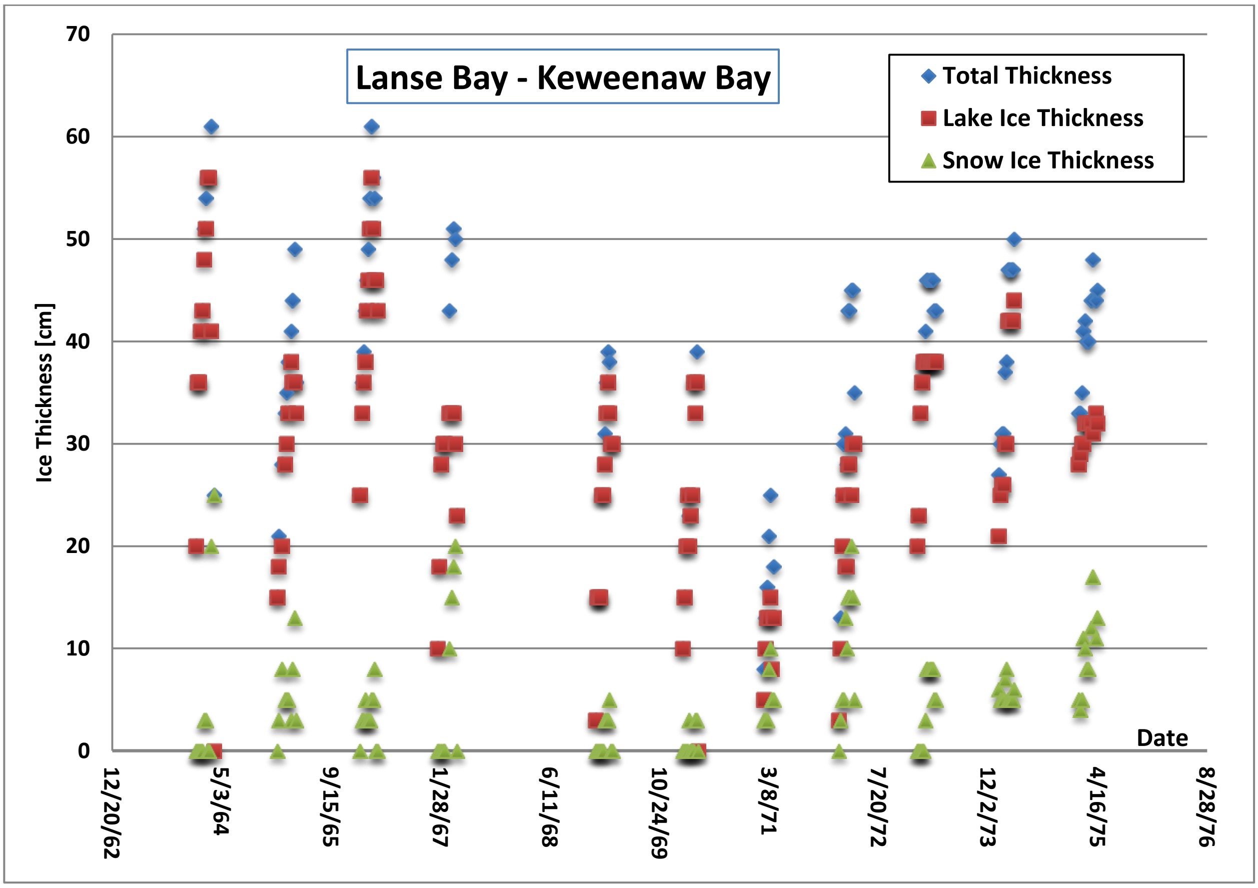

Figure 10.5. Measured ice thickness data from the National Ice and Snow Data Center

L'Anse Bay is located directly across the Keweenaw Waterway from the South Entry Lighthouse, at a distance of about ten miles. It is the closest NSIDC station that we are able to locate. The Portage Lake station is also in the relative vicinity of the observation site; however, it is an inland location. We decided to do the comparison study with data from the L'Anse Bay. Shown in Figure 10.7 are the curve fits of L'Anse Bay data, plotted again a 'seasonal' axis, combining all data points over the 1968-1979 collection period. We observe that the ice thickness data measured by the WISN instruments during the winter 2014 season are within the historical thickness values. WiBAR and AWAC + stereo data integration with the historical measured ice data was done by M. van Nieuwstadt; the MatLab script used to generate curves in Figure 10.7 is included in Appendix 10.4.

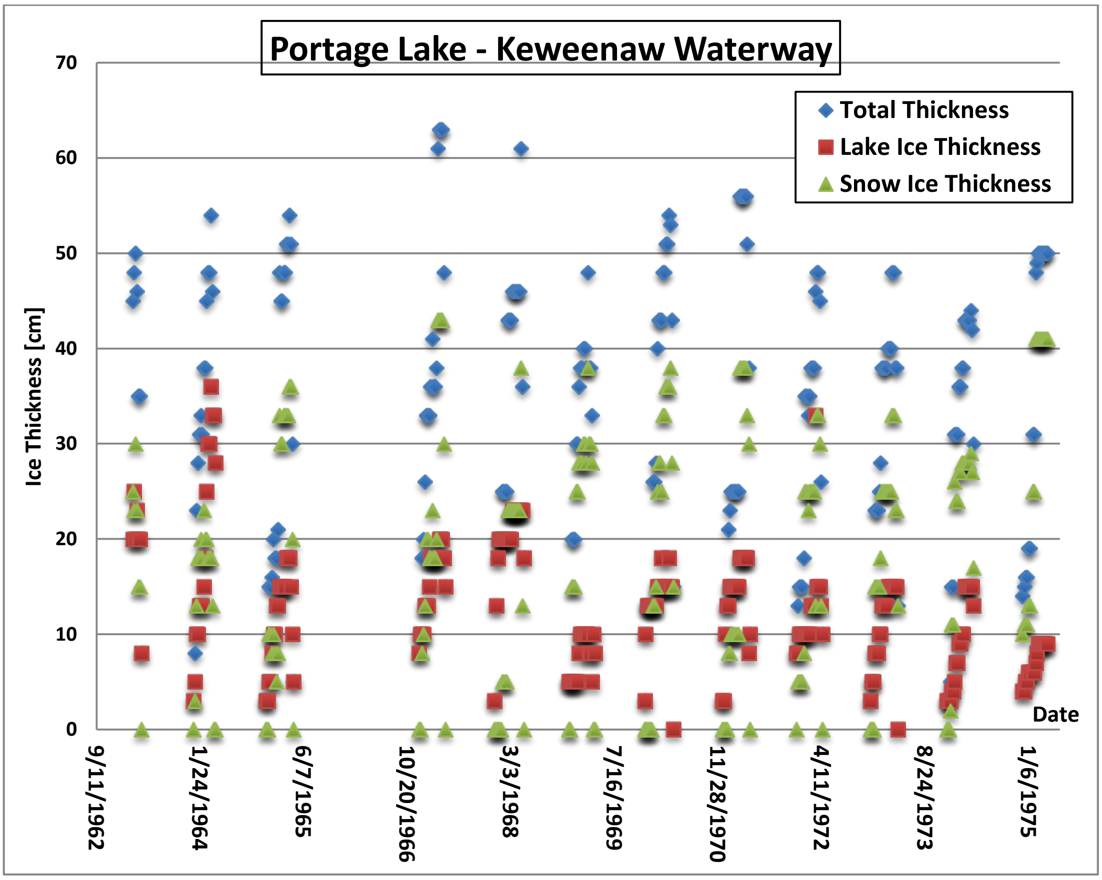

Figure 10.6. Measured ice thickness data from the National Ice and Snow Data Center

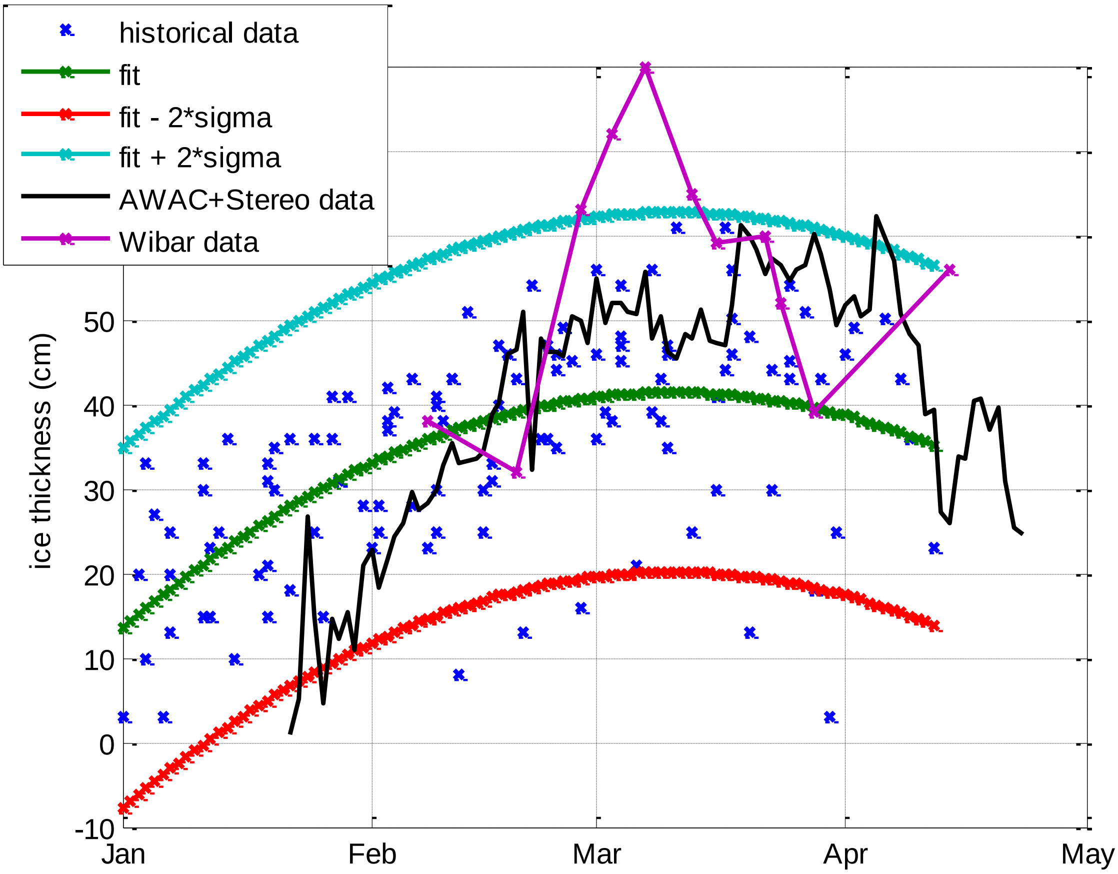

Figure 10.7. Seasonal charts of measured ice thickness in L'Anse Bay, in comparison to the WISN data, specifically AWAC + stereo and WiBAR.

11 PROJECT SUMMARY

In fulfillment of the DOE DE-EE0005376 contract, the University of Michigan Team (UM-Team) in partnership with the Michigan Technological University Team (MTU-Team) successfully completed a three-year project whose primary achievements were to:

- Measure the forces applied by Great Lakes ice on an offshore structure and correlate these forces with observed ice thickness,
- Capture the extreme of lake ice force to the extent possible, and
- Place these observations in the context of normal and exceptional Great Lakes ice coverage and climatologies.

Our strategy for observing ice forces versus ice thickness was to instrument an existing offshore structure in a location on the Great Lakes that likely would be exposed to massive ice interactions during most winters. The Statement of Work for the project proposed two winter observing seasons with the option of a third winter observing season if the first two seasons had anomalously light ice cover. The schedule was based upon a start date in late fall of 2011. The actual start date was not until late spring of 2012, which did not leave enough time before the winter of 2012-13 to select a Great Lakes Observing Site (GLOS), and to design, build, and test even a rudimentary Wind and Ice Sensing Network (WISN). We chose the alternate path of using the first winter observing season, the winter of 2012-13, to examine several sites, one of which, Lake Superior's South Entry Light of the Keweenaw Waterway, became our GLOS for the winter of 2013-14, and to test a breadboard version of a new concept for remotely measuring snowpack and freshwater ice thickness, the Wideband Autocorrelation Radiometer (WiBAR). As the first field implementation of WiBAR, we felt it advisable to validate our design in an actual field setting before committing to its inclusion in our WISN for the primary observing season. The decision to make the winter of 2013-14 our primary observing season was fortuitous in that, as one of the coldest winters on recent record, ice on Lake Superior was near a historical maximum, allowing us to delete the possible option of a third observing season.

Full scale, physical measurements of wave and ice force processes in sufficient detail to guide design decisions in the harsh winter environment of Lake Superior are challenging. Our successful acquisition of these measurements required development and deployment of WISN through our primary observing season, the winter and spring of 2013-2014. Using a cell phone command and data link and solar power, WISN operated autonomously for periods of days at a time. It sensed ice thicknesses using two techniques, (1) a combination of measured ice-surface height from digital photogrammetry and measured distance from lake-bottom to ice-base from an Acoustic Doppler Current Profiler (ADCP), and (2) a direct measure of ice thickness from the experimental WiBAR system. WISN sensed ice forces using a load cell, referred to as the Ice Force Measuring System (IFMS), which was designed, built, calibrated, and deployed at the GLOS for this task. Sophisticated data analytics allowed us to recover best estimates of ice thickness and pressure applied by the ice for the two-foot width of our load cell.

Ice thickness data from the GLOS site for the primary observing season were produced by WiBAR (Chapter 6) and by a combination of digital photogrammetry (Chapter 7) and ADCP (Chapter 8) and are shown in Figure 11.1a. The WiBAR observations are based upon the statistics of a noise signal. 'Hamid's results' refer to an early visual interpretation of these data. 'WiBAR SPICE' and 'WiBAR ESPRIT' refer to analyses employing statistical inference and represent a more reliable interpretation of the data. We believe WiBAR was 'seeing' layering in the ice during the second half of the winter season. This is not necessarily a limitation of the WiBAR concept, but likely a result of our simple implementation of the concept. More observations behind each data point would have reduced the statistical uncertainty of the inference and increased the sensitivity to the possibility of multiple layers. Hamid's 'outliers' are discussed more fully in Chapter 6.

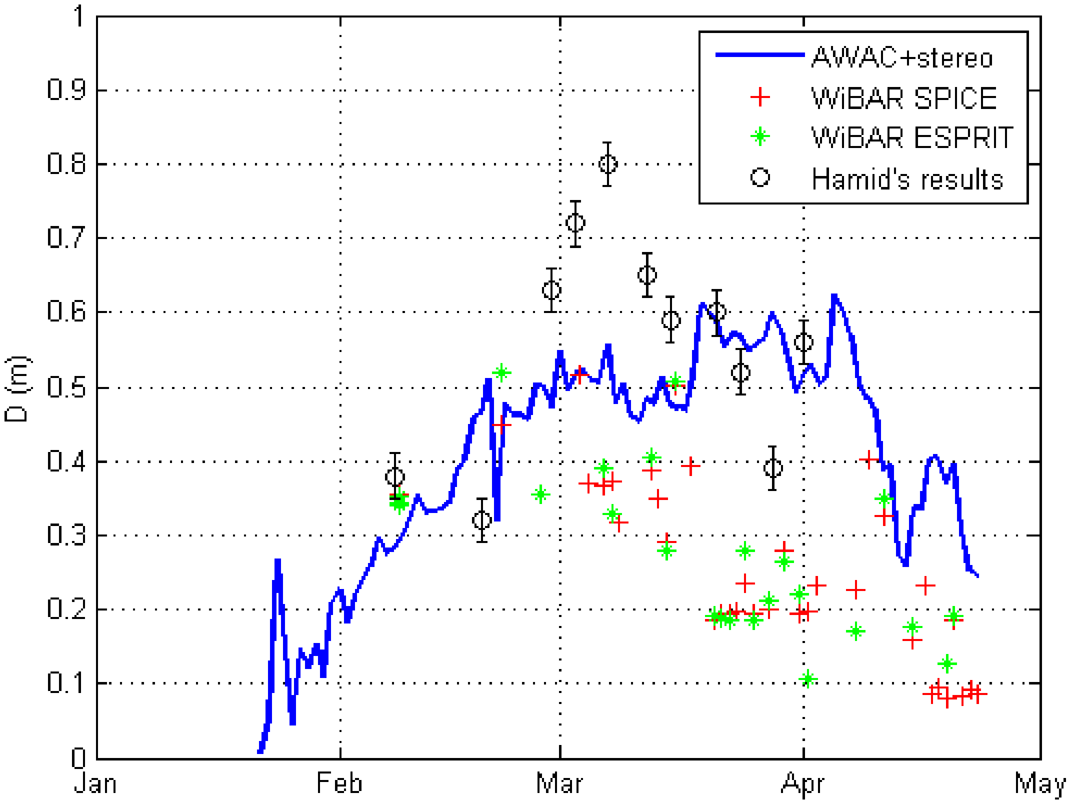

Figure 11.1a. Ice thicknesses at GLOS for the winter 2013-14 observing period.

Observed ice thicknesses are placed in an historical context (Chapter 10) in Figure 11.1b; data analysis was done by M. van Nieuwstadt. Observed ice thickness trends for the 2013-14 season is clearly consistent with historical annual patterns.

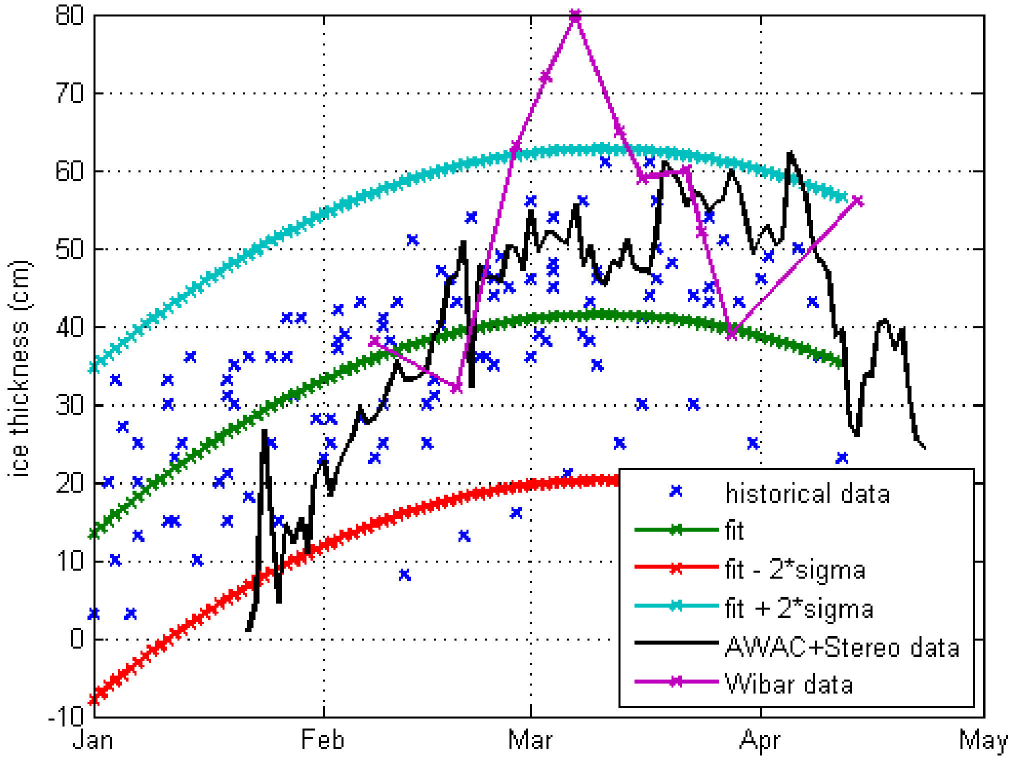

Figure 11.1b. Observed ice thicknesses and their historical context at the South Entry Light of the Keweenaw Waterway during the winter of 2013-14.

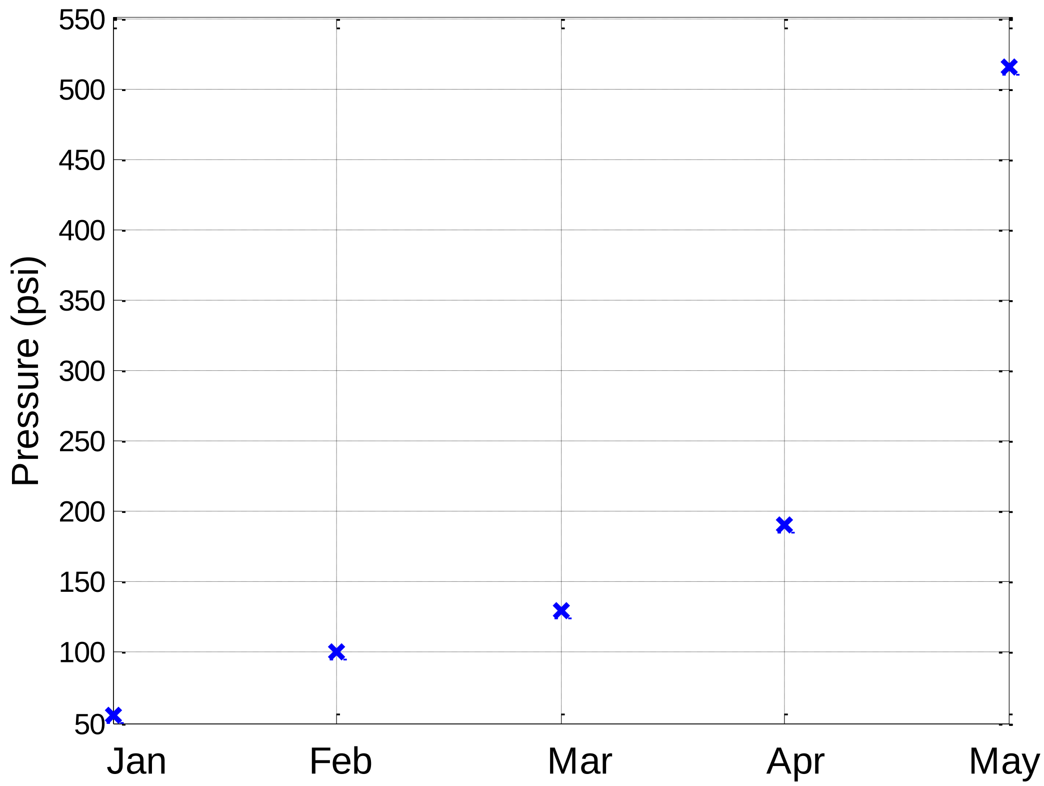

Figure 11.2. Ice pressure observed at our GLOS for winter 2013-14.

Maximum inferred ice pressures as a function of time-of-year are summarized in Figure 11.2. IFMS instrumentation and analyses of these measurements are described in Chapter 5 where maximum ice pressures are also compared with ice force measurements reported in the literature for other load cell structural widths.

An historical wind/wave and ice climatology for the Great Lakes is reported in Chapter 10. Maximum Ice cover data for the Great Lakes, largely available from NOAA's Great Lakes Environmental Research Laboratory (GLERL), are shown in Figure 11.3.

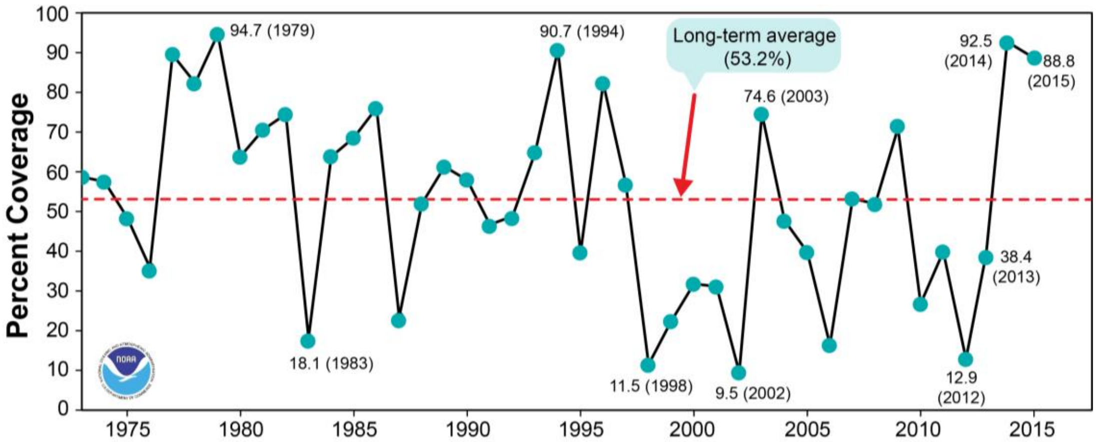

Figure 11.3. Annual maximum ice coverage averaged for the five Great Lakes, 1973-2016.

Prior to the Winter of 2013 -14, Lake Superior had enjoyed a prolonged period (approximately 17 years) of mild and relatively warm winters with very low ice cover punctuated by winters of ice cover in excess of 90% occurring approximately every five to seven years (Figure 11.4). The primary observing season for this investigation occurred during the most significant ice year for Lake Superior since 1979 (35 years). The severity of this measurement year (Winter 2013-14) is captured in Figure 11.5, a MODIS Ice image of the Keweenaw Peninsula at a time near the peak of ice growth.

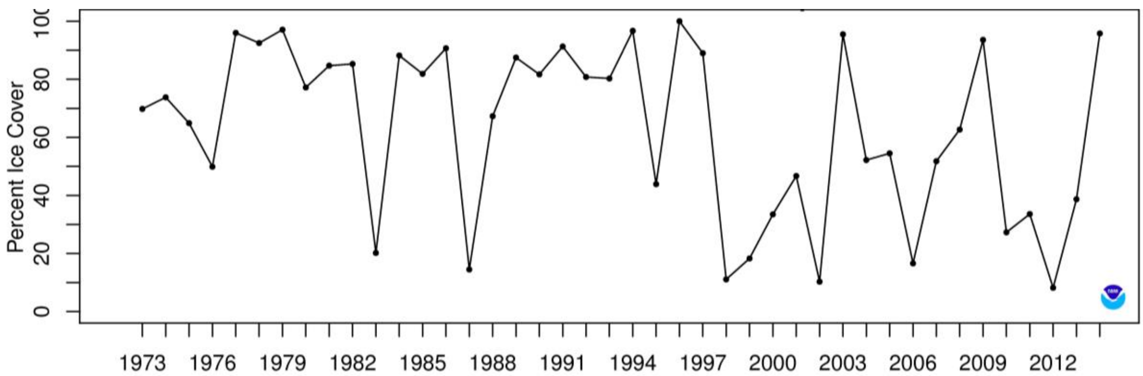

Figure 11.4. Annual maximum ice coverage for Lake Superior, 1973-2014.

Figure 11.5. MODIS image of Lake Superior ice coverage near the Keweenaw Peninsula, February 19, 2014.

We executed the observing plan and obtained the measurements described in this report in the context of a severe Great Lakes winter. During Great Lakes winters most over-water monitoring systems (vessels, buoys, and non-automated observation stations) are not available so some processes are understood through inference. A reasonable assumption is that with severe ice years also come severe wind episodes (described in Chapter 10). As can be seen in the MODIS ice image, very large blocks of ice are available to be set in motion by wind and currents, producing the potential for large ice impact loads on offshore structures. We believe that a large ice block, perhaps from a pressure ridge, was blown against the load cell in late winter during ice breakup causing the extreme pressure shown as the May pressure point in Figure 11.2. This high-pressure event also corresponds to the ADCP being knocked over. The ADCP was mounted on a lakebed tripod in 18 feet of water near the Ice Force Measuring System (IFMS). Figure 11.6 shows the ADCP lying on its side and Figure 11.7 shows a gouge in the lakebed that was not there at the beginning of the season. It appears that an ice mass large enough to have a keel extending 18 feet below the surface impacted the load cell and scoured the local lakebed. This might well have been the extreme event we had hoped to observe.

Figure 11.6. Image showing the ADCP on its side after the high ice force event in May 2014. The image was taken by a remotely controlled submersible.

Figure 11.7. Image of gouged lakebed in 18 feet of water near the ADCP.

Our investigative team was comprised of members from the University of Michigan, the UM-Team, and members from the Michigan Technological University, the MTU-Team. The UM-Team was responsible for project design, instrument development or procurement, instrument integration into the WISN system, data analysis, and project management. The

MTU-Team was responsible for system deployment, field support, management of the ADCP, and recovery of ADCP data.

If we were to offer 'lessons learned', there are at least three: (1) the power management approach was too conservative, (2) the WiBAR instrument should have taken more frequent data reading, and (3) WISN did not measure ice floe drift/velocity as expected due to firmware limitations of the ADCP.

Although no specific future work proposal is currently in progress, discussions are on-going in several areas. First, there is continuing need and interest in pursuing ice thickness measurement in the Great Lakes. The need comes from the shipping industry and from the U.S. Coast guard, in connection with transportation safety. The interest comes from the climatologists as validation tools for the Great Lakes climate models, assessing energy content of the lakes

TASKS SPECIFIED BY THE STATEMENT OF PROGRAM OBJECTIVES (SOPO)

Task I.I. Historical review and preliminary analysis of climatological data

Deliverable – Chapter 10: Hindcast modeling from the Wave Information Studies (WIS) of the Army Corps of Engineers (http://wis.usace.army.mil/) estimate the average wind speeds on the Great Lakes between 1979 and 2010 to have varied between 4.0 m/sec in the summer on Lake Superior to 8.6 m/sec. in winter on Lake Ontario with Lake Superior having the lowest annual winds speeds by ~1 m/sec. These hindcast winds might not be entirely reliable. The Stannard Rock Lighthouse, 20 miles to the ENE of the nearest point of the WIS hindcast consistently records winds in excess of the WIS estimates by ~2 m/sec.

The highest average WIS hindcast winds for Lake Superior are off the Keweenaw Peninsula. Those for Lake Michigan lie between the Door Peninsula and the Leelanau Peninsula. Those for Lake Huron surround the Bruce Peninsula. Those for Lake Erie surround the projection into Lake Erie of Norfolk County, Ontario. Finally, those for Lake Ontario surround Prince Edward, Ontario. All wind maxima approach 7.5 m/sec. WIS hindcast estimates for March, June, September, and December show December to have the highest wave heights and June to have the lowest. Lakes Erie and Ontario have the highest wave heights, peaking over 1 m, and Lake Superior has the lowest peak wave heights at ~ 0.8 m.

Our WISN ice thickness measurements were consistent in temporal pattern with the positive extremes of historical ice thicknesses data for Keweenaw Bay. Peak ice thicknesses of 60 cm at the WISN site are 2-sigma above the average winter distribution of ice thicknesses.

Task I.II. Site selection, and securing logistic support and approval

Deliverable (Chapter 5): Several Great Lakes sites were considered. In doing so, it soon became clear that the overriding criteria needed to be:

- Predictably thick ice driven by offshore winds and currents
- Safe access to WISN during winter for service and/or repair
- Reasonably inaccessible to vandals
- Nearby field service personnel

Prof. Guy Meadows, the project's original Principal Investigator (PI), transferred to Michigan Technological University in Houghton, MI, as the founding Director of their new Great Lakes Research Center (GLRC) during the period we were searching for our Great Lakes Observing Site (GLOS). Because GLRC was located near the historical maxima of winds, waves, and lake ice on Lake Superior, Prof. Tony England, the newly designated PI, enlisted Prof. Meadows and his organization as a Field Support subcontractor to the project. GLRC not only had the proximity for convenient access to both the Upper and Lower Entry Lights of the Keweenaw Waterway, they had the boats, trucks, and skills to safely work near those lighthouses in winter.

Both lighthouses are exposed to long fetches of Lake Superior. We explored their suitability as our GLOS during our first winter season, the winter of 2012-2013, and found access to the North Entry Light to be too dangerous while access to the South Entry Light would be cautiously safe via a ¼ mile jetty on days of relative calm. The South Entry Lighthouse was chosen as our primary GLOS and permission for access was sought and graciously granted by both the U.S. Coast Guard and the Historical Society of Michigan.

Task I.III. Field instrument testing and evaluation

Deliverable – (Chapters 5 through 9): The Wind and Ice Sensor Network (WISN) was developed and deployed on our chosen GLOS, the South Entry Light of the Keweenaw Waterway, for our primary observing period of fall, winter, and spring of 2013-2014. WISN comprised an Ice Force Measuring System (IFMS) developed by Prof. Dale Karr's team, a Wide-Band Autocorrelation Radiometer (WiBAR) developed jointly by Prof. Anthony England and Dr. Roger DeRoo, a Scene Capture System (SCS) developed by Dr. David Lyzenga, an Acoustic Doppler Current Profiler (ADCP) managed by Prof. Guy Meadows, and an Instrument Support System (ISS) developed by Dr. Line van Nieuwstadt. As Project Manager, Dr. van Nieuwstadt also led overall WISN integration.

IFMS (Chapter 5) was a half-ton load cell designed to hang in the water on the windward side of the South Entry Light to measure impact forces from floating ice. The sensing area of the IFMS was planar surface 2 ft wide by 5 ft tall. The cell, a watertight steel structure, had a front plate exposed to floating ice and a parallel back plate designed to rest against the stone face of the lighthouse abutment. The front plate had 9 equally spaced, horizontal, internal ribs instrumented with strain gages to measure deflection of the front plate. The system was calibrated with known loads. A combination of theory, calibration, and measured ice thickness was used to convert strains resulting from ice loads to force/unit area, or pressure, on the surface of the IFMS. The IFMS worked as designed throughout the measuring period.

The WiBAR (Chapter 6) was the first application of a new concept for remotely and deterministically measuring the thickness of dry snowpacks and freshwater ice. Because dry snowpacks and freshwater ice are both lossless and do not exhibit significant scatter darkening at frequencies below 10 GHz, neither of these media absorb radiation at these frequencies. Media that do not absorb at these frequencies do not emit Planck radiation at these frequencies. Radiance sensed by observing these media with a microwave radiometer is a combination of Planck radiance from underlying soil or water transmitted through the medium and down-welling sky radiance reflected by the medium. Because the upwelling radiance at these frequencies is dominant, this radiance becomes an electromagnetic noise signal that probes the snow or ice layer by traveling a multipath route through the snow or ice layer to the wideband radiometer. That is, a direct ray traverses through the layer once before being sensed by the radiometer, and a reflected ray traverses the layer three times before being sensed by the radiometer. Because the original signal appears as band-limited white noise, autocorrelation of the received signal yields a delayed peak representing twice the travel time in the layer. A reasonable estimate of the dielectric properties of the snow or ice layer permits a conversion of this travel time to snowpack or ice thickness.

WiBAR, a low-cost implementation of the concept, employed a wideband horn antenna, a pre-filter, two low noise amplifiers separated by isolators to eliminate internal reflections, a 3 GHz passband filter centered at 8.5 GHz, and a spectrum analyzer that subsampled down converting the signal to 0-3 GHz. The Fourier Transform of the power spectrum yielded the autocorrelation of the multipath signal. This autocorrelation exhibited a delayed peak corresponding to twice the travel time in ice layer.

Task I.IV. Initial winter field measurement program

Deliverable: We had tentatively chosen the North Entry Light to the Keweenaw Waterway as our GLOS. We found during our initial field season that accessing this site was too dangerous in winter. We also used the first season, winter 2013, to test a prototype version of the WiBAR.

Task I.V. Initial reduction and analysis of field data

Deliverable: Our findings allowed us to reorient our thinking toward using the South Entry Light to the Keweenaw Waterway the following year. Experience with the prototype WiBAR convinced us that we had a workable concept and permitted us to proceed with a robust design that functioned adequately through the harsh conditions of the second field season.

Task I.VI. Dissemination of initial findings

Deliverable: Please refer to Chapter 6 for details.

Task I.VII. Time-scale analysis of climatological data

Deliverable: As previously noted, the primary observing season was condensed to the winter of 2013-2014. The experimental data was placed in context of previously available historical data.

Task I.VIII. Final reduction and analysis of field data

Deliverable: N/A, as noted under Task I.VII.

Task I.IX. Final winter field measurement program

Deliverable: N/A, as noted under Task I.VII.

Task I.X. Initial reduction and analysis of second field data

Deliverable: N/A, as noted under Task I.VII.

Task I.XI. Dissemination of preliminary findings

Deliverable: Technical presentation and written publication submitted to peer reviewed journal.

Task II.I. Final data reduction and analysis

Deliverable: Final data analysis is included in this report: results summarized in the main body of the report while detailed analysis included in the appendices.

Task II.II. Development of dynamic models for structural loading

Deliverable: Models for dynamic behavior of ice-structure interactions were developed, appendix 5.2.

Task II.III. Development of design criteria

Deliverable: see Task II.II notes.

Task II.IV. Workshop/dissemination of final results

Deliverable: Please see published articles and conference papers.

Task III. Project Management and Reporting

Deliverable: Reports and other deliverables have been provided in accordance with the Federal Assistance Reporting Checklist following the instructions.

LIST OF PUBLICATIONS, PRESENTATIONS

Y. Zhang and D.G. Karr, 2015, "Determining Ice Pressure Distribution on a Stiffened Panel using Orthotropic Plate Inverse Theory", *in review*, Journal of Structural Engineering.

Y. Zhang, T.C. Remmers, B. Yu, and D.G. Karr, 2016, "Nonlinear Contact Dynamic Response Simulation of Matlock's Ice-structure Interaction Model using Fourier Analysis," *submitted* for the 23rd IAHR International Symposium on Ice, Ann Arbor MI.

Y. Zhang, D.G. Karr, A. W. England, L. van Nieuwstadt, R. De Roo, D. Lyzenga, 2015 Engineering Graduate Symposium (EGS) in Civil & Environmental Engineering (CEE) session; poster title: Determining Ice Pressure Distribution on Ice-force Measuring System (IFMS) Panel using Orthotropic Plate Inverse Theory.

H. Nejati, S.Y.E. Wong, R. De Roo, L. van Nieuwstadt, K. Sarabandi, G.A. Meadows, and A.W. England, ``A wideband autocorrelation radiometer for snowpack/lake ice thickness detection," submitted to IEEE Transactions on Geoscience and Remote Sensing, 2014.

H. Nejati, Passive Remote Sensing of Lake Ice and Snow using Wideband Autocorrelation Radiometer (WiBAR). PhD dissertation, University of Michigan, Ann Arbor, 2014.

H. Nejati, R. De Roo, L. van Nieuwstadt, K. Sarabandi, and A.W. England, ``Design and modeling of a wideband autocorrelation radiometer (WiBAR) as a snowpack thickness sensor," in A/V Recordings, IEEE International Geoscience and Remote Sensing Symposium (IGARSS '14), (Quebec, QC), 13-18 July 2014.

L. van Nieuwstadt, *et.al*, "Wave-Ice Sensor Network," poster session at Michigan Technological University, September 2014.

D.G. Karr, "Ice/Structure Interaction: Offshore Structural Design," Michigan Technological University, March 2013.

D.G. Karr, "Offshore Wind Turbines Vs. Winter on the Great Lakes," Michigan Alternative and Renewable Energy Center, October 2013.

D.G. Karr, "Ice/Structure Interaction Modelling for Offshore Wind Turbines in the Great Lakes," University of Toledo, January 2014.

D. Karr, "Ice/Structure Interaction Modeling for Offshore Structures," University of California Berkeley, February 2014.

D.G. Karr, "Measurement and Analysis of Extreme Wave and Ice Actions in the Great Lakes for Offshore Wind Platform Design" DOE 2014 Wind Power Peer Review Meeting, March 2014.

D.G. Karr, "Freshwater Ice Loading and Other issues in the Great Lakes," DOE/BOEM Workshop on Offshore Wind Energy Standards and Guidelines, Arlington, VA, June 2014.

APPENDIX 5.1

Determining Ice Pressure Distribution on a Stiffened Panel Using Orthotropic Plate Inverse Theory

Yuxi Zhang[3], Dale G. Karr[4]

ABSTRACT

Inverse algorithms are presented to calculate the variable pressure acting on a stiffened steel plate. The analytical models are formulated to calculate the quasi-static pressure distribution caused by the effects of ice. The loading pressure is calculated using strain measurements from a stiffened plate installed on a Keweenaw Peninsula lighthouse in Lake Superior. The linear relationships between pressure and strain values are obtained by both strip beam theory and orthotropic plate theory with respect to different forms of ice loading and available input. Fourier pressure terms are calculated from the strain measurements from the inverse orthotropic plate algorithms. Because the inverse solutions are not necessarily unique, multiple approaches are developed and compared.

Two of the approaches are applied using orthotropic plate theory to reflect the variability of the ice: the first sub-model presumes the pressure acts over the entire plate; the second sub-model presumes the pressure acts only within the depth of the measured ice thickness. Favorable comparisons are made of results determined from orthotropic plate theory to results from finite element analyses. A truncated singular value expansion method is applied to retain the robustness of the inverse process for the second sub-model. Both inverse approaches show results with satisfying accuracy and efficiency compared to the finite element analysis. In addition, laboratory calibration and an examination using the recorded data from field measurements exhibit the effectiveness of the presented approach. Inverse strip beam theory and the inverse orthotropic methods are applied for the evaluations. The peak ice pressures calculated by the inverse orthotropic plate theories are in the range of 3.5 MPa for the local contact ice pressures, and a maximum of 3.0 MPa for the average ice pressures over the entire plate.

Subject Headings:
Inverse Theory, Strip Beam Theory, Orthotropic Plate Theory, Pressure Variation Prediction, Truncated Singular Value Expansion, Pseudo Inverse, Laboratory Calibration.

INTRODUCTION

Offshore regions of the Arctic and the Great Lakes hold valuable resources in many respects for harvesting energy and serving as important shipping lanes. Ice loading poses a threat to structures in these regions; it is thus essential to evaluate the ice peak loadings using limited and site-specific data. Sanderson (1988) observed that global ice pressures are significantly lower than local ice pressures during ice crushing events; Palmer et al. (2009) developed an ice-pressure to ice-contact area curve. In a review of the ice-force measurements, Bjerkas (2007) described several methods for measuring the full-scale ice forcing and reported the peak ice pressures to be in the range of 0.6 to 1.8 MPa along the American shorelines. However, most of the previous experiments use load cells for data collection (Palmer and Croasdale, 2013), which are good for the contact force measurements at specific points rather than reflection of the force distribution over the entire plate (Jordaan et al., 2005). Few records can be found for ice loadings on stiffened offshore structures in the Great Lakes area. Driven by the need to evaluate the peak ice-loading in the Great Lakes area and to develop an efficient algorithm to accurately depict the

[3] Dept. of Naval Architecture and Marine Engineering, Univ. of Michigan, Ann Arbor, MI. yuxiz@umich.edu
[4]Ph.D, P.E., Dept. of Naval Architecture and Marine Engineering, Univ. of Michigan, Ann Arbor, MI. dgkarr@umich.edu

ice force distributions, our study involves the development of cost-efficient analytical models to inversely predict ice-pressure distributions from the limited measurements of ice thickness and structural strains. The input measurements of the ice thickness and the strains used in the analysis discussed here are obtained from the stiffened panel deployed in Lake Superior.

Ice Force Measurement System (IFMS)

The installation and operation of the Ice Force Measuring System (IFMS) have been completed as a portion of Department of Energy sponsored project entitled "Measurement and Analysis of Extreme Wave and Ice Actions in the Great Lakes for Offshore Wind Platform Design." Instrumentation was deployed in Lake Superior on a Keweenaw Peninsula lighthouse, where a large-scale laboratory for cold regions engineering experimentation is naturally formed. A data acquisition system captured readings from strain gages encased in the IFMS plate and ice-thicknesses were monitored from a radiometer located on the deck of the lighthouse (Fig. 1a and 1b). The physical dimensions of the IFMS plate with the numbering of ribs and the allocation of linear strain gages are sketched in Fig. 2a: $a = 1.5m$ is the depth of the plate defined along the vertical x-direction, $b = 0.6m$ is the width of the plate along the horizontal y-direction. Nine stiffeners are evenly distributed from the top to the bottom of the plate and are sequentially numbered from #0 to #8. The vertical spacing of the two near stiffeners is $t_1 = 0.15\ m$. Also, the upper right unloaded zero strain gage R_0 is used to diminish temperature effect and determine the change of stresses caused only by effects of ice. The linear horizontal strain gages R_{hsg} are located at the middle span of the ribs from rib #1 to rib #7. The vertical strain gages R_{vsg} are located at the back of the face plate and are aligned through the vertical midline of the plate. The center of the vertical strain gage is located midway between stiffeners. The vertical boundaries of the IFMS face plate are constrained by two stiff steel side-bars as shown in Fig. 2b.

Literature Review

The plate is composed of evenly distributed stiffeners and readily lends itself to application of orthotropic plate theory (OPT). Boot (1988) argued that the centroidal neutral axis of the cross section suffices for stress and displacement calculations if the shear deflection is negligible. Moreover, Deb et al. (1988) recommended using the technical orthotropic plate under uniform load after comparison of two linear finite element models using discrete plate beam formulation. Here, the IFMS stiffened panel is reasonably idealized as a structurally orthotropic plate given the feature of the uniformly distributed flexural rigidities along plate orthogonal directions (Shimpi and Patel, 2006).

While most analyses are forward calculations for structural response under known pressure, the inverse problem is to extract a physically practical pressure distribution caused by the effect of ice with limited structural measurements. Infinite degrees of loading conditions exist with respect to finite structural response inputs. Due to the lack of uniqueness, the inverse calculation is an optimization procedure for load parameter identifications and load extractions (Engl and Kugler 2005; Chock and Kapania 2003; Li and Kapania 2007). In many cases, small changes in the input strain readings will possibly result in extreme variations out of the physically feasible range in the forcing predictions (Starkey and Merrill 1989).

Classic methods to overcome these difficulties involve a regularization procedure to convert the ill-posed matrix to neighboring well-posed matrixes (Hansen and O'Leary 1993; Engl and Kugler 2005), thus to eliminate the instability of inverse matrix operation. However, this procedure may introduce extra error caused by a different level of approximation of the reciprocity gap of each simulation (Bonnet and Constantinescu 2005), when usually no *a priori* knowledge is available. The concept of reciprocity gap is introduced by Andrieux and Abda (1996) to describe the identified difference between the forward input and its inverse calculation of the inputs. Additionally, Ma et al. (2003) argued that a recursive inverse method may be applied to extract the forcing from noisy measurements of a structural response. However, the accuracy of these calculations rely heavily on the initial knowledge of force parameters, information which is unavailable in many cases. Furthermore, the key point towards a well-established inverse problem is the consistency of the description of the class of models to its input data (Snieder 1998). Thus, these iterative computation methods for a recursive process can be expensive and will not be an ideal consideration when limited accuracy is achievable with a few noise-encased inputs.

In the case of limited structural measurements and no *a priori* knowledge for ice forcing, the inverse problem can be defined as an under-determined problem with ill-posed relationships between the pressure and the structural response. Chock and Kapania (2003) applied a singular-value decomposition (SVD) technique followed by classic least-square methods to identify the pressure parameters for ill-posed inverse systems. Ewing et al. (1999) observed that the presented error percentages by SVD are of the same order to the input noise level from the recorded simulations.

Another widely applicable and similar approach is the truncated singular value expansion (TSVE) method (Engl and Kugler 2005, Semnani and Kamyab, 2008), where the singular values of the matrix are filtered by a “low pass filter” to retain the robustness of the matrix in dominant dimensions. Andrew and Patterson (1976) discussed the application of TSVE in image processing to best restore the original image by retaining the value of the condition number of the matrix. Leone and Soldovieri (2003) argued that the truncated domains of the matrix are observed to affect mainly the dimensions orthogonal to the aimed reconstruction space. More importantly, both SVD and TSVE are considered optimal when the coefficient matrix and its singular value decompositions are available (Engl and Kugler, 2005).

Furthermore, the forms of ice loading may remain in question. Kim et al. (2015) took the form of the ice load as a triangular prism, given that the peak ice pressure occurs at the frame supports. Riska et al. (2002) considered the line-like contact force considering small plate rigidity by using the multi-plate analysis method. However, Dempsey et al. (2001) argued that the description of line-like contact force is caused by rapidly fluctuating dense distribution of high pressure zones, which is specifically applicable to the relatively thin ice layer. Moreover, both the triangular prism model and the line-like ice model are based on the assumption of the elastic bodies of ice-structure interaction system.

In fact, non-simultaneous small-scale ice failure of a more uniform pressure distribution is usually the case for rigid plate (Riska et al.,2002; Kalenchuk and Kulesh, 2010). Jordaan et al. (2005) assumed a stationary process of ice-structure interaction to measure the ice load on the Molikpaq, Amauligak I-65 deployment. Also, the ice is considered to be in the failure mode of ductile crushing at a low drift speed (Bjerkås and Skiple, 2005; Wells et al., 2011). Based on the observations of limited ice motion, our paper considers the quasi-static ice-pressure acting on the plate. Considering the high rigidity of the IFMS plate, the medium-to-high ice-thickness measurements, and the very low ice-contact velocities, the pressure field is first reasonably presumed as uniform over the entire panel. This assumption leads to a simple horizontal strip beam formulation as a fast approach to estimate the averaged ice forcing. Furthermore, the vertical strip beam model is formulated to predict the contact ice pressure between two ribs. This second model allows us to access the deformation of the plate between stiffeners. These forward strip beam models and their inverse counterparts compare well to the finite element results under the assumed uniform pressures.

Next, the orthotropic plate theory is applied to capture the variability of the pressure over the plate. In the plate analyses, a trigonometric deflection field that satisfies the approximate boundary conditions is assumed. To calculate the Fourier pressure terms from limited strain inputs, two forward orthotropic models are derived with respect to the prescribed area over which the ice pressures are presumed to act: the first model presumes the pressure acts over the entire plate; the second model presumes the pressure acts only within the depth of the measured ice thickness. The convergence of the two approaches is studied through strain evaluations. The inverse counterparts of these models and the applications are discussed in detail. Results by the orthotropic plate theory and the inverse calculations satisfyingly agree with the finite element model under various loading situations.

METHODOLOGY

Strip Beam Theory (SBT)

A horizontal portion of the plate evenly spaced between two stiffeners is considered to form an Euler-Bernoulli strip beam (Fig. 3a). The dimensional parameters of a resulting T-shaped cross section are sketched in Fig. 3b. The beam ends are reasonably considered as fixed as a reflection of the constraints from the stiff side bars and back plate. In an effort to obtain a first estimation of the average ice pressure, a uniform ice-pressure p is assumed when the entire plate is fully covered by ice. The uniformly distributed load q on the horizontal beam is calculated by the product of the pressure p and the strip beam cross-section width $t_1 = 0.15\ m$. The effective elastic modulus of the upper flange (assumed to be in plane strain) E_1 is $220\ GPa$, and the elastic modulus of the steel of the web E_2 is $200\ GPa$. Thus, the distance C from the effective centroid of the cross-section to the bottom of the fiber is $0.08\ m$. The effective flexural rigidity $E_e I_y$ of the cross section is $6.49 \times 10^5\ \mathrm{N \cdot m^2}$. The relationship for strains located at the bottom of the mid-span of the stiffener under a given distributed load q is as follows:

$$\epsilon_{\mathrm{yy}} = \frac{\mathrm{Cb^2}}{24\mathrm{E_e I_y}} q = 1.85 \times 10^{-9} q \cdot m/N \tag{1}$$

Similarly, a vertical strip beam of width $t_v = 0.03\ m$ and of length $a_1 = 0.14\ m$ is analyzed between the span of two neighboring ribs. The dimensions of the vertical strip are sketched in Fig. 4. The distributed vertical-beam load is calculated as $q_v = p t_v$. Note that the three vertical linear strain gages are aligned along the middle of the plate at $y_0 = 0.31m$ as denoted by the vertical gray rectangles in Fig. 2.

The flexural rigidity is calculated $E_{ev} I_x = \frac{t_v h_p^3 E}{12(1-\mu^2)} = 7.71 \times 10^3\ N \cdot m^2$ with the effective elastic modulus E_{ev} as $220\ GPa$ under the plain stress assumption for strip beam theory. In this expression, t_v and h_p are the width and height for the cross-section respectively, and I_x is the moment of inertia for the vertical strip beam cross-section. Using the Euler-Bernoulli strip beam theory, the strain-loading relationship for a mid-point at the bottom of the ideal beam under the distributed load q_v for fixed ends is:

$$\epsilon_{xx} = \frac{h_p a_1^2}{48 E_{ev} I_x} q_v = 1.30 \times 10^{-9} q_v \cdot m/N \tag{2}$$

STRUCTURAL ORTHOTROPIC PLATE THEORY (OPT)

To evaluate the variable ice loading over the plate, the panel with closely distributed stiffeners is formulated as a structurally equivalent orthotropic plate. This idealization models the stiffened plate by an orthotropic homogeneous plate with rigidities averaged in orthogonal directions over the plate with respect to the form of orthotropy (Ventsel and Krauthammer 2001). Ice thickness is found to mainly affect the variability of ice forcing in the vertical direction for narrow structures (Frederking and Schuwarz, 1982; Leira et al., 2009). Thus, a uniform loading is assumed along the horizontal direction in the current analysis for the narrow IFMS plate.

Note the net deflection of the stiffeners does have some component due to shear deformation in addition to bending deflections. However, considering the geometric symmetry of the location of the horizontal linear strain gages, the contribution due to shear deformation is negligible in the calculation of the strain. Our analysis thus uses the small-deflection theory of thin-plate bending in the orthotropic plate (OPT) formulation to calculate the response of the plate. Two forward structural calculation models are set up via OPT analyses; both models apply the Navier's equations to simulate the deflection surface and to express the distributed load through the terms of Fourier coefficients. The first OPT model (OPT I) assumes the Fourier coefficients of the pressure to be expanded over the entire plate; the second OPT model (OPT II) constrains the pressure coefficients to be expressed within the area covered by the ice-thickness. Moreover, the OPT II model focuses on extracting the maximum peak ice pressure, and thus it is presumed that no pressure from current or wave acts on the plate beneath the ice. The ice thickness is measured from a deployed radiometer included in the IFMS instrumentation. Both forward calculations give accurate strain evaluations with great efficiency for the quasi-static stress analysis.

Based on the IFMS geometry, clamped boundary conditions are applied along the vertical edges of the plate (i.e. x-direction), and pinned boundaries are applied along the top and bottom edges of the plate (i.e. y-direction). The stiffened panel is first modeled with two stiff side bars and with the back plate on as a reflection of the actual construction of the IFMS plate. The second model consisting of only the stiffened face plate is fixed along the vertical edge and pinned along the horizontal edge. The designated strains calculated by these two FE models are observed to differ by less than 1%, thus justifying the boundary conditions of the second model as reasonable constraints in the OPT analysis.

To satisfy the boundary conditions, a double Fourier series function is composed for the displacement field $w(x, y)$. Let m=1..M, n=1..N, where M is the order of coefficient terms to be retained along the x direction, and N is the order of terms along the y direction:

$$w(x,y)=\sum_{m=1}^{M}\sum_{n=1}^{N}W_{mn}\sin(\frac{m\pi x}{a})[1-\cos(\frac{2n\pi y}{b})] \tag{3}$$

OPT I—Pressure Acting Over the Entire Plate

For OPT I, the coefficients $P_{I_{mn}}$ are used to express the pressure coefficients over the entire plate for the double series pressure solution $p_I(x, y)$:

$$p_I(x,y)=\sum_{m=1}^{M}\sum_{n=1}^{N}P_{I_{mn}}\sin(\frac{m\pi x}{a})\sin(\frac{n\pi y}{b}) \tag{4}$$

Using the assumption of uniform pressure along the y direction, the Fourier series of the pressure field p_I is expressed by retaining the coefficient terms over the x direction as denoted by P_{I_m}:

$$p_I(x,y)=\sum_{m=1}^{M}\sum_{n=1,3..}^{N_n}P_{I_m}\frac{4}{n\pi}\sin(\frac{m\pi x}{a})\sin(\frac{n\pi y}{b}) \tag{5}$$

Based on the Kirchhoff's small-deflection plate bending theory and orthotropic plate theory, the strain energy U of bending for orthotropic plate is expressed in integral form over the entire plate surface area A:

$$U=\frac{1}{2}\iint_A[D_x(\frac{\partial^2\omega}{\partial x^2})^2+D_y(\frac{\partial^2\omega}{\partial y^2})^2+2D_{xy}\frac{\partial^2\omega}{\partial x^2}\frac{\partial^2\omega}{\partial y^2}+4D_s(\frac{\partial^2\omega}{\partial y\partial x})^2]dA \tag{6}$$

Substituting (3) into (6) and integrating, the strain energy of bending for the plate is expressed by Fourier displacement terms:

$$U=\frac{1}{2}\sum_{m=1}^{M}\sum_{n=1}^{N}(\frac{3bm^4\pi^4}{4a^3}D_xW_{mn}{}^2-\frac{2m^2n^2\pi^4}{ab}D_{xy}W_{mn}{}^2+\frac{4an^4\pi^4}{b^3}D_yW_{mn}{}^2+\frac{4m^2n^2\pi^4}{ab}D_sW_{mn}{}^2) \tag{7}$$

To calculate the flexural rigidities, the representative T-shaped cross section for the OPT model is of the same dimensions as described for the horizontal strip beam (Fig. 5). The flexural and torsional rigidity formulas of the equivalent orthotropic plate are given by Ventsel and Krauthammer (2001) for several commonly encountered stiffener formations. The rigidities of the IFMS plate in Eq. (6) and Eq. (7) are calculated as:

$$D_y=\frac{EI_y}{t_1},D_x=\frac{Eh_p^3}{12(1-\frac{b_s}{t_1}+\frac{h_pb_s^3}{H^3})},D_{xy}=0,D_x\approx\frac{Gh^3}{12}+\frac{C_t}{2t_1} \tag{8}$$

where G is the torsional rigidity of the rib about its centroidal axis. Also, the external potential energy V is written as a function of the displacement and pressure terms integrated over the plate volume v:

$$V=\iiint_v w(x,y)p_I(x,y)dv=\sum_{m=1}^{M}\sum_{n=1}^{N}\sum_{j=1,3..}^{N}P_{I_m}\frac{4abW_{mn}}{\pi^2 j}[\frac{1}{j}-\frac{1}{2(j+2n)}-\frac{1}{2(j-2n)}] \tag{9}$$

Note that the same number of deformation coefficients are retained as that of the pressure coefficients, in which case m=1..M, n=1..N. Applying the principle of stationary total potential energy, $\frac{\partial \mathrm{U}}{\partial \mathrm{W_{mn}}} - \frac{\partial \mathrm{V}}{\partial \mathrm{W_{mn}}} = 0$, the deformation coefficients are obtained in relation to the Fourier pressure terms:

$$W_{mn} = \sum_{j=1,3..}^{N} P_{I_m} \frac{\frac{4ab}{\pi^2 j}[\frac{1}{j} - \frac{1}{2(j+2n)} - \frac{1}{2(j-2n)}]}{(\frac{3bm^4\pi^4}{4a^3}D_x - \frac{2m^2n^2\pi^4}{ab}D_{xy} + \frac{4an^4\pi^4}{b^3}D_y + \frac{4m^2n^2\pi^4}{ab}D_s)} \tag{10}$$

The horizontal strains are found from the displacement Fourier series and the strain-displacement relations:

$$\varepsilon_{yy} = -z_0 \sum_{m=1}^{M}\sum_{n=1}^{N} W_{mn} (\frac{2n\pi}{b})^2 \sin(\frac{m\pi x}{a})\cos(\frac{2n\pi y}{b}) \tag{11}$$

where z_0 is the distance of the point to the centroidal plane. The linear relationship of the strain value ϵ_{yy} to the pressure Fourier coefficient term P_{I_m} is:

$$\varepsilon_{yy} = -z_0 \sum_{m=1}^{M}\sum_{n=1}^{N} P_{I_m} (\frac{2n\pi}{b})^2 \sin(\frac{m\pi x}{a})\cos(\frac{2n\pi y}{b}) \frac{\sum_{j=1,3..}^{N} \frac{4ab}{\pi^2 j}[\frac{1}{j} - \frac{1}{2(j+2n)} - \frac{1}{2(j-2n)}]}{\frac{3bm^4\pi^4}{4a^3}D_x - \frac{3m^2n^2\pi^4}{ab}D_{xy} + \frac{4an^4\pi^4}{b^3}D_y + \frac{4m^2n^2\pi^4}{ab}D_s} \tag{12}$$

OPT II—Pressure Acting Over the Ice-covered Area

To capture more accurately the peak pressure over the ice covered area, the pressure coefficients of the Fourier series are constrained to act within a specific area defined by the measured ice thickness t_{ice}. Satisfying the same displacement boundary conditions stated in the previous model, the same displacement expression Eq. (3) is used, and the ice-covered area is assumed to be $t_{ice}b$. The pressure field $p_{II}(x,y)$ on the constrained area is then expanded by the coefficients P_{II_i}, where i is the order of the pressure coefficient along the x-direction. Similar to the OPT I summation, M and N are the total coefficient terms along x or y coordinate respectively:

$$p_{II}(x,y) = \sum_{i=1}^{M}\sum_{j=1,3..}^{N} \frac{4}{\pi j}\sin(\frac{i\pi\tilde{x}}{t_{ice}})\sin(\frac{j\pi y}{b})\cdot P_{II_i} \tag{13}$$

Here $\tilde{x} = x - x_1$, $\tilde{x} \subseteq [0, t_{ice}]$, $x_1$is the starting coordinate along x for the ice contact area.

Substituting (13) into Eq. (6), considering the external energy integral Eq. in (9), and applying stationary total potential energy, the relationship of Fourier coefficients for W_{mn} as a function of pressure coefficients P_{II_i} over the confined ice-covered area is obtained. Let $k = \frac{m}{a}$, where a is the depth of the plate vertically, W_{mn} is then expressed as follows:

if $ai \neq mt_{ice}$:

$$W_{mn} = \sum_i\sum_j \frac{4b}{k\pi^3 j}[\frac{1}{j} - \frac{1}{2(j+2n)} - \frac{1}{2(j-2n)}]\cdot \frac{a^2 i t_{ice}[(-1)^{i+1}\sin(\frac{m\pi(x_1+t_{ice})}{a}) + \sin(\frac{m\pi x_1}{a})]}{\pi(a^2i^2 - m^2 t_{ice}{}^2)(\frac{3bm^4\pi^4}{4a^3}D_x - \frac{2m^2n^2\pi^4}{ab}D_{xy} + \frac{4an^4\pi^4}{b^3}D_y + \frac{4m^2n^2\pi^4}{ab}D_s)} P_{II_i}$$

if $ai = mt_{ice}$:

$$W_{mn} = \sum_i\sum_j \frac{4b}{k\pi^3 j}[\frac{1}{j} - \frac{1}{2(j+2n)} - \frac{1}{2(j-2n)}] \frac{[\cos(k\pi x_1)k\pi t_{ice} - \frac{1}{2}\cos(k\pi x_1)\sin(2k\pi t_{ice}) + \sin(k\pi x_1)\sin^2(k\pi t_{ice})]}{\frac{3bm^4\pi^4}{4a^3}D_x - \frac{2m^2n^2\pi^4}{ab}D_{xy} + \frac{4an^4\pi^4}{b^3}D_y + \frac{4m^2n^2\pi^4}{ab}D_s} P_{II_i}$$

(14)

where $i = 1,2,..M$, $j = 1,3,..,N$, $m = 1,2,..M$, and $n = 1,2,..N$.

The linear relationship of the strain value ϵ_{yy} at (x, y) to the pressure Fourier coefficient terms for OPT II is calculated by substituting Eq. (14) into Eq. (11):

if $ai \neq mt_{ice}$:

$$\varepsilon_{yy}(x,y) = -z_0 \sum_{m=1}^{M}\sum_{n=1}^{N} (\frac{2n\pi}{b})^2 \sin(\frac{m\pi x}{a})\cos(\frac{2n\pi y}{b}) \cdot$$

$$\sum_{j=1,3..}^{N}\sum_{i=1}^{M} \frac{4b}{k\pi^3 j}[\frac{1}{j} - \frac{1}{2(j+2n)} - \frac{1}{2(j-2n)}] \cdot \frac{a^2 i t_{ice}[(-1)^{i+1}\sin(\frac{m\pi(x_1+t_{ice})}{a}) + \sin(\frac{m\pi x_1}{a})]}{\pi(a^2 i^2 - m^2 t_{ice}^2)(\frac{3bm^4\pi^4}{4a^3}D_x - \frac{2m^2n^2\pi^4}{ab}D_{xy} + \frac{4an^4\pi^4}{b^3}D_y + \frac{4m^2n^2\pi^4}{ab}D_s)} P_{IIi}$$

if $ai = mt_{ice}$:

$$\varepsilon_{yy}(x,y) = -z_0 \sum_{m=1}^{M}\sum_{n=1}^{N} (\frac{2n\pi}{b})^2 \sin(\frac{m\pi x}{a})\cos(\frac{2n\pi y}{b}) \cdot$$

$$\sum_{j=1,3..}^{N}\sum_{i=1}^{M} \frac{4b}{k\pi^3 j}[\frac{1}{j} - \frac{1}{2(j+2n)} - \frac{1}{2(j-2n)}] \cdot \frac{[\cos(k\pi x_1)k\pi t_{ice} - \frac{1}{2}\cos(k\pi x_1)\sin(2k\pi t_{ice}) + \sin(k\pi x_1)\sin^2(k\pi t_{ice})]}{(\frac{3bm^4\pi^4}{4a^3}D_x - \frac{2m^2n^2\pi^4}{ab}D_{xy} + \frac{4an^4\pi^4}{b^3}D_y + \frac{4m^2n^2\pi^4}{ab}D_s)} P_{II_i}$$

(15)

EVALUATION OF FORWARD FORMULATIONS

To compare the analytical solutions with the finite element verification results, three loading cases are considered: Loading Case # 1 (LC#1) is a uniform pressure of 0.69 MPa over the entire plate; Loading Case # 2 (LC#2) is a single half-sinusoidal pressure between two neighboring ribs with amplitude of 1.08 MPa; Loading Case # 3 (LC#3) is a constant patched pressure of 0.69 MPa distributed over the first four ribs from the top of the plate. LC#1 and LC#3 are applied to extract the average global ice pressure over the entire plate or the designated ice-covered area; the loading area of LC#3 approximates the measured ice-structure contact area with an example of the ice-thickness of $0.6\, m$. Additionally, LC#2 is used to simulate a local peak ice pressure between ribs. The Finite Element (FE) model is set up for the verification effort using the 3D solid element analysis, where shear effect is included.

Both the horizontal and vertical strains calculated by the SBT and OPT I are compared to the FE model results under LC#1, and the results are given in Table 1. It is observed that the horizontal linear strains ϵ_{yy} calculated by the SBT and by OPT I at the order of 6 satisfyingly agree with the values predicted from the FE model. In a closer evaluation, the absolute error ratio by SBT is defined as $e_{sbt} = |\frac{\epsilon_{yy}\ by\ SBT - mean(\epsilon_{yy} by\ FEA)}{mean(\epsilon_{yy}\ by\ FEA)}|$ and is calculated to be 3.4%. The error percentage presented by OPT I at the order of 6 is defined as $e_{optI} = |\frac{\epsilon_{yy}\ by\ OPTI - mean(\epsilon_{yy}\ by\ FEA)}{mean(\epsilon_{yy} by\ FEA)}|$ and is also approximately 3.4%. The close approximation achieved by both SBT and OPT I for uniform loading LC#1 for the horizontal linear strain evaluations validates the accuracy of neglecting the shear effect in the specific strain evaluations. It is noted that using Timoshenko beam theory including the shear deformation approximates better the displacements; however the strains at the HLSG remain unaffected by the shear deflection effect.

The vertical SBT agrees well with the FE analyzed in the vertical strain evaluations ϵ_{xx} at the VLSG locations. The calculated vertical strains by OPT I along the plate mid-line are compared with those obtained from the FE analysis, as is shown in Fig. 6. It is found that the vertical SBT model with fixed ends is 2% more rigid than the finite element model based on the calculated bending strains (Table 1). Thus the vertical SBT can be applied inversely to extract the contact ice-pressure between the ribs using the fixed end conditions for the IFMS plate analysis. The vertical linear strains ϵ_{xx} calculated by the OPT I are not comparable to the FE model at the designated vertical linear strain gages (VLSG) due to the smearing effect of the structural orthotropic plate assumption.

In further efforts to evaluate the OPT formulation, the horizontal strain solutions ϵ_{yy} are calculated by OPT I through Eq. (12) at the designated locations of the horizontal linear strain gages (HLSG). The strains are calculated at different orders as is shown in Fig 7. It is found that the OPT I converges very accurately at the order M=9 by the observation of an overlapping of its results to those at the order M=11 under all three loading conditions. In Fig. 7, The FEA results are represented by red crosses, and the strain solutions obtained by OPT I at the order of 6 are depicted by solid-blue lines. The calculated strain lines at the order of 6 suffice for reasonable accuracy. The error percentage defined by the difference ratio between the forward calculated analytical strains to those from the FE analysis is approximated to be within the range of 1.0% to 13.5% at the order of 6 or above.

The forward pressure simulation and strain solution under LC#1 by OPT II is the same as by OPT I. The exact pressure formulation is achieved at the order M=1 for LC #2, and the pressure field is then considered convergent at the order M=3 for LC #3, by OPT II (Fig.8). Compared to OPT I, OPT II converges faster in the forward pressure and strain evaluations; this faster convergence is more obvious when the ice-covered area is thinner. The strains calculated by OPT I are converging to the FE results more accurately with increased coefficient terms. However, this is not necessarily true for the strains calculated by OPT II to converge to the FE solution. Thus, in a forward simulation, OPT I is recommended for its accuracy and is applicable without the necessary input of ice-thickness; while OPT II is considered more efficient in describing the pressure distribution over a thinner ice-covered area, where the knowledge of ice-thickness is necessary. The strain to pressure relationships expressed through Eq. (15) are observed to be coupled and thus may yield ill-posed coefficient matrixes for a direct inverse of the OPT II algorithm. However the inverse of OPT II will be optimized through a process of system parameter identification to retain the stability of the inverse calculation, which is discussed later.

ORTHOTROPIC PLATE INVERSE THEORY (OPIT)

The orthotropic plate inverse theory (OPIT) is derived from the forward OPT formulations to obtain the pressure coefficient terms P_I or P_{II} through the established relationships from the strain measurements ϵ_{yy}. Using the Fourier coefficients of displacement coefficients W_{mn} in Eq. (10) and Eq. (14), the deformation terms can be expressed in linear matrix form:

$$\boldsymbol{W}_{l_n} = \boldsymbol{A}_{l_n}\boldsymbol{P}_l \qquad l = I, II \tag{16}$$

The column matrix $\boldsymbol{W}_{l_n}$ represents the n^{th} column of the $\boldsymbol{W}_l$ matrix, where $l = I$ indicates the OPT I algorithm and the $\boldsymbol{W}_I$ is then expressed though Eq. (10); $l = II$ indicates the OPT II algorithm and the $\boldsymbol{W}_{II}$ is thus expressed through Eq. (14). $\boldsymbol{A}_{l_n}$ is the displacement-pressure coefficient matrix; $\boldsymbol{P}_l$ represents the vector of Fourier coefficients for the pressure field with M elements; n ranges from 1 to N , and N is the total order satisfying the convergence of uniform pressure along the y-direction.

Similarly, the strain-displacement relationship in Eq. (11) is configured using the matrix $\mathbf{S}_{\mathrm{n}}$ with the subscript n representing the order along y-direction; the strain vector is expressed for the l_{th} OPT algorithm as follows:

$$\boldsymbol{\epsilon_{yy}} = \sum_{n=1}^{n=N} \mathbf{S}_{\mathrm{n}}\, \boldsymbol{W}_{l_n} \tag{17}$$

Here the I_{inp} input strains compose the strain vector $\boldsymbol{\epsilon_{yy}}$. For example, $I_{inp} = 6$ may be used based on the number of linear strains gages allocated on the IFMS. Substituting Eq. (16) into Eq. (17), the strain vector is expressed by the pressure terms as:

$$\boldsymbol{\epsilon_{yy}} = \sum_{n=1}^{n=N} \mathbf{S}_{\mathrm{n}}\, \boldsymbol{A}_{l_n}\boldsymbol{P}_l \tag{18}$$

Assuming the coefficient matrix to order of N, the general orthotropic inverse coefficient matrix operation is obtained in the following form:

$$\boldsymbol{P}_l = \sum_{n=1}^{n=N} \boldsymbol{A}_{l_n}{}^{-1}\boldsymbol{S}_n^{-1} \cdot \boldsymbol{\epsilon_{yy}} \tag{19}$$

OPIT I—Inverse Model I

The maximum number of coefficients is M_1 to be retrieved through the linear matrix operation described in (19); in OPIT I, $M_1 = I_{inp}$. For example, $I_{inp} = 6$, the coefficient vector is thus described as:

$$\boldsymbol{P}_I = [\mathrm{P}_{\mathrm{I}_1}\ \mathrm{P}_{\mathrm{I}_2}\mathrm{P}_{\mathrm{I}_3}\ \mathrm{P}_{\mathrm{I}_4}\ \mathrm{P}_{\mathrm{I}_5}\ \mathrm{P}_{\mathrm{I}_6}]' \tag{20}$$

The total HLSG measurements are taken from ribs #1 to rib #5 plus rib #7; the six linear strain input elements are defined in the strain vector:

$$\boldsymbol{\epsilon_{yy}} = [\varepsilon_{yy_1}\varepsilon_{yy_2}\varepsilon_{yy_3}\varepsilon_{yy_4}\varepsilon_{yy_5}\varepsilon_{yy_6}]' \tag{21}$$

The strain values can be calculated from Eq. (11) via both OPT methods. In the case of the horizontal linear strain gages: $y_0 = \frac{b}{2}$; x_g are the coordinates of the horizontal linear strain gages, here $g = 1..I_{inp}$. It is found:

$$\varepsilon_{yy}(x_g, y_0) = \varepsilon_{yy_g} = z_0(\frac{2\pi}{b})^2 \sum_{m=1}^{6}\sum_{n=1}^{N} \sin(\frac{m\pi x_g}{a})\cos(\frac{2n\pi y_0}{b})W_{mn} \tag{22}$$

The elements for the n^{th} strain-displacement matrix $\boldsymbol{S_n}$ are:

$$S(g,m)_n = z_0\left(\frac{2\pi}{b}\right)^2 \cdot \sin(\frac{m\pi x(g)}{a}) \cdot \cos(\frac{2n\pi y_0}{b}) \tag{23}$$

It is observed that N=33 will sufficiently allow for the convergence of uniform pressure along the y direction, thus, $N = 33$ is used in the following derivations and sample calculations. The elements in the diagonal displacement-pressure coefficient matrix $\boldsymbol{A_{I_n}}$ can be derived from Eq. (10) as follows:

$$A_I(m,m)_n = \sum_{j=1,3..}^{N} \frac{4ab[\frac{1}{j} - \frac{1}{2(j+2n)} - \frac{1}{2(j-2n)}]}{j\pi^2[\frac{3bm^4\pi^4}{4a^3}D_x - \frac{2m^2n^2\pi^4}{ab}D_{xy} + \frac{4an^4\pi^4}{b^3}D_y + \frac{4m^2n^2\pi^4}{ab}D_s]} \tag{24}$$

where, $j = 1,3,..,33$. Let the strain-pressure coefficients relation matrix $\boldsymbol{C_1}$ for OPIT I be defined by,

$$\boldsymbol{C_I} = \sum_{n=1}^{n=N} \boldsymbol{S}_n \boldsymbol{A}_{I_n} \tag{25}$$

The strain-pressure relationship is then established as,

$$\boldsymbol{\epsilon_{yy}} = \boldsymbol{C}_I \boldsymbol{P}_I \tag{26}$$

Inversely,

$$\boldsymbol{P}_I = \boldsymbol{C}_I^{-1} \boldsymbol{\epsilon_{yy}} \tag{27}$$

The matrix $\boldsymbol{C}_I^{-1}$ is a well-posed full-matrix with the condition number roughly equals 8.0 to calculate the pressure coefficient terms over the whole plate.

OPIT II—Inverse Model II

Still using I_{inp}strain inputs from the HLSG locations, the pressure Fourier coefficients are extracted over the constrained ice covered area. Similarly, M_2 is the maximum number of the pressure coefficient terms that can be calculated through the linear matrix operation by OPIT II, and $M_2 = I_{inp}$ in this initial evaluation of OPIT II. The pressure-displacement matrix $\boldsymbol{A}_{II_n}$ for OPIT II will be expressed in linear matrix form from the Eq. (14). Firstly, let:

$$e_{II}(m,i)_n = \frac{a^2 i t_{ice}}{\pi(a^2 i^2 - m^2 t_{ice}^2)}\left[(-1)^{i+1}\sin\left(\frac{m\pi(x_1+t_{ice})}{a}\right) + \sin\left(\frac{m\pi x_1}{a}\right)\right], \text{if } ai \neq mt_{ice}$$

$$e_{II}(m,i)_n = \frac{1}{2k\pi}\left[\cos(k\pi x_1)\,k\pi t - \frac{1}{2}\cos(k\pi x_1)\sin(2k\pi t_{ice}) + \sin(k\pi x_1)\sin^2(k\pi t_{ice})\right], \text{if } ai = mt_{ice} \tag{28}$$

where $i = 1 ... M_2$. Then using Eq. (16), the (m,i) element in matrix $\boldsymbol{A}_{II_n}$ is:

$$A_{II}(m,i)_n = \sum_{j=1,3..}^{33} \frac{b}{2j}[\frac{1}{j} - \frac{1}{2(j+2n)} - \frac{1}{2(j-2n)}] \frac{e_{II}(m,i)_n}{(\frac{3bm^4\pi^4}{4a^3}D_x - \frac{2m^2n^2\pi^4}{ab}D_{xy} + \frac{4an^4\pi^4}{b^3}D_y + \frac{4m^2n^2\pi^4}{ab}D_s)} \tag{29}$$

where $m = 1,..,M_2$.

The strain-displacement coefficient matrix $\boldsymbol{S_n}$ is independent of the form of pressure applied, and it is the same as in Eq. (23) for OPIT I. The inverse of the coefficient matrix $\boldsymbol{C_{II}}$ relating the strain vector to the pressure terms is calculated as the summation of the products of $\boldsymbol{S_n}$ and $\boldsymbol{A}_{II_n}$

$$\boldsymbol{C_{II}} = \sum_{n=1}^{n=N} \boldsymbol{S}_n \boldsymbol{A}_{II_n} \tag{30}$$

Similarly the strain-pressure relationship is then established as,

$$\boldsymbol{\epsilon_{yy}} = \boldsymbol{C}_{II} \boldsymbol{P}_{II} \tag{31}$$

Inversely,

$$\boldsymbol{P}_{II} = \boldsymbol{C}_{II}^{-1} \boldsymbol{\epsilon_{yy}} \tag{32}$$

TSVE Optimization—for OPIT II

The coefficient matrix $\boldsymbol{C}_{II}$ may be ill-posed when the order of the coefficient matrix M_2 increases to a certain degree, depending on the confinement of the ice-covered area for the pressure terms. The condition number of the forward coefficient matrix C_{II} is found to be over 10^3 for both LC#2 and for LC#3, when $M_2 = I_{inp} = 6$. A direct inverse of the OPT II model for LC#2 and LC#3 leads to variations in pressures which are out of the feasible range (Fig. 9a and 9b).

The reason is that the non-orthogonal Fourier coefficient matrix for OPT II is coupled and ill-posed, and this near singularity will intensify with the increment of the orders of the coefficients. The truncated singular value expansion method (TSVE) is first applied as an optimization procedure to truncate the order of the coefficient matrix to M_{trun}, and re-expand the truncated matrix through the pseudo inverse matrix operation (Hansen and O'Leary 1993; Chock and Kapania 2003). The philosophy of the optimization procedure is to truncate the terms of zero or near-zero singular values to control the condition number of the coefficient matrix (Hansen 1987; Semnani 2008; Semnani 2010). The optimal number of the pressure terms M_{trun} is determined through the TSVE procedure by applying a "low-pass" filter to filter out the values of the singular values $s_i(i = 1,2..M_2)$ that are smaller than e, where e is a prescribed lower limit subject to optimization according to different loading case. The TSVE optimization scheme is sketched in Fig. 10.

As a rule of thumb, the order k_c of the condition number indicates the level of accuracy caused by a loss of precision from the arithmetic method (Kaiman 1996). The minimum filtering value e for the "low-pass" filter is defined as $1/10^{\kappa_c}$. Chock and Kapania (2003) reported that the error by using only the singular value decomposition methods (SVD) in the steepest descents is however of similar order as that from the input noise level. A difference of 5% to 15% to those exact strains obtained from the FE model is found in the OPT II forward strain prediction at convergence. Thus by constraining e within the range of 10^{-6} to10^{-7}, the optimization process suffices to retain the robustness of the inversion of the matrix calculation to an error range of less than 15%. Finally, by re-expanding the coefficient matrix at the truncated order M_{trun}, the coefficient matrix is of dimension of M_{trun} by I_{inp} , as shown in Fig. 10. For simplicity, the OPIT II model refers to the inverse calculation of OPT II after the TSVE process in the following discussion.

Sample Inverse Calculations

In an effort to evaluate the pressure solution from strain measurements, six linear strain readings at the HLSG from the FE model serve as inputs to the OPIT I and OPIT II models. Three loading conditions are evaluated, and the results of the calculated pressure by both OPIT methods are compared to the exact pressure prescribed in the FE model, depicted as the plane layers in Fig. 11.

As discussed in the forward strain evaluations, the pressure solution by OPIT II under LC #1 is of exactly the same value as obtained by OPIT I (Fig. 11a). For LC#2, the peak pressure is calculated as 1.29 MPa with $M_{trun} = 2$ coefficient terms by OPIT II, while the peak value is evaluated as 0.41 MPa by OPIT I for LC#2. The amplitude is 1.57 MPa for LC#2 in the FE model (Fig. 11b).

For all load cases, the peak values and the integrated pressure over the ice-covered area calculated by the OPIT algorithms are compared with the FE model pressure values given in the FE model, and the results are listed in Table 2. For LC#3, integrating pressure over the ice-thickness, both algorithms achieve 80% of the FE result (Fig. 11c). The reduction of the integrated force is due to the Fourier approximation. The OPIT I extracts 6 coefficient terms while the OPIT II is truncated to 3 terms. From the results, it is observed that the OPIT I is stable in estimating ice pressure distribution with great accuracy for most loading cases, especially when the ice-covered area spans over one-half of the plate. The OPIT I is able to achieve an improved accuracy by increasing the coefficient terms with additional strain recordings. On the other hand, the peak value solution found by OPIT II for LC#2 is accurate to within 80%, retaining only two coefficient terms. The capability of capturing peak pressure by OPIT II is notably efficient and accurate when the ice-covered area is reduced.

LABORATORY CALIBRATION

Mechanical testing of the IFMS plate was undertaken for calibration and data acquisition verification prior to field deployment. The IFMS plate load test (without the back plate) was performed at the Civil and Environmental Engineering (CEE) Structural Engineering Laboratory at University of Michigan. The 14-inch diameter loading cylinder with a 14-inch square steel plate attached to the bottom of the cylinder was used (Fig. 12a). The IFMS face plate was loaded gradually from zero to 20 Kips in the first round. In the second round, the plate was reloaded at 5 Kip or 10 Kip per step until a maximum of 50 Kips. Considering the stiffness of the loading cylinder and the attached square plate, the contact area between the loading panel and the back of the IFMS plate is reasonably assumed as the circumferential line of the cylinder as shown the respective FE analysis (Fig. 12b). The displacements are prescribed in the FE model at the "line-shaped" contact area.

The resistance variation δR measured in the CEE lab tests is converted to linear strain values $\epsilon_{linear} = 0.0014\delta R\ ohms^{-1}$. Results from comparisons of two horizontal linear strain values on rib #3 and rib #4 from the FEA model are shown in Fig. 13a. It is observed the prescribed circular displacement from the finite element analysis gives satisfactory correlation for the total force. Additionally, the other linear strain recordings from the lab are compared with the FEA analysis shown in Fig. 13b. Taking into account that the FEA model calculated strains are very sensitive to the location of the loading area, it can be observed that both the linear horizontal strain gages and the linear vertical strain gages compare reasonably to the strains obtained from the loading tests conducted in the CEE lab. These results provided support for the conclusion that the linear strain gauges were behaving healthily.

The IFMS was then transported to Universal Metals of Calumet, MI, for welding and field instrumentation of the IFMS. Also at Universal Metals, the vertical frame for the IFMS support structure was manufactured and attached to the ice force measuring plate in October, 2013. A second test was performed at Michigan Technological University to check the performance of the system before the installation of the IFMS at the lighthouse.

FIELD MEASUREMENTS

The presented algorithms are applied using the field measured strains by the IFMS system on three specific days: Mar 18th, Apr 17th and May 01st, 2014. Photos showing the ice features have been recorded by a camera installed above the measuring stiffened panel. The ice accumulation reaching over the top of the plate is observed on Mar 18th; an event of accumulated ice pushing against the plate on April 17th (Fig. 14a), during which east winds were recorded by NOAA (9099018 Marquette C.G, MI). Additionally, correlated data of ice thickness are measured from the Wideband Autocorrelation Radiometer ice thickness sensor (WiBAR) and Acoustic Wave and Current Profiler (AWAC) below the ice surface from the lake bottom (Nejati, 2014). The recorded ice thickness from February to May is plotted in Fig. 14b. These measurements are used as inputs into the OPIT II algorithm for depth of ice coverage. Three linear horizontal gages were measured at 5 Hz on Mar 18th; also, six horizontal strain gages (HLSG) were recorded at 1 Hz on Apr 17th. The maximum strain variations recorded through the winter were observed on May 01st at 5 Hz in stormy weather with ice breaking-up. The pressures are calculated by both OPIT I and OPIT II from strain measurements on March 18th and April 17th, with the estimated ice thickness measurement applied as constraint for the OPIT II scheme. Ice thickness data were not available for the May 1st events.

The strain gage readings are examined for March 18th at 5 Hz, April 17th at 1 Hz and May 01st at 5 Hz as the input for the inverse pressure calculation algorithms. The strain variations are measured at the HLSG and are subtracted from the unloaded zero strain gage R_0. The recorded strain values and the retrieved forcing are given in Fig. 15 to Fig. 17. The pressure calculated by SBT are in good agreement with the results obtained by OPIT I, justifying an averaging effect of OPIT I by assuming pressure terms over the entire plate (Table 3).

Strain gage readings on rib #1, rib #3, and rib #5 are recorded as input for pressure extraction on March 18th at a sampling frequency of 5 Hz (Fig. 15a). Peak ice pressure is calculated as 0.84 MPa or 1.04 MPa through OPIT I; the OPIT II estimates the peak pressure to be 0.90 MPa with the constraint of ice thickness to be 0.6 m covering from the top of the plate (Fig. 15b). Six strain gages are recorded on April 17th; it is observed that the OPIT II estimates the peak ice contact pressure to be 1.35 MPa over the ice-covered area, which is slightly larger than the peak values calculated from OPIT I (Fig. 16).

Four strain gages on rib#1, rib#3, rib#5, and rib#7 showed the maximum strain variation through the winter season on May 01. Maximum ice contact pressure is calculated to be 3.5 MPa using the OPIT I algorithm with the given strain inputs shown in Fig. 17a and 17b; the calculated pressure is plotted in Fig. 17c. Note that the preliminary assessments of peak ice pressures are consistent with previous findings summarized by Bjerkas (2007) (Fig. 18). Additionally our peak measurements compare closely with this curve developed for prediction of extreme pressures for sea ice impacts as shown in Fig. 19 (Tõns et al., 2015), which of particular interest is the lower curve for first year ice. This correlation further indicates the effectiveness of the present approach to estimate the ice forcing distribution and local extreme pressure with limited strain measurements.

CONCLUSIONS

Inverse algorithms are formulated through forward analytical models to calculate the quasi-static pressure distribution on a stiffened plate. The stiffened panel is first modeled by strip beam theory (SBT) to estimate the uniform ice-loading over the entire plate and to extract the contact ice-load between two stiffeners. In order to reflect the variability of the ice-forcing, the plate is formulated as a structurally equivalent orthotropic plate to simulate the variable ice loading distribution along the depth of the plate (OPT I and OPT II).

In the forward formulations, the horizontal SBT and the OPT I are used when the stiffened panel is known to be fully covered by ice. While the horizontal SBT is limited to the form of uniform pressure; it is fast and stable under full ice-coverage. The OPT I is applicable for strain evaluation regardless of ice-covered area; moreover, the OPT I approximates closely to the exact strain solution at convergence. The vertical SBT and the OPT II set up the relationships between the ice-pressure distributions over a small portion of the plate to the structural strain-responses. The vertical SBT calculates accurately the wavy deformation between the ribs, an effect which is not captured if using the orthotropic plate formulation. Nevertheless, the OPT II is notable for its faster convergence, especially when the ice-covered area is comparatively thin.

The inverse counterparts derived from the forward formulations compare well with the sophisticated finite element analysis with respect to different assumptions in the form of ice loads. In the second orthotropic method, the inverse coefficient matrix of the OPT II is truncated through a "low pass filter" by a minimum value e via the TSVE optimization procedure, thus the stability of the matrix operation is retained. Three sample calculations using the FE input strains identify the stability and accuracy of the OPIT I method in predicting pressure distribution over the entire plate. The effectiveness of the OPIT II is observed in extracting the peak ice-pressure by retaining fewer pressure coefficient terms, especially for reduced span of ice-covered area.

In general, the inverse of the horizontal SBT is beneficial as an initial estimation of the averaged ice forcing when the number of structural inputs is extremely limited; the inverse of the vertical SBT provides a close estimation for contact ice-forcing between the ribs given the availability of vertical strain measurements. The OPIT I is always recommended for its accuracy to extract the variable ice-forcing when several strain measurements are available and the ice-thickness measurement is not available. Additionally, the number of coefficient terms obtained for convergence from the OPT I of 6 to 9 indicates the optimal number of strain deployments for this system. The OPIT II is notably efficient in approximating the amplitude of contact ice forcing, if the ice-thickness measurement for the span of the ice-contact area is available. Finally, the combination of both OPIT I and OPIT II is encouraged: first to get an evaluation of the distribution of the ice forcing over the entire plate, then to obtain more acute contact ice force amplitudes if the ice-thickness measurements are available.

The variable loading caused by the coupled effect of ice, wind and thermal forcing has been retrieved using the strain measurements recorded by the IFMS instrumentation through the winter season 2013-2014. Maximum pressure forcing of 3.54 MPa is observed on May 01 by OPIT II calculation, while a peak average pressure about 0.90 MPa to 1.30 MPa were found based on the strain measurements on April 17 and March 18, 2014.

ACKNOWLEDGEMENTS

The work described in this paper was supported by the Department of Energy of United States (DE-EF005376). An award for the first author from the Link Ocean Engineering and Instrumentation Ph.D. Fellowship Program is gratefully acknowledged. Also, the contribution of Dr. David R. Lyzenga in providing the figure of ice-thickness, Prof. Jason P. McCormick for his assistance and use of the laboratory facilities, and Nitin Garg for his contribution to the IFMS plate design are gratefully acknowledged. Assistance from personnel from the Great Lakes Research Center is also greatly appreciated: Dr. Guy Meadow, Michael Abbot, Jamey Anderson and Colin Tyrrell. Further assistance from DoE project principal investigator, Prof. Anthony England, David Boprie, Dr. Roger De Roo, and Dr. Lin Van Nieuwstadt is gratefully acknowledged.

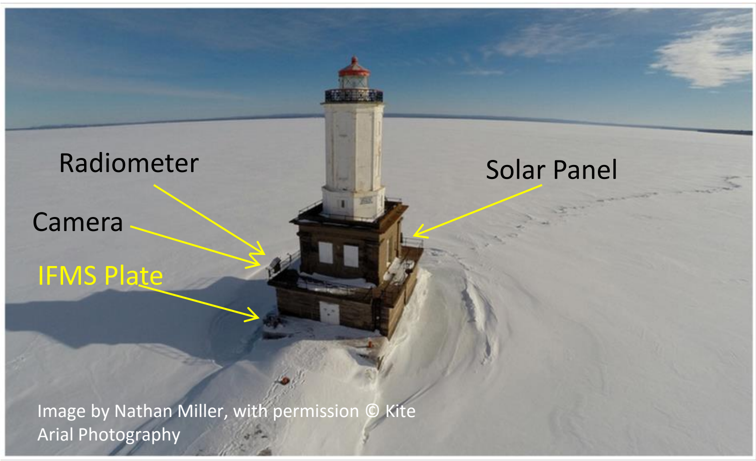

(a)

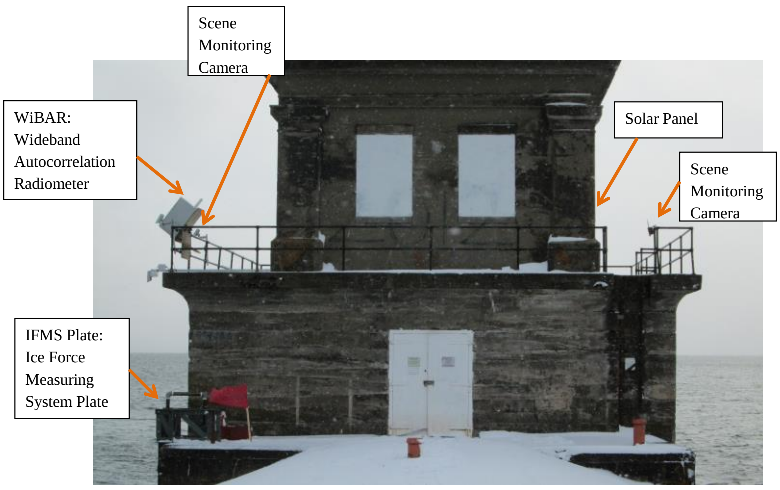

(b)

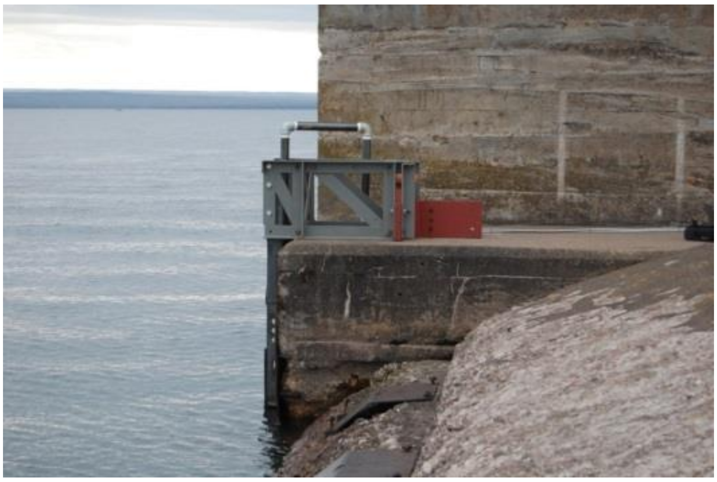

(c)

Fig. 1. (a) South Portage Entry Lighthouse and deployment IFMS; (b) view of the Lighthouse looking south for the deployment of the instrumentation; (c) side view of the framing for the IFMS plate after installation

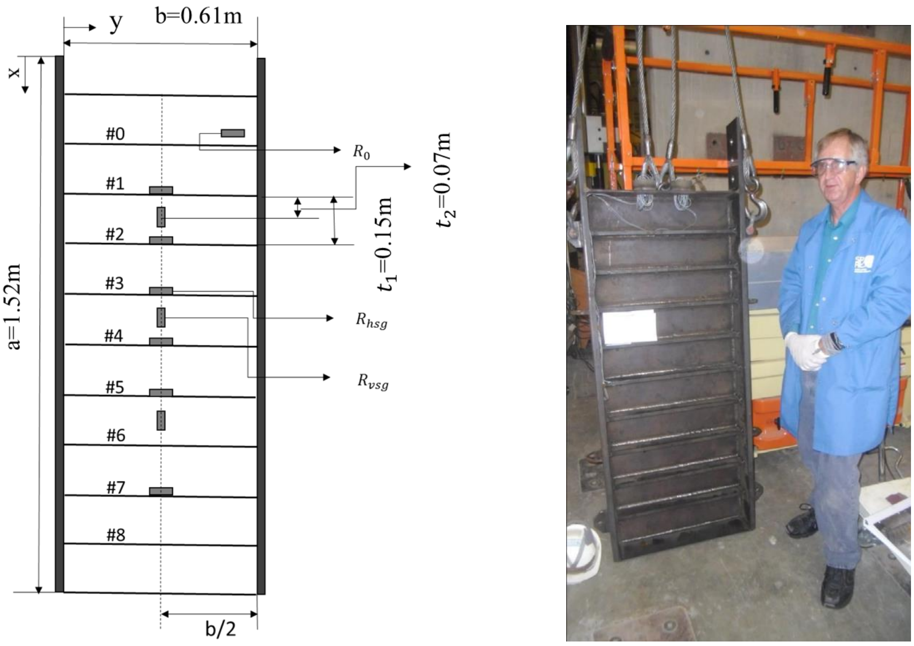

(a) (b)

Fig. 2. (a) Dimensions of the IFMS plate, arrangement of linear strain gages; (b) photo of IFMS plate during strain gage installation

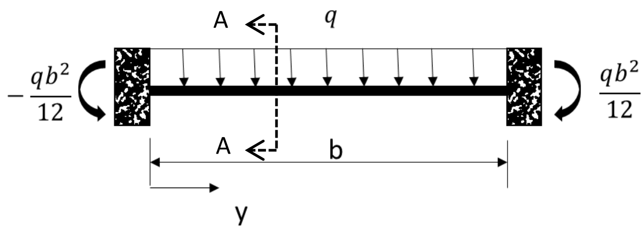

(a)

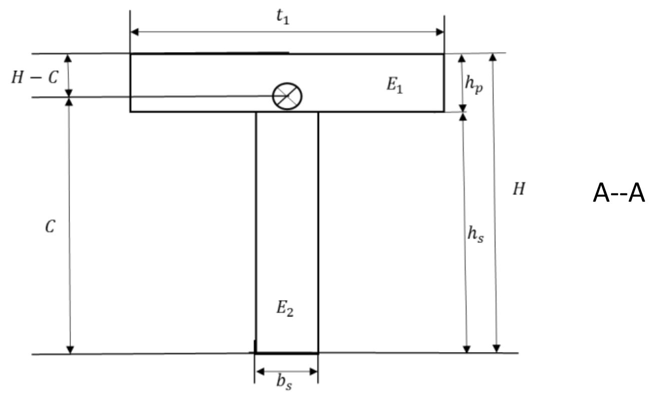

(b)

Fig. 3. (a) Euler-Bernoulli beam described for horizontal strip beam, (b) the T-shaped cross section of the horizontal SBT

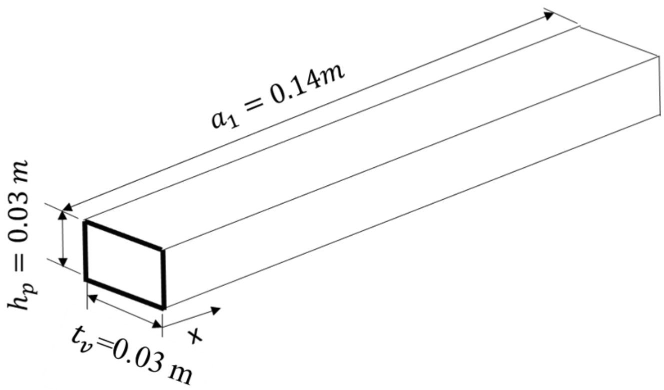

Fig. 4. Dimensions of the vertical strip beam between two ribs

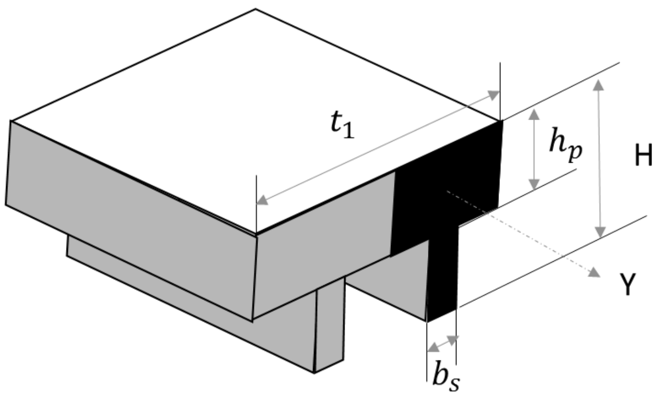

Fig. 5. T-shaped cross sections of the representative OPT I model

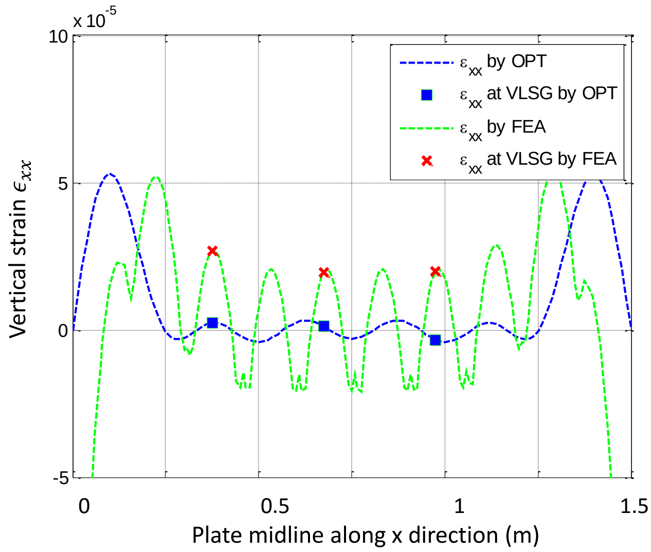

Fig. 6. Vertical linear strains ϵ_{xx} calculated by OPT I compared to FEA results, under LC#1

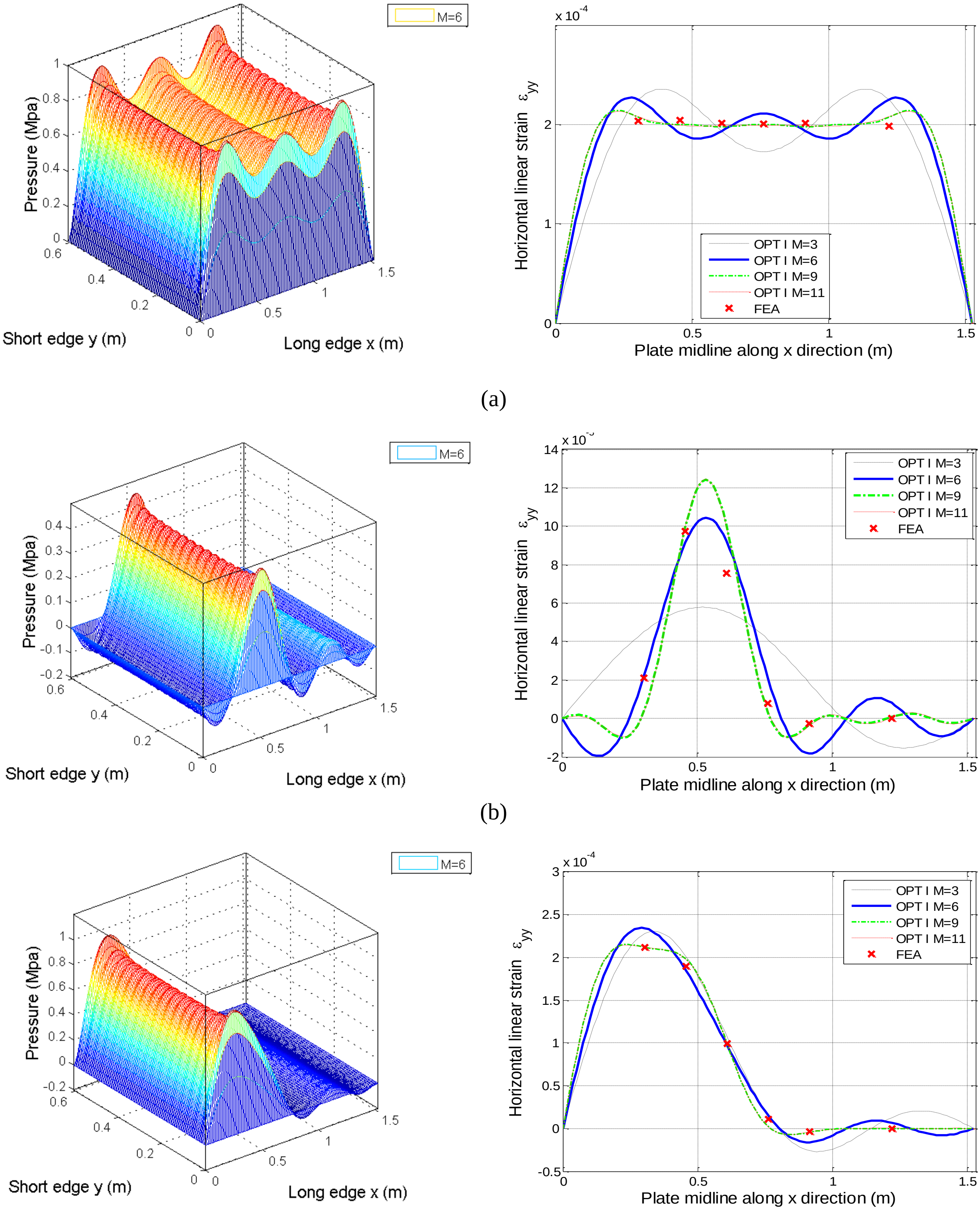

Fig. 7. Pressure predicted by OPT I and the Convergence of ϵ_yy by OPT I at different orders of M for (a) LC#1, (b) LC#2, (c) LC#3

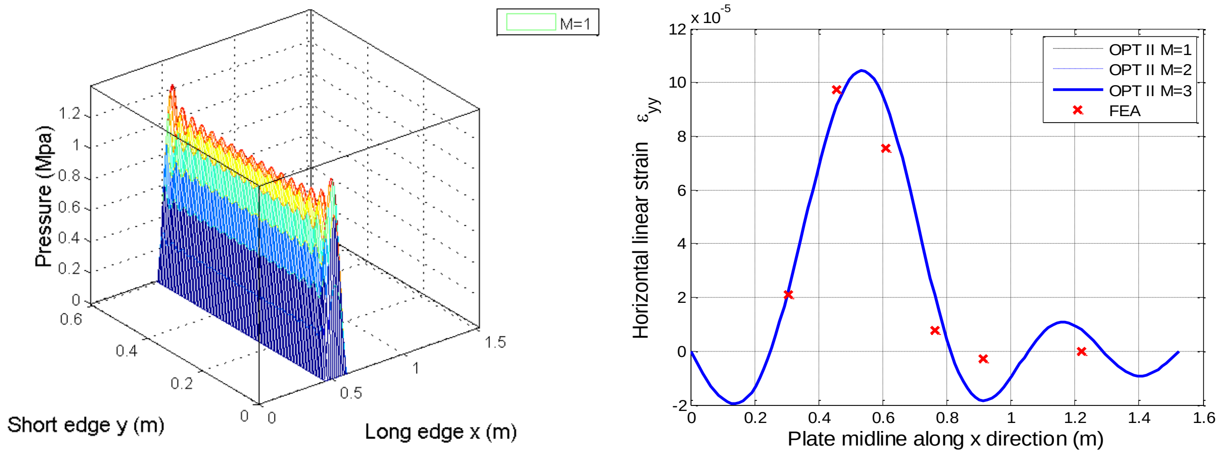

(a)

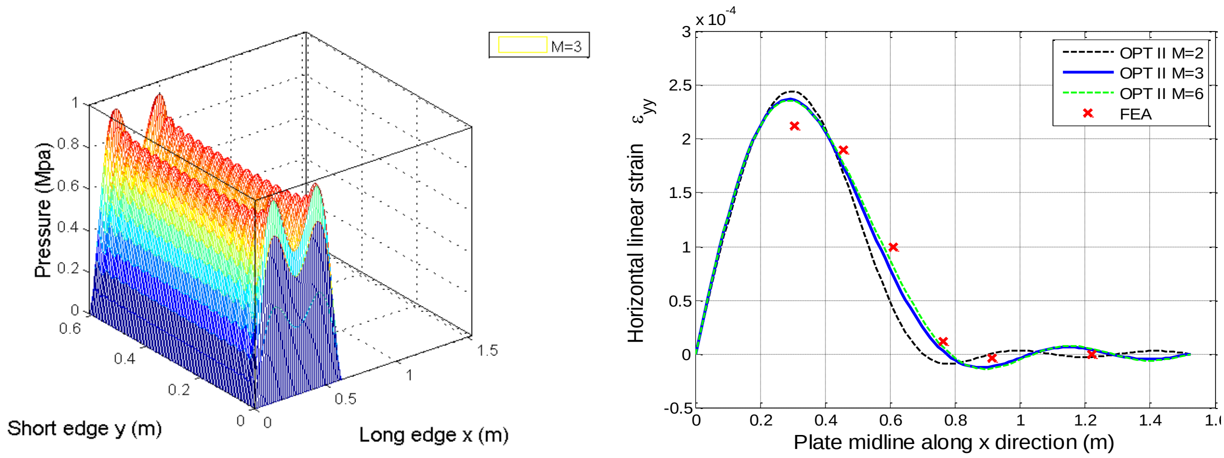

(b)

Fig. 8. Pressure predicted by OPT II and the calculated strains for (a) LC# 2 $M = 1$, (b) LC#3 $M = 3$

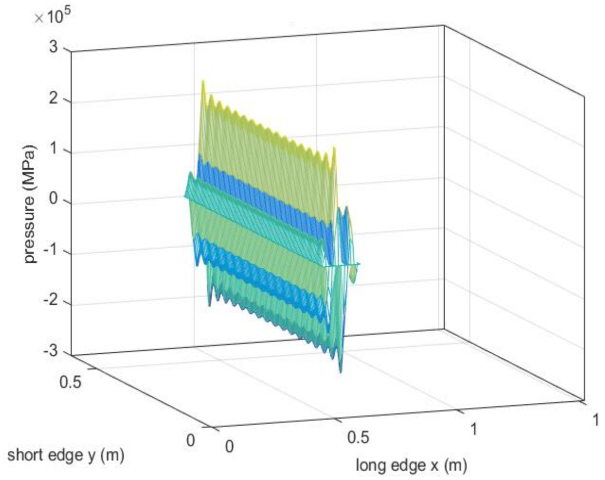

(a)

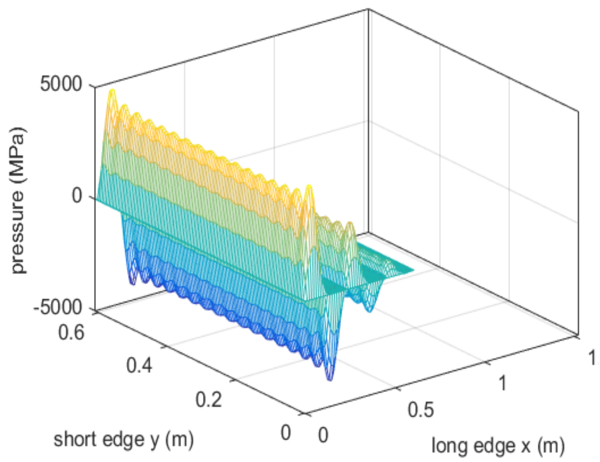

(b)

Fig. 9. Infeasible pressure solution by a direct inverse of OPT II without truncation for (a) LC#2, (b) LC#3

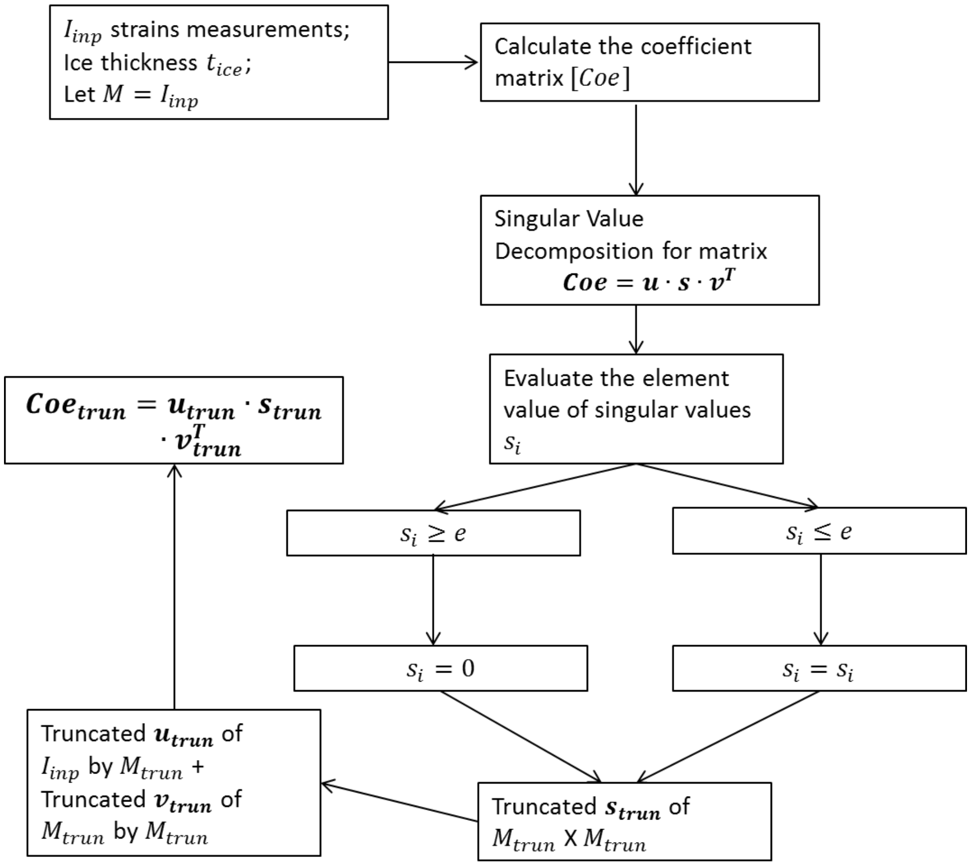

Fig. 10. Schematic diagram of the TSVE procedure for calculating of M_{trun} and $\boldsymbol{Coe_{trun}}$

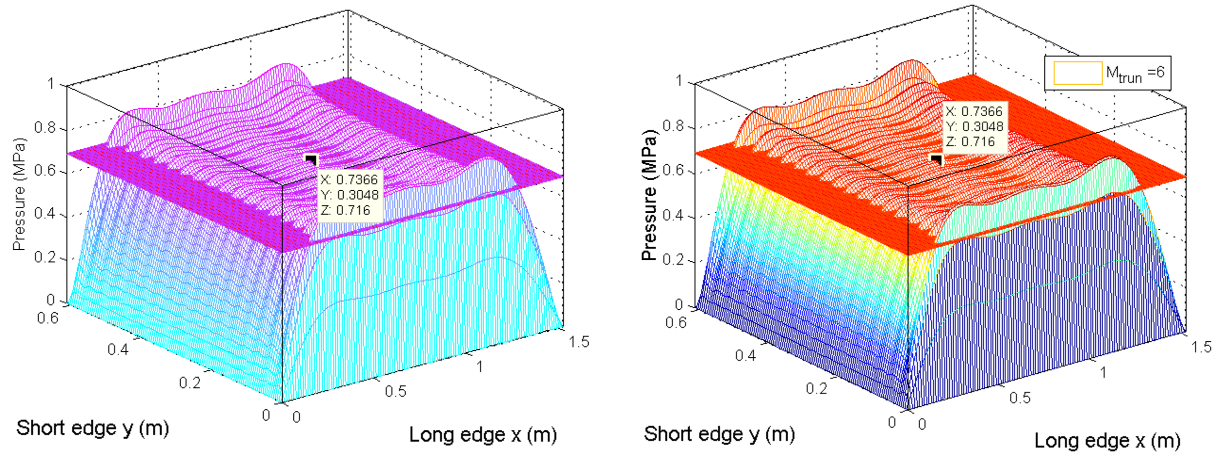

(a)

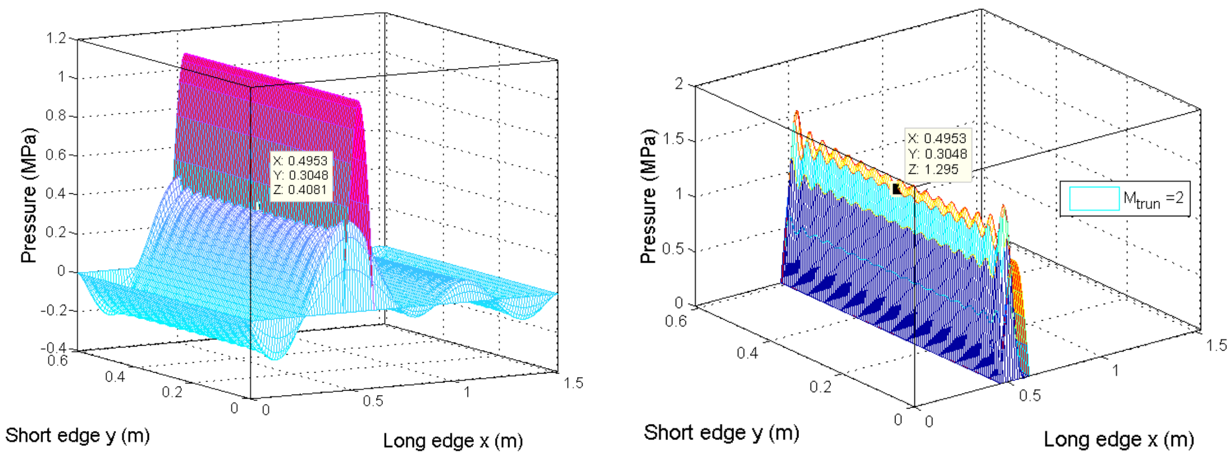

(b)

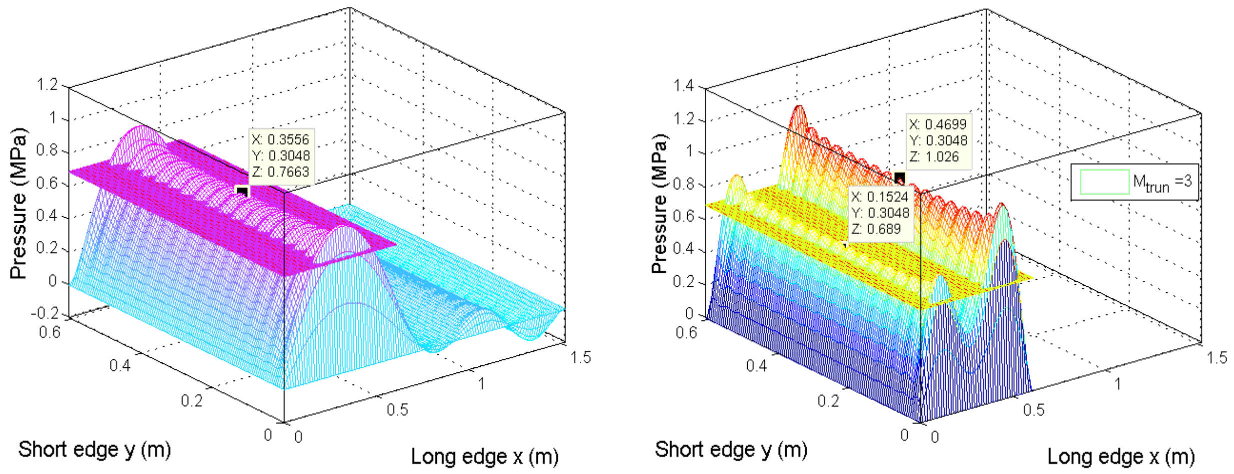

(c)

Fig. 11. Pressure extracted by OPIT I (left) and OPIT II (tright) for (a) LC#1, (b) LC#2, (c) LC#3

(a)

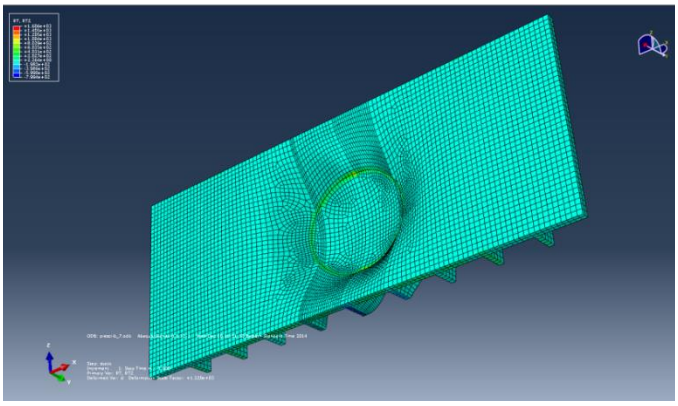

(b)

Fig. 12. (a) Test device for laboratory calibration, (b) the FEA model of the loaded IFMS plate subjected to prescribed ring loading

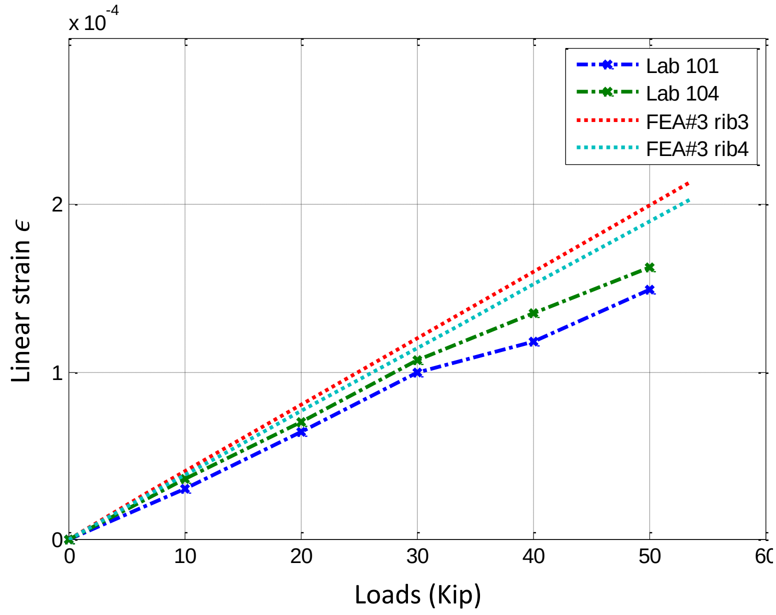

(a)

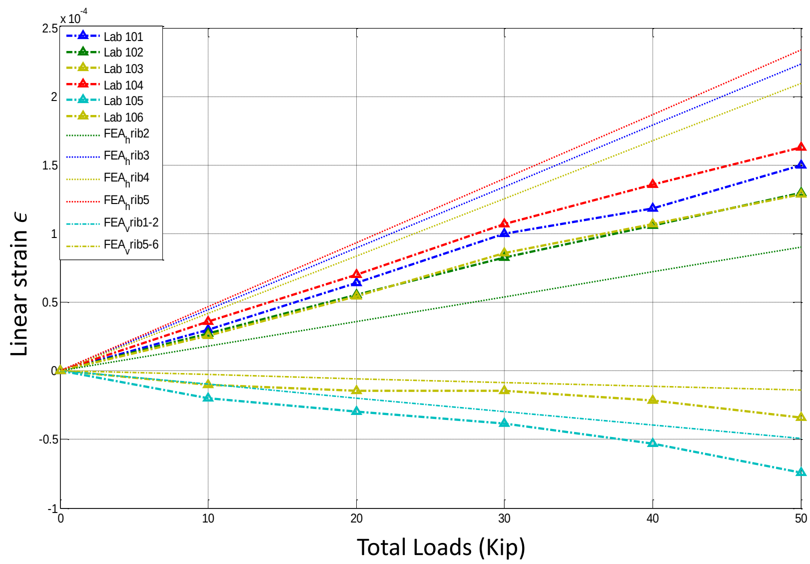

(b)

Fig. 13. (a) Linear strain ϵ_{linear} variation from the lab results compared to the strain on rib 3 and 4 from the FEA model; (b) strains converted from the laboratory test compared to strain obtained from FEA model with prescribed circular displacement

(a)

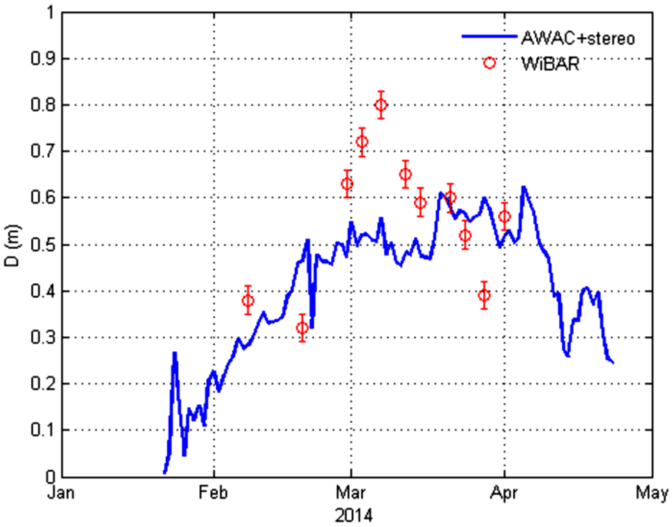

(b)

Fig. 14. (a) Photo on March 18, 2014 (left), April 17, 2014 (right); (b) ice-thickness measurements from Jan to May 2014 (adapted from Nejati, H, 2014)

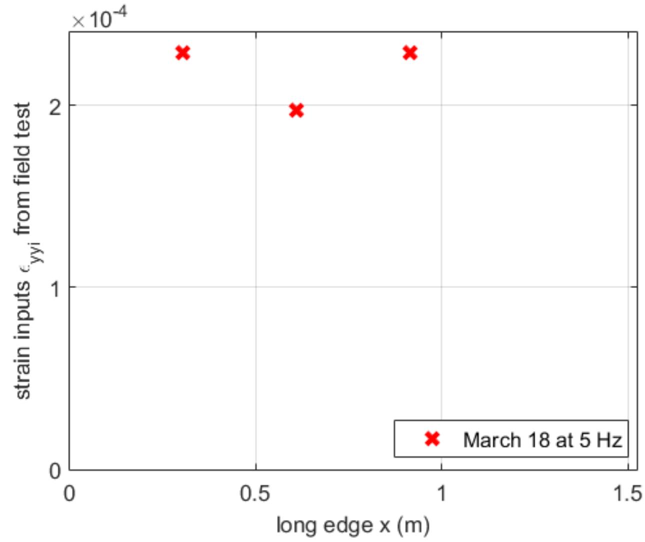

(a)

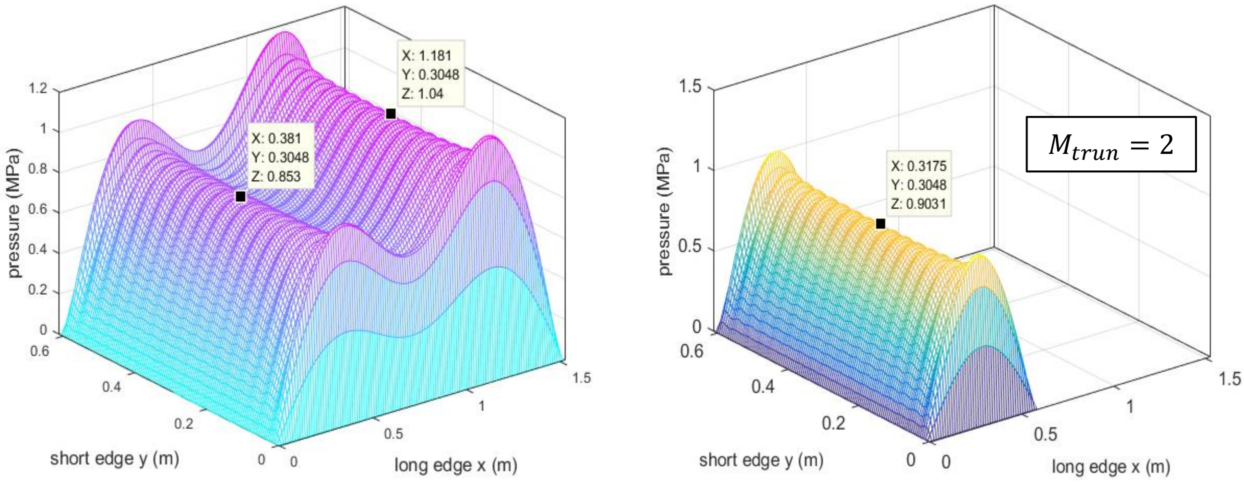

(b)

Fig. 15. (a) Three strain inputs from March 18, 2014; (b) pressure solution by OPIT I (left) and OPIT II (right)

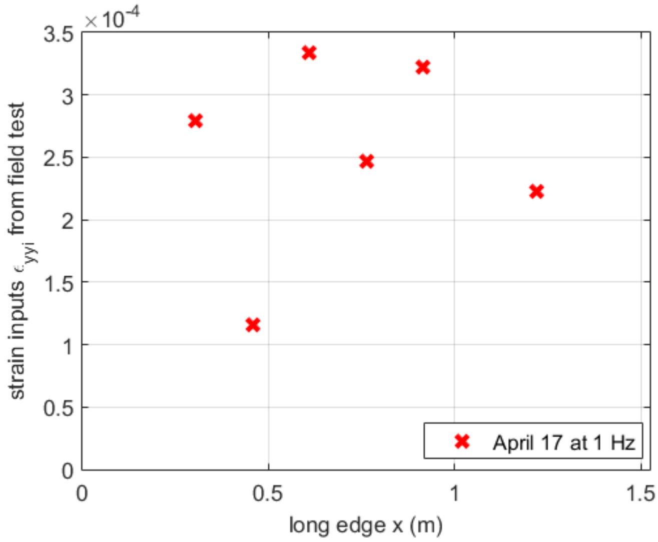

$\times 10^{-4}$
3.5
3
2.5
2
1.5
1
0.5
0
strain inputs ϵ_{yyi} from field test
April 17 at 1 Hz
0
0.5
1
1.5
long edge x (m)

(a)

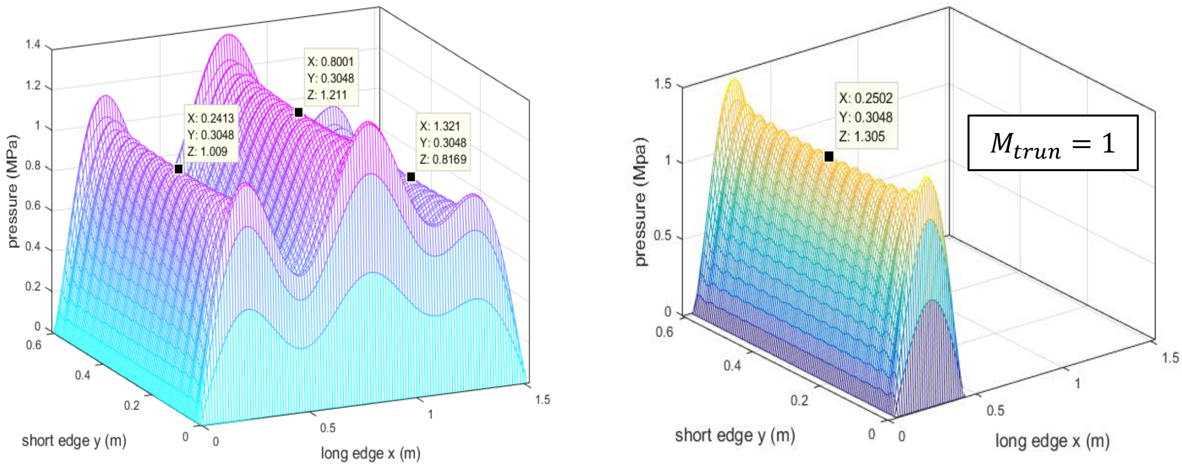

(b)

Fig. 16. (a) Six strain inputs from April 17, 2014; (b) pressure solution by the OPIT I (left) and OPIT II (right)

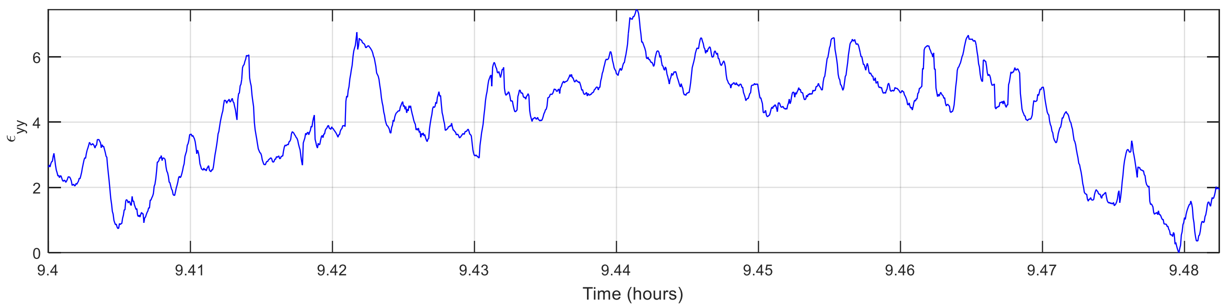

(a)

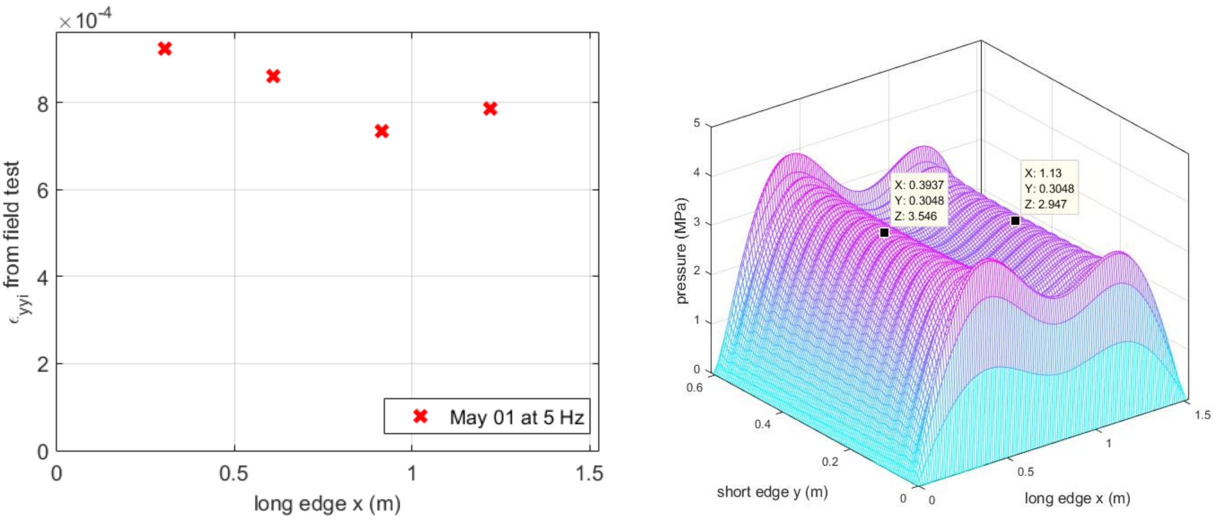

(b) (c)

Fig. 17. (a) Strain measurments on rib #5 on May 01st , (b) three input strains, (c) pressure solution by OPIT I

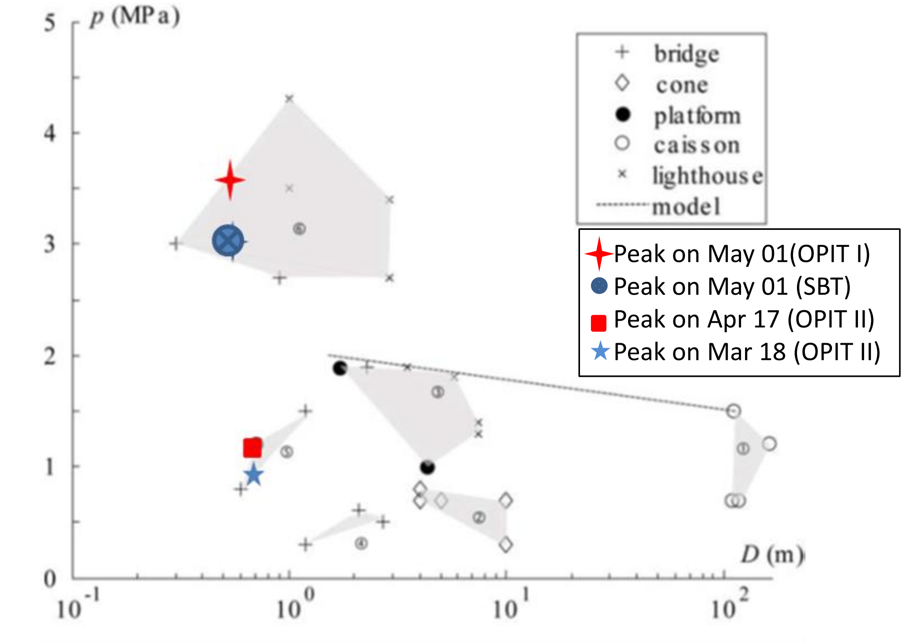

Fig. 18. Effective ice pressure vs. the structural width (adapted from Bjerkas, 2007)

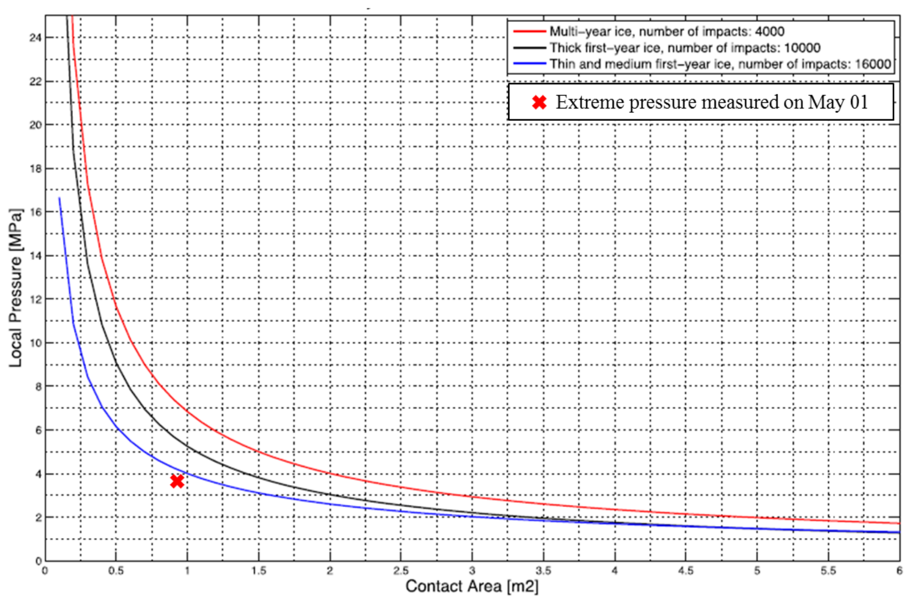

Fig. 19. Predicted extreme load pressure for the specific route and comparison to the extreme load pressure measured by IFMS on May 01 (adapted from Tõns et al., 2015b)

Table 1. Analytical strain evaluations compared to FE results (under LC#1)

Strain	SBT	OPT I at M=6	FE
$\epsilon_{yy} = \begin{pmatrix}\textbf{Rib \#1}\\ \textbf{Rib \#2}\\ \textbf{Rib \#3}\\ \textbf{Rib \#4}\\ \textbf{Rib \#5}\\ \textbf{Rib \#7}\end{pmatrix}$	1.95×10^{-4}	$\begin{pmatrix}2.10\\ 1.96\\ 2.03\\ 1.95\\ 2.03\\ 2.10\end{pmatrix} \times 10^{-4}$	$\begin{pmatrix}2.04\\ 2.04\\ 2.01\\ 2.00\\ 2.02\\ 1.98\end{pmatrix} \times 10^{-4}$
$\epsilon_{xx} = \begin{pmatrix}\mathbf{x = 0.38\ m}\\ \mathbf{x = 0.69\ m}\\ \mathbf{x = 0.99\ m}\end{pmatrix}$	2.26×10^{-5} (Fixed ends) 6.79×10^{-5} (Pinned ends)	-	- $\begin{pmatrix}2.40\\ 2.12\\ 2.11\end{pmatrix} \times 10^{-5}$

Note: SBT=Strip Beam Theory; OPT=Orthotropic Plate Theory; FE=Finite Element.

Table 2. Peak pressure value and integrated pressure over the ice covered area

Analysis Result	**Peak Pressure Value (MPa)**			**Integrated Pressure along depth of ice coverage (KN/m)**		
Load Condition	**Exact Loading**	**Solution by OPIT I**	**Solution by OPIT II**	**Exact Loading**	**Solution by OPIT I**	**Solution by OPIT II**
LC#1	0.69	0.72	0.72	1050.0	912.3	912.3
LC#2	1.08	0.41	1.30	105.0	55.8	95.7
LC#3	0.69	0.77	1.03	414.0	332.0	333.0

Table 3. Calculated peak pressure for field measurements by the SBT and the OPIT methods

Analysis Result		**Peak Pressure Value (MPa)**		
Measurement date	Ice thickness (m)	solution by SBT	solution by OPIT I	Solution by OPIT II
Mar 18 2014	0.6	0.81	0.85 and 1.04	0.90
Apr 17 2014	0.4	1.18	1.01, 1.21 and 0.82	1.31
May 01 2014	--	3.27	3.55 and 2.95	--

REFERENCES

Andrews, H. C., & Patterson, C. L. (1976). Singular value decompositions and digital image processing. Acoustics, Speech and Signal Processing, IEEE Transactions on, 24(1), 26-53.

Andrieux, S., & Abda, A. B. (1996). Identification of planar cracks by complete overdetermined data: inversion formulae. Inverse problems, 12(5), 553.

Bjerkås, M., & Skiple, A. (2005, June). Occurrence of continuous and intermittent crushing during ice-structure interaction. In Proceedings of the 18th International Conference of Port and Ocean Engineering under Arctic Conditions (POAC), Potsdam, USA (Vol. 3).

Bjerkås, M. (2007). "Review of Measured Full Scale Ice Forces to Fixed Offshore Structures." In Proceedings of the 26th International Conference on Offshore Mechanics and Arctic Engineering, San Diego, California, USA. OMAE2007-29048.

Bonnet, M., & Constantinescu, A. (2005). "Inverse problems in elasticity." Inverse problems, 21(2), R1.

Boot, J. C., & Moore, D. B. (1988). "Stiffened plates subject to transverse loading." International journal of solids and structures, 24(1), 89-104.

Chock, J. and R. Kapania (2003). “Load Updating for Finite Element Models”. AIAA Journal 41 (9), 1667–1673.

Deb, A., and Booton, M. (1988). "Finite element models for stiffened plates under transverse loading." Computers & Structures, 28(3), 361-372.

Deb, A., Deb, M., & Booton, M. (1991). "Analysis of orthotropically modeled stiffened plates." International Journal of Solids and Structures, 27(5), 647-664.

Dempsey, J. P., Palmer, A. C., & Sodhi, D. S. (2001). High pressure zone formation during compressive ice failure. Engineering fracture mechanics, 68(17), 1961-1974.

Engl, H. W., & Kügler, P. (2005). "Nonlinear inverse problems: theoretical aspects and some industrial applications." In Multidisciplinary methods for analysis optimization and control of complex systems (pp. 3-47). Springer Berlin Heidelberg.

Ewing, R. E., Lin, T., & Lin, Y. (1999). A mixed least-squares method for an inverse problem of a nonlinear beam Eq.. Inverse Problems, 15(1), 19.

Frederking, R., & Schwarz, J. (1982). Model tests of ice forces on fixed and oscillating cones. Cold Regions Science and Technology, 6(1), 61-72.

Hansen, P. C. (1987). "The truncated svd as a method for regularization." BIT Numerical Mathematics, 27(4), 534-553.

Hansen, P. C., & O'Leary, D. P. (1993). "The use of the L-curve in the regularization of discrete ill-posed problems." SIAM Journal on Scientific Computing, 14(6), 1487-1503.

Jordaan, Ian, Chun Li, Thomas Mackey, Arash Nobahar, and Jonathon Bruce. "Design Ice Pressure-Area Relationships: Molikpaq Data." (2005).

Jordaan, I. J. (2001). Mechanics of ice–structure interaction. Engineering Fracture Mechanics, 68(17), 1923-1960.

Kaiman, D. (1996). "A singularly valuable decomposition." College Mathematics Journal, 27(1), 2-23.

Kalenchuk, S. V., & Kulesh, V. A. (2010). Ice strength of sea-going ship hulls: stages of development, problems, perspectives. Engineering School Bulletin Far Eastern Federal University, Electronic scientific journal, 3(5).

Kim, L. V., Kulesh, V. A., & Tsuprik, V. G. (2015, July). Methodology for Experimental Determination of Local Ice Pressures on Flexible Hull of Platforms and Ships. In The Twenty-fifth International Offshore and Polar Engineering Conference. International Society of Offshore and Polar Engineers.

Leira, B., Børsheim, L., Espeland, Ø., & Amdahl, J. (2009). Ice-load estimation for a ship hull based on continuous response monitoring. Proceedings of the Institution of Mechanical Engineers, Part M: Journal of Engineering for the Maritime Environment, 223(4), 529-540.

Li, J., & Kapania, R. K. (2007). “Load updating for nonlinear finite element models.” AIAA journal, 45(7), 1444-1458.

Ma, C. K., Chang, J. M., & Lin, D. C. (2003). "Input forces estimation of beam structures by an inverse method." Journal of soun d and vibration, 259(2), 387-407.

Nejati, H. (2014). Passive Remote Sensing of Lake Ice and Snow using Wideband Autocorrelation Radiometer (WiBAR) (Doctoral dissertation, The University of Michigan).

Palmer, A. C., Dempsey, J. P., and Masterson, D. M. (2009). "A revised ice pressure-area curve and a fracture mechanics explanation." Cold regions science and technology, 56(2), 73-76.

Palmer, A., & Croasdale, K. (2013). Arctic offshore engineering. Singapore: World Scientific.

Riska, K., Uto, S., & Tuhkuri, J. (2002). Pressure distribution and response of multiplate panels under ice loading. Cold Regions Science and Technology, 34(3), 209-225.

Sanderson, T. J. O. (1988). "Ice Mechanics. Risks to Offshore Structures." Graham and Trotman, London, 253 p.

Sanderson, T. J. O. (1991). "Statistical analysis of ice forces." In Ice-Structure Interaction (pp. 439-457). Springer Berlin Heidelberg.

Semnani, A., & Kamyab, M. (2008). Truncated cosine Fourier series expansion method for solving 2-D inverse scattering problems. Progress In Electromagnetics Research, 81, 73-97.

Semnani, A., & Kamyab, M. (2010). "Solving Inverse Scattering Problems Using Truncated Cosine Fourier Series Expansion Method." INTECH Open Access Publisher.

Shimpi, R. P., & Patel, H. G. (2006). "A two variable refined plate theory for orthotropic plate analysis." International Journal of Solids and Structures, 43(22), 6783-6799.

Snieder, R. (1998). "The role of nonli unearity in inverse problems." Inverse Problems, 14(3), 387.

Sodhi, D. S. (1991). "Ice-structure interaction during indentation tests." In Ice-structure interaction (pp. 619-640). Springer Berlin Heidelberg.

Starkey, J. M., & Merrill, G. L. (1989). "On the ill-conditioned nature of indirect force-measurement techniques." Journal of Modal Analysis, 4(3), 103-108

Timoshenko, S., & Woinowsky-Krieger, S. (1959). "Theory of plates and shells (Vol. 2). New York: McGraw-hill.

Tõns, T., Ralph, F., Ehlers, S., & Jordaan, I. J. (2015, May). Probabilistic Design Load Method for the Northern Sea Route. In ASME 2015 34th International Conference on Ocean, Offshore and Arctic Engineering. American Society of Mechanical Engineers.

Ventsel, E., & Krauthammer, T. (2001). "Thin plates and shells: theory: analysis, and applications." Chapter 7.2 in Orthotropic and Stiffened Plates, CRC press.

Wells, J., Jordaan, I., Derradji-Aouat, A., & Taylor, R. (2011). Small-scale laboratory experiments on the indentation failure of polycrystalline ice in compression: Main results and pressure distribution. Cold Regions Science and Technology, 65(3), 314-325.

APPENDIX 5.2

Submitted to:

23rd IAHR International Symposium on Ice
Ann Arbor, Michigan USA, May 31to June 3, 2016

Nonlinear Contact Dynamic Response Simulation of Matlock's Ice-structure Interaction Model using Fourier Analysis

Yuxi Zhang, Thomas C. Remmers, Bingbin Yu, Dale G. Karr
University of Michigan, Ann Arbor
2600 Draper Dr., MI 48105
yuxiz@umich.edu
thomas.c.remmers@gmail.com
ybingbin@umich.edu
dgkarr@umich.edu

Continuous brittle crushing occurs in the movement of an ice sheet against an offshore structure. Matlock's ice-structure interaction model is used to simulate the behavior of the ice crushing by modeling ice teeth indentation contacting a spring-mass-dashpot structure. The dynamic behavior of this ice-structure interaction system is studied using Fourier analysis to predict the response of specific periodicity. The system's equations of motion are established with the assumption of continuous ice indentation. This assumption allows immediate contact of the structure with the next tooth at the time of fracturing of a previous tooth. The time histories of deflections are expressed through the non-linear dynamic equations. The kinematic initial conditions can be predicted at targeted periodicity via the Fourier analysis. Furthermore, given a representative system, the amplitudes of the dynamic vibration of the structure compare well to more precise periodic solutions found by the mathematical closed-form simulation.

Introduction

This paper considers the nonlinearity of a simplified ice-structure interaction model (Matlock et al., 1971) and predicts the kinematic response for the vibrations at specific periodicity. Previous studies indicate that periodic behavior of the ice-structure interaction is highly non-linear and difficult to predict due to geometrical variability in the intermittent ice breakage and contact to the structure (Karr et al., 1993). The average and maximum magnitude of the structural contact forces are determined for the structural motion responses (Jonkman, 2009 and Yu, 2014). The periodic cycles, the average contact forces and the magnitude of the oscillating force are key factors for estimating structural fatigue life.

It can be observed that the steady-state responses previously obtained were found by random selection of initial conditions. However, due to the limited experimental volume, it's not feasible to examine all possible combinations of inputs. Our aim is to predict the behavior of the dynamic response at any specific periodicity by expanding the equilibrium dynamic relations through the system parameters using Fourier analysis.

Based on Matlock's model, Karr et al. (1995) discussed the actual force time histories which show oscillations and are highly dependent upon the initial velocities and physical properties of the ice-structure dynamic system. Forces intermittently rise and drop with respect to the deflection and breakage of the ice-teeth; the cyclical forces thus form an intermittent repeating process. This dynamic system is complicated by the ice deformation response, variation in ice-properties, geometry of the contact interface, as well as the dynamics of repeated impacts in each cycle. The imperfect system may have random variation in the ice-pitch, ice-stiffness and ice-strength to reflect the complexity of a real problem. However, the perfect system discussed here is argued to be representative of the more complicated imperfect system by showing similar characteristics.

Many mathematical approaches have been applied to solve non-linear dynamic system response with similar features of intermittent contact forces. Wang (1994) used the Trigonometric Collocation method to eliminate the need to evaluate the integrals of systems of mild non-linearity. Wong et al. (1991) applied the Incremental Harmonic Balance (IHB) method to obtain all possible harmonic responses of unsymmetrical piecewise-linear systems. However, these methods are computationally expensive and still cannot predict the specific periodicity and its oscillating amplitude. Karr et al. (1995) and Yu (2014) discussed periodic solutions for the Matlock's ice-structure interaction model from the closed-form solution. However, the orbits of the steady-state periodic responses are not predictable *a priori* due to the numerical integrations over time steps and the non-linear nature of the dynamic relations. The periodic solutions are found only by simulation from arbitrary initial conditions.

While it has been noted in previous research that an overshoot effect will occur at the jump discontinuity using finite Fourier series, the Gibbs constant can be applied to reduce the over shooting effect (Foster and Richards, 1991). David and Shu (1997) discuss the sufficiency of achieving the same order of accuracy as in the case of smooth functions by applying expansion coefficients. We apply the traditional Gibbs constant $g = 0.1790$ to adjust the over shooting effect in calculation of the initial position of the structure in the dynamic system.

Mathematical Model

Based on Matlock's (1971) ice-structure interaction model, a first-order approximation for the dynamic ice-structure interaction modeling is a mass-spring-dashpot system with a single degree of freedom (Figure 1).

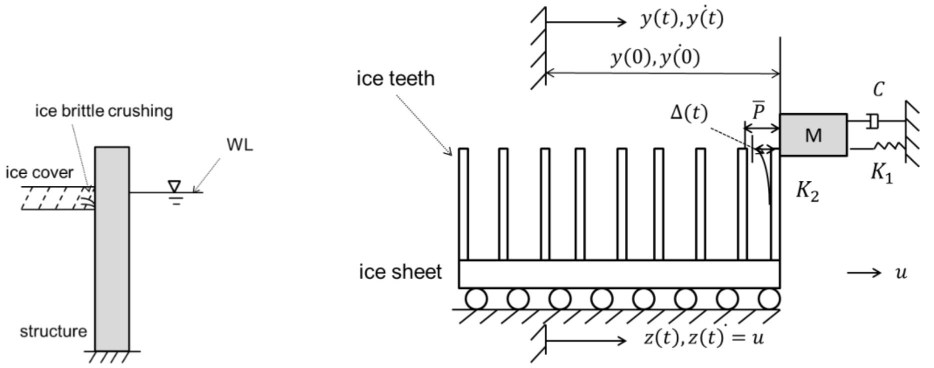

(a) (b)

Figure 1a. Ice brittle crushing against an offshore structure
Figure 1b. Simplified Matlock's dynamic model for ice-structure Interaction

The model parameters shown in Figure 1 are: M—oscillator mass; C—oscillator damping coefficient; K_1 – stiffness of oscillator spring; K_2 – ice teeth stiffness; $y(t)$ –displacement of the mass oscillator; $z(t)$—displacement of the ice sheet; $\Delta(t)$– deflection of ice-tooth; $\bar{P}$- distance between teeth interval (ice pitch); u—constant velocity of the ice-sheet in the x direction.

Following the normalization procedure of Karr et al. (1993), we define the non-dimensional system parameters with respect to the structure's stiffness K_1 and the maximum ice forcing F_{max} on the oscillator due to the ice teeth deflection at its maximum:

$$k_{ice} = \frac{K_2}{K_1} \quad \delta = \frac{\Delta}{\Delta_{max}} \quad \bar{y} = \frac{F_{max}}{K_1}$$
$$x = \frac{y}{\bar{y}} \quad U = \frac{u}{\bar{y}} \quad p = \frac{\bar{P}}{\bar{y}} \quad z_0 = \frac{z(t=0)}{\bar{y}} \qquad \textbf{[1]}$$

Time is normalized with respect to the natural angular velocity of the structure ω_n, N is the number of ice-breakage during each cycle of movement:

$$\tau = \omega_n t \quad \omega_n^2 = \frac{K_1}{M} \quad T = \frac{Np}{U} \qquad \textbf{[2]}$$

where T is the normalized period for a single cycle. Substituting the parameters in Eq. [1] and Eq. [2] into the equation of motions, we obtain the governing differential equations with non-dimensional parameters as follows:

$$\ddot{x}(\tau) + 2\zeta\dot{x}(\tau) + x(\tau) = \begin{cases} 0, \ \delta \le 0 \ or \ \delta = 1 \\ k_{ice}[z_0 + U\tau - x(\tau) - p(i-1)], \ 0 < \delta < 1 \end{cases} \qquad \textbf{[3]}$$

In Eq. [3] the normalized damping coefficient ζ is $\frac{C}{2M\omega_n}$, and z_0 is the initial position of the ice sheet at $\tau = 0$, and i is the tooth number active when in contact with the mass ($i = 1,2.3 \ldots$). At $\tau = 0$, the first tooth is in immediate contact with the mass with $\delta(0) = 0$ ($i = 1$).

Defining $d = p(i-1)$, the tooth deflection at the initial point $\delta(0)$ is 0. The kinematic expression for tooth deflection $\delta(\tau)$ is:

$$\delta(\tau) = [z_0 - x(\tau) + U\tau - d]k_{ice} \qquad \textbf{[4]}$$

In an effort to expand the deflection $\delta(\tau)$ in a Fourier series, it's assumed that no teeth separate from the mass during each cycle of movement. This assumption implies immediate contact with the following tooth at the fracture of a previous tooth and it is justified in the perfect dynamic system where the evenly distributed teeth pitch $\bar{P}$ equals the maximum tooth deflection Δ_{max}. Rearranging Eq. [3] by applying the constraint of $0 \leq \delta \leq 1.0$ yields:

$$\ddot{x}(\tau) + 2\zeta\dot{x}(\tau) + (1 + k_{ice})x(\tau) = k_{ice}[z_0 + U\tau - d] \qquad \mathbf{[5]}$$

For a periodicity of N-teeth breakage per cycle (P-N response), we have:

$$UT = Np \qquad \mathbf{[6]}$$

The breakage occurs at time $\tau = \alpha_i T$, where $i = 1..(N-1), N; \alpha_i$ is the time ratio within one cycle of period T when the i^{th} tooth breakage occurs, and $\alpha_N = 1$. The last two terms in Eq. [5] can then be expressed by the Heaviside step function as follows:

$$U\tau - d = U\tau - pH\{\tau - \alpha_1 T\} - pH\{t - \alpha_2 T\} \ldots - pH\{t - \alpha_N T\} \qquad \mathbf{[7]}$$

Defining $g(\tau) = k_{ice}(z_0 + U\tau - d)$, $g(\tau)$ is expanded in a Fourier series:

$$g(\tau) = k_{ice}(z_0 + U\tau - d) = z_0 k_{ice} + Utk_{ice} - k_{ice}p\sum_{i=1}^{i=N} H\{t - \alpha_i T\}$$
$$= \frac{a_0}{2} + \sum_{n=1}^{\infty}[a_n \cos(n\omega\tau) + b_n \sin(n\omega\tau)] \qquad \mathbf{[8]}$$

The Fourier coefficients are then:

$$a_0 = 2k_{ice}z_0 - Npk_{ice} + 2pk_{ice}\sum_{i=1}^{N}\alpha_i$$
$$a_n = \frac{pk_{ice}}{\pi n}\sum_{i=1}^{N}\sin(2\pi n\alpha_i) \qquad \mathbf{[9]}$$
$$b_n = -\frac{pk_{ice}}{\pi n}\sum_{i=1}^{N}\cos(2\pi n\alpha_i)$$

Substituting Eq. [9] into Eq. [5], the steady state displacement trajectory $x(\tau)$ is:

$$x(\tau) = \frac{a_0}{2(1+k_{ice})} + \sum_{n=1}^{\infty}\frac{[a_n \cos(nr\tau - \phi_n) + b_n \sin(nr\tau - \phi_n)]}{\sqrt{\beta_n}} \qquad \mathbf{[10]}$$

where

$$r = \frac{2\pi}{T} \qquad \mathbf{[11]}$$
$$\beta_n = [(1 + k_{ice}) - (nr)^2]^2 + (2\zeta nr)^2 \qquad \mathbf{[12]}$$
$$\phi_n = \text{atan}[\frac{2\zeta nr}{1 + k_{ice} - (nr)^2}] \qquad \mathbf{[13]}$$

The changes in displacement between two points of breakage are expressed by the following relation, $q = 1, 2, \ldots (N-1)$:

$$x(\tau)|_{t=\alpha_q T} - x(\tau)|_{t=0} = p(q - N\alpha_q) \qquad \mathbf{[14]}$$

Substituting Eq.[14] into Eq.[10], yields (N-1) equations for a specific Period-N response:

$$F(\alpha_q) =$$
$$\sum_{n=1}^{\infty}\frac{1}{n\sqrt{\beta_n}}\{\sum_{i=1}^{N}\sin(2n\pi\alpha_i)\left[cos\phi_n - \cos(2\pi n\alpha_q - \phi_n)\right] + \sum_{i=1}^{N}\cos(2n\pi\alpha_i)\,[sin\phi_n +$$
$$\sin(2\pi n\alpha_q - \phi_n)]\} - \frac{\pi}{k_{ice}}(q - N\alpha_q) = 0 \qquad \mathbf{[15]}$$

Furthermore, recalling the kinematic relationship for tooth deflection in Eq. [4] and the maximum deflection limit $\delta_{max} = 1.0$, we obtain the initial location z_0 for the ice sheet at time $\tau = 0$ as follows:

$$z_0 = -\frac{Npk_{ice}}{2} + pk_{ice}\sum_{i=1}^{N}\alpha_i + (1 + k_{ice})\sum_{n=1}^{\infty}\frac{(a_n cos\phi_n - b_n sin\phi_n)}{\sqrt{\beta_n}} \qquad \textbf{[16]}$$

The initial velocity of the oscillator at $\tau = 0$ is calculated as:

$$\dot{x}(\tau)|_{\tau=0} = \sum_{n=1}^{\infty}\frac{nr(a_n sin\phi_n + b_n cos\phi_n)}{\sqrt{\beta_n}} \qquad \textbf{[17]}$$

Periodic Motion Response Predictions

To seek the motion response for a specific periodicity, we first assume that the number of tooth breakages is N for each cycle. The N^{th}element α_N of the vector $\boldsymbol{\alpha}$ equals 1.0, and the remaining elements $\alpha_1 .. \alpha_{N-1}$are unknowns. The corresponding breaking time ratios α_i can be determined numerically from the $(N-1)$ non-linear equations $F(\alpha)$, as expressed in Eq. [15]. The corresponding time history of teeth deflection $\delta(\tau)$ is thus determined through the set $\boldsymbol{\alpha}$**,** but the $\boldsymbol{\alpha}$ must be examined to verify that the responses are within the constraints of 0.0 to 1.0. In the following sample calculations for a given system, periodic solutions of N=1 (P-1) to N=5 (P-5) have been examined and the calculated displacements are compared with the results from the closed-form solutions.

The system parameters used in the sample periodic motion predictions for both the Fourier analysis and the closed-form simulation are:

$$U = \frac{10}{54\pi},\ p = \frac{2}{9},\ k_{ice} = 4.5,\ \ \zeta = 0.06 \qquad \textbf{[18]}$$

Effort is given to verify the accuracy of the predicted amplitude of motion and the occurrence of tooth-breakage for specific periodicity. The fixed point at breakage for the closed-form P-1 solution is $(0) = 0.56, \dot{x}(0) = -0.015$. It is observed that the predicted displacement of P-1 response by Fourier analysis is in close agreement with the displacement simulated from the closed form solution (Figure 2a). However, at the time of tooth fracturing, it is observed that the displacement-time derivative from the Fourier simulation is larger than the velocity obtained by the closed-form solution. The normalized velocity at breakage is -0.015 from the closed-form solution, and it is -0.37 from the Fourier simulation. The increased velocity from the Fourier solution is caused by the Gibbs effect of overshooting at the point of discontinuity due to tooth-breakage. The ice-tooth deformation forcing obtained by Fourier analysis is gradual at the breakage of $\delta(\tau = \alpha_i T)$ rather than shifting directly to zero. The overshooting effect in tooth-deflection time history is approximated as 0.09 by the Gibbs constant g times one-half of the jump size at the point breakage (Figure 2b). There is thus a source of error in estimating the velocity of the mass at breakage due to the Gibbs effect. In fact, inputting the kinematic initial condition at breakage from the calculated P-1 response into the closed-form simulator, a periodic solution of P-5 is obtained.

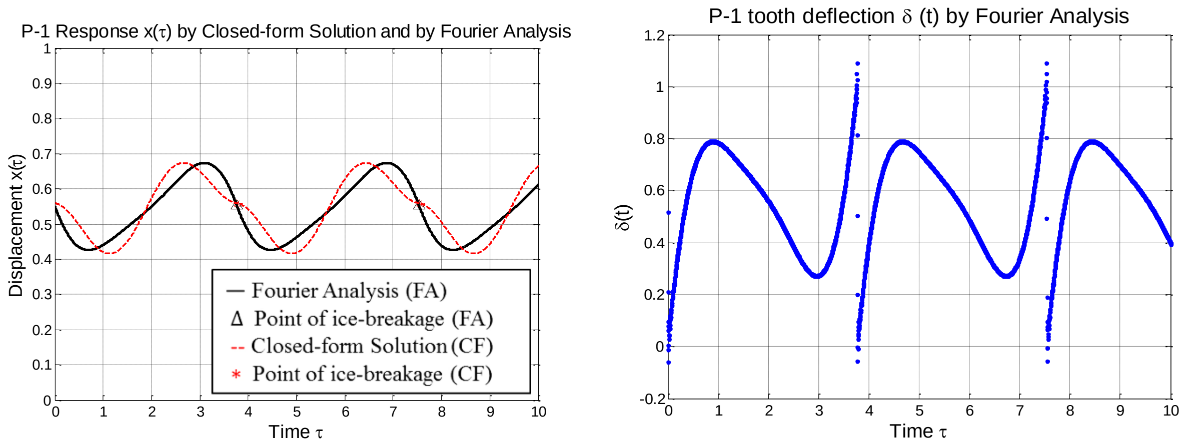

(a) (b)

Figure 2a. The P-1 response $x(\tau)$ obtained by Fourier series and Closed-form solution
Figure 2b. Tooth deflection $\delta(\tau)$ for a P-1 response by Fourier analysis

The $\boldsymbol{\alpha}$ components for P-3 response are calculated as $\alpha_1 = 0.095, \alpha_2 = 0.41$, which compares well to the vibrations in Karr et al.'s (1993) steady-state P-3 response (Figure 3). Less than 6.6% of difference in the amplitude of motion is found, and the tooth breakage occurrences are in close agreement. Also, similar observations are found for P-2 response.

In addition to this periodic response, another possible P-3 response is calculated from the Fourier analysis (Figure 4a). Moreover, we find possible P-4 solutions which are missing from the previous closed-form solutions (Karr et al., 1993). One typical simulation is shown in Figure 4b. It is observed that both the P-3 and P-4 responses resemble a portion of the oscillating motion from the close-form P-25 steady-state response (Figure 5a). The P-25 is obtained by inputting the Fourier calculated breakage initial conditions from the P-3 response: $x(0) = 0.49, \dot{x}(0) = -0.48$. Another closed-form solution with static initial condition $x(0) = 0, \dot{x}(0) = 0$ is shown in Figure 5b. It is noticed that the response consists of transient indentations during which the mass sweeps through 5, 4, 2 and 3 tooth-breakages respectively. The amplitudes of the transient response from Figure 5b resemble the motion amplitudes from the P-3 to P-4 responses calculated by Fourier analysis with the same number of tooth-breakage in one single sweeping oscillation (Figure 4).

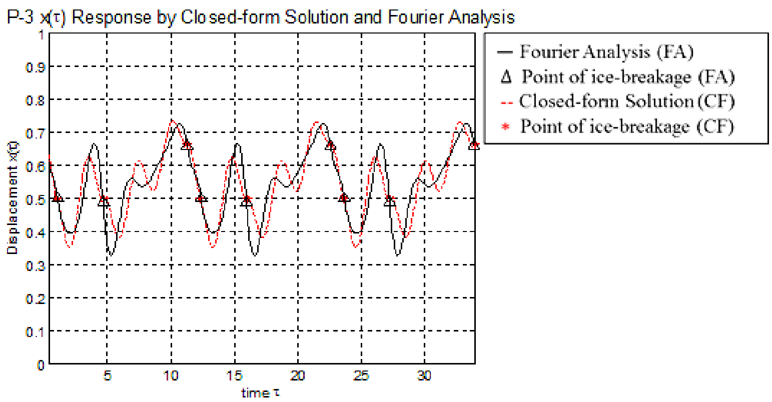

Figure 3. A P-3 response by Closed-form simulator ($x(0) = 0.66, \dot{x}(0) = 0.021$) and by Fourier series analysis ($\boldsymbol{\alpha} = [0.095, 0.41, 1.00]$)

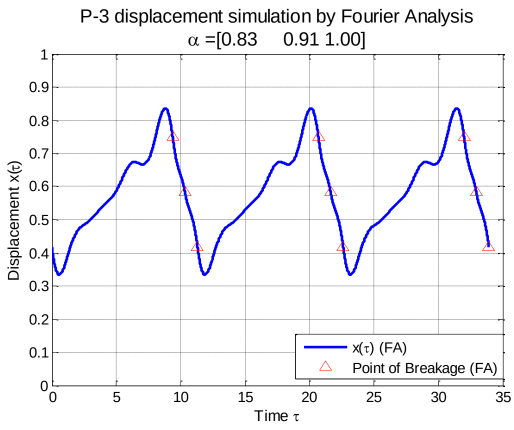

(a)

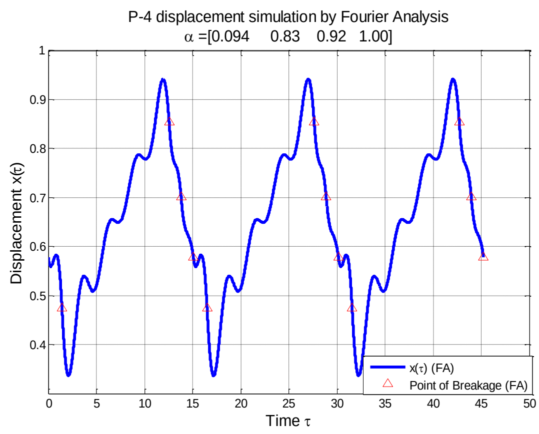

(b)

Figure 4a. A P-3 response calculated by Fourier analysis ($\boldsymbol{\alpha} = [0.83, 0.91, 1.00]$)
Figure 4b. A P-4 response calculated by Fourier analysis ($\boldsymbol{\alpha} = [0.094, 0.83, 0.92, 1.00]$)

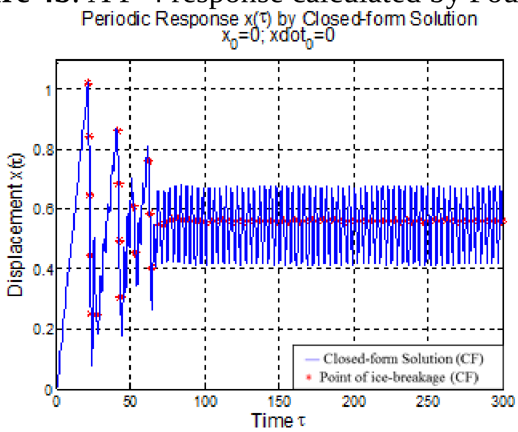

(a)

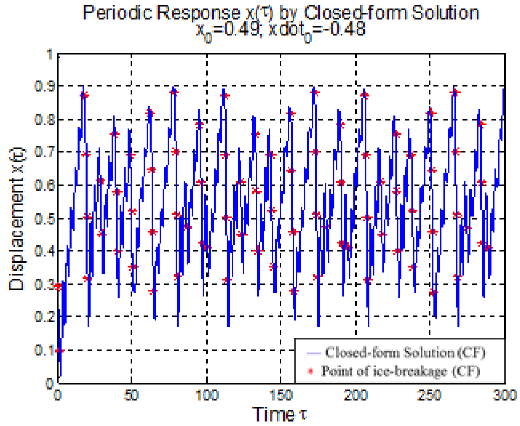

(b)

Figure 5a. Time history $x(\tau)$ by Closed-form solution with input $x(0) = 0.49, \dot{x}(0) = -0.48$
Figure 5b. Time history $x(\tau)$ by Closed-form solution with input $x(0) = 0, \dot{x}(0) = 0$

Finally, the time history of displacements for a P-5 response predicted by the Fourier analysis compare well to the steady-state closed-form solutions in terms of the motion of response and the tooth breakage occurrence (Figure 6). Furthermore, the predicted motion of amplitude for P-5 by Fourier analysis is in agreement with the transient response shown in Figure 5b with 5 teeth breaking in the first sweep. Closed-form solutions for steady-state P-1, P-2, P-3, P-5 and P-25 responses have been recorded by random initial inputs. The P-5 response features the maximum oscillating magnitude for our Fourier periodic solutions from P-1 through P-5 responses. The transient motion resembling the P-5 response shown in Figure 5b is thus not negligible. Therefore the Fourier analysis can be used to estimate the extreme motions of the dynamic system for both transient and steady-state response.

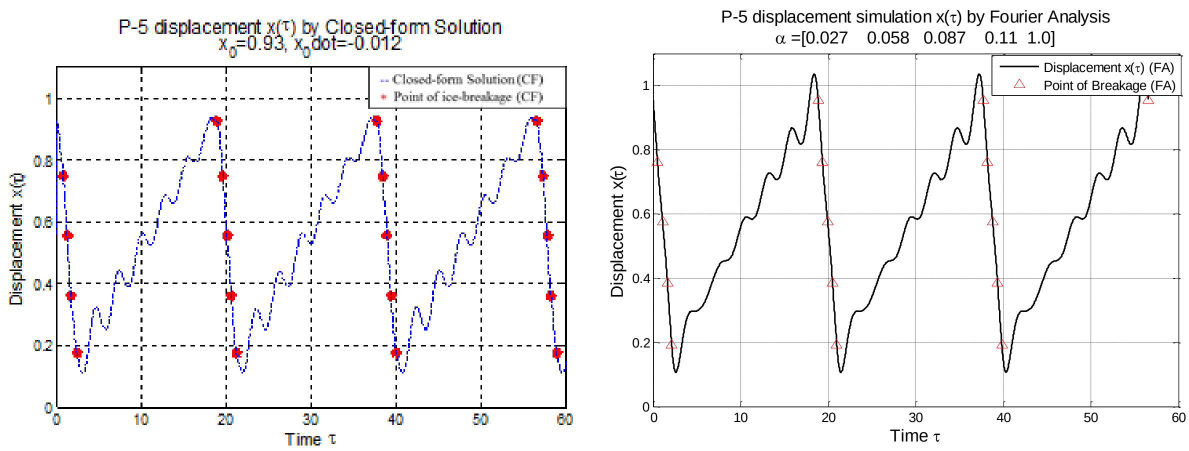

(a) (b)

Figure 6a. A P-5 response by Closed-form simulator (initial condition $x_0 = 0.93, \dot{x_0} = -0.012$).
Figure 6b. A P-5 response predicted by Fourier analysis ($\boldsymbol{\alpha} = [0.027, 0.058, 0.087, 0.11, 1.00]$)

Conclusions

In this paper, we expand the equations of motion in Fourier series, and set up the relationships among the system parameters to evaluate the responses for specific steady-state periodicity. Our approach establishes non-linear dynamic equations through Fourier analysis with respect to the number of tooth-breakages N per cycle. This method allows rapid estimation for the range of motion and the evaluation of structural contact forces. The amplitudes predicted by our Fourier analysis solution correspond well to the simulation results obtained from closed-form solutions with random initial condition selections. Furthermore, the time ratios of breakage are accurately predicted thus the cyclic behavior can be analyzed accordingly. Also, with the calculated structural periodic responses, the mean value and the magnitude of the oscillating contact forces can be obtained. These output parameters are key factors for strength fatigue life assessment. The previously un-detected periodic response of a P-4 is found through our Fourier solution. Further effort should be given to validate the basin of attractions given a representative system and more specific evaluation of the error range in the velocity predictions due to the Gibbs effect.

Acknowledgments

An award for the first author from the Link Ocean Engineering and Instrumentation Ph.D. Fellowship Program is gratefully acknowledged. The support by the Department of Energy of United States (DE-EF005376) for the research work is also gratefully acknowledged.

Reference

Choi, Yeon-Sun, and Sherif T. Noah. "Forced periodic vibration of unsymmetric piecewise-linear systems." Journal of Sound and Vibration 121, no. 1 (1988): 117-126.

Foster, J., & Richards, F. B. (1991). The Gibbs phenomenon for piecewise-linear approximation. The American Mathematical Monthly, 98(1), 47-49.

Jonkman, J. M. (2009). Dynamics of offshore floating wind turbines—model development and verification. Wind energy, 12(5), 459-492.

Karr, D. G., Troesch, A. W., & Wingate, W. C. (1993). Nonlinear dynamic response of a simple ice-structure interaction model. Journal of Offshore Mechanics and Arctic Engineering, 115(4), 246-252.

Matlock, H., Dawkins, W. P., & Panak, J. J. (1971). Analytical model for ice-structure interaction. Journal of the Engineering Mechanics Division, 97(4), 1083-1092.

Remmers, Thomas C. "Prediction of Nonlinear Contact Dynamics of an Ice-Structure Interaction Model using Fourier Analysis." Master's thesis, The University of Michigan, 1998.

Sodhi, D. S. (2001). Crushing failure during ice–structure interaction. Engineering Fracture Mechanics, 68(17), 1889-1921.

Wang, Y., & Wang, Z. (1994). Periodic response of piecewise-linear oscillators using trigonometric collocation. Journal of sound and vibration, 177(4), 573-576.

Wong, C. W., Zhang, W. S., & Lau, S. L. (1991). Periodic forced vibration of unsymmetrical piecewise-linear systems by incremental harmonic balance method. Journal of Sound and Vibration, 149(1), 91-105.

Yu, Bingbin. "Offshore Wind Turbine Interaction with Floating Freshwater Ice on the Great Lakes." PhD diss., The University of Michigan, 2014.

APPENDIX 6.1

A Wideband Autocorrelation Radiometer for Snowpack/Lake Ice Thickness Detection

Hamid Nejati, Sing Y. Emily Wong, Roger D. De Roo, Lin van Nieuwstadt, Kamal Sarabandi, Guy A. Meadows, and Anthony W. England

Abstract

The concept of wideband autocorrelation based radiometer (WiBAR) as a remote sensing tool for estimation of the thickness of any low-absorbing layered medium including snow or lake ice is demonstrated. The implemented WiBAR measures the power spectral density of the brightness temperature of a two-layer medium from which the thickness of the top penetrable layer is estimated using Wiener-Khinchin theorem. Analyzing the autocorrelation of the received brightness temperature provides an accurate estimate for the microwave transit time difference between the direct and the doubly reflected thermal emission paths and consequently the thickness of the snowpack/ice layer. The implemented WiBAR has been tested in several scenarios including snow (ice) layers over ground (fresh water) under varying snow/ice conditions and thicknesses. The thickness measurement accuracy of our radiometer is within 1.5*cm* for horizontally polarized (H-pol) far-field measurements.

H. Nejati, S. Y. E. Wong, and K. Sarabandi are with the Department of Electrical Engineering and Computer Science, University of Michigan, Ann Arbor, MI, 48109 USA e-mail: ({hnejati,emilywsy,saraband}@umich.edu).

R. D. De Roo is with the Department of Atmospheric, Oceanic, and Space Sciences, University of Michigan, Ann Arbor, MI, 48109 USA e-mail: (deroo@umich.edu).

L. van Nieuwstadt is with the Department of Atmospheric, Oceanic, and Space Sciences, University of Michigan, and Michigan Tech Research Institute (MTRI), Ann Arbor, MI, USA e-mail: (linevn@umich.edu).

G. A. Meadows is with the Great Lakes Research Center at Michigan Technological University, Houghton, MI, USA e-mail: (gmeadows@mtu.edu).

A. W. England is with the Electrical Engineering and Computer Science Department, Atmospheric, Oceanic, and Space Sciences Department, university of Michigan, Ann Arbor, and also dean of College of Engineering and Computer Science, University of Michigan, Dearborn, MI, USA e-mail: (england@umich.edu).

I. Introduction

Snowpack and lake ice are examples of layers at the surface of the Earth that have engineering significance. Snowpack is the accumulation of snow found mainly in mountainous and polar regions. The seasonal snowpack is vitally important for water resource management [1], flood and avalanche prediction [2], [3], and ecosystem and climate studies [4], [5]. The quantity of snow on the ground is highly variable in both space and time. Moreover, climate change is causing non-stationary annual statistics in the snowpack characteristics [6]–[12]. Thus, it is desirable to monitor the global snow pack in nearly daily time intervals.

Conventionally, the most common technique to remotely measure the accumulation of snow on the ground, as quantified by the snow water equivalent (SWE) or the thickness of snowpacks, has been differential scatter darkening [13]–[26]. This phenomenon is due to the volumetric scattering of the snow grains at microwave frequencies, usually 19 and $37GHz$. The scatter darkening is stronger at the higher frequency, and so the difference in the two brightness temperatures is considered to be proportional to the snow accumulation. A constant of proportionality is empirically derived to estimate the snowpack thickness or SWE. However, the empirical formula parameter is specific to the region [20], [21], [27]–[30] because details of the snowpack grain evolution differ geographically due to differences in regional climates. For example, the parameter derived for Finland is distinct from that for Canada [26]. In light of the fact that regional climates are changing, a more robust method of making this remote measurement is needed.

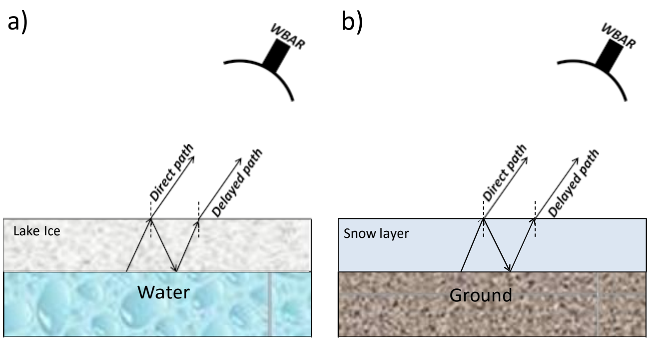

Figure 1. Test scenarios consist of (a) an ice layer on top of fresh water (Lake ice scenario) (b) snow layer on top of ground (snow scenario). The direct path of the brightness temperature of the underlying layer (TA) as well as the doubly reflected brightness temperature path are shown by solid arrows.

The lake ice thickness plays an important role in the total pressure exerted to the off-shore structures [31] and vessels in winter. Withstanding this pressure is a factor in the design of off-shore structures such as wind farms. Ice thickness is a factor in the navigability of frozen inland waterways [32]. The traditional way to measure the lake ice thickness is by drilling through the ice, which is a dangerous and labor-intensive task. Therefore, the development of an accurate, remote measurement of ice thickness without disturbing or breaking the ice is noteworthy.

Traditionally, microwave radiometers are the most common instrument to remotely sense snowpack accumulations [33], [34]. A radiometer is a passive microwave remote sensing instrument that can measure the brightness temperature of a scene. When ground/lake is covered by snow/ice, the received brightness temperature is a combination of the thermal emission of the underlying ground/lake water, the reflection of the down-welling sky brightness temperature, and the emission of the snowpack/lake ice. When the layer is dry, the major contribution to the detected brightness temperature is the thermal emission of the underlying medium, illustrated in Figure 1(a) and (b). This term is composed mainly of two parts. One is due to the direct transmission of the brightness temperature and the other is the result of the doubly reflected emitted wave inside the dry snow/ice layer due to reflection at the top and bottom interfaces. The doubly reflected wave has a transit time delay compared to the direct path wave and this delay is directly proportional to the thickness of the layer. The direct and the doubly reflected background brightness temperatures are shown by arrows in Figure 1 (a) and (b). The doubly reflected path experiences more attenuation due to more absorption and scattering in the snowpack/ice layer as well as reflection at the top and bottom interfaces. The attenuation of higher order paths (eg. quadruple reflected path) is high enough that we can ignore their presence in natural scenarios including lake ice and snowpack. The interference of the direct path with its delayed copy can be detected with a Wideband Autocorrelation Radiometer (WiBAR) to yield the layer's microwave transit time, which is proportional to the layer thickness.

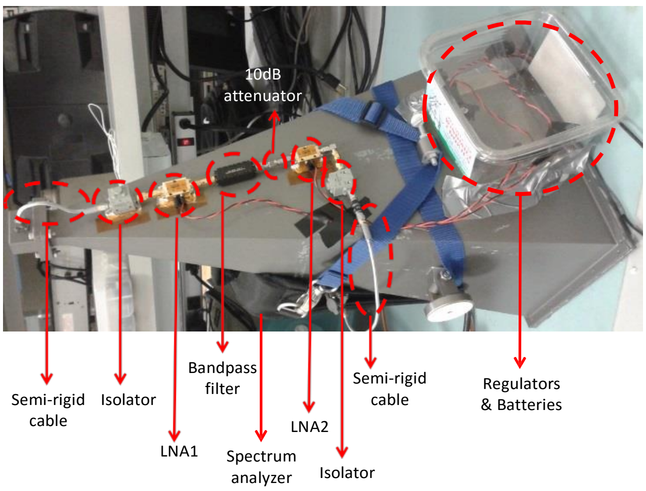

Figure 2. Photograph of an implementation of a WiBAR designed for measuring the thickness of lake ice.

A photo of one implementation of a wideband autocorrelation radiometer (WiBAR) is shown in Figure 2. We are utilizing our radiometer for three scenarios. In the first scenario, the thickness of air gap between a high dielectric thin sheet and water is detected to prove the operation of the instrument. Second scenario pertains to lake ice thickness detection, in which there is a layer of ice above water as shown in Figure 1(a). The last scenario is related to snow layer thickness detection, in which a layer of snow is naturally formed over ground as shown in Figure 1(b).

Our contributions in this paper are listed below:

- We demonstrate that the power spectral measurement is necessary and sufficient for auto-correlation calculation using Wiener-Khinchin theorem.
- We model and optimally design a wideband radiometer using a handheld spectrum analyzer for maximum performance efficiency. The microwave circuit models for signal path are also developed using commercial off-the-shelf components (COTS).
- We analyze the sensitivity of WiBAR using the actual microwave circuit components and spectrum analyzer characteristics.
- We perform on-site measurements of air gap, ice, and snow layer thicknesses and verify our results against *in-situ* measurements.

This paper is organized as follows: WiBAR is fully investigated in Section II. The proof of concept in time domain using computer simulations is presented in Subsection II-A. A model of the radiometer in time domain is also investigated. The proof of concept in the frequency domain using microwave circuitries is presented in Subsection II-B. The design procedure for the operation of optimized stable WiBAR is included in Section II-C. Then, the power spectral domain design is compared to the time domain design [35], [36]. Analysis of the sensitivity of the radiometer, noise-equivalent uncertainty in brightness temperature ($NE\Delta T$) is presented in Subsection II-D. The optimum values for the video bandwidth, resolution bandwidth, and frequency span are calculated in Section II-D. The calibration procedure to minimize the effect of WiBAR gain signature in the autocorrelation response is discussed in Subsection II-E. The detection of 'weak' sinusoidal signal in the bandwidth is explained in Subsection II-F. The effect of radio frequency interference (RFI) is also explained in Subsection II-G. The impact of surface roughness on the autocorrelation response of the system is explored in Subsection II-H. The on-site measurements and the post-processing results are presented in Section III. Several measurement results for air gap over water, lake ice, and naturally formed snow over asphalt are presented in Subsections III-A, III-C, and III-B, respectively. Finally, Section IV concludes the paper.

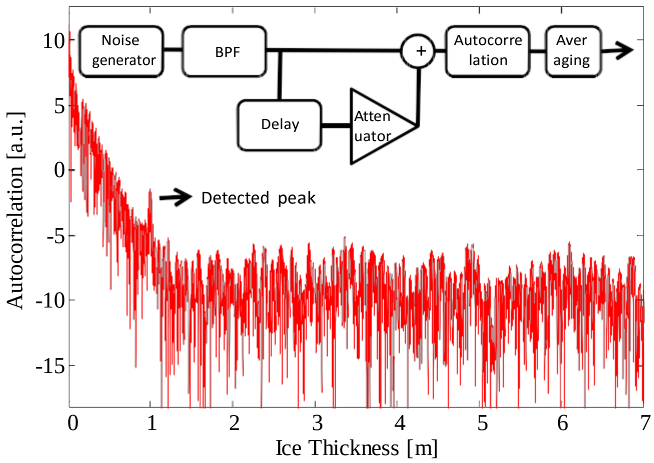

Figure 3. The software simulated recovery process of the autocorrelation radiometer in time-domain for a *1m* thick ice using a long integration time and a sharp bandpass filter (BPF). The block diagram of the process is shown in the inset.

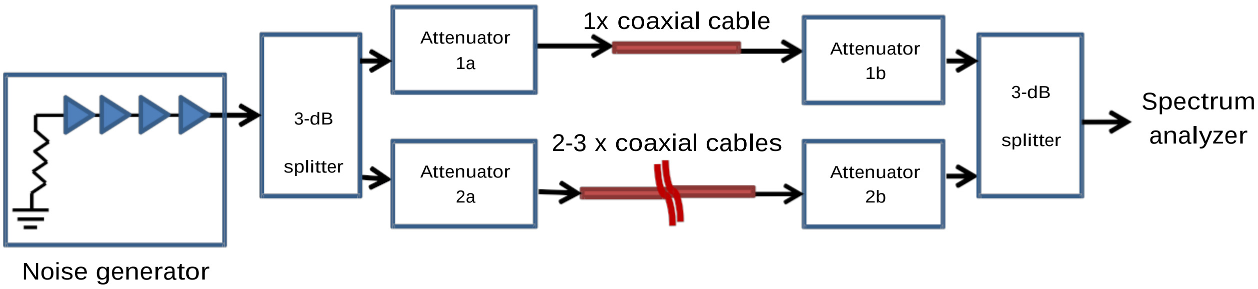

Figure 4. The block diagram of the low-order microwave circuit model for a single layer low-loss medium. The four attenuators control the relative magnitude of the direct and delayed signal paths. Different numbers of 30*cm* long coaxial cables (manf P1dB; p/n P1-SMAP/SMAP-141CJ-12) are used to control the relative delay of the two paths.

II. WIDEBAND AUTOCORRELATION RADIOMETER (WIBAR)

A wideband autocorrelation radiometer (WiBAR) measures the temporal autocorrelation of the received brightness signal. For a one-dimensional layered media including snowpacks and ice layers, the magnitude of the autocorrelation of the emission has maxima at the delays corresponding to the round trip travel time differences for waves experiencing different numbers of traverses of the layer. The bandwidth needed to observe the layer transit time is inversely proportional to the transit time, and because interesting snow and ice layers may not be very thick, a wide bandwidth for a WiBAR will be needed. However, the wide-bandwidth of WiBAR provides higher dynamic range and reduces the required integration time to extract the information.

By measuring the time delay between the brightness contained in the direct path and its doubly reflected copy, we can find the layer thickness. England has shown that the time delay, τ_{del} , is twice the layer transit time τ_r minus the excess travel time τ_f of the direct path to the radiometer in the air as given by equations (1) and (4) in [35].

$\tau_{del} = 2\tau_r - \tau_f$ where n is the refractive index of the ice/snow layer (presumed constant over depth), θ_1 is the incidence angle, c is the speed of light in free space, d is the thickness of ice/snow, and θ_2 is the angle of propagation within the layer, related to the incidence angle θ_1 by Snell's Law: $\sin\theta_1 = n\sin\theta_2$. The layer thickness is directly proportional to this time delay. This technique has the potential to find the thickness of any lowloss layered medium.

A WiBAR can be realized in the time-domain or frequency domain. The theory of operation of a time domain WiBAR is discussed by England [36] in introducing the WiBAR concept. In brief, the time-domain radiometer amplifies radiation incident upon its antenna and digitizes the signal. The resulting digital time series is used to generate the autocorrelation function. The wide bandwidth requirements make this approach difficult, but not impossible, to implement with modern technology.

A frequency domain WiBAR digitizes the power spectrum of the wideband signal, instead of the waveform. The autocorrelation is generated from the spectrum via an inverse Fourier transform according to the Wiener-Khinchin theorem. A distinct disadvantage of this approach is the lengthy data acquisition time, but the hardware can be readily implemented. For the purpose of demonstrating the existence of the geophysical signal, we implemented two WiBARs operating in the frequency domain: one, operating at $7-10$ GHz, is designed for lake ice, and, another operating at $1-3$ GHz, for snow packs.

In this section, we explored both time and frequency domain implementation methods in the Subsections II-A and II-B. Then, WiBAR optimal design procedure, sensitivity analysis, calibration procedure, thickness detection algorithms by calculating autocorrelation response and effect of RFI are thoroughly investigated in Subsections II-C to II-G.

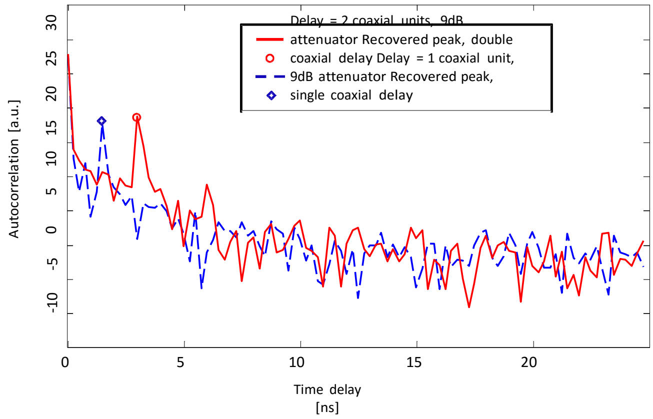

Figure 5. The autocorrelation response of the detected waveforms for one (blue dashed line) and two unit delays (red solid line). The doubly reflected path is attenuated 9*dB* more than the direct path.

A. Proof of concept- time domain software simulation

The time domain realization of WiBAR is done by processing the autocorrelation pattern of the received signal, called time-domain setup. The block diagram of the signal path in time-domain simulation is shown in the inset of Figure 3. The blackbody radiation of the background medium (water or soil) is modeled by a Gaussian noise generator due to central limit theorem. The signal then passes through a bandpass filter (BPF). The filtered noise travels through two different paths to mimic the direct path and doubly reflected path. The autocorrelation of the combined signal is then applied to an averaging stage to diminish its noise level.

A test scenario of a $1m$ ice sheet over water is considered and the simulated waveform of the emitted signal is fed through the block diagram shown in the inset of Figure 3. The bandpass filter is given a response similar to the filter used in the second implementation of WiBAR later in this section. The integration time and the attenuation of the doubly reflected wave are chosen as the worst case scenario to be $1\mu s$ and $-25dB$, respectively. The hardware implementation of this technique requires a digital signal processing (DSP) board with a very high speed analog to digital converter (ADC). In our desired frequency range of operation, a super-fast ADC is readily available but power hungry and expensive.

B. Proof of concept- frequency domain hardware simulations

In order to examine the possibility of frequency domain implementation, we have designed two microwave circuits that simulate the key physics of layered media. The first simulation only captures a single travel time difference and we call it the low-order circuit. The second simulation includes multiple reflections inside the layer and we call it the high-order circuit.

The low-order circuit is shown in Figure 4. The inherent thermal noise of a matched load is amplified using a series of cascaded noisy amplifiers. The amplified noise is split into two branches corresponding to the direct path and the delayed path. Attenuators are used to control the magnitude of the signal in each path. The time delay is adjusted by including different numbers of $30cm$ long coaxial cables in the delayed path. The noise waveforms are then merged and fed in to a spectrum analyzer. Detecting the relative time delay of the longer path is equivalent to detecting the thickness of the simulated layered medium. Since the doubly reflected path in a layer experiences more attenuation, the attenuation in the longer path (attenuator $2b$ in Figure 4) is larger than the one in the shorter path (attenuator $1b$ in Figure 4) by $9dB$. The difference between the amplitude of the zero-lag peak and the doubly reflected path peak is $9dB$ in Figure 5. Reference data required for calibration was obtained by disconnecting the coaxial units on the delayed path from the attenuators, providing infinite attenuation for that path. As a result of attenuators still present on the delayed path, the open ends of the delayed path remained matched at the splitter and combiner, preventing the creation of a new signal path due to reflections. Each coaxial cable assembly (manf P1dB; model P1-SMAP/SMAP-14ICJ-12) was measured on an Agilent $8722ES$ vector network analyzer to have about $1.5ns$ of group delay. The autocorrelation obtained from the inverse Fourier transform of the power spectral data is shown in Figure 5 for differential pathlengths of one and two coaxial assemblies. Figure 5 shows the successful reconstruction of the time delays (the hollow diamond and circle), which are equal to $1.5ns$ and $3ns$, as expected.

The block diagram of the high-order circuit is shown in Figure 6(a). The two 180 degree hybrid couplers play the role of interfaces between media. In this schematic, the upper hybrid coupler models the water-ice or snow-terrain interface. The lower hybrid coupler models the ice-air or snow-air interface. The amplified input noise source represents the emission of the underlying medium, which can be water or terrain. The rotation of the signal inside the loop is similar to multiple internal reflections inside the layered media. The time delay is primarily due to the microwave transit time of the transmission lines forming the loop, with a small contribution due to the delay through the couplers, attenuators, and adaptors. The reflected wave is 180 degree out of phase with the transmitted signal, and this phase shift is implemented by applying the input signal to the delta port of the 180 degree hybrid coupler. The input signal splits into two signals with 180 phase difference. The in-phased components of the upper hybrid coupler enter the delta port of the lower hybrid coupler. The signal then splits into two paths. The in-phase component representing transmission in air toward the radiometer enters the spectrum analyzer. The 180 out of phase signal rotates in the loop. This signal represents the internal reflection at the ice-air or snow-air interface, which remains inside the layer.

This high order circuit has been implemented and tested in the lab (as depicted in Figure 6 (a)) and, in order to better mimic the actual scenario, outdoors with the following three changes. In the outdoor scenario, (1) the termination on the right side of the bottom coupler is replaced by an antenna pointed to the sky, (2) the amplifier chain on the left side of the top coupler is replaced by a matched termination, and (3) the signal input to the spectrum analyzer is amplified. These changes produce a circuit supporting signal magnitudes that more closely resemble those in layered media on Earth.

The high order circuit is calibrated similarly to the low order circuit. The signal path representing the delayed ray (left side of the loop in Figure 6(a)) is attenuated strongly by disconnecting the cable and terminating the coupler ports. The spectrum measured during an experiment is normalized by the spectrum recorded during a calibration in order to remove spurious multipaths due to mismatches in the microwave components.

The autocorrelation response of the calibrated laboratory measurements with no attenuators in the loop is shown in Figure 6 (b). Each peak represents a(one?) transit time of the loop. The total cable length of $4\boldsymbol{ft} = 1.22m$ is chosen in this case. The electric length of the adapters as well as the couplers also needs to be considered in the calculation of total electric length. The autocorrelation response shows the overall length is $4.25\boldsymbol{ft} = 1.3m,$ which is very close to the expected value considering the electric path inside the hybrid couplers and adapters.

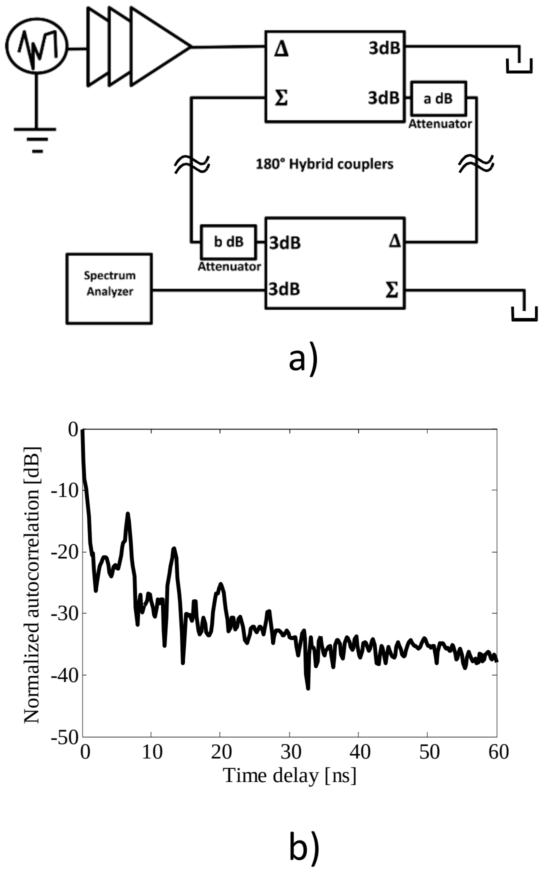

Figure 6. (a) The schematic of high-order microwave circuit model for a single layer low-loss medium. (b) The autocorrelation response of the high-order microwave circuit model demonstrating the delayed peaks.

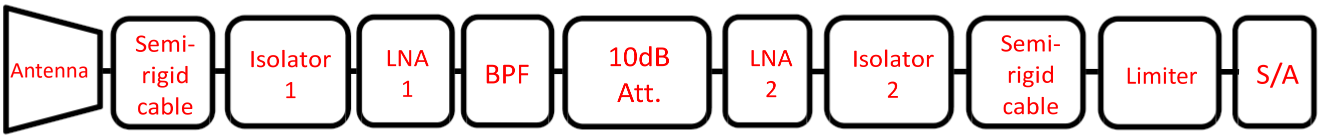

Figure 7. Block diagram of the wideband autocorrelation radiometer.

C. Lake ice radiometer design

The frequency range of operation of lake ice WiBAR is chosen to be $7 - 10\ GHz$. This frequency range is chosen for two reasons. First, lake ice is expected to have insignificant extinction at these and lower frequencies. Fresh water ice has minimal absorption in the entire microwave band. Scattering in lake ice is due to inclusions such as vegetation and air bubbles, and typical sizes of these compared to the wavelength place the scattering in the Rayleigh regime. Finally, both the top and bottom surfaces of lake ice are smooth when compared to the wavelength. The second reason (for this particular choice) is this frequency range is relatively free of radio frequency interferences (RFI) [37]. The chosen frequency band is optimal for lake ice detection or snow over flat terrain; however, in a snow layer thickness detection scenario over undulating terrain, lower frequencies are desirable. The radiometer is composed of standard gain horn antenna, low noise amplifiers (LNAs), a band pass filter (BPF), and hand held spectrum analyzer (S/A). Isolators and attenuators provide wideband matching between adjacent components. The wideband impedance matching is required to remove the internal oscillation in the structure due to the instability of the LNAs. In order to stabilize the chain of high gain amplifiers and make sure that they both operate on their linear gain regime, we added an attenuator between the amplifiers. The block diagram of the lake ice WiBAR is shown in Figure 7 and a photo of its implementation is shown in Figure 2.

The overall noise figure of this WiBAR is calculated using Friis formula to be $2.46dB$. The dominant contribution to the noise figure is the first LNA in the chain. The noise contribution of the components downstream of the LNA is negligible. Specially, the noise contribution of the BPF is much less than that of the attenuator and is neglected in the calculation of the noise figure

D. Sensitivity Analysis

1) Radiometer: The system temperature (T_{SYS}) is the summation of the noise temperature of the receiver plus the contribution from the antenna. T_{SYS} can be formulated as in (2).

$$T_{SYS} = \eta T_A + (1-\eta)T_p + F T_0, \qquad (2)$$

where T_A is the scene temperature. η is the radiation efficiency of the antenna. T_p is the antenna physical temperature, and F is the overall receiver noise factor. The third term in the right hand side of (2) is also known as T_{rec}. The sensitivity can be formulated as $\frac{\Delta T}{T_{SYS}}$, where ΔT is the minimum detectable temperature difference using WiBAR.

2) Spectrum Analyzer: A spectrum analyzer is an instrument that measures the power spectral density as a function of frequency. The received signal passes through an internal tunable super-heterodyne receiver, in which the intermediate frequency (IF) filter is swept through the overall bandwidth. This filter is also known as a resolution bandwidth filter. The filtered signal then enters a square-law detector. To diminish the noise, the detected power is averaged using a low pass filter known as the video bandwidth filter. The ratio of the resolution bandwidth to the video bandwidth determines the noise floor in the measurement [38].

An Agilent N9934C spectrum analyzer operates as the receiver in our WiBAR. Using the Wiener Khinchin theorem, the inverse Fourier transform of the power spectral density (Spectrum analyzer display) is equal to the autocorrelation response applied to the received data. By applying an external inverse Fourier transform to the spectrum analyzer data, the autocorrelation pattern can be estimated. The ripples in the frequency spectrum are transformed to the peaks in the autocorrelation domain.

In a spectrum analyzer, there are several parameters that should be tuned prior to operation for maximum achievable sensitivity, resolution, and data collection time. These parameters are the frequency span (F_S), sweep time (T_S), resolution bandwidth (B_r), and video bandwidth (B_V).

We start by choosing resolution bandwidth. Two signals that are separated by $\Delta f[Hz]$ and an amplitude difference of $\Delta A[dB]$ can be distinguished on spectrum analyzer if the resolution bandwidth is chosen as in (3).

$$\Delta A = -3 - (60-3)\frac{\Delta f - \frac{1}{2}B_{r3dB}}{\frac{1}{2}B_{r60dB} - \frac{1}{2}B_{r3dB}}$$

$$B_r = \frac{-114\Delta f}{10(3+\Delta A)-57} \quad (3)$$

B_{rndB} is the resolution bandwidth measured at ndB bandwidth. The default value for B_r is measured at $3dB$ bandwidth. Equation (3) is obtained by the characteristic of the resolution bandwidth filter , which is a bandpass filter.(the filter is a bandpass filter, not the characteristics) In the case that the spectrum analyzer is using digital filters, the number 10 in the denominator should be changed to 4. Using this formula, and the periodicity of the ripples, we can find an optimum value for the resolution bandwidth. In the case of thin ice, the resolution bandwidth can be set to $3MHz$ easily. In case of very thick ice without thickness variation and trapped air bubbles (the ideal case), the resolution bandpass filter will provide a margin of $4dB$ for the adjacent ripples to be detected using the same resolution bandwidth of $3MHz$. In case of a very thick layer, we need to use a smaller resolution bandwidth such as $1MHz$ for capturing the ripples.

In the spectrum analyzer, the sweep time (T_S) can be calculated using the resolution bandwidth (B_r), video bandwidth (B_V), and frequency span (F_S) as given by (4). The sweep time is the time required for a full sweep of the frequency span and can be translated as the waiting time for each measurement.

$$T_s = 2.694\,\frac{F_s}{B_r B_v} \quad (4)$$

Equation (4) is valid when $B_V < B_r$, which is the case in our measurements. The constant number in front of the fraction in (4) depends on the type of spectrum analyzer and is around 2.5 for different types of spectrum analyzers. In our setup, we have chosen $B_V = 300Hz$, $B_r = 3MHz$, $F_S = 3GHz$. The required sweep time was almost $9s$, which is in agreement with this formula. We did have some flexibility in reducing the frequency span, but in order to get higher accuracy in the autocorrelation peak and its spread, we aimed for maximum available span. The maximum span is equal to $3GHz$ in our measurement setup. The smallest suggested frequency span should cover at least 2 periods of the ripples. In case of very thin ice, this interval should be larger due to the relatively longer period of the ripples. The number of periods in the overall bandwidth (m) directly maps to the number of the frequency bin ($m+1$), in which the autocorrelation peak occurs. Due to strong self-correlation, this minimum number should be at least two or more.

The noise level in radiometers can be calculated using (5) [39].

$$\frac{\Delta T}{T_{SYS}} = \frac{1}{\sqrt{B\tau'}}$$

(5)

where B is the radiometer bandwidth and τ' is the integration time. In WiBAR, B should be substituted by resolution bandwidth and τ' by the time that the spectrum analyzer spends in each resolution element. Therefore, $\tau'=B_r/(df/dt) = B_rT_s/F_S$. By substituting for T_s from (4) in τ', the noise level can be calculated as in (6).

$$\frac{\Delta P}{P} = \frac{\Delta T}{T_{SYS}} = \frac{1}{\sqrt{2.694\ B_r/B_v}}$$

(6)

where P is the noise power and can be substituted by $kT_{SYS}B$. Equation (6) is the well known equation for the noise-equivalent uncertainty in brightness temperature, aka $NE\Delta T$ of a radiometer. Equation (6) can be used to set the video bandwidth based on the required sensitivity. It also suggests that by reducing video bandwidth and increasing resolution bandwidth, the maximum sensitivity can be achieved.

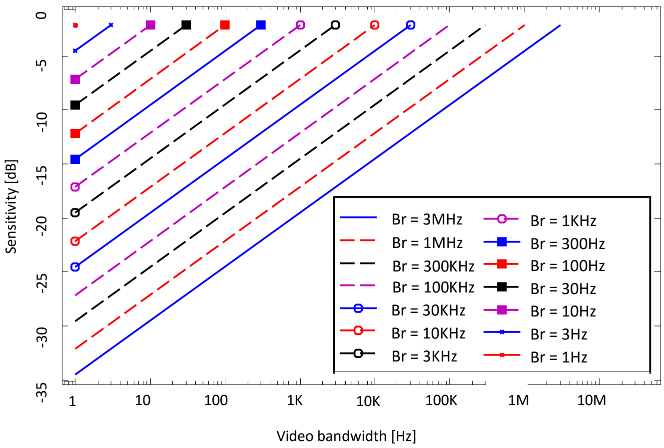

Figure 8. Variation of the $NE\Delta T$ as a function of video bandwidth for several values of resolution bandwidths.

Equation (3) can easily be satisfied even with the maximum value of resolution bandwidth, which is $3MHz$. The $NE\Delta T$ can be plotted as a function of video bandwidth for a range of possible resolution bandwidths as shown in Figure 8. The possible resolution bandwidths for a COTS spectrum analyzer can be formulated as $a \times 10^b Hz$, where $a \in \{1, 3\}$ and $b \in \{0, 1, 2, 3, 4, 5, 6\}$. The minimum required sensitivity can be calculated by considering the reflection of the brightness temperature at the top and bottom of the layer, the volumetric scattering inside the layer, and the surface scattering due to the roughness of the top and bottom interfaces. The volumetric scattering ranges from 2 to 8 dB/m, d depending on the volume fraction of air bubbles captured in the lake ice layer [40], [41]. The surface scattering from the top and bottom of the lake ice is within $2dB$ [42]. $NE\Delta T$ of less than $-20dB$ is desirable, and this can be achieved by setting the resolution bandwidth to $3MHz$ and the video bandwidth to $300Hz$. In the case of an airborne/spaceborne setup, the overall time of data collection is limited. Therefore, the design should aim for high sensitivity considering minimum achievable sweep time.

The optimum value for the video bandwidth and resolution bandwidth has been calculated using an optimization procedure. The constraint is sensitivity of less than $-20dB$ and the goal function is the sweep time. The optimum values for $F_S = 3GHz$ are listed in Table I. The best choice is for $B_r = 3MHz$ and $B_V = 300Hz$.

TABLE I
MINIMUM SWEEP TIME FOR OPTIMUM VIDEO AND RESOLUTION BAND WIDTHS

parameter	Optimum values			
Video bandwidth [Hz]	300	100	100	30
Resolution bandwidth [MHz]	3	3	1	3
Sweep time [s]	8.96	26.9	80.7	89.6
Sensitivity [dB]	-22.15	-24.54	-22.15	-27.15

E. Calibration Procedure

Since in WiBAR, the accurate absolute value of temperature is not required, the calibration procedure is different from other radiometers. In the calibration procedure, three sets of measurements are obtained from cold sky, hot absorber, and the layered medium.

In each resolution bandwidth the detected power spectral data is equal to $P(\omega) = kT(\omega)B_r G_S(\omega)$, where k is the Boltzmann's constant, T is the system temperature in Kelvin, B_r is the resolution bandwidth, and G_S is the radiometer gain. The system temperature consists of the summation of the receiver temperature (T_R) and the antenna aperture temperature (T_A). In the first measurement, sky measurement, $T_A(\omega) = T_{sky}(\omega)$, which is almost constant at our desired frequency band. In our other measurements, the antenna aperture temperature is equal to $T_A(\omega) = e(\omega)T_{object}$, where $e(\omega)$ is the emissivity and T_{object} is the physical temperature of the object and can be assumed constant. In our frequency range of interest the atmosphere can be considered lossless, when looking downward to the object. The physical temperature of the hot absorber and the slab are significantly larger than the sky temperature. The emissivity of the hot absorber is almost unity. The slab emissivity as a function of angular frequency is given by (7) [39].

$$e_{slab}(\omega) = \frac{(1-|\rho_1|^2)(1-|\rho_2|^2)}{1+|\rho_1|^2|\rho_2|^2+2|\rho_1||\rho_2|\cos\omega\tau_{del}} \quad (7)$$

where ρ_1 and ρ_2 are the top and bottom surface reflection coefficients, respectively. In this formulation, we assumed that the slab is almost lossless (low- absorbing and low scattering); therefore both the extinction and self-emission of the slab negligible.

In order to isolate $e_{slab}(\omega)$ from other frequency dependent parameters, we can use the ratio of the power spectral density of the slab corrected by that of sky over the hot absorber power spectral density corrected by that of sky as given by (8).

$$
\begin{aligned}
&\frac{P_{slab}-P_{sky}}{P_{abs}-P_{sky}} \\
&= \frac{G_{slab}(e_{slab}(\omega)T_{slab}+T_{R,slab})-G_{sky}(T_{sky}+T_{R,sky})}{G_{abs}(e_{abs}T_{abs}+T_{R,abs})-G_{sky}(T_{sky}+T_{R,sky})} \\
&= \frac{e_{slab}(\omega)T_{slab}G_{slab}+(T_{R,slab}G_{slab}-T_{R,sky}G_{sky})-T_{sky}G_{sky}}{e_{abs}T_{abs}G_{abs}+(T_{R,abs}G_{abs}-T_{R,sky}G_{sky})-T_{sky}G_{sky}} \\
&\approx \frac{(e_{slab}(\omega)T_{slab}-T_{sky})G_{slab}(\omega)}{(e_{abs}T_{abs}-T_{sky})G_{abs}(\omega)} \\
&\approx \frac{e_{slab}(\omega)T_{slab}-T_{sky}}{e_{abs}T_{abs}-T_{sky}},
\end{aligned}
\tag{8}
$$

The subscripts *abs*, *sky*, and *slab* corresponds to instantaneous value of T_R and G at the time those targets were observed. The following simplifications are considered; $T_{R,slab}G_{slab} = T_{R,sky}G_{sky} = T_{R,abs}G_{abs}$ and $G_{slab}(\omega) = G_{sky}(\omega) = G_{abs}(\omega)$. Equation (8) can be used in the calibration process to solve for the emissivity of the slab.

F. Autocorrelation Response

Finding the amplitude of the autocorrelation response from a finite set of spectral data is similar to spectral analysis of a truncated time series data. In our measurements, the spectral data demonstrate a periodic pattern that we call ripples. The spectral response of these ripples corresponds to a peak in the autocorrelation domain. We found that at least two ripples are required for detection of the layer thickness. The minimum detectable thickness is limited by the minimum ripples presented in the bandwidth of the WiBAR. The maximum thickness is limited by the resolution bandwidth and the number of points in spectrum analyzer.

Several spectrum estimation techniques have been utilized to recover the weak signal buried in noise. We found that the autoregressive technique based on Yule-Walker equation [43], [44] can estimate the autocorrelation response better than other techniques. The Yule-Walker equation is capable of reducing the spectrum noise and variance by computing the expectation of the model parameters convoluted with their lags. Therefore, the impact of ambient noise on the autocorrelation response is reduced significantly. The algorithm that we used to estimate the autocorrelation response is illustrated in Figure 9.

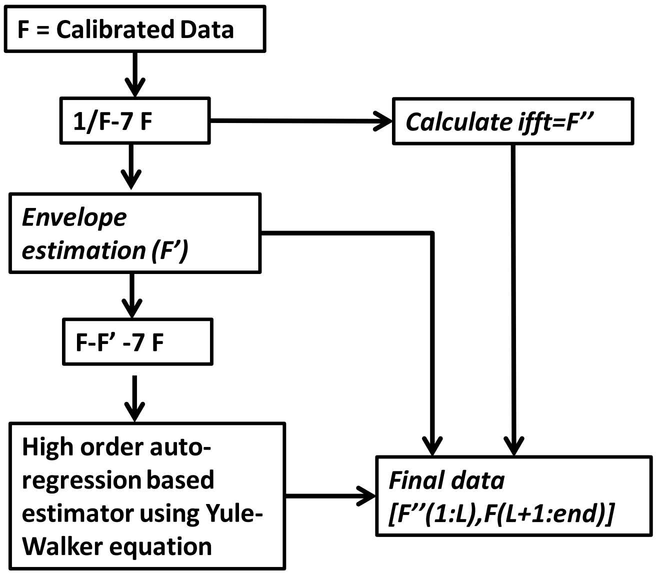

Figure 9. The spectrum estimation technique using Yule-Walker equation to reduce the noise.

G. Radio frequency interference

Remote sensing community demonstrates that microwave radiometry is subject to radio frequency interference (RFI) [45]. RFI is additive and narrowband. In our wideband implementation, the narrowband RFI is presented in power spectral data recording. However, applying the inverse Fourier transform in the post-processing unit diminishes the impact of RFI. Narrowband RFI can be modeled as impulse delta function in the power spectral domain. Applying the inverse Fourier transform to the impulse delta function equally distributes the power of RFI among different autocorrelation time components. Therefore, the effect of narrowband RFI is negligible. We are able to successfully recover the autocorrelation response in the presence of RFI.

(a)

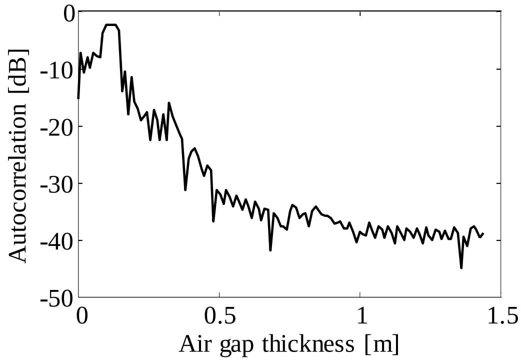

(b)

Figure 10. (a) The measurement setup for the thickness measurement of air gap over water. (b) The autocorrelation response of the measurement as a function of microwave transit time. The equivalent thickness is shown by the arrow in the inset.

H. Impact of surface roughness

The effect of roughness in our study is twofold. It reduces the amplitude of the delayed peak with respect to the zero-lag peak and it changes the emissivity. In order to formulate these effects, we derive the coherent reflectivity, and using the equation $e = 1 - |\Gamma|^2$, we can find coherent emissivity.

We calculate the coherent reflectivity by defining the following parameters. R_1 and T_1 are the reflection coefficient and transmission coefficients of the top interface in the absence of roughness from air into layer, R_2 is the reflection coefficient of the bottom interface in the absence of roughness from slab layer into underlying layer, r_1 and r_2 are the reduction in the reflection coefficient predicted by physical optics approximations for the top and bottom layers, respectively, when the wave is within the layer. t_1 is the change in the transmission coefficient due to the roughness predicted by physical optics approximation, when the wave is within the slab. The r' and t' are the changes in the reflection of transmission coefficients due to the surface roughness, when the wave is outside the slab. The coherent reflectivity by ray tracing is given by equation 9.

$$\Gamma = r_1 R_1 + t_1 t'_1 T_1 T'_1 r_2 e^{-j\omega\tau_{del}}$$

$$\times \left[1 - r'_1 R_1 R_2 r_2 e^{-j\omega\tau_{del}} + r'^2_1 R_1^2 r_2^2 R_2^2 e^{-j2\omega\tau_{del}} + \cdots\right]$$

$$= \frac{r_1 R_1 + r_2 R_2 e^{-j\omega\tau_{del}} (T_1 T'_1 t_1 t'_1 + r_1 r'_1 R_1 R'_1)}{1 + r'_1 R_1 r_2 R_2 e^{-j\omega\tau_{del}}} \qquad (9)$$

where index 1 refers to air and index 2 refers to the layer sandwiched between the top and bottom interfaces. For verification, if the interface is flat, all the r_1, r_2 , and t_1 are equal to 1. Due to the continuity of tangential fields, $T_i=1+R_i$ and $T'_i=1+R'_i$ for any interface i, $R_i = -R'_i$, by the expression for the reflection coefficient, and thus $T_1T'_1+R_1R'_1=1$ and the well–known reflection coefficient of a dielectric slab is obtained. The emissivity is given by (10):

$$e = \frac{\alpha+2R_1r_1R_2R_2[1-(T_1t_1T'_1t'_1-R_1r_1R'_1r'_1)]\cos\omega\tau_{del}}{1+R_1^2r_1^2R_2^2r_2^2+2R_1r_1R_2r_2\cos\omega\tau_{del}} \quad (10)$$

where

$$\alpha = 1 + R_1^2r_1^2R_2^2r_2^2 - R_1^2r_1^2 - R_2^2r_2^2(T_1t_1T'_1t'_1 - R_1r_1R'_1r'_1) \quad (11)$$

The delayed peak will go down by a value of 10 $\log_{10}(r' r_2)$. The value of the r_1, r , r_2, t_1, and t_2 can be estimated by physical optics (Kirchhoff) approximation as given by equation 12 [46].

$$r_1^2 = \exp\{-4k_0^2\sigma_1^2\cos^2\theta_1\}$$
$$r'^2_1 = \exp\{-4k_1^2\sigma_1^2\cos^2\theta_2\}$$
$$r_2^2 = \exp\{-4k_1^2\sigma_2^2\cos^2\theta_2\}$$
$$t_1^2 = t'^2_1 = \exp\{-(k_1\cos\theta_2 - k_0\cos\theta_1)^2\sigma_1^2\} \quad (12)$$

where σ_1 and σ_2 are the rms height of the surfaces on the top and bottom, respectively. k_i is the wave vector in the region i. The Kirchhoff condition is satisfied if $kl > 6$ and $l^2 > 2.76\sigma\lambda$, where l is the correlation length of the surface and $\lambda = 2\pi/k$ is the wavelength of the propagating wave. The reduction in the peak is shown in Figure 11.

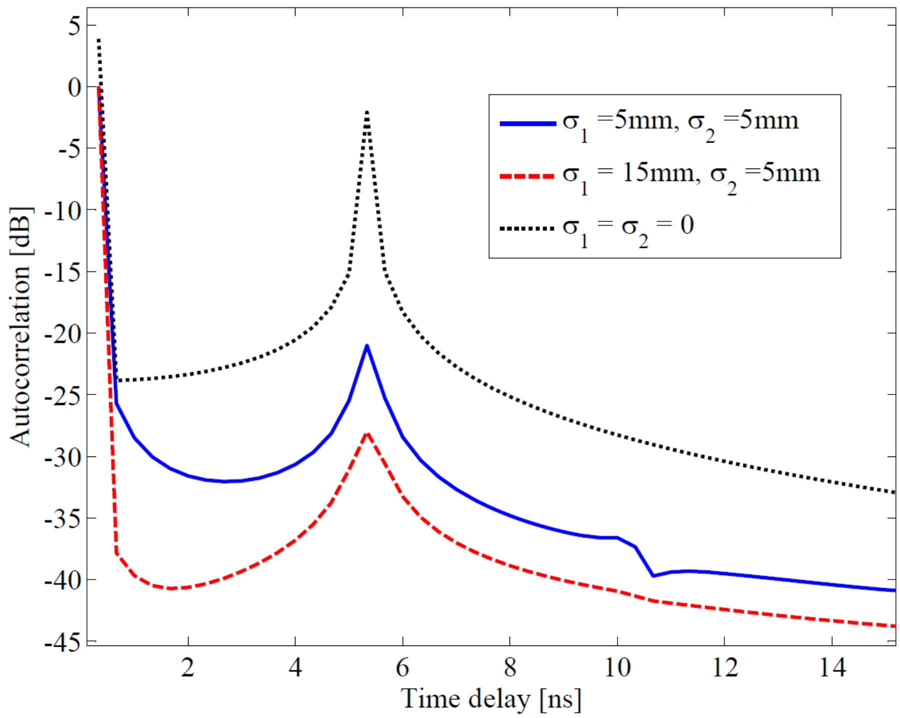

Figure 11. The reduction in the delay peak due to surface roughness is shown for several scenarios, in which an ice layer is over the water. The incident angle is assumed to be 45 degrees. The top and bottom layer rms height are shown in the inset. The inverse of the emissivity is used to calculate the autocorrelation response.

III. MEASUREMENT RESULTS

In this section the measurements are collected by a handheld spectrum analyzer ($AgilentN9344C$) with a maximum frequency of operation of $20GHz$. The resolution bandwidth is set to $3MHz$, the frequency span is $3GHz$ covering the frequency range of $7-10GHz$. The video bandwidth is fixed at $300Hz$ as suggested by the optimization procedure explained in Subsection II-D.2. The $NE\Delta T$ is $-22.15dB$. In order to verify the functionality of the WiBAR as well as the validity of our thickness detection algorithm, we have performed several measurements on different layered media including an air gap between water and a thin high dielectric constant sheet ($FR4$), fresh water ice, and snow layer over the terrain. In our analysis, we have assumed that the dielectric constant of ice at our frequency range of interest is 3.15 [47]. Based on theory and the measurements that we performed, the minimum detectable ice thickness should be $5cm$. We gathered the horizontally polarized (H-pol) far field measurements of lake ice or snow covered terrains using our implemented WiBAR at several locations in Michigan under varying conditions and thickness values. Rather than use of model-based estimates of the snowpack's average dielectric properties, we used the refractive index mixing formula and snow density profiles measured in snow pits. The reconstructed estimated snow thicknesses are in good agreement with *in-situ* measurements. The far-field measurement is the basis for remote sensing of ice and snow. The accuracy of the test scenarios verify the potential of the WiBAR for airborne/space-borne remote sensing of snow and ice. In the following Subsections III-A,III-C, and III-B, the far-field thickness measurement of air gap, lake ice, and snow over asphalt are presented.

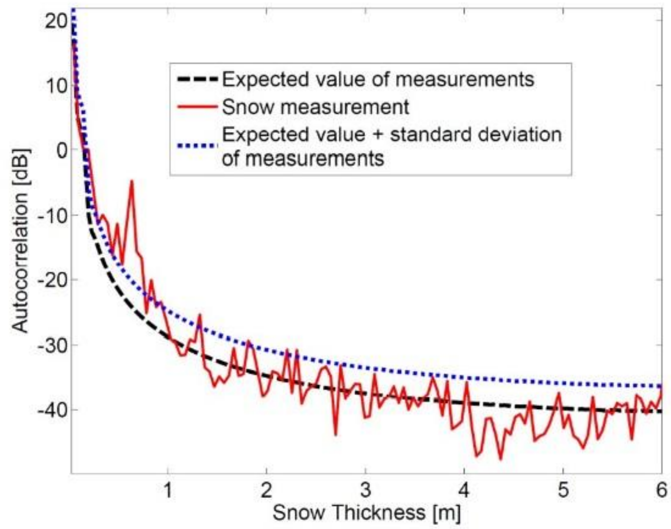

(a) **(b)**

Figure 12. (a) The measurement setup for the thickness measurement of snow over terrain. (b) The autocorrelation response of the measurement as a function of snow layer thickness. The expected value of the measurement as well as the summation of the expected value and the standard deviation are shown by dashed black line and dotted blue line, respectively.

A. Far-field measurement of air gap between fresh water and FR4 sheet

We claim that our WiBAR is capable of detecting the thickness of any low-absorbing layered media. In order to verify this claim, we prepared a test scenario in which an air gap is between water in a small pool and a high dielectric constant thin sheet. We chose $FR4$ due to its high dielectric constant and stiffness. Our calculations as well as simulation results show that the water emission is reflected back partially at the interface of the sheet. We verified our calculations by placing two antennas at the far field of each other with and without the sheet placed between them. We estimated the reflectivity to be 0.11. By placing the sheet over the pool, the water emission is partially reflected back and forth inside the air gap layer. Using WiBAR, we were able to find the thickness of the air gap for several scenarios by varying the water level in the pool. One test scenario as well as the reconstructed results are shown in Figure 10 (a) and (b), respectively.

The measurement results, shown in Figure 10 (b), are in good agreement with the *in −situ* measurement of the gap using a measure tape. The error in the measurement is within $0.6cm$.

(a)

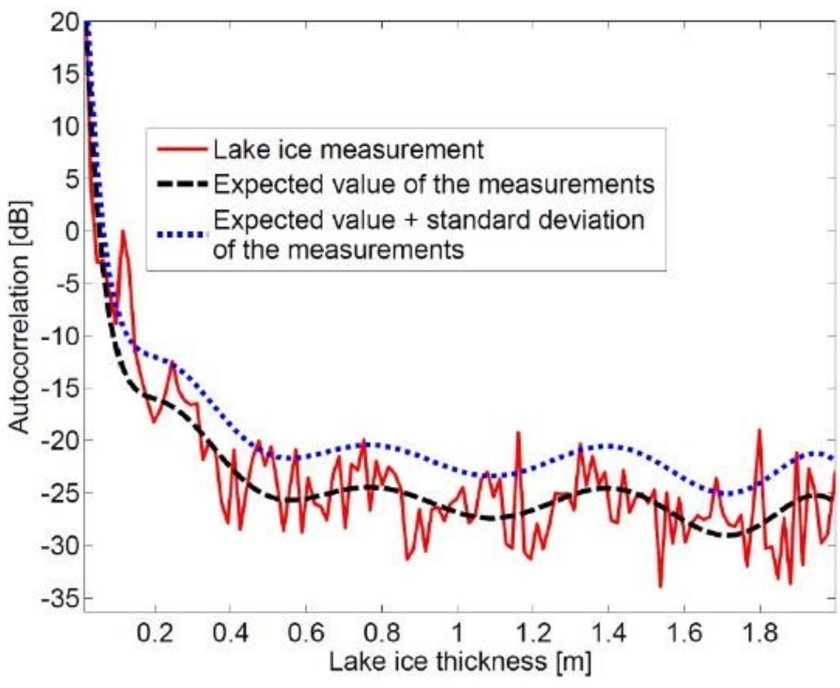

(b)

Figure 13. (a) The measurement setup for the thickness measurement of lake ice over water. (b) The autocorrelation response of the measurement as a function of the ice layer thickness. The expected value

of the measurement as well as the summation of the expected value and the standard deviation are shown by dashed black line and dotted blue line, respectively

B. Far-field measurement of snow layer

The second set of measurements was performed for further verification of the radiometer's operation. The first scenario considers a naturally formed snow pit with the depth of $64cm$ i over smooth terrain. The measurement set up as well as the autocorrelation response as a function of snow layer thickness are shown in Figure 12 (a) and (b), respectively. The field experiment was performed at University of Michigan Biological Station located at Pellston, MI.

The detected peak is located at $64.7cm$. The dielectric constant of snow is calculated using the refractive index mixing formula for a proper portion for the ice and air. The proper ratio is observed on site by measuring the density of the snow. The accuracy of this method is within $0.7cm$ for the snow measurements. The expected value is calculated by using only the estimated polynomial fitted envelope of the calibrated signal. This signal fed into the algorithm and the result is the expected. The variance is estimated using the sky or load measurements.

C. Far-field measurement of ice layer

The measurement is performed on a Dexter, MI pond with ice thickness around $11.7cm$. The thickness was measured *in-situ* using a hand drill by drilling a hole through the ice. We highlight that the *in-situ* measurements have accuracy within $1cm$ due to the ice layer perturbation caused by the drilling. The measurement set up is shown is Figure 13 (a) and the autocorrelation response is shown in Figure 13 (b). The accuracy of this measurement is within $0.87cm$. The ice thickness measurement using autocorrelation radiometer is in good agreement with the $in-situ$ measurement.

IV. CONCLUSION

The accuracy of a remote sensing estimation of low-loss dielectric layer thickness over a semi- infinite lossy medium is considered. This method is applied to the estimation of the thickness of snow or ice layer over ground or lake. This method is thoroughly modeled, simulated, and verified using the measured results obtained from a novel wideband auto-correlation radiometer (WiBAR). By transforming the power spectral data to the time domain, the thickness of the ice/snow layer is estimated. The optimal design for the radiometer is presented. The radiometer has been tested for several controlled experiments as well as natural scenarios including snow and ice layers where the accuracy is found to be within 1.5*cm* for H-pol far-field measurements compared to *in-situ* measurements.

V. ACKNOWLEDGMENT

The authors would like to thankfully acknowledge the financial support for this project, which was awarded by the Department of Energy (DoE) in Wind and Water Power Program (contract no. DE-EE0005376). We also thank the staff of Michigan Technological University in Great Lakes Research Center (Michael Abbott, Jamey Anderson, and Colin Tyrrell) for their kind help and support during our measurements in Keweenaw Peninsula, MI.

REFERENCES

[1] S. M. Olmstead, "Climate change adaptation and water resource management: Areview of the literature," *EnergyEconomics*, pp. 1–10, 2013.

[2] J. Schweizer, K. Kronholm, J. B. Jamieson, and K. W. Birkeland, "Review of spatial variability of snowpack properties and its importance for avalanche formation," *Cold Regions Science and Technology*, vol. 51, p. 253272, 2008.

[3] J. R. B. Waitt, T. C. Pierson, N. S. Macleod, R. J. Janda, B. Voight, and R. T. Holcomb, "Eruption-triggered avalanche, flood, and lahar at mount st. helenseffects of winter snowpack," *Science*, vol. 221, no. 4618, pp. 1394–1397, 1983.

[4] J. Lopez-Moreno, S. Goyette, and M. Beniston, "Impact of climate change on snowpack in the pyrenees: Horizontal spatial variability and vertical gradients," *Journal of Hydrology*, vol. 374, no. 3-4, p. 384396, 2009.

[5] B. Goodison, E. Barry, and A. E.Walker, "Use of snow cover derived from satellite passive microwave data as an indicator of climate change," *Ann. Glaciol.*, vol. 17, pp. 137–142, 1993.

[6] P. C. D. Milly, J. Beancourt, M. Falkenmark, R. M. Hirsch, Z. W. Kundzewicz, D. P. Lettenmaier, and R. J. Stouffer, "Stationarity is dead: Whither water management?" *Science*, vol. 319, no. 5863, pp. 573–574, Feb. 2008.

[7] M. C. Serreze, J. E. Walsh, F. S. Chapin, T. Osterkamp, M. Dyurgerov, V. Romanovsky, W. C. Oechel, J. Morison, T. Zhang, and R. G. Barry, "Observational evidence of recent change in the northern high-latitude environment," *Clim. Chang.*, vol. 46, no. 1/2, pp. 159–207, Jul. 2000.

[8] *Global Energy and Water Cycle Experiment (GEWEX) Continental-Scale International Project (GCIP): A review of progress and opportunities*. Washington, D.C.: Nat. Res. Council, Nat. Acad. Press, 1998.

[9] *Opportunities in the hydrologic sciences*. Washington, D.C.: Comm. Opportunities Hydrol. Sci., Nat. Res. Council, Nat. Acad. Press, 1991.

[10] "Report of Chapman conference on hydrological aspects of global climate change," *J. Geophys. Res.*, vol. 97, pp. 2675–2833, 1992.

[11] R. T. Sutton, B. Dong, and J. M. Gregory, "Land/sea warming ratio in response to climate change: Ipcc ar4 model results and comparison with observations," *Geophys. Res. Lett.*, vol. 34, p. L02701, 2007.

[12] C. J. Vrsmarty, L. D. Hinzman, B. J. Peterson, D. H. Bromwich, L. C. Hamilton, J. Morison, V. E. Romanovsky, M. Sturm, and R. S.Webb, "The hydrologic cycle and its role in arctic and global environmental change: A rationale and strategy for synthesis study," Arctic Res. Consort. U.S., Fairbanks, AK, Tech. Rep., 2000.

[13] A. W. England, "Thermal microwave emission from a halfspace containing scatterers," *Radio Sci.*, vol. 9, no. 4, pp. 447–454, Apr. 1974.

[14] ——, "Thermal microwave emission from a scattering layer," *J. Geophys. Res.*, vol. 80, no. 32, pp. 4484–4496, Nov. 1975.

[15] A. T. C. Chang, J. L. Foster, D. K. Hall, A. Rango, and B. K. Hartline, "Snow water equivalent estimation by microwave radiometry," *Cold Regions Sci. Technol.*, vol. 5, no. 3, pp. 259–267, Mar. 1982.

[16] T. Koike and T. Suhama, "Passive-microwave remote sensing of snow," *Ann. Glaciol.*, vol. 18, pp. 305–308, 1993.

[17] J. F. Galantowicz and A. W. England, "Seasonal snowpack radiobrightness interpretation using a SVAT-linked emission model," *J. Geophys. Res.*, vol. 102, no. D18, pp. 21 933–21 946, 1997.

[18] J. T. Pulliainen, J. Grandell, and M. T. Hallikainen, "Hut snow emission model and its applicability to snow water equivalent retrieval," *IEEE Trans. Geosci. Remote Sens.*, vol. 37, no. 3, pp. 1378–1390, May 1999.

[19] L. L. Wilson, L. Tsang, J. N. Hwang, and C. T. Chen, "Mapping snow water equivalent by combining a spatially distributed snow hydrology model with passive microwave remote-sensing data," *IEEE Trans. Geosci. Remote Sens.*, vol. 37, no. 2, pp. 690–704, Mar. 1999.

[20] J. T. Pulliainen and M. T. Hallikainen, "Retrieval of regional snow water equivalent from space-borne passive microwave observations," *Remote Sens. Environ*, vol. 75, no. 1, pp. 76–85, Jan. 2001.

[21] C. Derksen, B. Goddison, E. Ledrew, and A.Walker, "Combining SMMR and SSM/I data for time series analysis of central North American snow water equivalent," *J. Hydromet.*, vol. 4, no. 2, pp. 304–316, Apr. 2003.

[22] J.-J. Guo, L. Tsang, E. G. Josberger, A. W. Wood, J.-N. Hwang, and D. P. Lettenmaier, "Mapping the spatial distribution and time evolution of snow water equivalent with passive microwave measurements," *IEEE Trans. Geosci. Remote Sens.*, vol. 41, no. 3, pp. 612–621, Mar. 2003.

[23] R. E. Kelly, A. T. C. Chang, L. Tsang, and J. L. Foster, "A prototype AMSR-E global snow area and snow depth algorithm,"*IEEE Trans. Geosci. Remote Sens.*, vol. 41, no. 2, pp. 230–242, Feb. 2003.

[24] M. Durand, E. J. Kim, and S. A. Margulis, "Quantifying uncertainty in modeling snow microwave radiance for a mountain snowpack at the pointscale, including stratigraphic effects," *IEEE Trans. Geosci. Remote Sens.*, vol. 46, no. 6, pp. 1753–1767, Jun. 2008.

[25] B. B. Stankov, D. Cline, B. L.Weber, A. J. Gasiewski, and G. A.Wick, “High-resolution airborne polarimetric microwave imaging of snow cover during the NASA cold land processes experiment,” *IEEE Trans. Geosci. Remote Sens.*, vol. 46, no. 11, pp. 3672–3693, Nov. 2008.
[26] J. Lemmetyinen, C. Derksen, J. Pulliainen, W. Strapp, P. Toose, A. Walker, S. Tauriainen, J. Pihlflyckt, J.-P. Krn, and M. Hallikainen, “A comparison of airborne microwave brightness temperatures and snowpack properties across the boreal forests of Finland and western canada,” *IEEE Trans. Geosci. Remote Sens.*, vol. 47, no. 3, pp. 965–978, Mar. 2009.
[27] M. T. Hallikainen and P. A. Jolma, “Retrieval of the water equivalent of snow cover in Finland by satellite microwave radiometry,” *IEEE Trans. Geosci. Remote Sens.*, vol. GE-24, no. 6, pp. 855–862, Nov. 1986.
[28] M. T. Hallikainen, “Comparison of algorithms for retrieval of snow water equivalent from Nimbus-7 SMMR data in Finland,” *IEEE Trans. Geosci. Remote Sens.*, vol. 30, no. 1, pp. 124–131, Jan. 1992.
[29] M. J. McFarland, G. D. Wilke, and P. H. Harder, “Nimbus 7 SMMR investigation of snowpack properties in the northern great plains for the winter of 1978-1979,” *IEEE Trans. Geosci. Remote Sens.*, vol. GE-25, no. 1, pp. 3–46, Jan. 1987.
[30] A. T. C. Chang, J. L. Foster, D. K. Hall, D. A. Robinson, L. Peiji, and C. Meisheng, “The use of microwave radiometer data for characterizing snow storage in western China,” *Ann. Glaciol.*, vol. 16, pp. 26–30, 1992.
[31] J. Manwell, C. Elkinton, A. Rogers, and J. McGowan, “Review of design conditions applicable to offshore wind energy systems in the united states,” *Renewable and Sustainable Energy Reviews*, vol. 11, no. 2, pp. 210–234, 2007.
[32] E. Marshall and T. Randhir, “Effect of climate change on watershed system: a regional analysis,” *Climatic Change*, vol. 89, p. 263280, 2008.
[33] G. Macelloni, S. Paloscia, P. Pampaloni, and M. Tedesco, “Microwave emission from dry snow: A comparison of experimental and model results,” *IEEE Trans. Geosci. Remote Sens.*, vol. 39, no. 12, pp. 2649–2656, Dec. 2001.
[34] M. Brogioni, G. Macelloni, E. Palchetti, S. Paloscia, P. Pampaloni, S. Pettinato, E. Santi, A. Cagnati, and A. Crepaz, “Monitoring snow characteristics with ground-based multifrequency microwave radiometry,” *IEEE Trans. Geosci. Remote Sens.*, vol. 47, no. 11, pp. 3643–3655, Nov. 2009.
[35] A. W. England, “Wideband autocorrelation radiometric sensing of microwave travel time in snowpacks and planetary ice layers,” *IEEE Trans. Geosci. Remote Sens.*, vol. 51, no. 4, pp. 2316–2326, Apr. 2013, part 2.
[36] A. W. England, H. Nejati, and A. Mims, “Snowpack and freshwater ice sensing using autocorrelation radiometry,” in *IEEE IGARSS*, Vancouver, BC, Canada, Jul. 2011, pp. 3764–3767.
[37] https://science.nrao.edu/facilities/vla/observing/RFI.
[38] M. Bertocco and A. Sona, “On the measurement of power via a superheterodyne spectrum analyzer,” *IEEE Transactions on Iinstrumentation and Measurement*, vol. 55, no. 5, pp. 1494–1501, 2006.
[39] F. Ulaby, *Microwave Remote Sensing: Active and Passive, Volume II: Radar Remote Sensing and Surface Scattering and Emission Theory*. Addison-wesley, 1981.

[40] R. S. Vickers, “Microwave properties of ice from the great lakes,” Menlo Park: Stanford Research Institute,” SRI Project 3571, 1975.
[41] R. Leconte and P. D. Klassen, “Lake and river ice investigations in northern Manitoba using airborne SAR imagery,” *The Arctic Institute North America*, vol. 44, no. 5, pp. 153–163, 1991.
[42] H. Han and H. Lee, “Radar backscattering of lake ice during freezing and thawing stages estimated by ground-based scatterometer experiment and inversion from genetic algorithm,” *IEEE Transactions on Geoscience and Remote Sensing*, vol. 51, no. 5, pp. 3089–3096, 2013.
[43] P. Stoica and T. Soderstrom, “High-order Yule-Walker equations for estimating sinusoidal frequencies: The complete set of solutions,” *Signal processing*, vol. 20, no. 3, pp. 257–263, 1990.
[44] P. Stoica and R. L. Moses, *Introduction to spectral analysis*. Prentice hall, Upper Saddle River, NJ, 1997, vol. 1.
[45] R. D. D. Roo, S. Misra, and C. S. Ruf, “Sensitivity of the kurtosis statistic as a detector of pulsed sinusoidal rfi,” *IEEE Transactions on Geoscience and Remote Sensing*, vol. 45, no. 7, pp. 1938–1946, 2007.
[46] F. Ulaby, R. Moore, and A. Fung, *Microwave Remote Sensing: Active and Passive, Volume II: Radar Remote Sensing and Surface Scattering and Emission Theory*. Artech House, Inc, 1986.
[47] F. T. Ulaby, R. K. Moore, and A. K. Fung, *Microwave Remote Sensing: Active and Passive*. Artech House, 1986, vol.III, pp. 1065-2162.

APPENDIX 6.2

LAKE ICE MEASUREMENT DATA AND PROCESSING RESULTS

1. METHODS

In this report we are going to use different methods to find the propagation time τ_{delay} of microwaves through the low loss ice layer over the Lake Superior. Methods are 1.) Time Delay Estimation via Standard Inverse Fourier Transform (ifft) from the observation data, 2.) Time Delay Estimation via Rotational Invariance Techniques (ESPRIT) [1][2], and 3.) Time Delay Estimation via Sparse Covariance-Based Estimation Technique (SPICE) [3].

In the first method (standard iFFT), we detect the time delay as the largest peak after the zero delay peak from the autocorrelation response. In the second method (ESPRIT), we choose the largest peak after zero delay as the time delay in the ice or snow pack. In the last method (SPICE), we are looking for the largest peak in the range of 0.5 – 10 ns. The reason for choosing lower limit of 0.5 ns is to eliminate the peak at zero delay which is highest, and other peaks due to the radiometer itself. In addition, we have chosen the upper limit of 10 ns since peaks at delays higher than this do not contain much information in these measurements. In fact, we expect to see lower peaks at delay times more than 10 ns since signal levels are further attenuated. On the other hand, at some point, we may observe some peaks at higher time delays. They may be due to the conditions and settings at the time of measurements; in fact, detecting the time delay peak with WiBAR has been shown to be really sensitive to the settings at the time of measurement. However, in some figures such as Figure 1.1 to 1.3, we have chosen the upper limit of 25 ns, and we observed that there is only one peak at 3.858 ns. These three figures show the three techniques used to extract lake ice thickness.

To wrap it up, we estimate the time delay as the location of the largest peak, and then we need to do some subsequent operations in order to estimate the amplitude of these delay peaks. Results are collected in Table 1. We have used the term 'NaN' in Table 1, which means that the method was not able to detect the peak either because there were many peaks at the same amplitude close to each other, which may be due to the ice movement and change of the angle of incidence from the ice air interface such as Figure 1.4, or no peak was shown up in the range such as in Figure 1.5.

The refractive index of the ice n_i is $\sqrt{3.15}$. We use the following formula in order to estimate the thickness of the ice pack on the Lake Superior. The incident angle ϑ was 45° at the time of measurement.

$$\frac{1}{2} c\tau_{delay} \approx d\sqrt{n_i^2 - sin^2\vartheta} \qquad (1)$$

We report the time delays and their corresponding thicknesses of the ice pack on Lake Superior from February to April 2014.

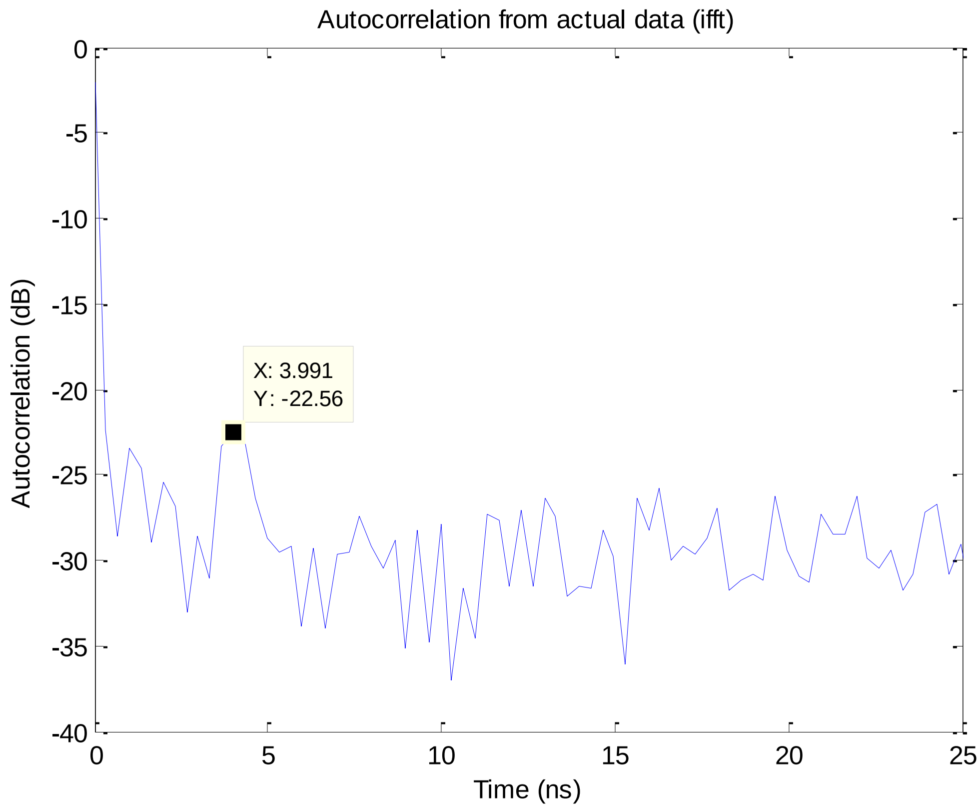

Lake ice results via Standard Inverse Fourier Transform (ifft)

Date	**Time**	**Measured delay by this method**	**Amplitude of the delay peak by this method**	**Ice Thickness**
2014 Feb 08	12:00:00	3.991 ns	-22.56 dB	36.77 cm

Fig. 1.1 Time Delay Estimation via Standard Inverse Fourier Transform (iFFT)

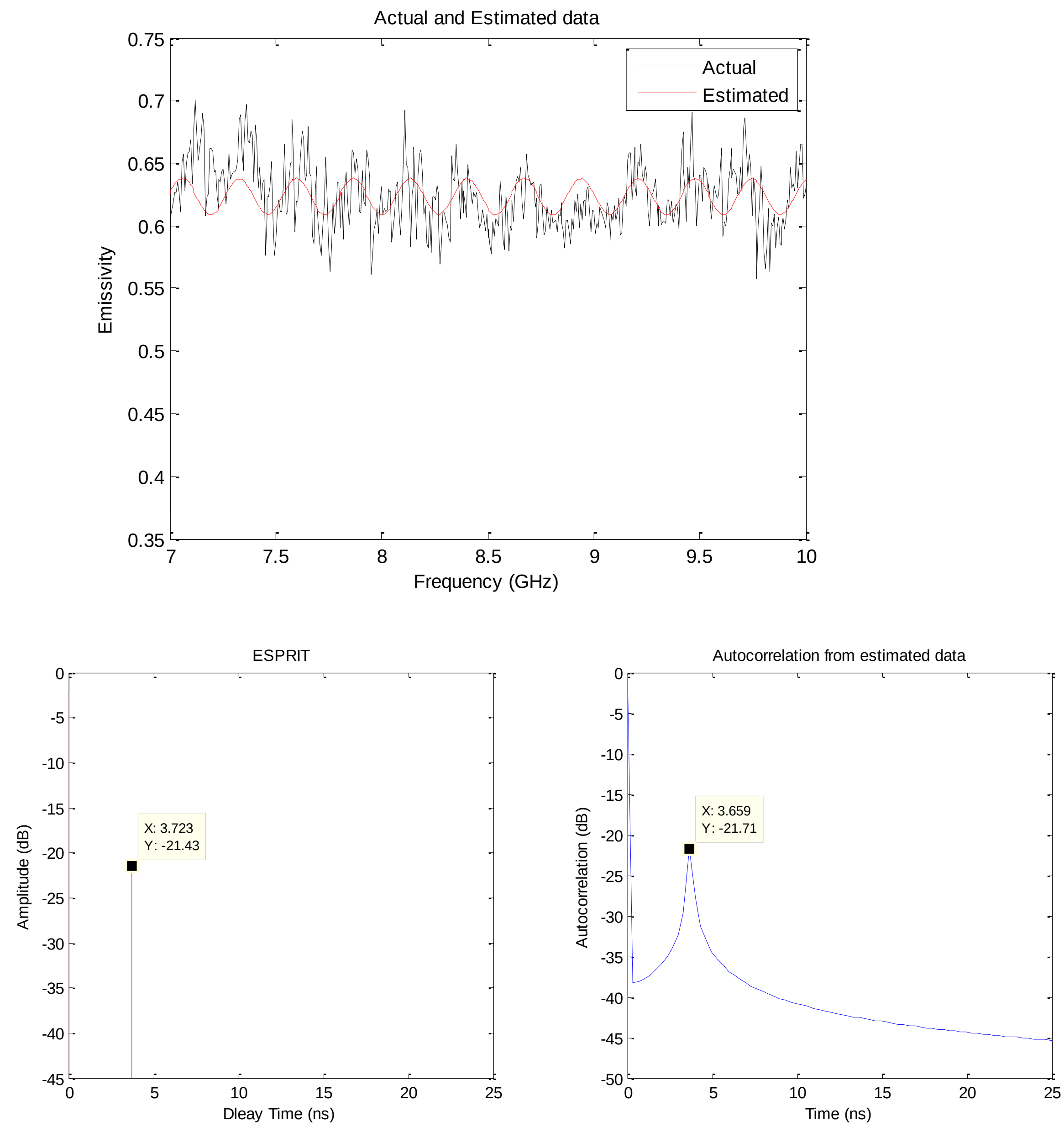

Lake ice results via Rotational Invariance techniques (ESPRIT)

Date	**Time**	**Measured delay by this method**	**Amplitude of the delay peak by this method**	**Ice Thickness**
2014 Feb 08	12:00:00	3.723 ns	-21.43 dB	34.30 cm

Fig. 1.2 Time Delay Estimation via ESPRIT Technique

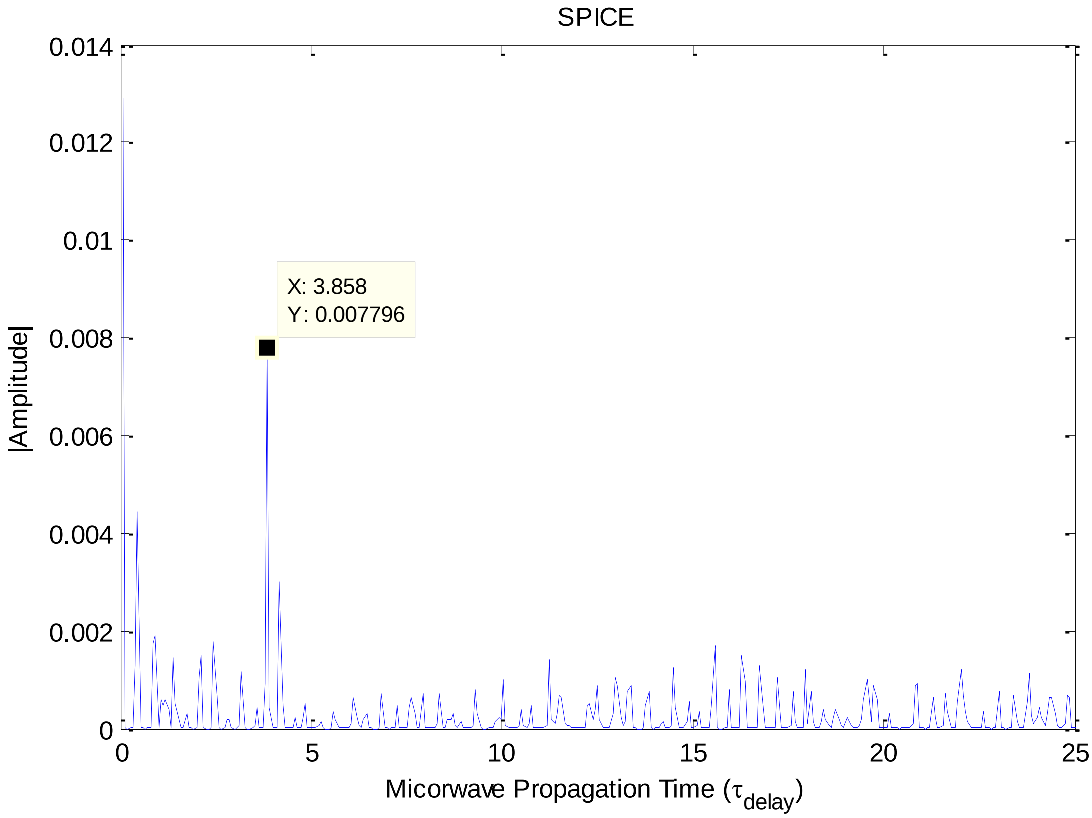

Time Delay Estimation via Sparse Covariance-Based Estimation Technique (SPICE)

Date	**Time**	**Measured delay by this method**	**Amplitude of the delay peak by this method**	**Ice Thickness**
2014 Feb 08	12:00:00	3.858 ns	-21.08 dB	35.55 cm

Fig. 1.3 Time Delay Estimation via SPICE Technique.

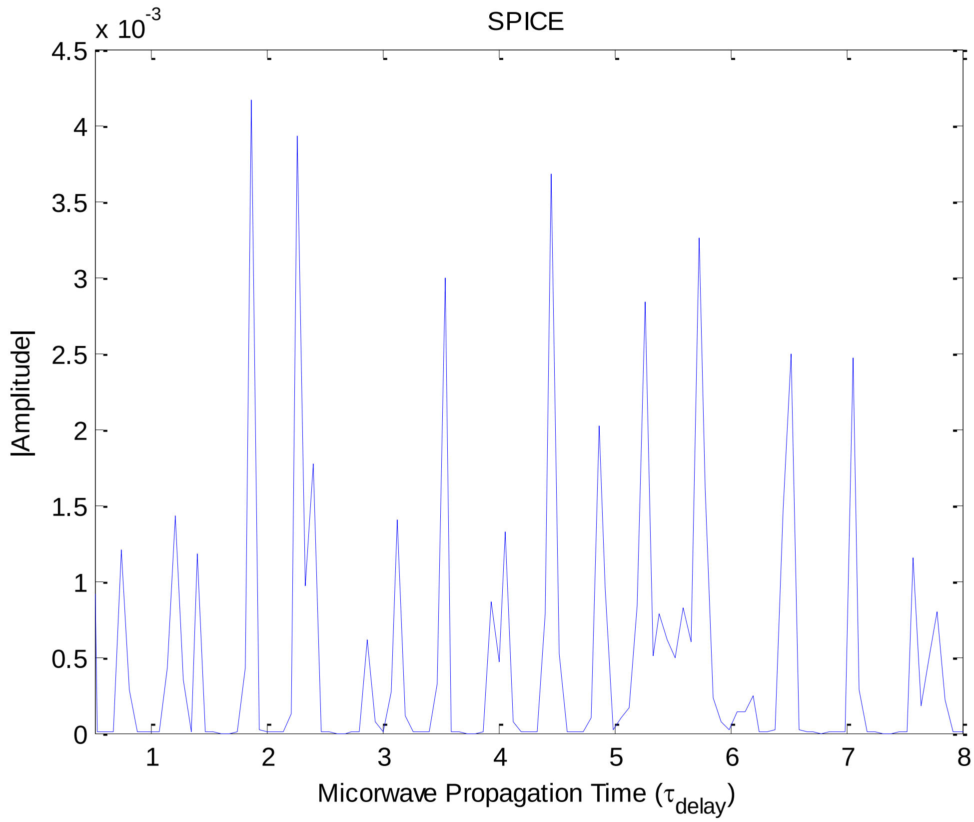

Time Delay Estimation via Sparse Covariance-Based Estimation Technique (SPICE)

Date	**Time**	**Measured delay by this method**	**Amplitude of the delay peak by this method**	**Ice Thickness**
2014 Mar 16	14:00:01	NaN	NaN	NaN

Fig. 1.4 Time Delay Estimation via SPICE Technique: extracted many peaks

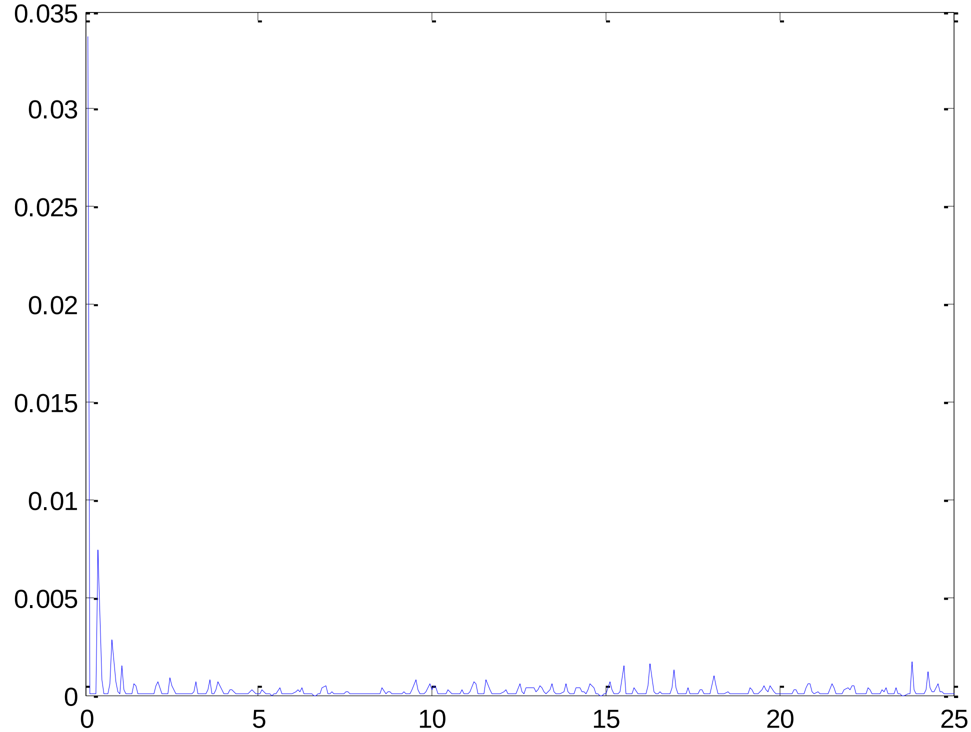

Table.3-3 Time Delay Estimation via Sparse Covariance-Based Estimation Technique (SPICE)

Date	**Time**	**Measured delay by this method**	**Amplitude of the delay peak by this method**	**Ice Thickness**
2014 Feb 08	15:30:02	NaN	NaN	NaN

Fig. 1.5 Time Delay Estimation via SPICE Technique: no ice thickness extracted

2. Results

The estimated time delay and their corresponding thicknesses of the ice pack on Lake Superior from February to April 2014 are shown in Figures 2.1 and 2.2, respectively.

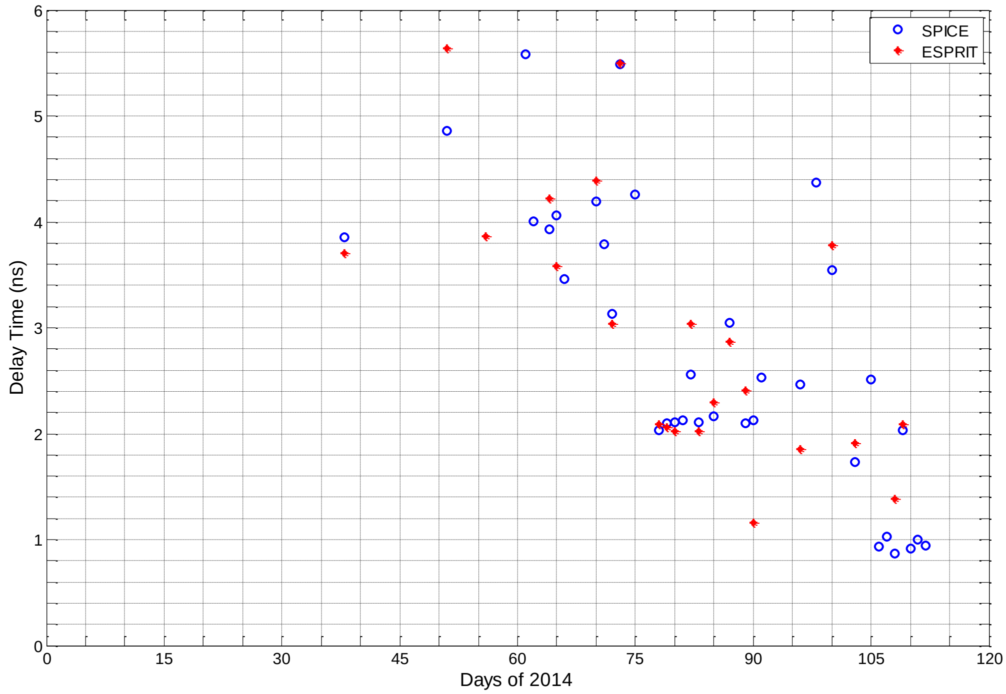

Figure 2.1 Time delay estimation over days of 2014.

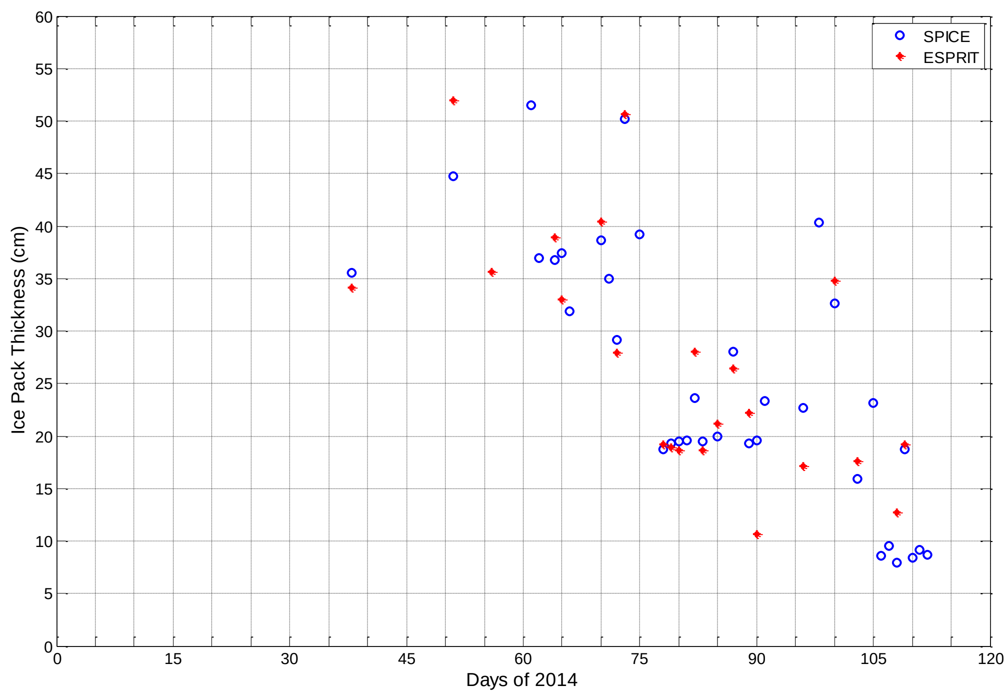

Figure 2.2 Ice pack thickness estimation over days of 2014

Table 1

	SPICE Technique			ESPRIT Technique			IFFT Technique		
Date and Time	**Delay (ns)**	**Amp. (dB)**	**Thickness (cm)**	**Delay (ns)**	**Amp. (dB)**	**Thickness (cm)**	**Delay (ns)**	**Amp. (dB)**	**Thickness (cm)**
2/8/14 12:00	3.858	-21.08	**35.55**	3.723	-21.43	**34.3**	3.991	-22.56	**36.77**
2/8/14 13:12	3.858	-21.11	**35.55**	3.838	-19.79	**35.36**	3.991	-21.82	**36.77**
2/8/14 15:30	NaN	NaN	NaN	NaN	NaN	NaN	NaN	NaN	NaN
2/8/14 16:00	NaN	NaN	NaN	3.708	-29.24	**34.16**	NaN	NaN	NaN
2/8/14 16:30	NaN	NaN	NaN	NaN	NaN	NaN	NaN	NaN	NaN
2/8/14 17:00	3.858	-28.77	**35.55**	NaN	NaN	NaN	NaN	NaN	NaN
2/9/14 8:05	NaN	NaN	NaN	NaN	NaN	NaN	NaN	NaN	NaN
2/19/14 13:47	NaN	NaN	NaN	NaN	NaN	NaN	NaN	NaN	NaN
2/19/14 14:41	NaN	NaN	NaN	NaN	NaN	NaN	NaN	NaN	NaN
2/20/14 11:10	NaN	NaN	NaN	NaN	NaN	NaN	NaN	NaN	NaN
2/21/14 11:10	4.856	-26.19	**44.74**	5.636	-24.59	**51.93**	NaN	NaN	NaN
2/26/14 14:00	NaN	NaN	NaN	3.867	-25.11	**35.63**	NaN	NaN	NaN
2/28/14 14:00	NaN	NaN	NaN	NaN	NaN	NaN	NaN	NaN	NaN
3/1/14 14:00	NaN	NaN	NaN	NaN	NaN	NaN	NaN	NaN	NaN
3/3/14 14:00	5.58	-24.43	**51.48**	NaN	NaN	NaN	NaN	NaN	NaN
3/4/14 14:00	4.008	-28.53	**36.93**	NaN	NaN	NaN	NaN	NaN	NaN
3/5/14 14:00	NaN	NaN	NaN	NaN	NaN	NaN	NaN	NaN	NaN
3/6/14 14:00	3.925	-25.75	**36.76**	4.224	-24.75	**38.92**	NaN	NaN	NaN
3/7/14 14:00	4.058	-25.57	**37.39**	3.584	-24.15	**33.02**	NaN	NaN	NaN
3/8/14 14:00	3.459	-24.89	**31.87**	NaN	NaN	NaN	NaN	NaN	NaN
3/9/14 14:00	NaN	NaN	NaN	NaN	NaN	NaN	NaN	NaN	NaN
3/10/14 14:00	NaN	NaN	NaN	NaN	NaN	NaN	NaN	NaN	NaN
3/11/14	NaN	NaN	NaN	NaN	NaN	NaN	NaN	NaN	NaN

14:00									
3/12/14 14:00	4.191	-22.91	**38.61**	4.39	-22.05	**40.45**	NaN	NaN	NaN
3/13/14 14:00	3.792	-20.22	**34.93**	NaN	NaN	NaN	NaN	NaN	NaN
3/14/14 14:00	3.127	-23.94	**29.11**	3.037	-24.04	**27.98**	NaN	NaN	NaN
3/15/14 14:00	5.488	-21.92	**50.22**	5.5	-22.79	**50.68**	NaN	NaN	NaN
3/16/14 14:00	NaN	NaN	NaN	NaN	NaN	NaN	NaN	NaN	NaN
3/17/14 14:00	4.257	-22.38	39.22	NaN	NaN	NaN	NaN	NaN	NaN
3/18/14 14:00	NaN	NaN	NaN	NaN	NaN	NaN	NaN	NaN	NaN
3/19/14 13:00	NaN	NaN	NaN	NaN	NaN	NaN	NaN	NaN	NaN
3/20/14 13:00	2.029	-21.23	**18.69**	2.088	-21.78	**19.24**	NaN	NaN	NaN
3/21/14 13:00	2.095	-26	**19.3**	2.057	-21.78	**18.95**	NaN	NaN	NaN
3/22/14 13:00	2.112	-27.08	**19.46**	2.026	-22.86	**18.66**	NaN	NaN	NaN
3/23/14 13:00	2.129	-26.85	**19.61**	NaN	NaN	NaN	NaN	NaN	NaN
3/24/14 13:00	2.561	-23.82	**23.59**	3.038	-25.69	**27.99**	NaN	NaN	NaN
3/25/14 13:00	2.112	-25.46	**19.46**	2.026	-21.72	**18.66**	NaN	NaN	NaN
3/26/14 13:00	NaN	NaN	NaN	NaN	NaN	NaN	NaN	NaN	NaN
3/27/14 13:00	2.162	-24.64	**19.92**	2.3	-22.72	**21.19**	NaN	NaN	NaN
3/28/14 13:00	NaN	NaN	NaN	NaN	NaN	NaN	NaN	NaN	NaN
3/29/14 13:00	3.043	-21.44	**28.04**	2.866	-22.77	**26.4**	NaN	NaN	NaN
3/30/14 13:00	NaN	NaN	NaN	NaN	NaN	NaN	NaN	NaN	NaN
3/31/14 13:00	2.095	-24.25	**19.3**	2.409	-23.08	**22.19**	NaN	NaN	NaN
4/1/14 13:00	2.129	-25.69	**19.61**	1.158	-29.48	**10.67**	NaN	NaN	NaN
4/2/14 13:00	2.528	-24.57	**23.29**	NaN	NaN	NaN	NaN	NaN	NaN
4/7/14 13:00	2.461	-19.54	**22.67**	1.857	-23.87	**17.11**	NaN	NaN	NaN
4/9/14	4.374	-24.19	**40.3**	NaN	NaN	NaN	NaN	NaN	NaN

9:46									
4/11/14 8:47	3.542	-25.77	**32.63**	3.779	-27.68	**34.82**	NaN	NaN	NaN
4/14/14 16:47	1.73	-24.34	**15.93**	1.908	-25.13	**17.58**	NaN	NaN	NaN
4/15/14 5:00	NaN	NaN	NaN	NaN	NaN	NaN	NaN	NaN	NaN
4/16/14 13:39	2.511	-22.88	**23.13**	NaN	NaN	NaN	NaN	NaN	NaN
4/17/14 5:00	0.931	-22.69	**8.58**	NaN	NaN	NaN	NaN	NaN	NaN
4/18/14 5:00	1.031	-23.62	**9.5**	NaN	NaN	NaN	NaN	NaN	NaN
4/19/14 5:00	0.8648	-20.16	**7.96**	1.383	-25.07	12.74	NaN	NaN	NaN
4/20/14 5:00	2.029	-21.23	**18.69**	2.088	-21.78	19.24	NaN	NaN	NaN
4/21/14 5:00	0.9147	-22.51	**8.42**	NaN	NaN	NaN	NaN	NaN	NaN
4/22/14 5:00	0.9978	-22.98	**9.19**	NaN	NaN	NaN	NaN	NaN	NaN
4/23/14 5:00	0.9474	-23.75	**8.73**	NaN	NaN	NaN	NaN	NaN	NaN

REFERENCES

[1] Stocia, P., and R. L. Moses (1997), Introduction to Spectral Analysis, vol. 1, Prentice Hall Upper Saddle River, NJ.

[2] S. Mousavi, "Covariance based Time Delay Estimation Method," *WiBAR Project Report*, document 164-0015x02, July 2015.

[3] P. Stoica, P. Babu, and Jian Li, "SPICE: A Sparse Covariance-Based Estimation Method for Array Processing," *Signal Processing, IEEE Transactions on*, vol.59, no.2, pp.629, 638, Feb. 2011.

APPENDIX 6.3

```
%D. Lyzenga, 15 Oct 2015
clear all;
 load StereoData
dns = datenum(2014,1,1) + fd - 1;

figure
subplot(2,1,1)
plot(dns,Zm/100,'r')
datetick
ylabel('Zc (m)')
title('Distance (downward) from camera to upper ice surface')
set(gca,'YLim',[5 7])
XLim = get(gca,'XLim');
grid on

load AWACdata

subplot(2,1,2)
plot(mean_t,dist2ice)
datetick
xlabel('2014')
ylabel('Za (m)')
title('Distance (upward) from AWAC to lower ice surface')
set(gca,'XLim',XLim)
set(gca,'YLim',[4 6])
grid on

figure
subplot(2,1,1)
plot(dns,-Zm/100,'r','LineWidth',2)
datetick
ylabel('Zu (m)')
title('Elevation of upper ice surface relative to camera')
set(gca,'YLim',[-7 -5])
XLim = get(gca,'XLim');
grid on

subplot(2,1,2)
plot(mean_t,dist2ice)
datetick
xlabel('2014 ')
ylabel('Zl (m)')
title('Elevation of lower ice surface relative to AWAC sensor')
set(gca,'XLim',XLim)
set(gca,'YLim',[4 6])
grid on

% resample to common time base

t1 = round(min(dns));
t2 = round(max(dns));
```

```
for t = t1:t2
 it = t-t1+1;
 in = find(floor(mean_t)==t); z1(it) = mean(dist2ice(in));
 in = find(floor(dns)==t); z2(it) = mean(Zm(in))/100;
end

ice_thickness = 11.2 - z1 - z2;
t = (t1:t2);

figure
plot(t,ice_thickness,'LineWidth',2)
datetick
xlabel('2014')
ylabel('D (m)')
title('combined ice thickness')
set(gca,'XLim',XLim)
set(gca,'YLim',[0 1])
grid on

fid = fopen('WiBAR_thickness.csv','rt');
nw = 0;
while(1)
  str = fgetl(fid);
  if (str==-1) break; end
  in = strfind(str,',');
  date = str(1:in(1)-1);
  nw = nw+1;
  tw(nw) = datenum(date);
  Thickness = sscanf(str(in(1)+1:end),'%f,%f')
  Tspice(nw) = Thickness(1)/100;
  Tesprit(nw) = Thickness(2)/100;
end

hold
plot(tw,Tspice,'r+',tw,Tesprit,'g*')
legend('AWAC+stereo','WiBAR SPICE','WiBAR ESPRIT')
legend boxoff
hold

% Hamid's WiBar results:

dw = [8,19,28,28+3,28+7,28+12,28+15,28+21,28+24,28+28,28+31+1]+31;
dnw = datenum(2014,1,1) + dw - 1;
Dw = [38,32,63,72,80,65,59,60,52,39,56];

hold
errorbar(dnw,Dw/100,0.03*ones(size(Dw)),'ko')
legend('AWAC+stereo','WiBAR SPICE','WiBAR ESPRIT','Hamid''s results')
legend boxoff
hold
```

APPENDIX 7.1

STEREO DISTANCE CALCULATIONS

Stereo measurements are made by a pair of cameras located at $\boldsymbol{r}_1 = (x_1, y_1, z_1)$ and $\boldsymbol{r}_2 = (x_2, y_2, z_2)$ which view a given object or feature in the directions specified by the unit vector $\boldsymbol{n}_1 = (u_1, v_1, w_1)$ for camera 1 and $\boldsymbol{n}_2 = (u_2, v_2, w_2)$ for camera 2. The line of sight or ray from the camera to the object is described by the equations $\boldsymbol{r} = \boldsymbol{r}_1 + \boldsymbol{n}_1 s_1$ for camera 1 and $\boldsymbol{r}' = \boldsymbol{r}_2 + \boldsymbol{n}_2 s_2$ for camera 2, where s_1 and s_2 are the distances along each line from the corresponding camera.

The distance (d) between any two points along these rays is given by

$$\begin{aligned} d^2 &= |\boldsymbol{r} - \boldsymbol{r}'|^2 = |\boldsymbol{r}_1 + \boldsymbol{n}_1 s_1 - \boldsymbol{r}_2 - \boldsymbol{n}_2 s_2|^2 = |\boldsymbol{r}_1 - \boldsymbol{r}_2|^2 + 2(\boldsymbol{r}_1 - \boldsymbol{r}_2)\cdot(\boldsymbol{n}_1 s_1 - \boldsymbol{n}_2 s_2) + |\boldsymbol{n}_1 s_1 - \boldsymbol{n}_2 s_2|^2 \\ &= |\boldsymbol{r}_1 - \boldsymbol{r}_2|^2 + 2(\boldsymbol{r}_1 - \boldsymbol{r}_2)\cdot(\boldsymbol{n}_1 s_1 - \boldsymbol{n}_2 s_2) + s_1^2 - 2(\boldsymbol{n}_1 \cdot \boldsymbol{n}_2) s_1 s_2 + s_2^2 \\ &= b^2 - 2(b_1 s_1 - b_2 s_2) + s_1^2 - 2\alpha s_1 s_2 + s_2^2 \end{aligned}$$

where $\alpha = \boldsymbol{n}_1 \cdot \boldsymbol{n}_2$, $\boldsymbol{b} = \boldsymbol{r}_2 - \boldsymbol{r}_1$, $b = |\boldsymbol{b}|$, $b_1 = \boldsymbol{b}\cdot\boldsymbol{n}_1$ and $b_2 = \boldsymbol{b}\cdot\boldsymbol{n}_2$. This distance is minimized when

$$\frac{\partial d^2}{\partial s_1} = -2b_1 + 2s_1 - 2\alpha s_2 = 0 \quad \text{and} \quad \frac{\partial d^2}{\partial s_2} = 2b_2 - 2\alpha s_1 + 2s_2 = 0\,.$$

These equations can be written in matrix form as

$$\begin{bmatrix} a_{11} & a_{12} \\ a_{21} & a_{22} \end{bmatrix} \cdot \begin{bmatrix} s_1 \\ s_2 \end{bmatrix} = \begin{bmatrix} b_1 \\ b_2 \end{bmatrix}$$

where $a_{11} = 1$, $a_{12} = -a_{21} = -\alpha$, and $a_{22} = -1$. The solution of this set of equations is

$$s_1 = \frac{1}{\Delta}\begin{vmatrix} b_1 & a_{12} \\ b_2 & a_{22} \end{vmatrix} = \frac{b_1 a_{22} - b_2 a_{12}}{a_{11}a_{22} - a_{12}a_{21}} = \frac{b_1 - \alpha b_2}{1-\alpha^2}\,,$$

$$s_2 = \frac{1}{\Delta}\begin{vmatrix} a_{11} & b_1 \\ a_{21} & b_2 \end{vmatrix} = \frac{b_2 a_{11} - b_1 a_{21}}{a_{11}a_{22} - a_{12}a_{21}} = \frac{\alpha b_1 - b_2}{1-\alpha^2}\,.$$

Ideally, the rays would intersect at the object and the minimum distance d would be zero. However, in practice this may not be the case, for a variety of reasons. The location of closest approach may still be taken as an estimate of the object location, and the minimum distance may be taken as a measure of the error in the estimate. Specifically, we will assume the object is located midway between the points $\boldsymbol{r} = \boldsymbol{r}_1 + \boldsymbol{n}_1 s_1$ and $\boldsymbol{r}' = \boldsymbol{r}_2 + \boldsymbol{n}_2 s_2$ where s_1 and s_2 are given by the above equations, *i.e*.

$$\boldsymbol{o} = (\boldsymbol{r}_1 + \boldsymbol{n}_1 s_1 + \boldsymbol{r}_2 + \boldsymbol{n}_2 s_2)/2 = \boldsymbol{r_c} + \boldsymbol{n}s$$

where $\boldsymbol{r_c} = (\boldsymbol{r}_1 + \boldsymbol{r}_2)/2$, $\boldsymbol{n} = (\boldsymbol{n}_1 s_1 + \boldsymbol{n}_2 s_2)/2s$, and $s = \sqrt{s_1^2 + 2\alpha s_1 s_2 + s_2^2}\Big/2$.

The unit vectors $\boldsymbol{n}_1$ and $\boldsymbol{n}_2$ can be determined from the coordinates of the object in each image. First we define a camera coordinate system with the x_i axis parallel to the row direction in the image (or focal plane), the y_i axis parallel to the column direction, and the z_i axis along the boresight direction of the camera. Next we define the azimuthal angle $\phi_i = \tan^{-1}(x_i / y_i)$ and the polar angle

$$\theta_i = \tan^{-1}(r_i / z_i) \quad \text{where } r_i = \sqrt{x_i^2 + y_i^2}\ .$$

The distances x_i, y_i, and z_i here refer to the coordinates of objects outside the camera. However, they may also be taken as coordinates in the image plane, where z_i is equal to the focal length, except that corrections may need to be made in r_i for lens distortion effects. The unit vector in the line of sight direction is then given by $\boldsymbol{n}_i = (\sin\theta_i \sin\phi_i, \sin\theta_i \cos\phi_i, \cos\theta_i)$ in the camera coordinate system. This direction vector can be translated into a global coordinate system (with axes *X*, *Y*, and *Z*, see Figure 1) using the rotation formula given in Appendix B. This can be done in three steps. First, if the camera x_i axis is not horizontal, *i.e*. parallel to the global $X-Y$ plane, the camera coordinate system can be rotated about the z_i axis by simply adding an offset to ϕ_i. Secondly, the camera coordinate system can be rotated about the vertical (*Z* axis) if necessary to bring the y_i axis into the *Y*–*Z* plane, and finally a rotation about the *X* axis can be effected in order to obtain the components of $\boldsymbol{n}_i$ in the global coordinate system.

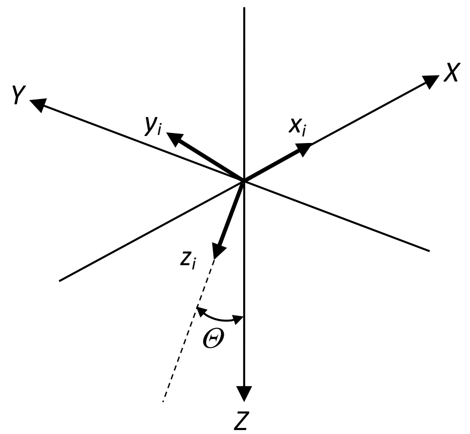

Figure 7.A.1. Diagram of camera (x_i, y_i, z_i) and global (X, Y, Z) coordinate systems. Note Z axis is defined as positive downward.

By design, the cameras were oriented such that the x_i axis is horizontal and the y_i axis is in the global Y–Z plane, so that it is only necessary to rotate $\boldsymbol{n}_i$ about the X axis through the angle Θ (nominally 30 degrees) between the camera z_i axis and the global Z axis. Using the rotation formula in Appendix B, this becomes

$$\boldsymbol{n}_i' = \boldsymbol{n}_i \cos\Theta + (\boldsymbol{n}_i \times \boldsymbol{x}_i)\sin\Theta + \boldsymbol{x}_i\,(\boldsymbol{n}_i \cdot \boldsymbol{x}_i)(1-\cos\Theta)\,.$$

The components of the rotated vector are

$$n_{ix}' = n_{ix} = \sin\theta_i \sin\phi_i\,,$$

$$n_{iy}' = n_{iy}\cos\Theta + n_{iz}\sin\Theta = \cos\theta_i \sin\Theta + \sin\theta_i \cos\Theta \cos\phi_i\,,$$

$$n_{iz}' = n_{iz}\cos\Theta - n_{iy}\sin\Theta = \cos\theta_i \cos\Theta - \sin\theta_i \sin\Theta \cos\phi_i\,.$$

The same result is obtained by computing the coordinates of the original direction vector in the global coordinate system, *i.e.*

$$n_{iX} = \boldsymbol{n}_i \cdot \boldsymbol{X} = n_{ix} = \sin\theta_i \sin\phi_i\,,$$

$$n_{iY} = \boldsymbol{n}_i \cdot \boldsymbol{Y} = n_{iy}\cos\Theta + n_{iz}\sin\Theta = \cos\theta_i \sin\Theta + \sin\theta_i \cos\Theta \cos\phi_i\,,$$

$$n_{iZ} = \boldsymbol{n}_i \cdot \boldsymbol{Z} = -n_{iy}\sin\Theta + n_{iz}\cos\Theta = \cos\theta_i \sin\Theta - \sin\theta_i \sin\Theta \cos\phi_i\,,$$

where we have used

$$\boldsymbol{x}_i \cdot \boldsymbol{X} = 1, \quad \boldsymbol{y}_i \cdot \boldsymbol{X} = 0, \quad \boldsymbol{z}_i \cdot \boldsymbol{X} = 0\,,$$

$$\boldsymbol{x}_i \cdot \boldsymbol{Y} = 0\,, \quad \boldsymbol{y}_i \cdot \boldsymbol{Y} = \cos\Theta\,, \quad \boldsymbol{z}_i \cdot \boldsymbol{Y} = \sin\Theta\,,$$

$$\boldsymbol{x}_i \cdot \boldsymbol{Z} = 0\,, \quad \boldsymbol{y}_i \cdot \boldsymbol{Z} = -\sin\Theta\,, \quad \boldsymbol{z}_i \cdot \boldsymbol{Z} = \cos\Theta\,.$$

APPENDIX 7.2

ROTATION OF A VECTOR ABOUT AN AXIS

The rotation of the vector $\boldsymbol{v}$ about the axis specified by the unit vector $\boldsymbol{a}$ yields the vector

$$\boldsymbol{v}' = \boldsymbol{v}\cos\theta + (\boldsymbol{v}\times\boldsymbol{a})\sin\theta + \boldsymbol{a}(\boldsymbol{v}\cdot\boldsymbol{a})(1-\cos\theta)$$

where θ is the angle of rotation about $\boldsymbol{a}$. This is not easy to derive but is easy to confirm. The properties required of $\boldsymbol{v}'$ are that (1) its length must equal that of $\boldsymbol{v}$, (2) its component along the axis of rotation must equal that of $\boldsymbol{v}$, and (3) the component of $\boldsymbol{v}'$ normal to the axis of rotation must lie at an angle θ from that of $\boldsymbol{v}$. The first property is confirmed by noting that length of $\boldsymbol{v}'$ as given by the above equation is the square root of

$$\begin{aligned}\boldsymbol{v}'\cdot\boldsymbol{v}' &= (\boldsymbol{v}\cdot\boldsymbol{v})\cos^2\theta + |\boldsymbol{v}\times\boldsymbol{a}|^2\sin^2\theta + (\boldsymbol{v}\cdot\boldsymbol{a})^2(1-\cos\theta)^2 + 2(\boldsymbol{v}\cdot\boldsymbol{a})^2\cos\theta(1-\cos\theta)\\ &= (\boldsymbol{v}\cdot\boldsymbol{v})\cos^2\theta + |\boldsymbol{v}\times\boldsymbol{a}|^2\sin^2\theta + (\boldsymbol{v}\cdot\boldsymbol{a})^2\sin^2\theta = \boldsymbol{v}\cdot\boldsymbol{v}\,.\end{aligned}$$

The component of $\boldsymbol{v}'$ along the axis of rotation is

$$(\boldsymbol{v}'\cdot\boldsymbol{a})\boldsymbol{a} = (\boldsymbol{v}\cdot\boldsymbol{a})\boldsymbol{a}\cos\theta + (\boldsymbol{v}\cdot\boldsymbol{a})\boldsymbol{a}(1-\cos\theta) = (\boldsymbol{v}\cdot\boldsymbol{a})\boldsymbol{a}\,.$$

The component of $\boldsymbol{v}'$ normal to the axis of rotation is

$$\boldsymbol{v}' - (\boldsymbol{v}'\cdot\boldsymbol{a})\boldsymbol{a} = \boldsymbol{v}' - (\boldsymbol{v}\cdot\boldsymbol{a})\boldsymbol{a} = \boldsymbol{v}\cos\theta + (\boldsymbol{v}\times\boldsymbol{a})\sin\theta - \boldsymbol{a}(\boldsymbol{v}\cdot\boldsymbol{a})\cos\theta$$

while the component of $\boldsymbol{v}$ normal to this axis is $\boldsymbol{v}-(\boldsymbol{v}\cdot\boldsymbol{a})\boldsymbol{a}$. The dot product of these two components is

$$\begin{aligned}[\boldsymbol{v}'-(\boldsymbol{v}\cdot\boldsymbol{a})\boldsymbol{a}]\cdot[\boldsymbol{v}-(\boldsymbol{v}\cdot\boldsymbol{a})\boldsymbol{a}] &= [\boldsymbol{v}\cos\theta + (\boldsymbol{v}\times\boldsymbol{a})\sin\theta - \boldsymbol{a}(\boldsymbol{v}\cdot\boldsymbol{a})\cos\theta]\cdot[\boldsymbol{v}-(\boldsymbol{v}\cdot\boldsymbol{a})\boldsymbol{a}]\\ &= (\boldsymbol{v}\cdot\boldsymbol{v})\cos\theta - (\boldsymbol{v}\cdot\boldsymbol{a})^2\cos\theta\,.\end{aligned}$$

Since the lengths of $\boldsymbol{v}$ and $\boldsymbol{v}'$ are equal, and the lengths of their components along the axis of rotation are equal, the lengths of their normal components are also equal, and are given by the square root of $v_n^2 = (\boldsymbol{v}\cdot\boldsymbol{v}) - (\boldsymbol{v}\cdot\boldsymbol{a})^2$. The angle between these components is therefore given by the inverse cosine of $[\boldsymbol{v}'-(\boldsymbol{v}\cdot\boldsymbol{a})\boldsymbol{a}]\cdot[\boldsymbol{v}-(\boldsymbol{v}\cdot\boldsymbol{a})\boldsymbol{a}]/v_n^2 = \cos\theta$.

APPENDIX 8

```
% MTU GLRC ICE PROCESSING
% C.Kontoes NortekUSA 2014.08
% * this script is an example and NOT offical Nortek code
% [Z:\kontoes On My Mac\Desktop\GLRC\AWAC1234_GLRC_ICE.wad]
%  1   Month                  (1-12)
%  2   Day                    (1-31)
%  3   Year
%  4   Hour                   (0-23)
%  5   Minute                 (0-59)
%  6   Second                 (0-59)
%  7   Pressure               (dbar)
%  8   AST Distance1 (Beam4)           (m)
%  9   AST Distance2 (Beam4)           (m)
% 10   AST Quality (Beam4)             (counts)
% 11   Analog input
% 12   Velocity (Beam1|X|East)         (m/s)
% 13   Velocity (Beam2|Y|North)        (m/s)
% 14   Velocity (Beam3|Z|Up)           (m/s)
% 15   Amplitude (Beam1)               (counts)
% 16   Amplitude (Beam2)               (counts)
% 17   Amplitude (Beam3)               (counts)
%========== set up parameters =========
ATM = 10.1325;
%mean atm pressure in dbar
% Crop when AWAC was out of the water or knocked over, etc
Crop AWACdates = datenum([[1999 1 1 0 0 0];
[2014 6 1 0 0 0]]);

% Use offsetDates to trip time period for pressure offset calculation
offsetDates = datenum([[2013 12 13 0 0 0]; [2013 12 30 0 0 0]]);

% Load wave data file
wad = load('AWAC1234_GLRC_ICE.wad');
%========================================
raw_t = datenum(wad(:,[3 1 2 4 5 6]));
% convert time to matlab time
it = find(raw_t >= cropAWACdates(1) & raw_t < cropAWACdates(2));% crop useable dates
raw_t = raw_t(it,:); % raw_times
raw_p = wad(it,7); % raw_pressure
raw_wave = wad(it,8); % wave = raw_ast1
raw_ice = wad(it,9); % ice = raw_ast2
```

```
% Plot data
figure(1);
plot(raw_t,raw_wave,'g', raw_t,raw_ice,'c', raw_t,raw_p,'b')
legend('raw-wave', 'raw-ice', 'raw-p');
% reshape vectors into columnwise bursts
burst_t = reshape(raw_t,2048,[]);
burst_p = reshape(raw_p,2048,[]);
burst_wave = reshape(raw_wave,2048,[]);
burst_ice = reshape(raw_ice,2048,[]);

%%%% Do a little quality control since the mount was wobbly.
% despike bursts
figure(2)
ds1 = burst_wave;
ds2 = burst_ice;
% despiking involves recursive 8,6,4*std to remove outliers.
% I also added a very simple single point check to remove anything that is
% impossible (i.e. change in elevation exceeds possible acceleration)
for n = 1:size(ds1,2)
  tmp1 = ds1(:,n);
  tmp2 = ds2(:,n);
  for nn = [8 6 4]
    tmp1(tmp1 > (nanmean(tmp1) + nn*std(tmp1)) | ...
      tmp1 < (nanmean(tmp1) - nn*std(tmp1)))=nan;
    tmp2(tmp2 > (nanmean(tmp2) + nn*std(tmp2)) | ...
      tmp2 < (nanmean(tmp2) - nn*std(tmp2)))=nan;
  end
  % check for exceeding the speed of a "slow rain drop" i.e. 3m/s (thanks google)
  tmp1(abs(diff(tmp1)) > 1.5)=nan;
  tmp2(abs(diff(tmp2)) > 1.5)=nan;

  % if burst has more than 10% bad ast data, discard entire burst
  if numel(find(isnan(tmp1)))/2048 > 0.10
    disp([num2str(n) ' = bad burst AST1'])
    tmp1 = nan(size(tmp1));
  end
  if numel(find(isnan(tmp2)))/2048 > 0.10
    disp([num2str(n) ' = bad burst AST2'])
    tmp2 = nan(size(tmp2));
  end
  ds1(:,n) = tmp1; % replace raw burst data with despiked burst
```

```
%%% the following will allow you to see the effects of the AST QC per
%%% burst (this will take a LONG time)
%figure(999)
%plot(burst_t(:,n),burst_wave(:,n),'g', burst_t(:,n),ds1(:,n),'r')
%title(['Burst # ' num2str(n)])
%pause(.1)
end

% Average despiked burst data
mean_t = nanmean(burst_t);
mean_p = nanmean(burst_p);
mean_wave = nanmean(ds1);
mean_ice = nanmean(ds2);

figure(1), hold on
plot(mean_t,mean_p,'k-*', mean_t,mean_wave,'r-*');
legend('raw-wave', 'raw-ice', 'raw-p', 'mean-p', 'mean-wave');
datetick;

% Crop data for pre ice conditions for pressure offset calculation
it2 = find(mean_t > offsetDates(1) & mean_t < offsetDates(2));
T = mean_t(it2);
P = mean_p(it2);
WAVE_AST1 = mean_wave(it2);
ICE_AST2 = mean_ice(it2);
figure(1)
plot(T,P,'b', T,WAVE_AST1,'g', T,P-WAVE_AST1,'r')
legend('raw-wave', 'raw-ice', 'raw-p', 'mean-p', 'mean-wave','press', 'wave-ast1', 'residual')
datetick
% import Baro pressure data
fid = fopen('Baro Data 2.txt');
b = textscan(fid, '%f%*c%f%*c%f%f%*c%f%f');
fclose(fid)
% build matlab datenum from timestamp in .txt
% NOTICE: -4hr time zone correction on b{4}
raw_baro_t = datenum(double([b{3} b{1} b{2} b{4}-4 b{5} zeros(length(b{5}),1) ]));
raw_baro_p = b{6}-ATM;

% figure(2)
% plot(mean_t,mean_p,'b-*', raw_baro_t, raw_baro_p, 'k-*')
% legend('mean-p', 'raw-baro-p')

% resample raw_baro_P at times in T
```

```
BARO_P = interp1(raw_baro_t, raw_baro_p, T);
figure(2), hold on
plot(T,P,'b', T,BARO_P,'g', T,WAVE_AST1,'m')
legend('P', 'BARO-P', 'WAVE-AST1')
offset_P = P - BARO_P - WAVE_AST1;
disp(' '), disp('Calculated Pressure Offset = '), disp(' ')
disp(['   ' num2str(nanmean(offset_P)) ' dbar']), disp(' ')

%%%%% OFFSET = THIS TURNS OUT TO BE -0.2650 dbar
% corrected Pressure = AWAC with corrected offset and baro pressure removed
corr_P = P - nanmean(offset_P) - BARO_P;

figure(2), hold on
plot(T,corr_P,'k', T,corr_P-WAVE_AST1,'r', ...
   [T(1) T(end)],[nanmean(corr_P-WAVE_AST1)
nanmean(corr_P-WAVE_AST1)],'R-.')
legend('P', 'BARO-P', 'WAVE-AST1', 'corr-p', 'P-Offset', 'mean-P-Offset')
ylabel('dbar')

%  THE FOLLOWING WILL CALCULATE ICE KEEL ON THE FULL DATA SET
% resample raw_baro_P at times mean_t (i.e. burst mean times)
mean_baro_p = interp1(raw_baro_t, raw_baro_p, mean_t);
mean_corr_p = mean_p - nanmean(offset_P) - mean_baro_p;
depth_P = mean_corr_p;
% atler with salinity changes?
dist2ice = mean_ice;  % alter with salinity changes?
ICE_DRAFT = depth_P - dist2ice; %i.e. mean_corr_p - mean_ice

figure(3)
plot(mean_t,mean_p, mean_t,mean_corr_p, mean_t,mean_ice, mean_t,ICE_DRAFT)
legend('mean-p','mean-corr-p','ice-ast2','ICE-DRAFT')
ylabel('dbar')
figure(4)
plot(mean_t,ICE_DRAFT)
datetick
xlabel('date/time')
ylabel('ice draft (m)')
title('AWAC based ice draft, 2013-2014')
grid on

% looks reasonable according to http://earthobservatory.nasa.gov/IOTD/view.php?id=83541
```

Appendix 10.1 MATLAB Script for Monthly Wind/Wave Avg. Time Series

```
clear
%S. Polisuk, Fall 2014
%Record number of stations in current lake:
num_stations = 511; %number of '.onlns' files in the current director

%Initialize output tables:
december_windspeeds = zeros(2012-1979,num_stations+1);
march_windspeeds = zeros(2012-1979,num_stations+1);
june_windspeeds = zeros(2012-1979,num_stations+1);
september_windspeeds = zeros(2012-1979,num_stations+1);

december_waveheights = zeros(2012-1979,num_stations+1);
march_waveheights = zeros(2012-1979,num_stations+1);
june_waveheights = zeros(2012-1979,num_stations+1);
september_waveheights = zeros(2012-1979,num_stations+1);

%%
for filecount = 1:num_stations
    tic
    clear baddata
    disp(filecount)
    %Create three-digit current station number with proper amount of preceding zeros:
    if filecount < 10
    filenum = ['00' num2str(filecount)];
    elseif filecount < 100
    filenum = ['0' num2str(filecount)];
    else
    filenum = num2str(filecount);
    end

    %Read in this station's data:
    stationinfo = dlmread(['ST95' filenum '.onlns']);
    datedata = stationinfo(:,1);
    datestring = num2str(datedata);
    %Initialize date logical vectors outside loop to optimize speed:
    isyear = str2num(datestring(:,1:4)); %will be used to select only entries for current year
    ismonth = str2num(datestring(:,5:6));

    %INNER LOOP: From 1979 to 2012
    for year = 1979 : 2012
    %Select for this year:
```

```
        iscurrentyear = isyear == year; %logical vector used to select only entries for current year

        %DECEMBER=====================================================
        %Select only the specific month we need:
        iscurrentmonth = ismonth == 12; %select only those entries from the current month

%Make a vector of hourly WIND SPEEDS for the month and add its average to the output table:
        wind_data = stationinfo(:,5);
        wind_data = wind_data(iscurrentyear & iscurrentmonth);
%selects all entries from this year and month
        %Delete all erroneous entries:
        baddata = wind_data < 0;
        wind_data(baddata)=[];
        %Write this month's average wind speed to the output table (values of -99 or -999):
        december_windspeeds(year-1978,filecount) = mean(wind_data);

        %Make a vector of hourly WAVE HEIGHTS for the month:
        wave_data = stationinfo(:,10);
        wave_data = wave_data(iscurrentyear & iscurrentmonth); %selects all entries from this year and
month
        %Delete all erroneous entries (values of -99 or -999):
        baddata = wave_data < 0;
        wave_data(baddata)=[];
        %Write this month's average wave height to the output table:
      december_waveheights(year-1978,filecount) = mean(wave_data);

        %MARCH========================================================
        %Select only the specific month we need:
        iscurrentmonth = ismonth == 4; %select only those entries from the current month

%Make a vector of hourly WIND SPEEDS for the month and add its average to the output table:
        wind_data = stationinfo(:,5);
        wind_data = wind_data(iscurrentyear & iscurrentmonth);
%selects all entries from this year and month
        %Delete all erroneous entries:
        baddata = wind_data < 0;
        wind_data(baddata)=[];
        %Write this month's average wind speed to the output table (values of -99 or -999):
        march_windspeeds(year-1978,filecount) = mean(wind_data);

          %Make a vector of hourly WAVE HEIGHTS for the month:
        wave_data = stationinfo(:,10);
```

```
	wave_data = wave_data(iscurrentyear & iscurrentmonth); %selects all entries from this year and 
month
	%Delete all erroneous entries (values of -99 or -999):
	baddata = wave_data < 0;
	wave_data(baddata)=[];
	%Write this month's average wave height to the output table:
	march_waveheights(year-1978,filecount) = mean(wave_data);

	%JUNE=======================================================
	%Select only the specific month we need:
	iscurrentmonth = ismonth == 6; %select only those entries from the current month
 %Make a vector of hourly WIND SPEEDS for the month and add its average to the output table:
	wind_data = stationinfo(:,5);
	wind_data = wind_data(iscurrentyear & iscurrentmonth); 
%selects all entries from this year and month
	%Delete all erroneous entries:
	baddata = wind_data < 0;
	wind_data(baddata)=[];
	%Write this month's average wind speed to the output table (values of -99 or -999):
	june_windspeeds(year-1978,filecount) = mean(wind_data);

	%Make a vector of hourly WAVE HEIGHTS for the month:
	wave_data = stationinfo(:,10);
	wave_data = wave_data(iscurrentyear & iscurrentmonth); %selects all entries from this year and 
month
	%Delete all erroneous entries (values of -99 or -999):
	  baddata = wave_data < 0;
	wave_data(baddata)=[];
	%Write this month's average wave height to the output table:
	june_waveheights(year-1978,filecount) = mean(wave_data);


	%SEPTEMBER=======================================================
	%Select only the specific month we need:
	iscurrentmonth = ismonth == 9; %select only those entries from the current month
 %Make a vector of hourly WIND SPEEDS for the month and add its average to the output table:
	wind_data = stationinfo(:,5);
	wind_data = wind_data(iscurrentyear & iscurrentmonth); %selects all entries from this year and 
month
	%Delete all erroneous entries:
	baddata = wind_data < 0;
	wind_data(baddata)=[];
	%Write this month's average wind speed to the output table (values of -99 or -999):
```

```
        september_windspeeds(year-1978,filecount) = mean(wind_data);

            %Make a vector of hourly WAVE HEIGHTS for the month:
            wave_data = stationinfo(:,10);
            wave_data = wave_data(iscurrentyear & iscurrentmonth);
%selects all entries from this year and month
            %Delete all erroneous entries (values of -99 or -999):
            baddata = wave_data < 0;
            wave_data(baddata)=[];
            %Write this month's average wave height to the output table:
        september_waveheights(year-1978,filecount) = mean(wave_data);
            end
            toc
end

%Now average the monthly averages from all the stations into one lake-wide monthly average for each
year
for j = 1:34
            %DECEMBER:
            dec_wind = december_windspeeds(j,1:end-1);
            dec_wind(isnan(dec_wind)) = [];
            december_windspeeds(j,end) = mean(dec_wind);
            dec_wave = december_waveheights(j,1:end-1);
            dec_wave(isnan(dec_wave)) = [];
            december_waveheights(j,end) = mean(dec_wave);
            %MARCH:
            march_wind = march_windspeeds(j,1:end-1);
            march_wind(isnan(march_wind)) = [];
            march_windspeeds(j,end) = mean(march_wind);
            march_wave = march_waveheights(j,1:end-1);
            march_wave(isnan(march_wave)) = [];
            march_waveheights(j,end) = mean(march_wave);
            %JUNE:
            june_wind = june_windspeeds(j,1:end-1);
            june_wind(isnan(june_wind)) = [];
            june_windspeeds(j,end) = mean(june_wind);
            june_wave = june_waveheights(j,1:end-1);
            june_wave(isnan(june_wave)) = [];
            june_waveheights(j,end) = mean(june_wave);
            %SEPTEMBER:
            sept_wind = september_windspeeds(j,1:end-1);
            sept_wind(isnan(sept_wind)) = [];
            september_windspeeds(j,end) = mean(sept_wind);
```

```
        sept_wave = september_waveheights(j,1:end-1);
        sept_wave(isnan(sept_wave)) = [];
        september_waveheights(j,end) = mean(sept_wave);
end

%Finally, write these yearly averages to .csv files:
lakename = 'Lake_Superior';
%DECEMBER:
csvwrite([lakename '_Yearly_December_WindSpeed_Avgs.csv'], december_windspeeds(:,end));
csvwrite([lakename '_Yearly_December_WaveHeight_Avgs.csv'], december_waveheights(:,end));
%MARCH:
csvwrite([lakename '_Yearly_March_WindSpeed_Avgs.csv'], march_windspeeds(:,end));
csvwrite([lakename '_Yearly_March_WaveHeight_Avgs.csv'], march_waveheights(:,end));
%JUNE:
csvwrite([lakename '_Yearly_June_WindSpeed_Avgs.csv'], june_windspeeds(:,end));
csvwrite([lakename '_Yearly_June_WaveHeight_Avgs.csv'], june_waveheights(:,end));
%SEPTEMBER:
csvwrite([lakename '_Yearly_September_WindSpeed_Avgs.csv'], september_windspeeds(:,end));
csvwrite([lakename '_Yearly_September_WaveHeight_Avgs.csv'], september_waveheights(:,end));
```

Appendix 10.2: MATLAB Script for Preprocessing WIS-NDBC Validation

```
% Great Lakes Wave Information Studies Climate Data Manipulation
% Matt Irish, 5 September 2014
% We'll read in data sequentially for an entire lake and (later) make calculations
%with it. Loading all the .onlns files into arrays station-by-station, we'll
%have to make our calculations file-by-file, and average/conglomerate each file's
%output at the end.
 %BEFORE RUNNING THIS SCRIPT: put all the .onlns files for the lake into the current folder.
% To automate the file reading, make a structure of all the filenames that end in ".csv":
filenames = dir('*.onlns'); %asterisk punctuation signifies all files with that extension. Fancy!
 %Preallocate vector size for efficiency:
avgwindspeeds = zeros(length(filenames),4);

% Start the "for" loop that will run through each file, importing, doing
% calculations and then moving on to the next point.
tic
 station_id = 499; %number of '.onlns' file we're querying
 %Read in the data
stationdata = dlmread(['ST95' filenum '.onlns']);
 %Put the info for this station into our main matrix. Each row in our matrix
%will contain one station's location and average windspeed.
avgwindspeeds(:,1) = stationdata(1,2); %station ID
avgwindspeeds(:,2) = stationdata(1,3); %latitude
avgwindspeeds(:,3) = stationdata(1,4); %longitude
 %Values of "-999" indicate error values where windspeeds weren't
%possible to record or the data was flawed. We'll get rid of the whole row for these values. We need to
eliminate these
%efficiently, using a logical vector:
baddata = stationdata(:,5) < 0;
stationdata(baddata,:) = [];
 %Now add the time average of the windspeeds for this location to our final matrix:
avgwindspeeds(filecount,4) = mean(stationdata(:,5));
%puts avg wave height in column 4
toc
 %Now write our table to a csv file:
csvwrite('wis_avg_windspeed_lake_michigan', avgwindspeeds);
 %Make the lat, lon, and windspeed columns their own vectors for easy use:
wind_lat = avgwindspeeds(:,2);
wind_lon = avgwindspeeds(:,3);
wind_speeds = avgwindspeeds(:,4);
```

APPENDIX 10.3

```
################################################
#	Carl Lachner
#	16 October 2015
#	DoE Ice Project:  NSIDC data parsing script
################################################
#Start of Script
locFile = open('ice.loc', 'r')
dataFile = open('data2.dat', 'r')
outputFile = open('output.csv', 'w')
locationDict = {}
for line in locFile:
	location = line[4:35]
	code = line[:3]
	locationDict[code] = location

print >> outputFile, 'Location,Date,Total Thickness,Lake Ice Thickness,’
print >> outputFile, ‘Snow Ice Thickness,Estimated Flag'

for line in dataFile:
	print >> outputFile, locationDict[line[:3]] + ',' + line[6:8] + '/' + line[8:10] + '/' + line[4:6]
	print >> ',' + line[11:14] + ',' + line[14:17] + ',' + line[17:20] + ',' + line[10]
```

APPENDIX 10.4

MatLab processing script for ice thickness data curve fitting, 1968 – 1979, contributed by Michiel van Nieuwstadt:

```
%% proc_ice.m
%% mvn, 19nov15

[ndata, text, alldata]  = xlsread('GreatLakesIceThicknessData.xlsx', 'output.csv');

yearvec = [1968, 1969, 1970, 1971, 1973, 1974, 1975, 1976, 1977, 1978, 1979];

ind0 = [1160, 1173, 1185, 1200 ,1210 ,1228, 1246 ,1261 ,1282 ,1303 ,1322 , 1336];
%%ind1 = [1172, 1184, 1199,1209 ,1227 ,1245, 1260 ,1281 ,1302 ,1321 ,1335 ];

dates_1968 = text(1160:1172,2);
dates_1969 = text(1173:1184,2);
dates_1970 = text(1185:1199,2);
dates_1971 = text(1200:1209,2);
dates_1973 = text(1210:1227,2);
dates_1974 = text(1228:1245,2);
dates_1975 = text(1246:1260,2);
dates_1976 = text(1261:1281,2);
dates_1977 = text(1282:1302,2);
dates_1978 = text(1303:1321,2);
dates_1979 = text(1322:1335,2);

   for i2 = 1:length(yearvec),
      yr = yearvec(i2);
      str3 = ['t_tot_', num2str(yr), ' = ndata((ind0(1, ', num2str(i2), ')-1):(ind0(1, ', num2str(i2+1),
')-2), 1);'];
      eval(str3);
      str4 = ['t_tot_', num2str(yr), ' = t_tot_', num2str(yr), '(~isnan(t_tot_', num2str(yr), '));'];
      eval(str4);
   end;

if 1 == 1,
datesn_1968 = datenum(dates_1968) - datenum('1/1/1968');
datesn_1969 = datenum(dates_1969) - datenum('1/1/1969');
datesn_1970 = datenum(dates_1970) - datenum('1/1/1970');
datesn_1971 = datenum(dates_1971) - datenum('1/1/1971');
datesn_1973 = datenum(dates_1973) - datenum('1/1/1973');
datesn_1974 = datenum(dates_1974) - datenum('1/1/1974');
datesn_1975 = datenum(dates_1975) - datenum('1/1/1975');
datesn_1976 = datenum(dates_1976) - datenum('1/1/1976');
```

```
datesn_1977 = datenum(dates_1977) - datenum('1/1/1977');
datesn_1978 = datenum(dates_1978) - datenum('1/1/1978');
datesn_1979 = datenum(dates_1979) - datenum('1/1/1979');
else,
   for i2 = 1:length(yearvec),
   end;
end;

for i2 = 1:length(yearvec),
   yr = yearvec(i2);
   ystr = num2str(yr);

   str5 = ['datesn_', ystr, ' = datesn_', ystr, '(1:length(t_tot_', ystr, '));'];
   eval(str5);

   eval(['xx0 = datesn_', ystr, ';']);
   eval(['y0 = t_tot_', ystr, ';']);
   X = [ones(length(xx0),1), xx0, xx0.^2];
   coef = X\y0;
   yest = X*coef;
   eval(['y_', ystr, '_est = yest;']);
end;

   alldates = [datesn_1968; datesn_1969; datesn_1970; datesn_1971;  datesn_1973; datesn_1974;
datesn_1975; datesn_1976; ...
      datesn_1977; datesn_1978; datesn_1979];
   all_t = [t_tot_1968; t_tot_1969; t_tot_1970; t_tot_1971; t_tot_1973; t_tot_1974; t_tot_1975;
t_tot_1976; t_tot_1977; ...
      t_tot_1978; t_tot_1979];

   X_all = [ones(length(alldates),1), alldates, alldates.^2];
   coef_all = X_all\all_t;
   all_t_est = X_all*coef_all;
   std_fit = std(all_t_est - all_t);
   x_all_fit = (min(alldates):1:max(alldates))';
   X_all_fit = [ones(length(x_all_fit),1), x_all_fit, x_all_fit.^2];
   all_t_fit = X_all_fit*coef_all;

alldn = datenum(2014,1,1) + alldates;
allfitdn = datenum(2014,1,1) + x_all_fit;


load StereoData
dns = datenum(2014,1,1) + fd - 1;
load AWACdata
```

```
% resample to common time base

t1 = round(min(dns));
t2 = round(max(dns));

for t = t1:t2
 it = t-t1+1;
 in = find(floor(mean_t)==t); z1(it) = mean(dist2ice(in));
 in = find(floor(dns)==t); z2(it) = mean(Zm(in))/100;
end

ice_thickness = (11.2 - z1 - z2)*100; % cm
t_ice_thickness = (t1:t2);

wibardata_dates = datenum(['02/08/15'; '02/19/15'; '02/27/15'; '03/03/15'; '03/07/15'; '03/13/15';
'03/16/15'; ...
    '03/22/15'; '03/24/15'; '03/28/15'; '04/14/15']) - datenum('01/01/2015');
wibardata_t = [38; 32; 63; 72; 80; 65; 59; 60; 52; 39; 56];
wibardata_dates_dn = datenum(2014,1,1) + wibardata_dates;

figure(100); clf;
plot(alldn, all_t, 'x', allfitdn, all_t_fit, 'x-', ...
    allfitdn, all_t_fit-2*std_fit, 'x-', ...
    allfitdn, all_t_fit+2*std_fit, 'x-', ...
    t_ice_thickness, ice_thickness,'k', ...
    wibardata_dates_dn, wibardata_t,   'x-', 'LineWidth', 2);
grid on;
datetick;
legend('historical data', 'fit', 'fit - 2*sigma', 'fit + 2*sigma','AWAC+Stereo data','Wibar data', 4);
ylabel('ice thickness (cm)')
```